STRUCTURE AND PHOTO-INDUCED ELECTRON TRANSFER IN IONIC LIQUIDS

by

BONING WU

A dissertation submitted to the

School of Graduate Studies

Rutgers, The State University of New Jersey

In partial fulfillment of the requirements

For the degree of

Doctor of Philosophy

Graduate Program in Chemistry and Chemical Biology

Written under the direction of

Edward W. Castner, Jr.

And approved by

_____

_____

_____

_____

_____

New Brunswick, New Jersey

January, 2018

ABSTRACT OF THE DISSERTATION

Structure and Photo-Induced Electron Transfer in Ionic Liquids

By BONING WU

Dissertation Director:

Edward W. Castner, Jr.

Applications of ionic liquids (ILs) require a thorough understanding of the structures and reaction dynamics in these ionic solvents. The current thesis contributes to this understanding through two major projects. The first project examines the bulk structure of ILs and the second involves photo-induced bimolecular electron transfer reactions in IL solvents. In the structure project, we report structural properties for a series of silicon-substituted ionic liquids and some liquid zwitterions, comparing their structures to those of analogous "simple" ionic liquids. Structure factors of the liquids were measured using high energy X-ray diffraction and also computed from molecular dynamics simulations. As part of the simulation work, new transferable parameters for specific ILs were calibrated and added to the existing force fields. In the electron transfer project, we systematically studied the bimolecular electron transfer reactions in ILs by measuring reductive fluorescence quenching using steady-state and time-resolved methods. Molecular dynamics simulations and density-functional methods were used to explore solvation structures and electronic couplings between electron donors and acceptors. We suggest that the small-amplitude motions within contact F-Q pairs, which gate

the electronic coupling, to be the limiting dynamics of intrinsic bimolecular electron transfer rates in ILs.

Acknowledgements

I acknowledge many people who had helped me in the long journey toward the goal of obtaining a Ph. D. degree.

First I thank my advisor, Prof. Edward Castner. He not only provided excellent guidance of on my research, but also gave much useful advice and strong recommendations regarding to my future career. I thank the senpai in the lab, Dr. Min Liang, Dr. Marie Thomas, Dr. Sufia Khatun, for teaching me the lab's techniques, and my other labmates, Ms. Aleksandra Barbara Biedron, Ms. Man Zhao and Ms. Yu Wang for their help with experiments and discussions.

I thank Prof. Mark Maroncelli from Penn State for his help in my research, Prof. Juan Carlos Araque from Benedictine College and Prof. Claudio Margulis from University of Iowa for sharing their computational resources. I also thank all the group members in the Maroncelli and Margulis groups for helpful discussions.

I also thank many other people at Rutgers University, especially Profs. David Case, Eric Garfunkel and Robert Hayes for joining my committee, Dr. Nagarajan Murali for the assistance with the PG-SE NMR experiments, Prof. KiBum Lee and Mr. Letao Yang for assistance with the cyclic voltammetry experiments, Prof. Gene Hall for X-ray fluorescence experiments and Dr. Alexei Ermakov for the help repairing lab instruments.

I thank NSF and DOE for the research fundings.

I thank Prof. Eric Vauthey at University of Geneva, Prof. Sharon Lall-Ramnarine at Queensborough Community College, Prof. James Wishart at Brookhaven National Lab, Prof. Hideaki Shirota at Chiba University, Profs. Kosuke Kuruda, Takatsugu Endo and Kenji Takahashi from Kanazawa University and Dr. Peng Liu at Rutgers University for sharing samples with us.

I thank the scientists at APS Sector 11, Dr. Olaf J. Borkiewicz, Kevin A. Beyer and Dr. Karena W. Chapman, for their help in X-ray data collection.

I thank all my friends and classmates at Rutgers University.

Finally I thank my parents, grandparents and all my other relatives, who raised me and supported me during my research career.

Table of Contents

List of Abbreviations

APS:	Advanced Photon Sources
CK:	Collins-Kimball model
CM:	Classical Marcus model
COM:	Center of Mass
CT state:	the Charge Transfer State
CV:	Cyclic Voltammetry
DFT:	Density Functional Theory
ES:	Extended Sink model
ET:	Electron Transfer
FSDP:	First Sharp Diffraction Peak
IL:	Ionic Liquids
IRF:	instrument response function
LE state:	the Locally Excited State
MD Simulations:	Molecular Dynamics Simulations
NMR:	Nuclear Magnetic Resonance
PG-SE:	pulse-gradient spin echo
PME:	Particle Mesh Ewald
RTIL:	Room temperature ionic liquids
SiIL:	Silicon Containing Ionic Liquids
SM:	Smoluchowski model
TCSPC:	Time Correlated Single Photon Counting
$BETI^-$:	bis(pentafluoroethanesulfonyl)imide
C_4DMAP^+:	N-butyl-4-dimethylaminopyridinium
C_8DMAP^+:	N-octyl-4-dimethylaminopyridinium
$C_{10}DMAP^+$:	N-decyl-4-dimethylaminopyridinium
$C(CN)_3^-$:	tricyanomethanide
CH_3CN:	acetonitrile
C-mim^+:	1-methyl-3-neopentylimidazolium
CNA:	9-cyanoanthracene
CNMeA:	9-cyano-10-methylanthracene
DCNA:	9,10-dicyanoanthracene
DMA:	N,N-dimethylaniline
DMAP:	N-alkyl-4-dimethylaminopyridinium
DMPT:	N,N-dimethyl-p-toluidine
FSI^-:	bis(fluorosulfonyl)imide
$Im_{2,1}^+$:	1-ethyl-3-methylimidazolium
$N(CN)_2^-$:	dicyanamide
NTf_2^-:	bis(trifluoromethylsulfonyl)imide
OAc^-:	acetate
OE_2eim^+/OAc^-:	1-[2-(2-methoxyethoxy)ethyl]-3-ethyl-imidazolium acetate
OE_2imC_3C:	1-[2-(2-methoxyethoxy)ethyl]-3-(3-carboxypropyl)-imidazolium
OE_2imC_5C:	1-[2-(2-methoxyethoxy)ethyl]-3-(3-carboxypentyl)-imidazolium
$P_{14,6,6,6}^+$:	hexyltetradecylphosphonium
SCN^-:	thiocyanate
$SeCN^-$:	selenocyanate
Si-mim^+:	1-trimethylsilylmethyl-3-methyl-imidazolium
SiOSi-mim^+:	1-pentamethyldisiloxymethyl-3-methyl-imidazolium
Si-$pyrr^+$:	1-trimethylsilylmethyl-3-methyl-pyrrodinium
Si-C_3-mim^+:	1-methyl-3-trimethylsilylpropylimidazolium

Si-C_3-$Pyrr^+$:	N-methyl-N-trimethylsilylpropylpyrrolidinium
TBAP:	tetrabutylammonium perchlorate
TCNA:	2,6,9,10-tetracyanoanthracene
TrCNA:	2,9,10-tricyanoanthracene
Zw-IL:	Zwitterionic Liquids

B. Wu, M. Maroncelli, and E. W. Castner, Jr., "Photoinduced Bimolecular Electron Transfer in Ionic Liquids.", *J. Am. Chem. Soc.*, **2017**, doi: 10.1021/jacs.7b07611.

B. Wu, M. Liang, M. Maroncelli, and E. W. Castner, Jr., "Photo-Induced Bimolecular Electron Transfer from Cyano-Anions in Ionic Liquids.", J. Phys. Chem. B, **2015**, *119*, 14790–14799, doi: 10.1021/acs.jpcb.5b09216.

B. Wu, Y. Yamashita, T. Endo, K. Takahashi, and E. W. Castner, Jr., "Structure and Dynamics of Ionic Liquids: Trimethylsilylpropyl-Substituted Cations and Bis(sulfonyl)-amide Anions.", J. Chem. Phys., **2016**, *145*, 244506, doi: 10.1063/1.4972410.

B. Wu, H. Shirota, S. I. Lall-Ramnarine, E. W. Castner, Jr., "Structure of ionic liquids with cationic silicon-substitutions.", J. Chem. Phys., **2016**, *145*, 114501, doi: 10.1063/1.4962257.

Chapter 1

Introduction

Room temperature ionic liquids (RTILs) are salts having melting points below 100°. Their low vapor pressures, wide electrochemical windows, high viscosities and the tunabilities of their physical properties lead to many applications, [14, 15] including a variety of energy technologies. [26, 67, 115] Notable successes include the use of ILs as electrolytes in batteries, electrical double-layer capacitors, fuel cells, and solar cells. [7, 36, 38, 40, 53, 66, 70] To more fully realize the potential of ILs for energy related applications, it is crucial to understand the structure and reaction dynamics in these ionic solvents.

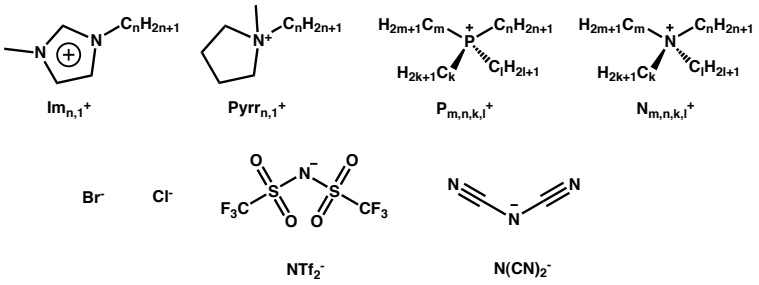

Figure 1.1: Some common ionic liquid cations and anions.

Figure 1.1 shows some common cations and anions used in creating room temperature ionic liquids. The cations shown are 1-alkyl-3-methylimidazolium ($Im_{n,1}^+$), 1-alkyl-1-methylpyrrolidinium ($Pyrr_{n,1}^+$), tetraalkylphosphonium ($P_{m,n,k,l}^+$) and tetraalkylammonium ($N_{m,n,k,l}^+$) cations. The anions shown are bromide (Br^-), chloride (Cl^-), bis(trifluoromethylsulfonyl)imide (NTf_2^-) and dicyanamide ($N(CN)_2^-$). In these cations or some anions, the net charges distributed among many atoms, which decrease the

magnitude of lattice energy of their crystals, making them stable liquids at room temperature. In this work, we also explore the properties of many kinds of specially functionalized ionic liquids, including ILs with silicon substituted chains, zwitterionic liquids (Zw-ILs), and electron donating ionic liquids, as shown later in Figures 1.4, 1.5 and 1.8.

1.1 Introduction to Molecular Dynamics Simulations

Classical molecular dynamics (MD) simulations are used in this work to study the liquid structures and interactions between molecules. In these simulations, a classical Hamiltonian is used to describe the system, with a classical potential energy surface defined using force fields. These force fields include bonded interactions, such as bond stretching, angle bending and dihedral torsions, as well as non-bonded interactions electrostatic and van der Waals interactions.

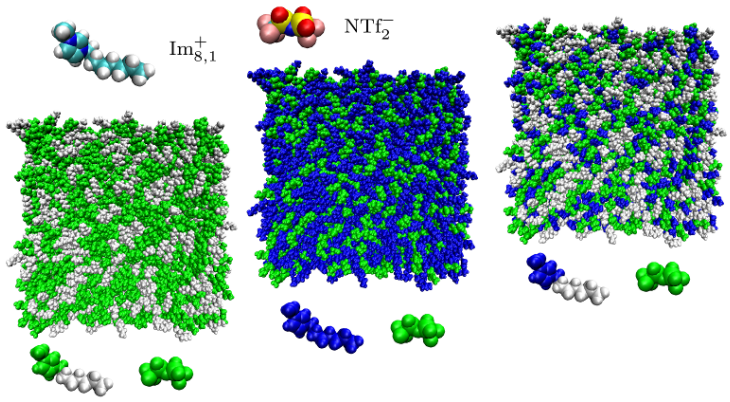

Figure 1.2: Figure from Ref. 10. Snapshots of simulation boxes of the ionic liquid $Im^+_{8,1}$ / NTf_2^-. The three snapshots show the same box, using different color schemes. Left: the nonpolar groups are colored white and the polar groups green. Middle: cations are blue and anions are green. Right: cation heads are blue, cation tails are white and anions green. Figure modeled from Ref. 52 and used simulation data from Ref. 27.

In an all-atom MD simulation, a box with periodic boundary conditions is set up. Figure 1.2 provided an example box used for simulation $Im^+_{8,1}$ / NTf_2^-. Newton's equations of motion for each atom in the system are solved in small time steps, deriving

forces from the negative derivatives of the potential functions. The coordinates and velocities of each atom can be recorded at each time step. Using MD simulations, the time-averaged structure and time evolution of a system can be studied. In this work, we only analyzed structual information. All MD simulations done in this work used GROMACS package. [1] Other popular classical MD package today includes AMBER, DL_POLY, LAMMPS and so on.

1.2 Introduction to the Structure Factor

The structure factor $S(q)$ describes the scattering pattern of a condensed material. For isotropic materials like a powder or liquid, $S(q)$ is a function of the scalar magnitude of the scattering vector q, which is related to the scatter angle 2θ and wavelength λ by $q = 4\pi \sin(\theta)/\lambda$. q and $S(q)$ are defined in reciprocal space, and related to distances d in real space by $q = 2\pi/d$, according to the Bragg equation. Peaks in $S(q)$ indicate periodicity in the system at $d = 2\pi/q$. In crystalline solids, sharp peaks are usually present, which indicates well-defined structure, while in liquids, peaks are usually broad since liquid structures are much amorphous.

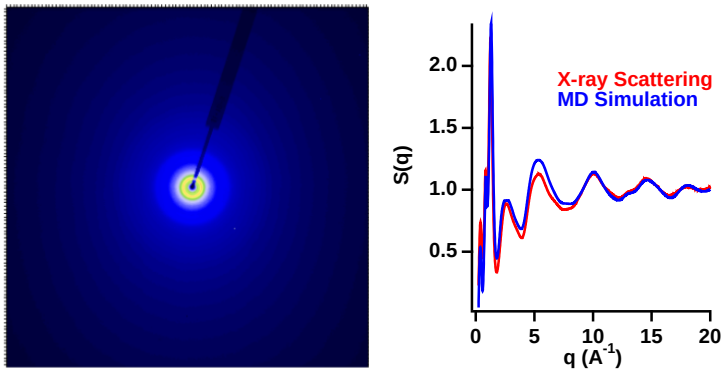

Figure 1.3: Left: 2-D scattering pattern of the ionic liquid Si-C_3-mim^+ / NTf_2^- (See Figure 1.4). Right: $S(q)$ of same IL obtained from X-ray scattering

In this work, we used two methods to obtain $S(q)$. One is high-energy X-ray scattering. The left panel of Figure 1.3 shows the 2-D scattering pattern of an IL. Integrating this figure from the center to the edge, applying a series of corrections, provides $S(q)$,

which is plotted as the red curve in the right panel. We also obtain $S(q)$ from MD simulations. From simulation trajectories we can compute the radial distribution $g(r)$ between pairs of all atoms, and $S(q)$ obtained from $g(r)$ after a Fourier transform. The simulated $S(q)$ for this IL is shown as the blue curve in the right panel.

1.3 Structures of Ionic Liquids

The local structures and interactions in ionic liquids are typically obtained from X-ray scattering, neutron scattering and molecular dynamics simulations. [5, 9, 11, 20, 22, 29–32, 41, 43, 45, 49, 50, 57, 68, 69, 75, 82, 85, 86, 91, 93–95, 108–110] For ILs based on NTf_2^- anion, there is a sharp division between inter- and intra-molecular structure at q=2 Å^{-1}.[88] For the intermolecular structure regime ($q < 2$Å^{-1}), there are three peaks in this region of $S(q)$. The *adjacency peak*, with a maximum typically found at about $q \sim$ 1.4 Å^{-1}, arises from the interactions of ions with their closest neighbors. The *charge-charge correlation peak* is usually centered near q=0.8 Å^{-1}. It reveals interactions between ions and their second coordination shell. For those ILs with sufficiently large spatial extent, a *pre-peak* or *first sharp diffraction peak* (FSDP) appears at the lowest values of q, typically in the range from 0.2-0.6 Å^{-1}.[4, 50, 51] Most commonly, the FSDP results from intermediate range order arising from nano-domain segregation between non-polar alkyl tails on either the cations[43, 52, 64, 86, 107] or anions[65, 83] that locally separate from the polar anionic and cationic head groups. Recently, we have reported that more polar groups such as a pentamethyldisiloxy tail can also lead to this kind of nano-phase segregation.[117] A third mechanism for such intermediate range order can arise from H-bonding networks in ionic liquids such as ethyl- and propyl-ammonium nitrate.[39, 42, 43, 109]

1.4 Silicon Substituted Ionic Liquids

Viscosity is one of the key design parameters for ionic liquids (ILs) in many specific applications, since ambient temperature viscosities for many of the most commonly used ILs lie in the range from 10-1,000 cP, one or more orders of magnitude

larger than for common neutral solvents. Shirota et al. demonstrated that replacing certain carbon atoms in ionic liquids cations by silicon atoms can dramatically reduce their shear viscosities by a factor of 1.6 or 7.4, depending on the nature of the anion.[96] Using femtosecond optical heterodyne-detected Raman-induced Kerr effect spectroscopy, they found a correlation between reduced viscosities and lower intermolecular vibrational frequencies for Si-mim$^+$ / NTf_2^- compared to C-mim$^+$ / NTf_2^-.[96, 98] This effect was further investigated by expanding the series of ILs to include pentamethyldisiloxy and silylphenyl groups,[98] and by studying the transport properties of the anions and cations using pulsed-gradient spin-echo (PG-SE) NMR[16] and laser transient-grating methods.[25] Low viscosities and high conductivities have also been reported for other Si-ILs.[12, 73] Applications using Si-ILs have been reported for gas separations,[8] as polymer gel electrolytes for dye-sensitized solar cells,[47, 114] and as surfactant materials.[104]

Recently, ionic liquids with silicon-substituted cations have found several applications. Bara et al. studied the CO_2 separation performance of ionic liquids with silicon-containing functional groups, and demonstrated that when compared with N_2 and CH_4, CO_2 was more permeable in each supported ionic liquid membrane.[8] Orel and co-workers used trimethoxysilyl substituted ionic liquids as the gel electrolyte in dye-sensitized solar cells.[47, 114] Bulut et al. synthesized two ionic liquids containing siloxane-functionalized cations and tetraalkoxyaluminate anions, and found they have even lower viscosities and higher conductivities than their NTf_2^- analogues. [12] Ionic liquids containing a siloxy (Si-O-Si) moiety have also been used as surface active materials, in which they show significant ability to reduce the surface tension of water.[104] The ILs having Si-mim$^+$ cations paired with either BF_4^- or NTf_2^- anions show lower surface tensions than for the homologs based on the C-mim$^+$ cation.[96, 97]

The chemical structures of all cations and anions are shown in Fig. 1.4. To address the question of how the choice of functional groups on IL anions or cations leads to significant changes in viscosity, we study the structure of these ionic liquids. Using high-energy X-ray scattering and molecular dynamics (MD) simulations, we have studied the structure of ionic liquids with three silicon containing cations,

1-trimethylsilylmethyl-3-methyl-imidazolium cation (Si-mim$^+$), 1-pentamethyldisiloxymethyl-3-methyl-imidazolium (SiOSi-mim$^+$) and 1-trimethylsilylmethyl-3-methyl-pyrrodinium (Si-pyrr$^+$). The appropriate control for comparing carbon vs. silicon is the homologous cation 1-methyl-3-neopentylimidazolium (C-mim$^+$). The same bis(trifluoromethylsulfonyl)amide anion (NTf_2^-) is used for each of the four ionic liquids.

We also discuss ILs with two different silicon-containing cations with longer –$(CH_2)_3Si(CH_3)_3$ tails, 1-methyl-3-trimethylsilylpropylimidazolium (Si-C_3-mim$^+$) and N-methyl-N-trimethylsilylpropylpyrrolidinium (Si-C_3-Pyrr$^+$). We note that both of these cations have a similar spatial extent to the SiOSi-mim$^+$ cation, while the trimethylsilylpropyl group is less polar than the pentamethyldisiloxy group.

We are also interested in the effect of the anionic size and properties on the bulk structure of the ILs. In this study, we report structural details for the Si-C_3-mim$^+$ cation paired with each of three sulfonylimide based anions: bis(fluorosulfonyl)imide (FSI^-), bis(trifluoromethanesulfonyl)imide (NTf_2^-) and bis(pentafluoroethanesulfonyl)imide ($BETI^-$). There are some studies focusing on the effect of anion type on structure of ILs, [65, 83, 84, 92, 95] but there are fewer reports on the dependence of IL structure on anion size and anion chain length.

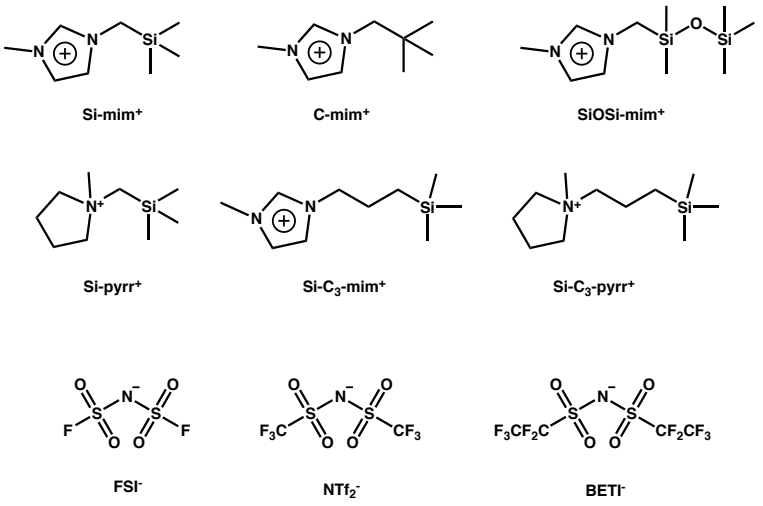

Figure 1.4: Chemical structures of the cations and anion of silicon-substituted ILs used in this study.

Unique features of the Si-ILs appear not only in the liquid structure factors and ionic interactions, but also in transport properties.[16, 25, 73, 96, 98] Recently, Endo *et al.* revealed that solute diffusion in Si-ILs, particularly for small sizes of diffusing molecules, is faster than for similar C-ILs when compared using the Stokes-Einstein plot, *i. e.*, normalizing by $T/(\eta \times r)$. This clearly indicates that solute diffusion mechanism differs in each medium, which we will show is likely to be the case for diffusion of the IL anions and cations themselves. In the last section of our results, anionic and cationic self-diffusion coefficients for Si-ILs were measured with PG-SE NMR and compared to those for C-ILs.

1.5 Zwitterionic Liquids

We have also studied the bulk liquid structures of a set of Zw-ILs and their homologous ILs using both experimental and computational methods. The Zw-ILs we study here have been developed by Kuroda, *et al.* as enhanced solvents for cellulose dissolution while maintaining low toxicity and biocompatibility. These unique properties enable the conversion of cell walls to ethanol in a one-pot reaction.[59]

Prior to Kuroda's work, Yoshizawa-Fujita, *et al.*, clearly identified the importance of using ethylene oxide repeat units in the molecular structures of Zw-IL to reduce the melting points below room temperature.[120] These Zw-ILs, as well as the liquid mixtures of some other zwitterions and ionic liquids, have been developed because of their propensity to yield significantly increased conductivity for Li^+ on addition of lithium bis(trifyl)amide, which makes them of great interest as potential battery electrolytes.[77, 118–120] Zwitterionic mixtures are also being considered for carbon dioxide capture and sequestration applications.[44]

Because there are potential advantages of Zw-ILs relative to other electrolytes, it seems urgent to understand their structural properties and to compare them with the structures of corresponding aprotic ILs. Here we report our structural results on two novel zwitterionic liquids, 1-[2-(2-methoxyethoxy)ethyl]-3-(3-carboxypropyl)-imidazolium (OE_2imC_3C) and 1-[2-(2-methoxyethoxy)ethyl]-3-(3-carboxypentyl)-imidazolium

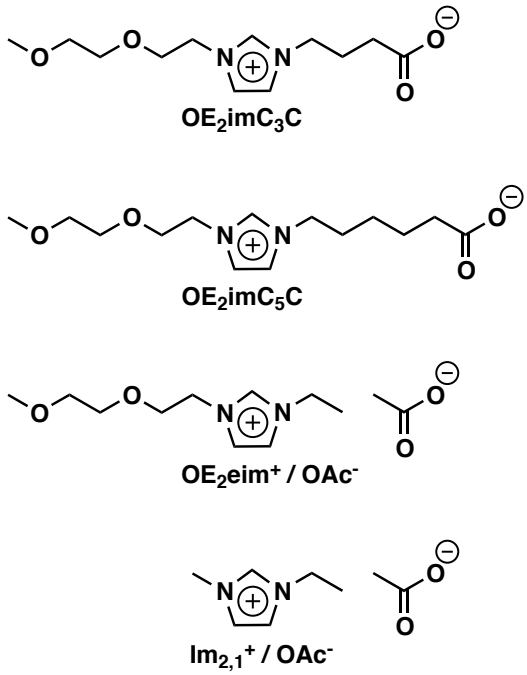

Figure 1.5: The molecular structures of the ionic liquids studied in this work. The top two species are zwitterionic liquids and the bottom two are typical monovalent aprotic ionic liquids.

(OE_2imC_5C).[59] The aprotic IL homolog of OE_2imC_3C is 1-[2-(2-methoxyethoxy)ethyl]-3-ethyl-imidazolium acetate (OE_2eim^+/OAc^-). Examination of the structures shown in Fig. 1.5 shows that elimination of a single carbon-carbon bond in the OE_2imC_3C Zw-IL leads to the aprotic IL structure of OE_2eim^+/OAc^-. Because the structure of 1-ethyl-3-methylimidazolium acetate ($Im^+_{2,1}/OAc^-$) is very well characterized, we have included this IL in our study to examine the effect of removing the 2-(2-methoxyethoxy)ethyl (diether) group. Below we report our investigations of the four liquids shown in Fig. 1.5 using high-energy X-ray scattering and molecular dynamics simulations.

1.6 Photo-Induced Electron Transfer

Of interest in the present work are bimolecular reactions between an electron donor and acceptor and how such reactions differ in ionic liquids relative to more conventional solvents. The kinetics of electron transfer are measured here using fluorescence quenching,

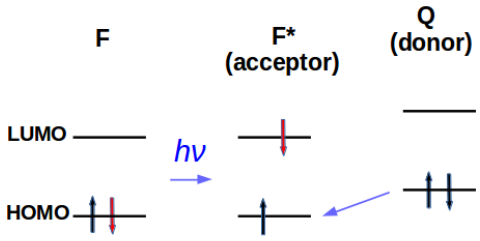

Figure 1.6: Electron transfer between an electron acceptor (A, or fluorophore) by a donor (D, or quencher). GS = ground state, LE = locally excited state.

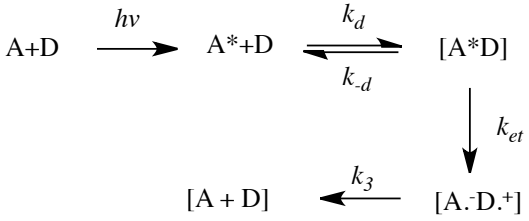

Figure 1.7: Reaction scheme of photo-induced bimolecular electron transfer in solvents.

as shown in 1.6. Schematically, excitation of a fluorophore promotes one electron, and a hole is left for accepting an electron from the quencher (electron donor), which shuts off (quenches) emission.

The steps involved in a bimolecular electron transfer process are shown in Figure 1.7. As shown in this figure, two processes may be determining the total quenching rate that we observed: the diffusion limited rate constant k_d and intrinsic electron transfer rate k_{et}.

The rates of bimolecular electron transfer reactions are determined by the interplay between the diffusive approach of the reactants and the rate of electron transfer between proximal donor-acceptor pairs. Under the assumption that electron transfer occurs immediately and irreversibly upon donor-acceptor contact, the reaction is diffusion limited and the rate constants under steady-state conditions can be described by the Smoluchowski equation. [100, 101] If diffusion coefficients are estimated from solvent viscosity η using the Stokes-Einstein hydrodynamic law, one obtains the simple expression:

$$k_d = \frac{8k_BT}{3\eta} \tag{1.1}$$

where k_B is Boltzmann's constant, and T is the absolute temperature.

1.7 Photo-Induced Electron Transfer in Ionic Liquids

Because electron transfer is a key component in many energy transduction process, it is crucial to understand how both ground-state (thermal) and photoinduced electron-transfer processes are affected by the purely ionic medium presented by ionic liquids. Particularly for the fast reactions accessible by photo-excitation, a number of investigations of both intramolecular [61] and intermolecular [37, 56, 62, 74, 99, 112, 116] electron transfer have shown that complex behavior, not usually observed in neutral organic solvents or aqueous systems, results from the much slower solvation in ionic liquids.

For example, Eq. 1.1 is usually sufficiently accurate for estimating diffusion-limited electron transfer rates in conventional low-viscosity solvents. However, photo-induced bimolecular reactions in ionic liquids are often one to two orders of magnitude larger than values predicted by this equation.[37, 56, 62, 74, 99, 112, 116] These faster rates are mainly due to the fact that the high viscosities of ionic liquids slow diffusion to such an extent that most reaction occurs outside of the steady-state limit and cannot be characterized by a time-independent rate constant. [56, 62] Other factors are that the Stokes-Einstein equation sometimes grossly underestimates the diffusivity of neutral solutes in ionic liquids, as well as the fact that Eq. 1.1 neglects the quenching that occurs at separations larger than the contact distance. [48, 62]

In this work we seek to clarify the influence of reactant diffusion on electron transfer in ionic liquids, using time-resolved fluorescence to measure the reductive quenching of a series of aromatic fluorophores (excited-state electron acceptors) by a variety of neutral and anionic quenchers (electron donors). The choice of quenchers is motivated by the fact that both experiments[48, 54, 113] and simulations[6] have shown that small neutral and charged species diffuse at widely different rates in ionic liquids. Whereas small

neutral solutes can diffuse through an ionic liquid with minimal disruption to the tightly coupled charge structure of the liquid, small ionic solutes incorporate into this structure and are often caged for extended periods.[6] One might anticipate that this qualitative difference would give rise to differences in how neutral and ionic solutes react, beyond the effect of charge on diffusion rates alone. The present study explores this possibility using the general approach established in our two prior studies.[62, 116] The first of these studies measured reductive fluorescence quenching of 9,10-dicyanoanthracene (DCNA) by N,N-dimethylaniline (DMA) in a number of different ionic liquids. [62] That work, together with an independent and contemporaneous report by Koch et al.[56] provided the first explanations of the unexpectedly rapid quenching previously reported in ionic liquids. In a subsequent study, we proposed a set of small cyano-based anionic quenchers and measured their reactions with the same excited-state fluorophore, DCNA, in a single ionic liquid. [116] The present report greatly extends these prior studies by considering the reactions between five cyanoanthracene fluorophores and six quenchers in CH_3CN and two ionic liquids.

The fluorophores, quenchers, and solvents examined in this study are shown in Figure 1.8. The sequential addition of CN groups to the anthracene chromophore systematically modifies both their $S_0 - S_1$ gaps and reduction potentials, making them popular in systematic studies of electron transfer.[13, 23, 34, 55, 71, 78, 111, 121] In a similar manner, cyano substituents serve to modify the oxidation potentials of the anionic quenchers over a wide range. The combination of these quenchers and fluorophores enables us to examine reactions with driving forces spanning the normal, activationless, and inverted regimes. This extensive data set also enables us to comment on the recent debate over the presence of a rate turnover at large driving forces in ionic liquids and other high-viscosity media.[3, 19, 21, 58, 76, 79, 81, 89, 90] We do not find evidence for such a turnover, at least not within the 2.0 eV range of driving force accessed here.

The rates of these quenching reactions are measured in two ionic liquids and one conventional organic solvent. The ionic liquids are 1-ethyl-3-methylimidazolium bis(trifluoromethylsulfonyl)amide ($Im^+_{2,1}$ / NTf_2^-) and trihexyl(tetradecyl)phosphonium bis-(trifluoromethylsulfonyl)amide ($P^+_{14,6,6,6}$ / NTf_2^-). The neutral solvent CH_3CN is chosen

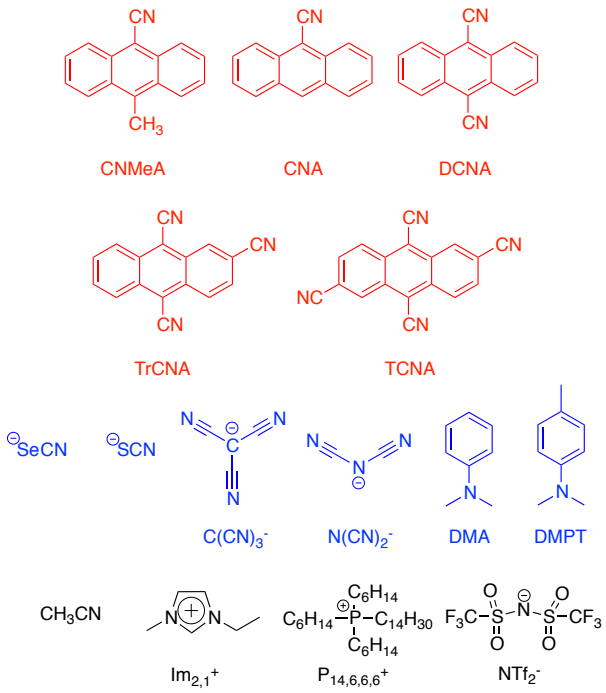

Figure 1.8: The fluorophores (acceptors), quenchers (donors) and solvents in red, blue and black, respectively. In ionic liquid solutions the cations for anionic quenchers match the solvent cation; e.g., for $Im^{+}_{2,1}$ / NTf^{-}_{2} solutions, Q = $Im^{+}_{2,1}$ / $SeCN^{-}$.

for comparison, given its role as a solvent standard for electron transfer reactions. The viscosities of these three solvents are 0.343 (CH_3CN), 32.0 ($Im^+_{2,1}$ / NTf^-_2) and 346 mPa s ($P^+_{14,6,6,6}$ / NTf^-_2).[28, 62, 106] This 1000-fold variation in solvent viscosities provides a wide range of expected reaction rates and should emphasize differences in the diffusion of neutral and charged species. $Im^+_{2,1}$ / NTf^-_2 is a relatively simple ionic liquid lacking the domain structure possessed by liquids having longer alkyl chains. Based on solvatochromic data [33] the polarity of $Im^+_{2,1}$ / NTf^-_2 is expected to be similar to that of CH_3CN. $P^+_{14,6,6,6}$ / NTf^-_2 is a much more complex solvent, possessing unusually large alkyl domains.[63] In this solvent, neutral and anionic quenchers might be expected to behave quite differently as a result of different preference for solvation in polar *vs.* nonpolar domains.[63]

The kinetics of these quenching reactions are measured here using a combination of steady-state fluorescence and time correlated single photon counting (TCSPC) methods. [62, 116] The resulting data are interpreted first using a Stern-Volmer analysis, followed by various diffusion-reaction models.

Diffusion-reaction models have been widely used to investigate bimolecular electron transfer rates,[2, 24, 35, 46, 56, 60, 72, 79–81, 87, 102, 103, 105] and they are essential for accurate interpretation of situations where non-stationary kinetics are observed, for example at high quencher concentrations or when diffusion is slow. We consider four reaction models of increasing complexity in order to investigate how much can be learned about the electron transfer process from the quenching data. First we attempt to fit the data to the seminal model of Smoluchowski [100, 101] and its extension by Collins and Kimball.[17, 18] Neither of these models, which assume reaction only at a single contact distance, are able to adequately fit the nonexponential fluorescence decays observed in the ionic liquids. Next we consider an *extended sink* model in which reaction occurs throughout a finite spatial region rather than at a single distance. This model provides good fits to the quenching data observed in all three solvents using only three adjustable parameters: the relative reactant diffusion coefficient, the width of the reaction zone, and the rate constant within the reaction zone.

We finally consider reaction models based on electron transfer theories. Because the number of parameters needed to specify such models is much greater than required to fit the quenching data, we use molecular dynamics and density functional theory calculations to provide information about the equilibrium distribution of reactants and the electronic coupling between them. These calculations highlight the fact that the planar fluorophores used here are in contact with quenchers over a range of center of mass separations, rendering any characterization by a spherically symmetric diffusion model a coarse approximation. Attempts to fit the quenching data to simple electron transfer models incorporating both the nonadiabatic and solvent-controlled adiabatic limits fail to account for the very broad range of reaction free energies over which electron transfer rates in the ionic liquids remain nearly constant. This rate leveling points to some shortcoming of the electron transfer models. We conjecture that this leveling may be related to the rate at which reactive pairs at contact are able to undergo the small-amplitude motions that serve to gate electron transfer in these sluggish media.

Bibliography

[1] M. J. Abraham, T. Murtola, R. Schulz, S. Páll, J. C. Smith, B. Hess, and E. Lindahl. GROMACS: High performance molecular simulations through multi-level parallelism from laptops to supercomputers. *SoftwareX*, 1–2:19–25, 2015.

[2] G. Angulo, D. R. Kattnig, A. Rosspeintner, G. Grampp, and E. Vauthey. On the Coherent Description of Diffusion-Influenced Fluorescence Quenching Experiments II: Early Events. *Chem.–Eur. J.*, 16:2291–2299, 2010.

[3] G. Angulo, A. Rosspeintner, M. Koch, and E. Vauthey. Comment on "observation of the marcus inverted region for bimolecular photoinduced electron-transfer reactions in viscous media". *J. Phys. Chem. B*, 120, 2016.

[4] H. V. R. Annapureddy, H. K. Kashyap, P. M. De Biase, and C. J. Margulis. What is the Origin of the Prepeak in the X-ray Scattering of Imidazolium-Based Room-Temperature Ionic Liquids? *J. Phys. Chem. B*, 114:16838–16846, 2010.

[5] J. C. Araque, J. J. Hettige, and C. J. Margulis. Modern Room Temperature Ionic Liquids, a Simple Guide to Understanding Their Structure and How It May Relate to Dynamics. *J. Phys. Chem. B*, 119:12727–12740, 2015.

[6] J. C. Araque, S. K. Yadav, M. Shadeck, M. Maroncelli, and C. J. Margulis. How is Diffusion of Neutral and Charged Tracers Related to the Structure and Dynamics of a Room-Temperature Ionic-Liquid? Large Deviations from Stokes-Einstein Behavior Explained. *J. Phys. Chem. B*, 119:7015–7029, 2015.

[7] M. Armand, F. Endres, D. R. MacFarlane, H. Ohno, and B. Scrosati. Ionic-liquid materials for the electrochemical challenges of the future. *Nat. Mater.*, 8:621–629, 2009.

[8] J. E. Bara, T. K. Carlisle, C. J. Gabriel, D. Camper, A. Finotello, D. L. Gin, and R. D. Noble. Guide to CO_2 Separations in Imidazolium-Based Room-Temperature Ionic Liquids. *Ind. Eng. Chem. Res.*, 48(6):2739–2751, 2009.

[9] C. E. S. Bernardes, K. Shimizu, A. I. M. C. L. Ferreira, L. M. N. B. F. Santos, and J. N. C. Lopes. Structure and Aggregation in the 1,3-Dialkyl-imidazolium Bis(trifluoromethylsulfonyl)imide Ionic Liquid Family: 2. From Single to Double Long Alkyl Side Chains. *J. Phys. Chem. B*, 118:6885–6895, 2014.

[10] A. B. Biedron. Surface studies of ionic liquids at interfaces, 2016.

[11] O. Borodin, D. L. Price, B. Aoun, M. A. Gonzalez, J. B. Hooper, M. Kofu, S. Kohara, O. Yamamuro, and M.-L. Saboungi. Effect of water on the structure of a prototype ionic liquid. *Phys. Chem. Chem. Phys.*, 18:23474–23481, 2016.

[12] S. Bulut, M. A. A. Rani, T. Welton, P. D. Lickiss, and I. Krossing. Preparation of $[Al(hfip)_4]^-$Based Ionic Liquids withSiloxane-Functionalized Cations and Their PhysicalProperties in Comparison with Their $[Tf_2N]^-$ Analogues. *ChemPhysChem*, 13:1802–1805, 2012.

[13] L. Burel, M. Mostafavi, S. Murata, and M. Tachiya. Transient Effect in Fluorescence Quenching by Electron Transfer. 4. Long-Range Electron Transfer in a Nonpolar Solvent. *J. Phys. Chem. A*, 103(30):5882–5888, 1999.

[14] E. W. Castner, Jr., C. J. Margulis, M. Maroncelli, and J. F. Wishart. Ionic Liquids: Structure and Photochemical Reactions. *Annu. Rev. Phys. Chem.*, 62:85–105, 2011.

[15] E. W. Castner, Jr. and J. F. Wishart. Spotlight on ionic liquids. *J. Chem. Phys.*, 132, 2010.

[16] S. H. Chung, R. Lopato, S. G. Greenbaum, H. Shirota, E. W. Castner, Jr., and J. F. Wishart. A nuclear magnetic resonance study of room temperature ionic liquids with $CH_2Si(CH_3)_3$ vs. $CH_2C(CH_3)_3$ substitutions on the imidazolium cations. *J. Phys. Chem. B*, 111:4885–4893, 2007.

[17] F. C. Collins. Diffusion in chemical reaction processes and in the growth of colloid particles. *J. Colloid. Sci.*, 5:499–505, 1950.

[18] F. C. Collins and G. E. Kimball. Diffusion-controlled reaction rates. *J. Colloid Sci.*, 4:425–437, 1949.

[19] A. K. Das, T. Mondal, S. Sen Mojumdar, and K. Bhattacharyya. Marcus-like Inversion in Electron Transfer in Neat Ionic Liquid and Ionic Liquid-Mixed Micelles. *J. Phys. Chem. B*, 115(16):4680–4688, 2011.

[20] M. G. Del Popolo and G. A. Voth. On the structure and dynamics of ionic liquids. *J. Phys. Chem. B*, 108:1744–1752, 2004.

[21] B. Dereka, M. Koch, and E. Vauthey. Looking at photoinduced charge transfer processes in the ir: Answers to several long-standing questions. *Acc. Chem. Res.*, 50:426–434, 2017.

[22] K. B. Dhungana, L. F. O. Faria, B. Wu, M. Liang, M. C. C. Ribeiro, C. J. Margulis, and E. W. Castner, Jr. Structure of cyano-anion ionic liquids: X-ray scattering and simulations. *J. Chem. Phys.*, 145:024503, 2016.

[23] J. P. Dinnocenzo, A. M. Feinberg, and S. Farid. Multiple Intermolecular Exciplexes in Highly Polar Solvents. *J. Phys. Chem. A*, 121:3662–3670, 2017.

[24] D. D. Eads, B. G. Dismer, and G. R. Fleming. A subpicosecond, subnanosecond, and steady-state study of diffusion-influenced fluorescence quenching. *J. Chem. Phys.*, 93:1136–1148, 1990.

[25] T. Endo, S. Nemugaki, Y. Matsushita, Y. Sakai, H. Ozaki, Y. Hiejima, Y. Kimura, and K. Takahashi. Fast solute diffusivity in ionic liquids with silyl or siloxane groups studied by the transient grating method. *Chem. Phys.*, 472(15):128–134, 2016.

[26] G. G. Eshetu, M. Armand, H. Ohno, B. Scrosati, and S. Passerini. Ionic liquids as tailored media for the synthesis and processing of energy conversion materials. *Energy Environ. Sci.*, 9:49–61, 2016.

[27] J. H. Fetherolf, B. Wu, S. Ramati, J. F. Wishart, S. Lall-Ramnarine, and E. W. Castner, Jr. Comparing the effect of alkyl chain length and branching on imidazolium and pyrrolidinium ionic liquid structure. *J. Chem. Phys.*, to be submitted, 2017.

[28] A. P. Froba, H. Kremer, and A. Leipertz. Density, Refractive Index, Interfacial Tension, and Viscosity of Ionic Liquids [EMIM][EtSO4], [EMIM][NTf2], [EMIM][N(CN)2], and [OMA][NTf2] in Dependence on Temperature at Atmospheric Pressure. *J. Phys. Chem. B*, 112:12420–12430, 2008.

[29] K. Fujii, R. Kanzaki, T. Takamuku, Y. Kameda, S. Kohara, M. Kanakubo, M. Shibayama, S. ichi Ishiguro, and Y. Umebayashi. Experimental evidences for molecular origin of low-Q peak in neutron/x-ray scattering of 1-alkyl-3-methylimidazolium bis(trifluoromethanesulfonyl)amide ionic liquids. *J. Chem. Phys.*, 135(24):244502, 2011.

[30] K. Fujii, S. Seki, S. Fukuda, T. Takamuku, S. Kohara, Y. Kameda, Y. Umebayashi, and S.-i. Ishiguro. Liquid structure and conformation of a low-viscosity

ionic liquid, N-methyl-N-propyl-pyrrolidinium bis(fluorosulfonyl) imide studied by high-energy X-ray scattering. *J. Mol. Liq.*, 143:64–69, 2008.

[31] K. Fujii, Y. Soejima, Y. Kyoshoin, S. Fukuda, R. Kanzaki, Y. Umebayashi, T. Yamaguchi, S.-i. Ishiguro, and T. Takamuku. Liquid Structure of Room-Temperature Ionic Liquid, 1-Ethyl-3-methylimidazolium Bis-(trifluoromethanesulfonyl) Imide. *J. Phys. Chem. B*, 112(14):4329–4336, 2008.

[32] S. Fukuda, M. Takeuchi, K. Fujii, R. Kanzaki, T. Takamuku, K. Chiba, H. Yamamoto, Y. Umebayashi, and S.-i. Ishiguro. Liquid structure of N-butyl-N-methylpyrrolidinium bis(trifluoromethanesulfonyl) amide ionic liquid studied by large angle X-ray scattering and molecular dynamics simulations. *J. Mol. Liq.*, 143:2–7, 2008.

[33] A. M. Funston, T. A. Fadeeva, J. F. Wishart, and E. W. Castner, Jr. Fluorescence Probing of Temperature-Dependent Dynamics and Friction in Ionic Liquid Local Environments. *J. Phys. Chem. B*, 111:4963–4977, 2007.

[34] N. Ghoneim, C. Hammer, E. Haselbach, D. Pilloud, P. Suppan, and P. Jacques. Comparative electron-transfer quenching rates of 9,10-dicyanoanthracene by various donors in solvents of different polarities. *J. Chem. Soc., Faraday Trans.*, 89:4271–4273, 1993.

[35] V. Gladkikh, A. I. Burshtein, G. Angulo, S. Pagès, B. Lang, and E. Vauthey. Kinetics and Yields of Electron Transfer in the Inverted Region. *J. Phys. Chem. A*, 108:6667–6678, 2004.

[36] J. B. Goodenough and K.-S. Park. The Li-Ion Rechargeable Battery: A Perspective. *J. Am. Chem. Soc.*, 135:1167–1176, 2013.

[37] C. M. Gordon and A. J. McLean. Photoelectron transfer from excited-state ruthenium(II) tris(bipyridyl) to methylviologen in an ionic liquid. *Chem. Commun.*, pages 1395–1396, 2000.

[38] M. Grätzel. Dye-sensitized solar cells. *J. Photochem. Photobiol., C*, 4:145–153, 2003.

[39] T. L. Greaves, D. F. Kennedy, S. T. Mudie, and C. J. Drummond. Diversity Observed in the Nanostructure of Protic Ionic Liquids. *J. Phys. Chem. B*, 114:10022–10031, 2010.

[40] P. Hapiot and C. Lagrost. Electrochemical Reactivity in Room-Temperature Ionic Liquids. *Chem. Rev.*, 108:2238–2264, 2008.

[41] C. Hardacre, J. D. Holbrey, C. L. Mullan, T. G. A. Youngs, and D. T. Bowron. Small angle neutron scattering from 1-alkyl-3-methylimidazolium hexafluorophosphate ionic liquids (C(n)mim PF6 , n=4, 6, and 8). *J. Chem. Phys.*, 133(7):074510, 2010.

[42] R. Hayes, S. Imberti, G. G. Warr, and R. Atkin. Pronounced sponge-like nanostructure in propylammonium nitrate. *Phys. Chem. Chem. Phys.*, 13:13544–13551, 2011.

[43] R. Hayes, G. G. Warr, and R. Atkin. Structure and Nanostructure in Ionic Liquids. *Chem. Rev.*, 115:6357–6426, 2015.

[44] D. J. Heldebrant, P. K. Koech, M. T. C. Ang, C. Liang, J. E. Rainbolt, C. R. Yonker, and P. G. Jessop. Reversible zwitterionic liquids, the reaction of alkanol guanidines, alkanol amidines, and diamines with CO2. *Green Chem.*, 12:713–721, 2010.

[45] J. J. Hettige, J. C. Araque, H. K. Kashyap, and C. J. Margulis. Communication: Nanoscale structure of tetradecyltrihexylphosphonium based ionic liquids. *J. Chem. Phys.*, 144:121102, 2016.

[46] N. Joshi, M. L. Johnson, I. Gryczynski, and J. R. Lakowicz. Radiation boundary conditions in collisional quenching of fluorescence; determination by frequency-domain fluorometry. *Chem. Phys. Lett.*, 135:200–207, 1987.

[47] V. Jovanovski, E. Stathatos, B. Orel, and P. Lianos. Dye-sensitized solar cells with electrolyte based on a trimethoxysilane-derivatized ionic liquid. *Thin Solid Films*, 511-512:634âĂŞ637, 2006.

[48] A. Kaintz, G. Baker, A. Benesi, and M. Maroncelli. Solute Diffusion in Ionic Liquids, NMR Measurements and Comparisons to Conventional Solvents. *J. Phys. Chem. B*, 117:11697–11708, 2013.

[49] R. Kanzaki, T. Mitsugi, S. Fukuda, K. Fujii, M. Takeuchi, Y. Soejima, T. Takamuku, T. Yamaguchi, Y. Umebayashi, and S. Ishiguro. Ion-ion interaction in room temperature ionic liquid 1-ethyl-3-methylimidazolium tetrafluoroborate studied by large angle X-ray scattering experiment and molecular dynamics simulations. *J. Mol. Liq.*, 147:77–82, 2009.

[50] H. K. Kashyap, J. J. Hettige, H. V. R. Annapureddy, and C. J. Margulis. SAXS anti-peaks reveal the length-scales of dual positive-negative and polar-apolar ordering in room-temperature ionic liquids. *Chem. Commun.*, 48:5103–5105, 2012.

[51] H. K. Kashyap, C. S. Santos, H. V. R. Annapureddy, N. S. Murthy, C. J. Margulis, and E. W. Castner, Jr. Temperature-Dependent Structure of Ionic Liquids: X-ray Scattering and Simulations. *Faraday Discuss.*, 154:133–143, 2012.

[52] H. K. Kashyap, C. S. Santos, N. S. Murthy, J. J. Hettige, K. Kerr, S. Ramati, J. Gwon, M. Gohdo, S. I. Lall-Ramnarine, J. F. Wishart, C. J. Margulis, and E. W. Castner, Jr. Structure of 1-Alkyl-1-methylpyrrolidinium Bis(trifluoromethylsulfonyl)amide Ionic Liquids with Linear, Branched, and Cyclic Alkyl Groups. *J. Phys. Chem. B*, 49:15328–15337, 2013.

[53] R. Kawano, T. Katakabe, H. Shimosawa, M. K. Nazeeruddin, M. Grätzel, H. Matsui, T. Kitamura, N. Tanabe, and M. Watanabe. Solid-state dye-sensitized solar cells using polymerized ionic liquid electrolyte with platinum-free counter electrode. *Phys. Chem. Chem. Phys.*, 12:1916–1921, 2010.

[54] Y. Kimura, Y. Kida, Y. Matsushita, Y. Yasaka, M. Ueno, and K. Takahashi. Universality of Viscosity Dependence of Translational Diffusion Coefficients of

Carbon Monoxide, Diphenylacetylene, and Diphenylcyclopropenone in Ionic Liquids under Various Conditions. *J. Phys. Chem. B*, 119:8096–8103, 2015.

[55] M. Koch, R. Letrun, and E. Vauthey. Exciplex Formation in Bimolecular Photoinduced Electron-Transfer Investigated by Ultrafast Time-Resolved Infrared Spectroscopy. *J. Am. Chem. Soc.*, 136:4066–4074, 2014.

[56] M. Koch, A. Rosspeintner, G. Angulo, and E. Vauthey. Bimolecular Photoinduced Electron Transfer in Imidazolium-Based Room-Temperature Ionic Liquids Is Not Faster than in Conventional Solvents. *J. Am. Chem. Soc.*, 134:3729–3736, 2012.

[57] M. Kofu, M. Nagao, T. Ueki, Y. Kitazawa, Y. Nakamura, S. Sawamura, M. Watanabe, and O. Yamamuro. Heterogeneous Slow Dynamics of Imidazolium-Based Ionic Liquids Studied by Neutron Spin Echo. *J. Phys. Chem. B*, 117(9):2773–2781, 2013.

[58] M. Kumbhakar, A. Manna, M. Sayed, A. Kumar, and H. Pal. Observation of the Marcus Inverted Region for Bimolecular Photoinduced Electron-Transfer Reactions in Viscous Media. *J. Phys. Chem. B*, 118:10704–10715, 2014.

[59] K. Kuroda, H. Satria, K. Miyamura, Y. Tsuge, K. Ninomiya, and K. Takahashi. Design of Wall-Destructive but Membrane-Compatible Solvents. *Nature Communications*, submitted, 2017.

[60] J. R. Lakowicz, J. Kuśba, H. Szmacinski, M. L. Johnson, and I. Gryczynski. Distance-dependent fluorescence quenching observed by frequency-domain fluorometry. *Chem. Phys. Lett.*, 206:455–463, 1993.

[61] H. Y. Lee, J. B. Issa, S. S. Isied, E. W. Castner, Jr., Y. Pan, C. L. Hussey, K. S. Lee, and J. F. Wishart. A Comparison of Electron-Transfer Dynamics in Ionic Liquids and Neutral Solvents. *J. Phys. Chem. C*, 116:5197–5208, 2012.

[62] M. Liang, A. Kaintz, G. A. Baker, and M. Maroncelli. Bimolecular Electron Transfer in Ionic Liquids: Are Reaction Rates Anomalously High? *J. Phys. Chem. B*, 116:1370–1384, 2012.

[63] M. Liang, S. Khatun, and E. W. Castner, Jr. Communication: Unusual structure and transport in ionic liquid-hexane mixtures. *J. Chem. Phys.*, 142:121101, 2015.

[64] J. N. C. Lopes and A. A. H. Pádua. Molecular Force Field for Ionic Liquids III: Imidazolium, Pyridinium, and Phosphonium Cations; Chloride, Bromide, and Dicyanamide Anions. *J. Phys. Chem. B*, 110:19586–19592, 2006.

[65] M. Macchiagodena, F. Ramondo, A. Triolo, L. Gontrani, and R. Caminiti. Liquid Structure of 1-Ethyl-3-methylimidazolium Alkyl Sulfates by X-ray Scattering and Molecular Dynamics. *J. Phys. Chem. B*, 116:13448–13458, 2012.

[66] D. R. MacFarlane, M. Forsyth, P. C. Howlett, J. M. Pringle, J. Sun, G. Annat, W. Neil, and E. I. Izgorodina. Ionic Liquids in Electrochemical Devices and Processes: Managing Interfacial Electrochemistry. *Acc. Chem. Res.*, 40:1165–1173, 2007.

[67] D. R. MacFarlane, N. Tachikawa, M. Forsyth, J. M. Pringle, P. C. Howlett, G. D. Elliott, J. James H. Davis, M. Watanabe, P. Simon, and C. A. Angell. Energy applications of ionic liquids. *Energy Environ. Sci.*, 7:232–250, 2014.

[68] A. Mariani, M. Campetella, C. Fasolato, M. Daniele, F. Capitani, L. Bencivenni, P. Postorino, S. Lupi, R. Caminiti, and L. Gontrani. A joint experimental and computational study on ethylammonium nitrate-ethylene glycol 1:1 mixture. Structural, kinetic, dynamic and spectroscopic properties. *J. Mol. Liq.*, 2016.

[69] A. Mariani, O. Russina, R. Caminiti, and A. Triolo. Structural organization in a methanol:ethylammonium nitrate (1:4) mixture: A joint X-ray/Neutron diffraction and computational study. *J. Mol. Liq.*, 212:947–956, 2015.

[70] M. S. Miran, T. Yasuda, M. A. B. H. Susan, K. Dokko, and M. Watanabe. Electrochemical properties of protic ionic liquids: correlation between open circuit potential for H_2/O_2 cells under non-humidified conditions and δpKa. *RSC Adv.*, 3:4141–4144, 2013.

[71] S. E. Mylon, S. N. Smirnov, and C. L. Braun. Exciplex Dipole Moments:âĂĽ Cyanoanthracene Acceptors and Methyl-Substituted Benzene Donors. *J. Phys. Chem. A*, 102:6558–6564, 1998.

[72] T. L. Nemzek and W. R. Ware. Kinetics of diffusion-controlled reactions. Transient effects in fluorescence quenching. *J. Chem. Phys.*, 62:477–489, 1975.

[73] H. Niedermeyer, M. A. A. Rani, P. D. Lickiss, J. P. Hallett, T. Welton, A. J. P. White, and P. A. Hunt. Understanding siloxane functionalised ionic liquids. *Phys. Chem. Chem. Phys.*, 12:2018–2029, 2010.

[74] A. Paul and A. Samanta. Photoinduced Electron Transfer Reaction in Room Temperature Ionic Liquids: A Combined Laser Flash Photolysis and Fluorescence Study. *J. Phys. Chem. B*, 111:1957–1962, 2007.

[75] M. G. D. Pópolo, R. M. Lynden-Bell, and J. Kohanoff. Ab Initio Molecular Dynamics Simulation of a Room Temperature Ionic Liquid. *J. Phys. Chem. B*, 109(12):5895–5902, 2005.

[76] D. Rehm and A. Weller. Kinetics of Fluorescence Quenching by Electron and H-atom Transfer. *Isr. J. Chem.*, 8:259–271, 1970.

[77] A. Rocha, T. Carvalho, P. Vidinha, and N. M. T. Louren¸co. Synthesis and Properties of Room-Temperature Choline Carboxylate Zwitterionic Ionic Liquids as Potential Electrolytes. *ChemPlusChem*, 77(12):1106–1111, 2012.

[78] A. Rosspeintner, G. Angulo, and E. Vauthey. Driving Force Dependence of Charge Recombination in Reactive and Nonreactive Solvents. *J. Phys. Chem. A*, 116:9473–9483, 2012.

[79] A. Rosspeintner, G. Angulo, and E. Vauthey. Bimolecular Photoinduced Electron Transfer Beyond the Diffusion Limit: The Rehm-Weller Experiment Revisited with Femtosecond Time Resolution. *J. Am. Chem. Soc.*, 136:2026–2032, 2014.

[80] A. Rosspeintner, D. Kattnig, G. Angulo, S. Landgraf, G. Grampp, and A. Cuetos. On the Coherent Description of Diffusion-Influenced Fluorescence Quenching Experiments. *Chem.–Eur. J.*, 13:6474–6483, 2007.

[81] A. Rosspeintner, M. Koch, G. Angulo, and E. Vauthey. Spurious Observation of the Marcus Inverted Region in Bimolecular Photoinduced Electron Transfer. *J. Am. Chem. Soc.*, 134:11396–11399, 2012.

[82] O. Russina, S. De Santis, and L. Gontrani. Micro- and mesoscopic structural features of a bio-based choline-amino acid ionic liquid. *RSC Adv.*, 6:34737–34743, 2016.

[83] O. Russina, L. Gontrani, B. Fazio, D. Lombardo, A. Triolo, and R. Caminiti. Selected chemical-physical properties and structural heterogeneities in 1-ethyl-3-methylimidazolium alkyl-sulfate room temperature ionic liquids. *Chem. Phys. Lett.*, 493:259–262, 2010.

[84] O. Russina, F. Lo Celso, M. Di Michiel, S. Passerini, G. B. Appetecchi, F. Castiglione, A. Mele, R. Caminiti, and A. Triolo. Mesoscopic structural organization in triphilic room temperature ionic liquids. *Faraday Discuss.*, 167:499–513, 2013.

[85] O. Russina and A. Triolo. New experimental evidence supporting the mesoscopic segregation model in room temperature ionic liquids. *Faraday Discuss.*, 154:97–109, 2012.

[86] O. Russina, A. Triolo, L. Gontrani, R. Caminiti, D. Xiao, J. Hines, Larry G., R. A. Bartsch, E. L. Quitevis, N. Pleckhova, and K. R. Seddon. Morphology and intermolecular dynamics of 1-alkyl-3-methylimidazolium bis(trifluoromethane)sulfonylamide ionic liquids: structural and dynamic evidence of nanoscale segregation. *J. Phys.: Condens. Matter*, 21(42):424121, 2009.

[87] V. O. Saik, A. A. Goun, and M. D. Fayer. Photoinduced electron transfer and geminate recombination for photoexcited acceptors in a pure donor solvent. *J. Chem. Phys.*, 120:9601, 2004.

[88] C. S. Santos, H. V. R. Annapureddy, N. S. Murthy, H. K. Kashyap, E. W. Castner, Jr., and C. J. Margulis. Temperature-dependent structure of methyltributylammonium bis(trifluoromethylsulfonyl)amide: X ray scattering and simulations. *J. Chem. Phys.*, 134:064501, 2011.

[89] S. Sarkar, S. Mandal, C. Ghatak, V. G. Rao, S. Ghosh, and N. Sarkar. Photoinduced electron transfer in an imidazolium ionic liquid and in its binary mixtures with water, methanol, and 2-propanol: Appearance of marcus-type of inversion. *J. Phys. Chem. B*, 116:1335–1344, 2012.

[90] S. Sarkar, R. Pramanik, C. Ghatak, V. G. Rao, and N. Sarkar. Photoinduced intermolecular electron transfer in a room temperature imidazolium ionic liquid: An excitation wavelength dependence study. *Chem. Phys. Lett.*, pages 211–216, 2011.

[91] S. Sharma, A. Gupta, and H. K. Kashyap. How the Structure of Pyrrolidinium Ionic Liquids Is Susceptible to High Pressure. *J. Phys. Chem. B*, 120:3206–3214, 2016.

[92] K. Shimizu, A. A. Freitas, and J. N. C. Lopes. Structural characterization of the [CnC1im][C4F9SO3] ionic liquid series: Alkyl versus perfluoroalkyl side chains. *J. Mol. Liq.*, 2016.

[93] K. Shimizu, M. F. C. Gomes, A. A. H. Pádua, L. P. Rebelo, and J. N. C. Lopes. Three commentaries on the nano-segregated structure of ionic liquids. *J. Mol. Struct.: TheoChem*, 946:70–76, 2010.

[94] K. Shimizu and J. N. C. Lopes. Probing the structural features of the 1-alkyl-3-methylimidazolium hexafluorophosphate ionic liquid series using Molecular Dynamics simulations. *J. Mol. Liq.*, 210:257–263, 2015.

[95] K. Shimizu and J. N. C. Lopes. Comparing the structure of different ionic liquid series: Bistriflamide v. hexafluorophosphate; pure v. equimolar mixtures. *Fluid Phase Equilib.*, 418:181–191, 2016.

[96] H. Shirota and E. W. Castner, Jr. Why Are Viscosities Lower for Ionic Liquids with -CH2Si(CH3)3 vs -CH2C(CH3)3 Substitutions on the Imidazolium Cations? *J. Phys. Chem. B*, 109:21576–21585, 2005.

[97] H. Shirota and H. Fukazawa. Atom Substitution Effects in Ionic Liquids: A Microscopic View by Femtosecond Raman-Induced Kerr Effect Spectroscopy. In A. Kokorin, editor, *Ionic Liquids: Theory, Properties, New Approaches*, chapter 9, pages 201–224. InTech, Rijeka, Croatia, February 2011.

[98] H. Shirota, J. F. Wishart, and E. W. Castner, Jr. Intermolecular Interactions and Dynamics of Room Temperature Ionic Liquids That Have Silyl- and Siloxy-Substituted Imidazolium Cations. *J. Phys. Chem. B*, 111:4819–4829, 2007.

[99] A. Skrzypczak and P. Neta. Diffusion-Controlled Electron-Transfer Reactions in Ionic Liquids. *J. Phys. Chem. A*, 107:7800–7803, 2003.

[100] M. Smoluchowski. Three lectures on diffusion, Brownian movement and coagulation of colloidal particles. *Phys. Z.*, 17:585–599, 1916.

[101] M. Smoluchowski. Mathematical Theory of the Kinetics of the Coagulation of Colloidal Solutions. *Z. Phyik. Chem.*, 92:129–168, 1917.

[102] L. Song, R. C. Dorfman, S. F. Swallen, and M. D. Fayer. Influence of diffusion on photoinduced electron transfer. *J. Phys. Chem.*, 95:3454–3457, 1991.

[103] S. F. Swallen, K. Weidemaier, H. L. Tavernier, and M. D. Fayer. Experimental and Theoretical Analysis of Photoinduced Electron Transfer– Including the Role of Liquid Structure. *J. Phys. Chem.*, 100:8106–8117, 1996.

[104] J. Tan and S. Feng. Effect of Counterions on Micellization of Pyrrolidinium Based Silicone Ionic Liquids in Aqueous Solutions. *J. Chem. Eng. Data*, 59:1830–1834, 2014.

[105] H. L. Tavernier and M. D. Fayer. Solute–solute spatial distribution in hydrogen bonding liquids probed with time-dependent intermolecular electron transfer. *J. Chem. Phys.*, 114:4552, 2001.

[106] H. Tokuda, K. Hayamizu, K. Ishii, M. A. B. H. Susan, and M. Watanabe. Physicochemical Properties and Structures of Room Temperature Ionic Liquids. 2. Variation of Alkyl Chain Length in Imidazolium Cation. *J. Phys. Chem. B*, 109:6103–6110, 2005.

[107] A. Triolo, O. Russina, H.-J. Bleif, and E. Di Cola. Nanoscale segregation in room temperature ionic liquids. *J. Phys. Chem. B*, 111(18):4641–4644, 2007.

[108] A. Triolo, O. Russina, R. Caminiti, H. Shirota, H. Y. Lee, C. S. Santos, N. S. Murthy, and E. W. Castner, Jr. Comparing intermediate range order for alkyl- vs. ether-substituted cations in ionic liquids. *Chem. Commun.*, 48:4959–4961, 2012.

[109] Y. Umebayashi, W.-L. Chung, T. Mitsugi, S. Fukuda, M. Takeuchi, K. Fujii, T. Takamuku, R. Kanzaki, and S.-i. Ishiguro. Liquid Structure and the Ion-Ion Interactions of Ethylammonium Nitrate Ionic Liquid Studied by Large Angle X-Ray Scattering and Molecular Dynamics Simulations. *J. Comput. Chem. Jpn*, 7(4):125–134, 2008.

[110] S. M. Urahata and M. C. C. Ribeiro. Structure of ionic liquids of 1-alkyl-3-methylimidazolium cations: A systematic computer simulation study. *J. Chem. Phys.*, 120(4):1855–1863, 2004.

[111] E. Vauthey. Direct Measurements of the Charge-Recombination Dynamics of Geminate Ion Pairs Formed upon Electron-Transfer Quenching at High Donor Concentration. *J. Phys. Chem. A,*, 105:340–348, 2001.

[112] R. C. Vieira and D. E. Falvey. Photoinduced Electron-Transfer Reactions in Two Room-Temperature Ionic Liquids: 1-Butyl-3-methylimidazolium Hexafluorophosphate and 1-Octyl-3-methylimidazolium Hexafluorophosphate. *J. Phys. Chem. B*, 111:5023–5029, 2007.

[113] M. A. Vorotyntsev, V. A. Zinovyeva, and M. Picquet. Diffusional transport in ionic liquids: Stokes-Einstein relation or “sliding sphere” model? Ferrocene (Fc) in imidazolium liquids. *Electrochim. Acta*, 55:5063–5070, 2010.

[114] A. S. Vuk, V. Jovanovski, A. Pollet-Villard, I. Jerman, and B. Orel. Imidazolium-based ionic liquid derivatives for application in electrochromic devices. *Sol. Energy Mater. Sol. Cells*, 92:126–135, 2008.

[115] J. F. Wishart. Energy applications of ionic liquids. *Energy Environ. Sci.*, 2:956–961, 2009.

[116] B. Wu, M. Liang, M. Maroncelli, and E. W. Castner, Jr. Photoinduced Bimolecular Electron Transfer from Cyano Anions in Ionic Liquids. *J. Phys. Chem. B*, 119:14790–14799, 2015.

[117] B. Wu, H. Shirota, and E. W. Castner, Jr. Structure of Ionic Liquids with Cationic Silicon-Substitutions. *J. Chem. Phys.*, 145:114501, 2016.

[118] M. Yoshizawa, M. Hirao, K. Ito-Akita, and H. Ohno. Ion conduction in zwitterionic-type molten salts and their polymers. *J. Mater. Chem.*, 11:1057–1062, 2001.

[119] M. Yoshizawa and H. Ohno. Anhydrous proton transport system based on zwitterionic liquid and HTFSI. *Chem. Commun.*, pages 1828–1829, 2004.

[120] M. Yoshizawa-Fujita, T. Tamura, Y. Takeoka, and M. Rikukawa. Low-melting zwitterion: effect of oxyethylene units on thermal properties and conductivity. *Chem. Commun.*, 47:2345–2347, 2011.

[121] J. Zhou, R. P. Shah, B. R. Findley, and C. L. Braun. Long Distance Photoinduced Electron Transfer in Solutions:âĂLa mechanism for Producing Large Yields of Free Ions by Electron Transfer Quenching. *J. Phys. Chem. A*, 106:12–20, 2002.

Chapter 2

Methods

2.1 Experimental Methods

2.1.1 Preparation and Purification of Chemicals

The molecular structures of compounds we used are shown in Figures 1.4 1.5 and 1.8.

9-cyano-10-methylanthracene (CNMeA) was a gift from Dr. Peng Liu of Harvard University. 9-cyanoanthracene (CNA) was purchased from Sigma-Aldrich and recrystallized in ethanol. 9,10-dicyanoanthracene (DCNA) was purchased from TCI-America and recrystallized from a mixture of pyridine and acetonitrile.[26] 2,9,10-tricyanoanthracene (TrCNA) and 2,6,9,10-tetracyanoanthracene (TCNA) were kindly provided by Prof. Eric Vauthey of the University of Geneva.

The charged quenchers, 1-ethyl-3-methylimidazolium thiocyanate ($Im^+_{2,1}$ / SCN^-), dicyanamide ($Im^+_{2,1}$ / $N(CN)^-_2$), and tricyanomethanide ($Im^+_{2,1}$ / $C(CN)^-_3$), as well as trihexyltetradecylphosphonium dicyanamide ($P^+_{14,6,6,6}$ / $N(CN)^-_2$) and tricyanomethanide ($P^+_{14,6,6,6}$ / $C(CN)^-_3$) were purchased from IoLiTec. 1-ethyl-3-methylimidazolium selenocyanate ($Im^+_{2,1}$ / $SeCN^-$), trihexyltetradecylphosphonium thiocyanate ($P^+_{14,6,6,6}$ / SCN^-) and selenocyanate ($P^+_{14,6,6,6}$ / $SeCN^-$) were synthesized following literature methods.[69] All ionic liquids were dried under vacuum (2×10^{-2} mbar) for 48 hours and stored at -10 °C in an argon glovebox, where the water and oxygen levels were controlled to below 0.1 and 0.7 ppm, respectively. The neutral quenchers N,N-dimethylaniline (DMA) and N,N-dimethyl-p-toluidine (DMPT) were purchased from Sigma-Aldrich, distilled under reduced pressure, degassed using three freeze-pump-thaw cycles, and then stored in the glovebox.

Anhydrous acetonitrile was purchased from Sigma-Aldrich and stored under argon. Ultra-high purity (>99.5%) ionic liquids 1-ethyl-3-methylimidazolium bis(trifluoromethylsulfonyl)imide ($Im^+_{2,1}$ / NTf^-_2), and trihexyltetradecylphosphonium bis-(trifluoromethylsulfonyl)imide were purchased from IoLiTec and were used as received, apart from drying.

The ionic liquid quenchers $Im^+_{2,1}$ / $SeCN^-$, $P^+_{14,6,6,6}$ / SCN^- and $P^+_{14,6,6,6}$ / $SeCN^-$ were synthesized using a similar method to that described in the literature [69].

$Im^+_{2,1}$ / $SeCN^-$: Briefly, 3.0 g of $Im^+_{2,1}/Cl^-$ solid was added to 60 mL acetone. Subsequently about 20 mL of acetonitrile was added to the mixture drop by drop under stirring until all solids are dissolved. The solution was bubbled with argon for 15 min and then 10 mL acetone solution containing 4.5 g of KSeCN was added into mixture. The mixture was then stirred with argon bubbling for 1 h, before filtering under an atmosphere of argon. The solvent was removed using a rotary evaporator. The yellow liquid obtained was dissolved in 20 mL CH_2Cl_2, then filtered through a membrane filter. The solvent was removed, the the liquid was dried under 2×10^{-2} mbar for 48 h. The liquid was filtered again using a membrane filter in an argon glovebox and kept at -10 °C in the argon glovebox freezer until use.

$P^+_{14,6,6,6}$ / SCN^-: 1.4 g (0.0172 mol) NaSCN was dissolved in 20 mL acetone, to which a 50 mL acetone solution of 5.3 g (0.0102 mol) $P^+_{14,6,6,6}$ / Cl^- was added. The solution was bubbled with argon and stirred for one hour, then filtered. The solvent was removed under vacuum at 30 °C. The residual colorless liquid was dissolved in 25 mL CH_2Cl_2, filtered, and CH_2Cl_2 was then removed under vacuum at 30 °C. The obtained colorless liquid was evacuated at 2×10^{-2} mbar for 48 h, and kept at -10 °C under argon in a glovebox. Yield: 2.0 g (36%). ^{1}H-NMR (400 MHz, $CDCl_3$, ppm): 2.2-2.4 (m, 8H, (CH_2)$_4$-P), 1.35-1.7 (m, 16H, CH_2-CH_2-CH$_2$-P), 1.1-1.35 (m, 32H, alkyl chain in $P^+_{14,6,6,6}$), 0.7-0.9 (m, 12H, 4× CH_3) ^{13}C-NMR (100.6 MHz, $CDCl_3$, ppm): 130.9 (SCN^-), 13-32 ($P^+_{14,6,6,6}$). ^{31}P-NMR (162 MHz, $CDCl_3$, ppm): 32.7 ($P^+_{14,6,6,6}$). The absence of sodium and chloride ions was confirmed by X-ray fluorescence spectra.

$P^+_{14,6,6,6}$ / $SeCN^-$ 1.8 g KSeCN (0.0126 mol) was dissolved in 20 mL acetone, in which a 50 mL acetone solution of 5.3 g (0.0102 mol) $P^+_{14,6,6,6}$ / Cl^- was added, then the solution

was bubbled under argon for 2 hours with stirring. All other procedures were the same as for $P^+_{14,6,6,6}$ / SCN^-. 3.0 g (50%) of a pale yellow liquid were obtained. ^{1}H-NMR (400 MHz, $CDCl_3$, ppm): 2.2-2.4 (m, 8H, $(CH_2)_4$-P), 1.4-1.7 (m, 16H, CH_2-CH_2-CH_2-P), 1.1-1.4 (m, 32H, alkyl chain in $P^+_{14,6,6,6}$), 0.7-1.0 (m ,12H, 4× CH_3) ^{13}C-NMR (100.6 MHz, $CDCl_3$, ppm): 117.7 (SCN^-), 13-32 ($P^+_{14,6,6,6}$). ^{31}P-NMR (162 MHz, $CDCl_3$, ppm): 32.7 ($P^+_{14,6,6,6}$). The absence of potassium and chloride was confirmed by X-ray fluorescence spectra. **Note:** *The $SeCN^-$ anion is extremely toxic and a hazard to the environment.*

The syntheses of the ILs Si-mim$^+$ / NTf_2^-, C-mim$^+$ / NTf_2^- and SiOSi-mim$^+$ / NTf_2^- were described previously.[65, 66] The Si-pyrr$^+$ / NTf_2^- IL was prepared in the same manner.

Si-pyrr$^+$ / NTf_2^-: Trimethylsilylmethyl bromide (4.83 g, 28.9 mmol) was added to 1-methylpyrrolidine (2.46 g, 28.9 mmol) in acetonitrile solution (10 mL) in a flask equipped with a reflux condenser and magnetic stirrer, and the soluction was heated and stirrted at 70-75 °C in an oil bath for 14 hours. Residual solvent and reactants were removed by rotary evaporation. The intermediate product was 5.71 g (22.6 mmol). To effect the anion change, the Si-pyrr$^+$/Br^- product was dissolved in water (10 mL), and aqueous lithium bis(trifluoromethylsulfonyl)imide solution (6.50 g, 22.6 mmol in 10 mL water) was added. After the mixture was stirred at room temperature for 1 hour, the aqueous solution was decanted. The ionic liquid layer was dissolved in dichloromethane (20mL) and washed in water (5 × 10 mL). The dichloromethane was evaporated, and the ionic liquid obtained was dried in vacuo at 80 °C for more than 12 hours. The yield was 69%. ^{1}H-NMR (300 MHz, d_6DMSO): δ=0.20 (s, 9H, Si(CH_3)$_3$), 2.18 (br, 4H, NCH_2CH_2), 2.99 (s, 3H, NCH_3), 3.11 (s, 2H, NCH_2Si), 3.30-3.40 (m, 2H, NCH_2CH_2), 3.50-3.60 (m,2H, NCH_2CH_2). MS (+ve): m/z 172, (Si-pyrr$^+$) 624 (2Si-pyrr$^+$/ NTf_2^-); MS(-ve) m/z 280 (NTf_2^-).

The synthetic procedure for ionic liquids Si-C_3-mim$^+$ / NTf_2^-, Si-C_3-mim$^+$ / FSI^-, Si-C_3-mim$^+$ / $BETI^-$ and Si-C_3-Pyrr$^+$ / NTf_2^- was reported previously,[20] hence only a brief description is presented here. All starting materials were used as received,

including 1-methylimidazole and 1-methylpyrrolidine (both from Acros Organics), 3-chloropropyltrimethylsilane (Gelest), potassium bis(fluorosulfonyl)amide (Kanto Kagaku), lithium bis(trifluoromethylsulfonyl)amide (Kanto Kagaku), and lithium bis-(pentafluoroethanesulfonyl)amide (Kishida Kagaku). First, chloride salts were obtained by the quaternization of either 1-methylimidazolium or 1-methylpyrrolidinium with 3-chloropropyltrimethylsilane, typically in acetonitrile solutions at 353 K for 48 h under an argon atmosphere. Appropriate purifications were performed for the product chloride salts, including washing with ethyl acetate, recrystallization, and decolorizing with activated charcoal. The Si-ILs were prepared from the corresponding chloride salts by ion exchange with the lithium or potassium salt of K^+/FSI^-, Li^+/NTf_2^-, or $Li^+/BETI^-$. The ILs obtained were washed with distilled water several times until they passed the $AgNO_3$ test and were again decolorized with activated charcoal. Characterization of the samples was done using ^1H, ^{13}C, and ^{19}F NMR spectroscopies.

2.1.2 Fluorescence Quenching Experiments

Steady-state fluorescence and time correlated single photon counting (TCSPC) spectroscopies were used to measure the quenching between fluorophores and quenchers. Both steady-state and time-resolved fluorescence was excited using vertical polarization with emission measurements taken at magic angle polarization. Concentrations of the fluorophores (cyano-substituted anthracenes) were adjusted so that the optical densities of the peaks of the lowest energy absorption maxima were in the range of 0.1 – 0.3 in a 1 cm path fused silica fluorescence cuvette. The one exception was that the absorbance of TCNA in $P^+_{14,6,6,6}$ / NTf_2^- was 0.06, limited by solubility. The CH_3CN solutions were directly prepared inside the glovebox. The ionic liquid solutions were prepared in the air, then dried under 2×10^{-2} mbar for 48 h at ambient temperature, and stored in the glovebox.

The peak of the lowest energy absorption maximum was selected to excite the fluorophores in both steady-state and time-resolve fluorescence. The UV/vis spectra show that the absorption of impurities in solvents and quenchers are negligible at all excitation and emission wavelengths.

The steady-state and time-resolved fluorescence of each fluorophore-quencher (F-Q) pair were measured at a series of 4–5 quencher concentrations. The maximum quencher concentration was typically between 0.05 – 0.1 M in CH_3CN and 0.15 – 0.3 M in the ionic liquids. These concentrations were determined by weighing the solution before and after addition of the quencher. All solutions for quenching experiments were prepared in an argon glovebox.

Steady state fluorescence spectra were measured with a Spex Fluoromax-3 fluorometer using a 1 nm bandpass. The relative fluorescence intensity at each quencher concentration was obtained by integrating a 40 nm region around the bluest emission maximum in the steady-state spectrum. Time-resolved emission decays were recorded using the TCSPC technique as previously described.[27] The emission bandpass was 2.5 nm and the time window varied from 35 ns to 160 ns, depending on system. The instrument response function (IRF) was measured using a non-dairy creamer suspension, and the full width at half maximum (FWHM) was 0.12 ns for the 35 ns time window, 0.15 ns for the 120 ns window and 0.2 ns for the 160 ns window. Temperatures were controlled to 298.2 ± 0.1 K during all measurements. TCSPC data were fit to a multi-exponential model (Eq. 2.1) with 3 – 5 time constants using a convolute and compare algorithm,

$$I(t) = I(0) \sum_{j=1}^{n} A_j \int_0^{t_f} e^{-(t-p)/\tau_j} R(p) dp \quad \text{and} \quad \sum_{j=1}^{n} A_j = 1 \tag{2.1}$$

where $R(p)$ is the instrument response function, and τ_j and A_j are the time constant and amplitude of the jth exponential decay, respectively. [27, 40, 41, 77] The average quenching time constant determined from TCSPC data is defined as the average of all time components: $< \tau >= \sum_{i=1}^{n} A_i \tau_i$.

2.1.3 Diffusivities from PG-SE NMR

The diffusivities of DMA and DMPT in all three solvents were measured using the pulse-gradient spin echo (PG-SE) NMR technique as described previously. [79] The mixtures used for quenching experiments at the highest [Q] were directly used for

diffusion measurements. These mixtures were filled in 3 mm diameter NMR tubes in the glovebox, and then flame sealed. The tube was placed in another 5 mm diameter NMR tube, which was filled with D_2O for gradient shimming. A bipolar pulse pair stimulated echo (D-BPP-STE) pulse sequence [80] was used with a Doty Scientific model 16–38 diffusion probe installed on a 400 MHz Varian DirectDrive spectrometer. Spin-echo intensities under 20 different amplitudes of the magnetic field gradients were measured and the diffusion coefficients obtained using the method described previously. [22, 42] The magnetic gradient was calibrated using a standard D_2O sample, from which the HDO diffusion of D_2O was calibrated to be 1.9×10^{-9} m^2/s at 298 K. [2] All measurements were done at 298 K, which was also the temperature for all quenching experiments. The diffusion coefficients of the solutes and the cations can be obtained from ^1H signals, and the NTf_2^- anion diffusivities were obtained from the ^{19}F signals.

2.1.4 Cyclic Voltammetry

The oxidation potentials of electron donors in acetonitrile were measured using Cyclic Voltammetry (CV). The potential was controlled by a BASi model EC Epsilon controller. A BASi MF-2013 platinum working electrode was used, a platinum wire was served as counter electrode, and a BASi MF-2062 non-aqueous Ag+/Ag electrode was used as reference. The working electrode was polished using an alumina suspension and rinsed using methanol, water and acetone, respectively, before each measurement. The half wave potential of the ferrocenium/ferrocene (Fc^+/Fc) couple was used to calibrate the reference electrode. Roughly 0.002 M of the electron donating ionic liquid was added to a solution of 0.1 M tetrabutylammonium perchlorate (TBAP) as the supporting electrolyte. All samples were made under an argon atmosphere in a glovebox. The half-wave potentials for the reversible and quasi-reversible systems ($Im_{2,1}^+$ / $SeCN^-$ and $Im_{2,1}^+$ / SCN^-) were calculated by averaging anodic and cathodic peaks. E(1/2) for the totally irreversible systems ($Im_{2,1}^+$ / $C(CN)_3^-$ and $Im_{2,1}^+$ / $N(CN)_2^-$) were estimated to be equal to the half-peak potentials. The acetonitrile with [TBAP] =0.1 M but with no electron donating ILs, and [$Im_{2,1}^+$ / NTf_2^-]=0.01 M solution in the TBAP acetonitrile electrolyte solution were also measured to show the zero background conditions.

2.1.5 High-Energy Synchrotron X-ray Scattering

The ionic liquids were dried under vacuum at 2×10^{-2} mbar and ambient temperature for more than 48 hours while stirred, and then temporarily sealed with beeswax while in a glovebox under argon atmosphere with oxygen and water levels below 0.1 and 0.4 ppm, respectively. Samples were contained in 2 mm quartz capillaries (Hampton Research) or 3 mm NMR tubes (Sigma-Aldrich), which were then flame sealed. High-energy X-ray scattering experiments for pair distribution function analysis were performed at the Advanced Photon Sources (APS) beamline 11-ID-B. The X-ray wavelength was 0.21140 Å, corresponding to a photon energy of 58.66 keV. The forward-scattered X-rays are recorded using a Perkin-Elmer amorphous silicon 2D area detector. The sample-to-detector distance is calibrated using the powder diffraction pattern from CeO_2, and is typically about 22.7 cm, providing scattering data in the range of scattering vector $q = 4\pi sin\theta/\lambda$ between 0.2 to 20 Å^{-1}. The corrected X-ray intensities $I(q)$ vs. q were obtained by integrating raw data using Fit2D software.[31] The structure factors $S(q)$ were obtained using PDFgetX2 software[59] following a series of corrections that include Compton Scattering and oblique incidence angles.

2.2 Theoretical Methods

2.2.1 Studying Ionic Liquid Structures Using Molecular Dynamics Simulations

Simulation Parameters

Molecular dynamics simulations are run using the GROMACS 5.0.4 package with GPU acceleration.[1, 4, 58] In this work, each simulation box with periodic boundary conditions contained 1,000 ion pairs. We used the following protocol to equilibrate all simulation boxes: The box was initialized during a 500 ps simulation in which the charges of all atoms were scaled to 10% of the defined values then the charges were scaled to 50% of full charge definition for another 500 ps. Berendsen pressure and temperature coupling are applied.[4] Next all the atoms are scaled to full charges, and

a simulated annealing protocol was used with heating from 298 to 598 K in 500 ps, followed by a 5 ns equilibration using a Nosé-Hoover thermostat[53, 54] and Parrinello-Rahman barostat at 598 K.[56] The simulation boxes were then annealed from 598 to 298 K over 500 ps. The annealed boxes were equilibrated at 1 bar and 298 K for another 10 ns, again using a Nosé-Hoover thermostat [53, 54] and Parrinello-Rahman barostat.[56] The final production run for calculating $g(r)$ and $S(q)$ functions is done for 2 ns with coordinates saved every 1 ps, so that $g(r)$ is averaged over 2001 snapshots. In the equilibration and final production run, the equations of motion were integrated using the leap-frog algorithm with a time step of 0.001 ps, the default parameter in GROMACS.[1, 58] We also used the default Verlet cutoff scheme in GROMACS,[1, 58] with neighboring list radii and cutoffs for Coulomb and Lennard-Jones interactions all set to 1.5 nm. Long range electrostatic potentials were calculated using the Particle Mesh Ewald (PME) summation method[14, 21] with an interpolation order of 6 and a FFT grid spacing of 0.08 nm in a 3D periodic geometry.

Force Fields for Ionic Liquids

In the simulations, we used the modified OPLS-AA force field [61] for ionic liquids by Lopes and Pádua, called the CL&P force field,[46] with some augment parameters calibrated from this work. The total potential of the system is the sum of the bonded interactions and non-bonded interactions:

$$V_{total} = V_{bonded} + V_{non-bonded} \tag{2.2}$$

where the bonded parameters include contributions from bonds, angles, proper dihedral angles and improper dihedral angles:

$$
\begin{aligned}
V_{bonded} = \quad & V_{bond} + V_{angle} + V_{dih} + V_{imdih} \\
= \quad & \sum_b \frac{1}{2} k_b (r_b - r_b^0)^2 \\
+ \quad & \sum_a \frac{1}{2} k_a^\theta (\theta_a - \theta_a^0)^2 \\
+ \quad & \sum_d \sum_{n=0}^{5} C_n (\cos(\phi_d))^n \\
+ \quad & \sum_{imd} k_\phi (1 + cos(n\phi - \phi_s))
\end{aligned}
\tag{2.3}
$$

and non-bonded parameters include Lennard-Jones (L-J) type van der Waals parameters and Coulomb interactions:

$$
\begin{aligned}
V_{non-bonded} &= V_{LJ} + V_{coulomb} \\
&= \sum_i \sum_j 4\epsilon_{ij} ((\frac{\sigma_{ij}}{\epsilon_{ij}})^{12} - (\frac{\sigma_{ij}}{\epsilon_{ij}})^6) + \frac{1}{4\pi\epsilon_0} \frac{q_i q_j}{r_{ij}}
\end{aligned}
\tag{2.4}
$$

the L-J force between different atoms were combined using the combining rule given in Eq. 2.5. The intra-molecular non-bonded potential between atoms that are connected by bonds or angles are excluded, and all non-bonded 1,4 interactions are scaled by a factor of 0.5.

$$
\sigma_{ij} = (\sigma_i \sigma_j)^{1/2}; \epsilon ij = (\epsilon_i \epsilon_j)^{1/2} \tag{2.5}
$$

Most force field parameters were from the OPLS-AA force field [34, 61, 73], the CL&P force field by Lopes and Pádua. [43–46, 64] and a previous augmentation of the CL&P force field. [15] The missing parameters are determined using the following procedures:

Lennard-Jones parameters: The parameters for silicon atom are modified from those in the OPLS-AA force field,[61] which originally came from the GROMOS53A6 force field. [55]

Atomic charges: Most atomic charges were determined from fits to the electrostatic potentials using the CHeLPG algorithm [5] also at the MP2/cc-pVTZ level using Gaussian 09 Package D01[24]. The partial charge for silicon and its connected atoms

are obtained using the method for the COMPASS force field,[70, 71] for which Si will donate 0.135 electrons to each of its neighboring carbon atoms and 0.2225 electrons to each bonded oxygen atom. These charge additions or subtractions are made based on CL&P charges. For example, the charge on a C1 atom, which is the carbon connected to ring nitrogen, is set to -0.17 in the CL&P force field. Thus for Si-mim$^+$ or Si-pyrr$^+$ cations, the carbon atom at same position, which bridges the imidazolium or pyrrolidinium ring and the silicon atom is set to -0.305 (from -0.17 - 0.135). In the CL&P force field, the quaternary carbon atom at C2 position is set to 0.13 in order to balance the molecular charge. In Si-mim$^+$ and Si-pyrr$^+$, since this carbon is replaced by silicon, 4×0.135 charge is added to it to make a +0.67 charge for Si atoms, and the charge on CSi, the carbon in terminal CH_3 group, is set to -0.315 by removing 0.135 from -0.180. The charge on silicon atoms and oxygen atom in SiOSi-mim$^+$ are also determined using this way. Using this method, we can keep the charge on imidazolium or pyrrolidinium backbone same as that in CL&P force field, and make our force field transferable.

Bond and angle parameters: Most bond lengths and angles were assigned based on geometries optimized at the MP2/cc-pVTZ level and X-ray structure.The X-ray structure data were from the Cambridge Crystallographic Data Center. [29] The entry reference codes for each compound is a six-digit code with prefix "CSD", and the codes are LUQHAH, BEJFOL, PARBUF, SUPLUK, SUZXER, TMSSIMP10, WEPHEE and YUPXOX for silicon ILs, BEMFAA, CEDHAU, PAMDIS, PAMDOY and ZZZAIJ01 for $SeCN^-$, AFUNOF, GOGPAV, MOSYEA, PODCUI for SCN^-, AMCYME, NATCYM and OVUFAN for $C(CN)_3^-$, CAMWAQ and CNANTH for cyano-substituted anthracenes, DMAFBZ01, FAXGOB, GOGWEG, LIYSIV, REDDAF and SENJAW for DMA and DMPT. Specific parameters for the molecular ions containing silicon atoms are adapted using parameters from the GROMOS 53a6 force field [55] and the force fields for polysilane proposed by Frierson et al.[23] and Sun et al.[70, 71]

Missing angles and dihedral torsion profiles using relaxed scan. The missing angle bending and dihedral angle torsion force constants are obtained by fitting a potential surface to equations, as described in the CL&P articles.[43, 44, 46]. The bending or torsion contribution to the potential energy is obtained by subtracting the

total bending/torsion energy from quantum results using the non-bonded contribution obtained from a single molecule MD run. The total energy is obtained from quantum calculations after a relaxed scan of the desired angle/dihedral using Gaussian 09 calculations[24] at the MP2/cc-pVTZ level of theory. For some dihedrals calculations were done at the MP2/cc-pVTZ//HF/6-31G(d) level, following Ref. 43. That means the geometry of molecule at a fixed dihedral is optimized HF/6-31g(d) level, then a single point energy is calculated at the MP2/cc-pVTZ level. The non-bonded contribution of the potential is obtained using a molecular dynamics simulation of a single molecule, in which all force constants are set to zero and all coordinates of the molecule are frozen to fix the molecular geometry at the lowest energy previously obtained from quantum calculations. We did not further optimize the geometry during the single molecule MD run. The non-bonded 1,4-interactions are scaled by a factor of 0.5. The fitted bending/torsion force constants were examined by re-inserting them back in single molecule MD run to reproduce the original quantum results.

Typically, the free rotation of a methyl group bonded to a silicon atom is obtained using two model molecules: tetramethylsilane $Si(CH_3)_4$ and hexamethyldisiloxane ($(CH_3)_3SiOSi(CH_3)_3$). The potential energies are shown in the left panel of Fig. 2.1. The fitted energy profile of C-Si-C-H in $Si(CH_3)_4$ is split into nine C*-Si*-C*-HC dihedral angles, which have a 120 degree angles relative to each other. The O-Si-C-H torsion profile in $(CH_3)_3SiOSi(CH_3)_3$ is split into three OS-Si*-C*-HC angles after subtracting six C*-Si*-C*-HC dihedral angles in the same way.

The energy profiles for the other dihedral angles are shown in the right panel of Fig. 2.1. Dihedral angles for Si*-OS-Si*-C* in SiOSi-mim$^+$ are also obtained by relaxed scanning of the Si-O-Si-C dihedral in $(CH_3)_3SiOSi(CH_3)_3$ at the MP2/cc-pVTZ level. This angle is split into three Si*-OS-Si*-C* dihedral profiles. The rotation of the Si-O bond is nearly barrierless, which is consistent with literature results. [6, 7] The NA-C1-Si*-CT dihedral angles in Si-mim$^+$ and SiOSi-mim$^+$ are obtained by scanning the N-C-Si-C angles in the Si-mim$^+$ cation at the MP2/cc-pVTZ//HF/6-31G(d) level, following Ref. 43. This angle can be split into 3 NA-C1-Si*-CT and 6 C*-Si*-C*-HC dihedral angles, with the latter value being the one obtained previously. The

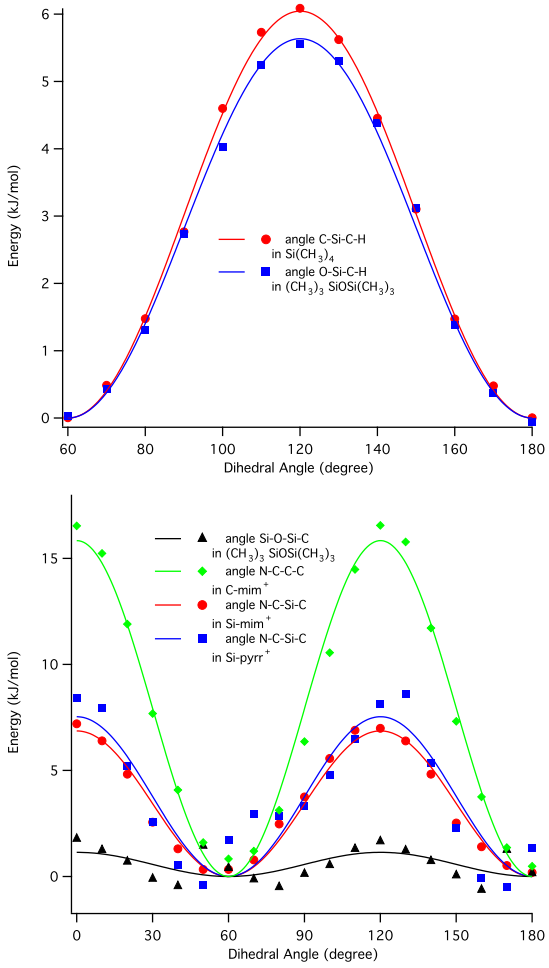

Figure 2.1: Fits to the potential energy vs. dihedral angle.

NT-C1-Si-CT dihedral angle in Si-pyrr$^+$ is optimized for the Si-pyrr$^+$ cation at the MP2/cc-pVTZ//HF/6-31G(d) level. It was split into three NT-C1-Si-CT angles and six C*-Si*-C*-HC angles.

The bending potentials for the C-Si-O and Si-O-Si angles in SiOSi-mim$^+$ were also determined by relaxed scanning of the $(CH_3)_3SiOSi(CH_3)_3$ molecule at the MP2/cc-pVTZ level. The fits are shown in Fig. 2.2. We find that for the Si-O-Si angle, the energy minimum after subtracting non-bonded interactions is smaller than for the minimum of the quantum results, or 141.8°. The angle Si-O-Si angle in SiOSi-mim$^+$ is set to 137.8° so the average angle from the MD trajectory is close to the value determined by X-ray crystallography, or 145.9 °.[52].

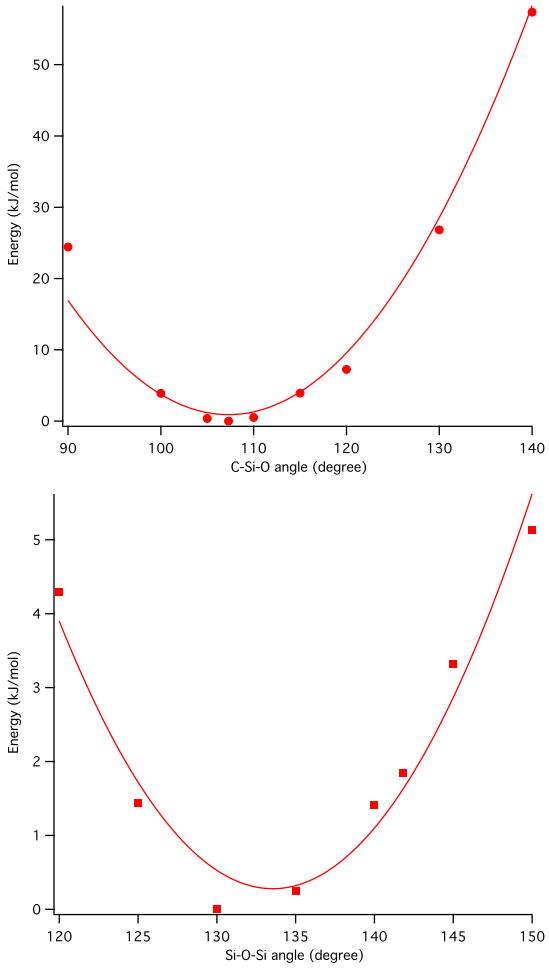

Figure 2.2: Fits of the potential energy to the C-Si-O and Si-O-Si angles.

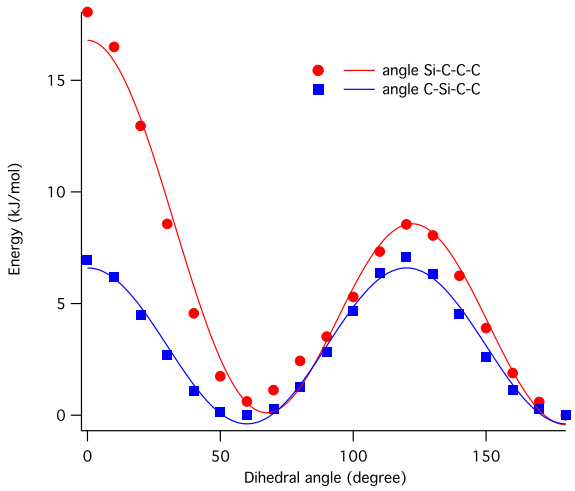

Figure 2.3: The fitting of two dihedral angles for the trimethylsilylpropyl group.

To obtain the torsion profiles for the two needed dihedral angles, CT-CT-CT-Si and CT-CT-Si-CT, the same methods used in our previous work are adopted here.[78] A virtual molecule, trimethylpropylsilane ($CH_3CH_2CH_2Si(CH_3)_3$) is proposed for dihedral scanning. The torsion barriers for the selected dihedral angles are obtained by subtracting total energy and the contribution of non-bonded parameters. The total quantum energy is from a relaxed scan with a step length of 10 degree at MP2/cc-pVTZ level, and the non-bonded contribution is obtained using a single molecule molecular dynamics simulations in which the atomic positions are fixed at the result of relaxed optimization. The 1,4 interactions are scaled by a factor of 0.5 in this scan. The scan and fits of energy profile is shown in Fig. 2.3. The red curve is the result of fits of Si-C-C-C angle in $CH_3CH_2CH_2Si(CH_3)_3$, which contains one CT-CT-CT-Si angle, 4 HC-CT-CT-HC angles, two HC-CT-CT-CT angles and two Si-CT-CT-HC angles. The blue curve is for the C-Si-C-C angle, which can be split to six Ct-Si-CT-HC and three CT-Si-CT-CT angles. The profiles of HC-CT-CT-HC, HC-CT-CT-CT, Si-CT-CT-HC and Ct-Si-CT-HC can be obtained from OPLS-AA force field [61] and previous work, [78], therefore our desired angle, CT-CT-CT-Si and CT-CT-Si-CT can be obtained after subtracting them.

All the parameters used are list in the following tables:

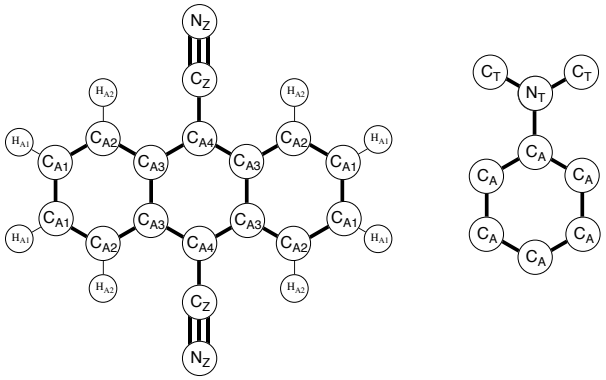

Figure 2.4: The atom labels for DCNA (left) and DMA backbone (right).

Table 2.1: Force field parameters used for MD simulations. The parameters not shown are the same as in the OPLS-AA force field [61] or the augmented CL&P force field. [15, 43–45]

Cyanoanthracenes			
atomtype	$q(e)$	σ(nm)	ϵ (kJ mol^{-1})
CA1	-0.037	0.355	0.29288
CA2	-0.2195	0.355	0.29288
CA3	0.172	0.355	0.29288
CA4	-0.281	0.355	0.29288
CZ	0.456	0.365	0.62760
NZ	-0.468	0.320	0.71128
HA1	0.090	0.242	0.12552
HA2	0.141	0.242	0.12552
bondtype	r_b^0(nm)	k_b(kJ mol^{-1} nm^{-2})	r_b^{xray} (nm)
CA1-CA1	0.1415	392459	0.1419
CA1-CA2	0.1374	392459	0.1366
CA2-CA3	0.1418	392459	0.1427
CA3-CA4	0.1410	392459	0.1409
CA*-HA*	0.1080	307105	
CA4-CZ	0.1425	334720	0.1442
CZ-NZ	0.1176	543920	0.1147
angles	θ_a^0(deg)	k_a(kJ mol^{-1} rad^{-2})	
CA*-CA*-CA*	120	527.18	119.5 $\sim$ 120.5
CA*-CA*-HA*	120	292.88	
CA*-CA*-CZ	120	585.76	118.7 $\sim$ 122.6
CA*-CZ-NZ	180	1255.20	179.2
proper dihedrals	C_0	C_2	
X-CA*-CA*-Y	30.3340	-30.3340	
CA*-CA*-CZ-NZ	0	0	
improper dihedrals	k_ϕ	n	ϕ_s
-CA--*	4.60	2	180
anionic quenchers, $C(CN)_3^-$, $SeCN^-$ and SCN^-			
bondtype	r_b^0(nm)	k_b(kJ mol^{-1} nm^{-2})	
C-C	0.141	334720	
Se-C	0.188	418400	
S-C	0.164	418400	
C-N	0.115	774600	
DMA and DMPT			
angles	θ_a^0(deg)	k_a(kJ mol^{-1} rad^{-2})	
CA-NT-CT	115	418.40	
CT-NT-CT	115	433.46	
dihedrals	C_0	C_2	
CA-CA-NT-CT	30.3340	-30.3340	

The parameters are shown in Table 2.2 and Table 2.3, using the atom labels shown in Fig. 2.5.

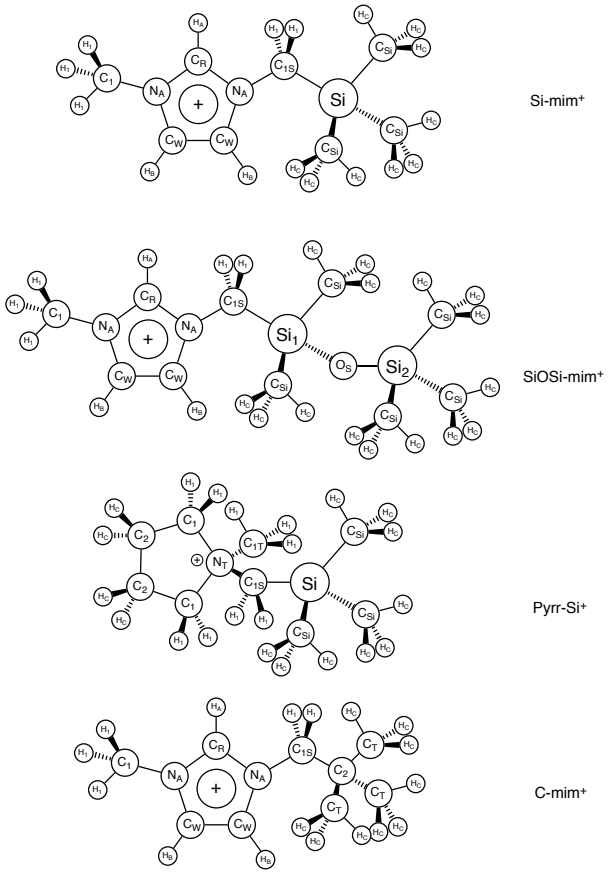

Figure 2.5: The atom labels for the four IL cations.

The force field parameters for the Si-C_3-mim$^+$ and Si-C_3-Pyrr$^+$ cations are shown in Table 2.4, with the atom labels defined in Fig. 2.6.

Table 2.2: Force field parameters for imidazolium cations. The atom labels are shown in Fig. 2.5. Some parameters for C-mim$^+$ given in Ref. 43 are not listed here.

L-J parameters

Atomtype	σ_i	ϵ_i	q_i	Source	Atomtype	σ_i	ϵ_i	q_i	Source
C1	0.350	0.27614	-0.170	Ref. 43	CT	0.350	0.27614	-0.180	Ref. 43
C1S	0.350	0.27614	-0.305	Ref. 43, 70	CSi	0.350	0.27614	-0.315	Ref. 43
CW	0.355	0.29288	-0.130	Ref. 43	CR	0.355	0.29288	-0.110	Ref. 43
NA	0.325	0.71128	0.150	Ref. 43	HA	0.242	0.12552	0.210	Ref. 43
HB	0.242	0.12552	0.210	Ref. 43	HC	0.250	0.12552	0.060	Ref. 43
Si	0.339	2.44704	0.670	OPLS-AA[a] , Ref. 70	Si1	0.339	2.44704	0.758	OPLS-AA[a], Ref. 71
Si2	0.339	2.44704	0.627	OPLS-AA[a], Ref. 71	OS	0.290	0.58576	-0.445	OPLS-AA, Ref. 71
H1	0.250	0.12552	0.130	Ref. 43	C2	0.350	0.27614	0.130	Ref. 43

Bond and angle parameters

Bond type	r_b^0	k_b	Source of r_b^0	Source of k_b	Bond type	r_b^0	k_b	Source of r_b^0	Source of k_b
CW-CW	0.1341	435200	Ref. 43	Ref. 43	CR,CW-H*	0.1080	284500	Ref. 43	Ref. 43
C*-H1,HC	0.1090	284500	Ref. 43	Ref. 43	NA-C1,C1S	0.1466	282000	Ref. 43	Ref. 43
C1S-Si*	0.1933	359000	this work [d]	Gromos53A6	NA-CR	0.1315	399200	Ref. 43	Ref. 43
NA-CW	0.1378	357400	Ref. 43	Ref. 43	Si*-CSi	0.1870	359000	this work [d]	Gromos53A6
Si*-OS	0.1660	472000	this work [e]	Gromos53A6					

Angle type	θ_a^0	k_a	Source of θ_a^0	Source of k_a	Angle type	θ_a^0	k_a	Source of θ_a^0	Source of k_a
CW-NA-CR	108.0	585.8	Ref. 43	Ref. 43	CW-NA-C1,C1S	125.6	585.8	Ref. 43	Ref. 43
CR-NA-C1,C1S	126.4	585.5	Ref. 43	Ref. 43	NA-CR-HA	125.1	292.9	Ref. 43	Ref. 43
NA-CR-NA	109.8	585.8	Ref. 43	Ref. 43	NA-CW-CW	107.1	585.8	Ref. 43	Ref. 43
NA-CW-HB	122.0	292.9	Ref. 43	Ref. 43	CW-CW-HB	130.9	292.9	Ref. 43	Ref. 43
NA-C1,C1S-H1	110.7	313.8	Ref. 43	Ref. 43	NA-C1,C1S-CT,Si,Si1	112.7	488.3	Ref. 43	Ref. 43
C1S-Si-CSi	106.5	450.0	this work[e]	Gromos53A6	CSi-Si-CSi	112.3	450.0	this work[e]	Gromos53A6
C1S-Si1-CSi	108.0	450.0	this work[e]	Gromos53A6	CSi-Si1-CSi	113.6	450.0	this work[e]	Gromos53A6
C1S-Si1-OS	101.4	176.2	this work[e]	this work	CSi-Si1-OS	112.3	176.2	this work[e]	this work
Si1-OS-Si2	137.8	64.8	this work[e]	this work	OS-Si2-CSi	107.5	176.2	this work[e]	this work
CSi-Si2-CSi	111.3	450.0	this work[e]	Gromos53A6	Si*-C*-HC	110.8	193.3	Ref. 23	Ref. 23

Dihedral angle parameters [b,c]

Dihedral angle type	C_0	C_1	C_2	C_3	Source
NA-C1S-Si*-CSi,OS	0.4724	1.4172	0.0000	-1.8896	this work
C*-Si*-C*-H1,HC	0.3358	1.0074	0.0000	-1.3432	this work
OS-Si*-C*-HC	0.2676	0.8028	0.0000	-1.0704	this work
Si*-OS-Si*-C*	0.1897	0.5697	0.0000	-0.7588	this work
NA-C1-C2-CT	1.3846	4.1539	0.0000	-5.1325	this work

Improper dihedral type	k_{im}	ϕ_s	n	Source
-CR,CW--*	180	4.600	2	OPLS-AA
-NA--*	180	4.185	2	OPLS-AA

Units: σ_i: nm ; ϵ_i : kJ mol^{-1} ; r_b^0 : nm ; k_b : kJ mol^{-1} nm^{-2} ; k_a : kJ mol^{-1} rad^{-2} ;

[a] Originally copied from GROMOS force field [55] [b] The dihedral types that can be found in Reference 43 are not listed here.

[c] $C_4 = C_5 = 0$ in all cases. [d] Obtained by comparing optimized structure at the MP2/cc-pVTZ level and x-ray results. [29] [e] obtained by comparing optimized structures at the MP2/cc-pVTZ level and x-ray results.[52]

Table 2.3: Force field parameters for Si-pyrr$^+$ cations. The atom labels are shown in Fig. 2.5.

L-J parameters

Atomtype	σ_i	ϵ_i	q_i	Source	Atomtype	σ_i	ϵ_i	q_i	Source
C1	0.350	0.27614	-0.170	Ref. 44	C1T	0.350	0.27614	-0.170	Ref. 44
C2	0.350	0.27614	0.010	Ref. 44	CSi	0.350	0.27614	-0.315	Ref. 44, 70
C1S	0.350	0.27614	-0.305	Ref. 44, 70	H1	0.250	0.12552	0.130	Ref. 44
HC	0.250	0.12552	0.060	Ref. 44	Si	0.339	2.44704	0.670	OPLS-AA, Ref. 70
NT	0.325	0.71128	0.120	Ref. 44, 46					

Bond and angle parameters

Bond type	r_b^0	k_b	Source of r_b^0	Source of k_b	Bond type	r_b^0	k_b	Source of r_b^0	Source of k_b
NT-C1S,C1	0.1505	307105	this work[c]	OPLS-AA	NT-C1T	0.1485	307105	this work[c]	OPLS-AA
C*-H*	0.1090	284512	OPLS-AA	OPLS-AA	C1-C2	0.1529	224262	this work[c]	OPLS-AA
C2-C2	0.1548	224262	this work[c]	OPLS-AA	C1S-Si	0.1940	359000	this work[b,c]	Gromos53A6
Si-CSi	0.1870	359000	this work[b]	Gromos53A6					

Angle type	θ_a^0	k_a	Source of θ_a^0	Source of k_a	Angle type	θ_a^0	k_a	Source of θ_a^0	Source of k_a
C1-NT-C1	101.6	418.4	this work[c]	OPLS-AA	C1-NT-C1T,C1S	111.0	418.4	this work[c]	OPLS-AA
C1T-NT-C1S	110.6	418.4	this work[c]	OPLS-AA	HC-C1,C1T-NT	107.6	292.9	this work[c]	OPLS-AA
C2-C1-NT	104.6	669.4	this work[c]	OPLS-AA	HC-C1,C2,CSi-HC	107.8	276.1	OPLS-AA	OPLS-AA
HC-C1-C2	113.5	313.8	this work[c]	OPLS-AA	C1,C2-C2-HC	110.7	313.8	OPLS-AA	OPLS-AA
C1-C2-C2	104.9	488.3	this work[c]	OPLS-AA	NT-C1S-Si	121.9	669.4	this work[c]	Gromos53A6
NT-C1S-HC	106.3	292.9	this work[c]	Gromos53A6	HC-C1S-HC	106.6	276.1	this work[c]	Gromos53A6
HC-C1S-Si	107.4	313.8	this work[c]	Gromos53A6	C1S-Si-CSi	107.7	450.0	this work[c]	Gromos53A6
CSi-Si-CSi	111.1	450.0	this work[c]	Gromos53A6	Si-CSi-HC	110.8	193.3	Ref. 23	Ref. 23
HC-C1T-HC	110.0	276.1	this work[c]	OPLS-AA					

Dihedral angle parameters [a]

Dihedral angle type	C_0	C_1	C_2	C_3	Source
C*-Si-C*-HC	0.3358	1.0074	0.0000	-1.3432	this work
NT-C*-Si-C*	0.5840	1.7520	0.0000	-2.3360	this work
C*-NT-C*-H*	0.6318	1.8954	0.0000	-2.5271	OPLS-AA
C*-C*-NT-C*	3.0418	-1.3514	0.5188	-2.2092	OPLS-AA
H*-C*-C*-NT	0.8033	2.4010	0.0000	-3.2133	OPLS-AA
C*-C*-C*-NT	5.7718	-2.6715	0.9581	-4.0585	OPLS-AA
H*-C*-C*-H*	0.6276	1.8828	0.0000	-2.5104	OPLS-AA
C*-C*-C*-H*	0.6276	1.8828	0.0000	-2.5104	OPLS-AA
C*-C*-C*-C*	2.9288	-1.4644	0.2092	-1.6736	OPLS-AA

Units: σ_i: nm ; ϵ_i : kJ mol^{-1} ; r_b^0 : nm ; k_b : kJ mol^{-1} nm^{-2} ; k_a : kJ mol^{-1} rad^{-2} ;

[a] $C_4 = C_5 = 0$ in all cases. [b] obtained by comparing optimized structures at the MP2/cc-pVTZ level and x-ray results.[29] [c] taking results from optimized structures at the MP2/cc-pVTZ level.

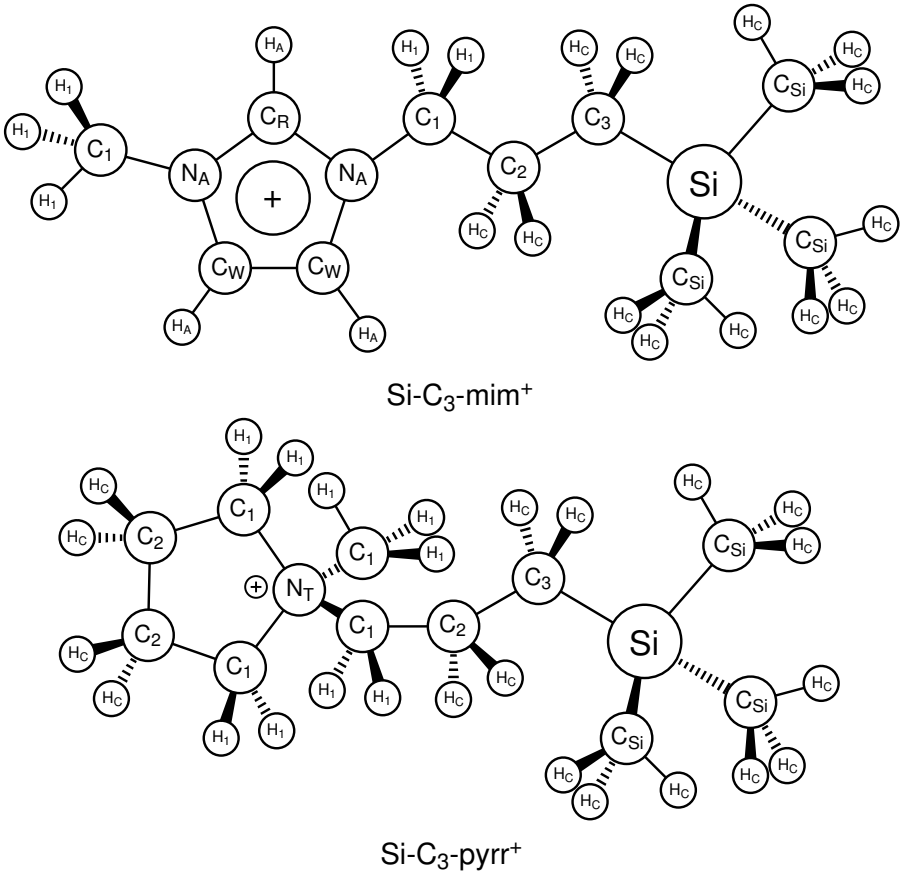

Figure 2.6: Atom labels for the Si-C_3-mim$^+$ and Si-C_3-Pyrr$^+$ cations.

Table 2.4: Force field parameters used for Si-C_3-mim$^+$ and Si-C_3-Pyrr$^+$ cations.

L-J parameters

Atomtype	σ	ϵ	q	Source	Atomtype	σ	ϵ	q	Source
C1	0.350	0.27614	-0.170	Ref. 43	C2	0.350	0.27614	0.010	Ref. 44
C3	0.350	0.27614	-0.255	Ref. 43, 70	CSi	0.350	0.27614	-0.315	Ref. 43, 70
CW	0.355	0.29288	-0.130	Ref. 43	CR	0.355	0.29288	-0.110	Ref. 44
NA	0.325	0.71128	0.150	Ref. 43	HA	0.242	0.12552	0.210	Ref. 43
HC	0.250	0.12552	0.060	Ref. 43	Si	0.339	2.44704	0.540	OPLS-AA[a], Ref. 70
H1	0.250	0.12552	0.130	Ref. 43	NT	0.325	0.71128	0.120	Ref. 44

Bond and angle parameters [a]

Bond type	r_b^0	k_b	Source of r_b^0	Source of k_b	Bond type	r_b^0	k_b	Source of r_b^0	Source of k_b
C3-Si	0.1907	359000	this work [d]	Gromos53a6	Si-CSi	0.1870	359000	Gromos53a6	Gromos53a6
CSi-HC	0.1090	284500	CL&P	CL&P					

Angle type	θ_a^0	k_a	Source of θ_a^0	Source of k_a	Angle type	θ_a^0	k_a	Source of θ_a^0	Source of k_a
C2-C3-Si	113.8	488.3	this work[e]	OPLS-AA	C3-Si-CSi	108.2	450.0	this work[e]	Gromos53a6
CSi-Si-CSi	110.7	450.0	this work[e]	Gromos53a6	HC-C3-Si	108.3	193.3	this work[e]	Ref. 23
Si-CSi-HC	110.8	193.3	this work[e]	Ref. 23					

Dihedral angle parameters [a,b]

Dihedral angle type	C_0	C_1	C_2	C_3	Source
CT-Si-CT-HC	0.3358	1.0074	0.0000	-1.3432	this work
CT-CT-CT-Si	-1.2584	-1.5312	4.8460	-2.0564	this work
CT-CT-Si-CT	0.4923	1.4771	0.0000	-1.9692	this work

Units: σ: nm ; ϵ : kJ mol^{-1} ; r_{ij}^0 : nm ; k_{ij}^b : kJ mol^{-1} nm^{-2} ; k_{ijk}^θ : kJ mol^{-1} rad^{-2} ;

[a] Only can't be found in CL&P force field [43, 44, 46] are listed here [b] C1, C2, C3 and CSi are all count as CT here

Structure Factor Calculation

The radial pair distribution functions $g(r)$ between all atom pairs are obtained from the trajectory of the production run. The structure functions can be calculated using Equation 2.6 as described previously: [8, 38, 63]

$$S(q) = \frac{\rho_0 \sum_i \sum_j x_i x_j f_i(q) f_j(q) \int_0^\infty 4\pi r^2 (g_{ij}(r) - 1) \frac{sin(qr)}{qr} W(r) dr}{[\sum_i^n x_i f_i(q)]^2} \tag{2.6}$$

where ρ_0 is the number density of the box, $g_{ij}(r)$ is the radial distribution function between atom type i and atom type j, respectively. x_i and $f_i(q)$ are the mole fraction and atomic form factor [13, 16, 57] of atom type i, respectively, and $W(r) = \sin(2\pi r/L)/(2\pi r/L)$ is the Lorch function; $W(r)$ is introduced to reduce the effect of finite truncation of r.[15, 17, 36–38, 47, 63]

Santos *et al.* showed the value of partitioning the structure factor into anion-anion, anion-cation and cation-cation contributions:[63]

$$S(q) = S_{a-a}(q) + S_{c-a}(q) + S_{a-c}(q) + S_{c-c}(q) \tag{2.7}$$

The concepts date back to the partitioning of the pair distribution by Lebowitz in 1964[39] and for the structure factor of a binary mixture of hard spheres by Ashcroft and Langreth in 1967.[3]

Here we have made a slight change from the approach used by Santos *et al.*[63] for calculating the partial $S(q)$ structure factors. The structure factors that result are unchanged relative to Santos *et al.*,[63] but the normalization of the radial pair distribution functions $g_{ij}(r)$ is changed so that each individual $g_{ij}(r)$ is normalized to unity rather than having the sum normalized, as was done by Santos *et al.*[63] The partial pair distribution functions used here are given below:

$$
\begin{aligned}
g_{ic-jc}(r) &= \frac{V}{N_{ic}N_{jc}} \sum_{i\in c}^{N_{ic}} \sum_{j\in c}^{N_{jc}} \frac{\delta(r_{ij}-r)}{\frac{4}{3}\pi((r+\delta r)^3 - r^3)} \\
g_{ic-ja}(r) &= \frac{V}{N_{ic}N_{ja}} \sum_{i\in c}^{N_{ic}} \sum_{j\in a}^{N_{ja}} \frac{\delta(r_{ij}-r)}{\frac{4}{3}\pi((r+\delta r)^3 - r^3)} \\
g_{ia-jc}(r) &= \frac{V}{N_{ia}N_{jc}} \sum_{i\in a}^{N_{ia}} \sum_{j\in c}^{N_{jc}} \frac{\delta(r_{ij}-r)}{\frac{4}{3}\pi((r+\delta r)^3 - r^3)} \\
g_{ia-ja}(r) &= \frac{V}{N_{ia}N_{ja}} \sum_{i\in a}^{N_{ia}} \sum_{j\in a}^{N_{ja}} \frac{\delta(r_{ij}-r)}{\frac{4}{3}\pi((r+\delta r)^3 - r^3)}
\end{aligned}
\tag{2.8}
$$

with the subscripts a and c denoting anionic and cationic atoms, respectively, V is the volume of the box. The number of anionic atoms is given by N_{ia} and the number of cationic atoms by N_{ic}. Each radial pair distribution can be directly calculated using the radial distribution analyzing program *g_rdf* embedded in GROMACS, and each pair distribution function converges to unity. The partial structure factors are calculated using the following equations:

$$
\begin{aligned}
S_{c-c}(q) &= \frac{\rho_0 \sum_i \sum_j x_{ic}x_{jc}f_i(q)f_j(q) \int_0^\infty 4\pi r^2 (g_{ic-jc}(r)-1)\frac{\sin(qr)}{qr}W(r)dr}{[\sum_i^n x_i f_i(q)]^2} \\
S_{a-a}(q) &= \frac{\rho_0 \sum_i \sum_j x_{ia}x_{ja}f_i(q)f_j(q) \int_0^\infty 4\pi r^2 (g_{ia-ja}(r)-1)\frac{\sin(qr)}{qr}W(r)dr}{[\sum_i^n x_i f_i(q)]^2} \\
S_{c-a}(q) &= \frac{\rho_0 \sum_i \sum_j x_{ic}x_{ja}f_i(q)f_j(q) \int_0^\infty 4\pi r^2 (g_{ic-ja}(r)-1)\frac{\sin(qr)}{qr}W(r)dr}{[\sum_i^n x_i f_i(q)]^2} \\
S_{a-c}(q) &= \frac{\rho_0 \sum_i \sum_j x_{ia}x_{jc}f_i(q)f_j(q) \int_0^\infty 4\pi r^2 (g_{ia-jc}(r)-1)\frac{\sin(qr)}{qr}W(r)dr}{[\sum_i^n x_i f_i(q)]^2}
\end{aligned}
\tag{2.9}
$$

where x_{ia} and x_{ic} are the fractions of anionic and cationic atoms of type i, respectively. Thus

$$
x_{ic} = \frac{N_{ic}}{N_i}x_i, \quad x_{ia} = \frac{N_{ia}}{N_i}x_i, \tag{2.10}
$$

and it becomes clear that all of the partial structure factors are identical to values in Equations A6 and A7 from Santos et al.[63]

We have generalized the approach of Kashyap et al.[37] by introducing one additional flavor of sub-ionic partitioning, where the cation contributions from the methylimidazolium part and the functional group, *e.g.*, the trimethylsilylmethyl group on Si-mim$^+$, are considered independently.[37] For this case, the partitioning of the structure factor is written as

$$S(q) = S_{h-h}(q) + 2S_{h-t}(q) + 2S_{h-a}(q) + S_{t-t}(q) + 2S_{t-a}(q) + S_{a-a}(q), \qquad (2.11)$$

where h indicates the cationic head group, or methylimidazolium; t denotes the cationic substituent, and a denotes the anion.[37]

2.2.2 Electronic Structure Calculations

van der Waals Volume

Two methods can be used to calculate the van der Waals volume of a molecule. The first is to use the Monte Carlo method implemented in Gaussian 09 [24] at a B3LYP/6-311+G(d,p) level on the 0.002 e/a_0^3 isodensity surface. Typical keywords used in Gaussian program is "b3lyp/6-311+g(d,p) volume IOp(6/45=5000) IOp(6/46=20)". We also calculated van der Waals volumes using the volume increment method, [19] where the parameters for Se are from Zhao et al.[82] In both cases, radii are calculated from the volumes using the spherical approximation.

Inner-Sphere Reorganization Energy

Inner-sphere reorganization energies were calculated as the sum of isolated fluorophore and quencher energies at the B3LYP/6-311+G(d,p) level using Gaussian 09 software [24] and the relations:

$$\lambda_{in} = \lambda_{in}(F) + \lambda_{in}(Q) \ , \qquad (2.12)$$

$$\lambda_{in}(F) = E(F^*)F^- - E(F^*)F^* \qquad \lambda_{in}(Q) = E(Q)Q^+ - E(Q)Q \ . \tag{2.13}$$

In these equations, $E(X)Y$ denotes the energy of X at the geometry optimized for Y, and F^* means a fluorophore molecule in its first excited state.

Solvation Radii

The effective solvent radii of the fluorophore and quencher, $r_{\mathrm{solv}}(F)$ and $r_{\mathrm{solv}}(Q)$, are estimated as follows. First, the solvent reorganization energy of each species is calculated at the B3LYP/6-311+G(d,p) level, using an IEF-PCM model of acetonitrile via

$$\lambda_{solv}(F) = E(F^*)_{solv(F^-)} - E(F^*)_{solv(F^*)} \qquad \lambda_{solv}(Q) = E(Q)_{solv(Q^+)} - E(Q)_{\mathrm{solv(Q)}} \ . \tag{2.14}$$

In these equations $E(X)_{solv(Y)}$ is the energy of state X in the solvent equilibrated for Y. The solvation energies obtained in acetonitrile are used to solve for the effective solvation radius in the following equation:

$$\lambda_{solv}(F/Q, \mathrm{CH_3CN}) = \frac{e^2}{4\pi\epsilon_0}\left[\frac{1}{2r_{\mathrm{solv}}(F/Q)}\right]\left[\frac{1}{n^2_{\mathrm{CH_3CN}}} - \frac{1}{\epsilon_{r,\mathrm{CH_3CN}}}\right]. \tag{2.15}$$

Electronic Coupling

The electric coupling matrix elements between fluorophores and quenchers are calculated using the effective 2-state Generalized Mulliken-Hush (GMH) model [9, 62] using quantities obtained from time-dependent density functional theory (TD-DFT) calculations on isolated F-Q pairs. TD-DFT calculations of the first 5–8 singlet states were done at the CAM-B3LYP/6-311+G(d,p) level using Gaussian 09, version D01 [24]. The CAM-B3LYP functional was compared with the ωb97xd functional,[10] and very similar results were obtained.

In the effective 2-state Generalized Mulliken-Hush (GMH) model, H_{DA} between states 1 and 2 is calculated using the following equations: [9, 62]

$$H_{1,2}^{\text{bare}} = \frac{\mu_{12}\Delta_{12}E}{\sqrt{(\Delta_{12}\mu)^2 + 4\mu_{12}^2}} \ , \tag{2.16}$$

$$H_{1,2}^{\text{dressed}} = H_{1,2}^{\text{bare}} + \Delta_{12}E(\frac{\epsilon}{\alpha} - \frac{4\mu_{12}^2\epsilon}{\alpha^3} - \frac{\mu_{12}(\mu_{11}-\mu_{22})\delta}{\alpha^3}) \ , \tag{2.17}$$

$$\text{where} \qquad \epsilon = \frac{\mu_{13}\mu_{32}}{\mu_{22}-\mu_{33}}, \qquad \delta = \frac{\mu_{13}^2 - \mu_{23}^2}{\mu_{22}-\mu_{33}} \qquad \text{and} \qquad \alpha = \sqrt{(\Delta_{12}\mu)^2 + 4\mu_{12}^2} \ , \tag{2.18}$$

$\Delta_{12}E$ is the electronic energy difference between the locally excited state and the charge transfer state. $H_{1,2}^{\text{bare}}$ is the original two state GMH model result, and $H_{1,2}^{\text{dressed}}$ is the effective two state modification by Rust et al., which is very close to the three-state GMH result. [62] In these equations, $\Delta\mu_{12}$ is the difference of the dipole moments of the initial and final states: $\Delta\mu_{12} = |\boldsymbol{\mu_{11} - \mu_{22}}|$. μ_{ii} is the dipole moment of state i, obtained by Hirshfeld population analysis, and μ_{ij} is the transition dipole moment between state i and state j, calculated using the Multiwfn program. [48] All the dipole moments μ_{ii} or μ_{ij} are the projections of the vectors onto the electron transfer direction. [9]

For our applications, state 1 is the lowest locally excited (LE) state, 2 is the particular charge transfer (CT) state having the largest oscillator strength with the LE state among the CT states at lower energy. State 3 is the ground state (GS). The GS is always selected as a reference because in most cases it is the state having the largest dipole coupling to both the LE and CT states.

The electron - hole distance ΔR for each excited state, as defined by Guido et al., [30] is also calculated using the Multiwfn program. [48] In most cases, ΔR for the charge transfer state is almost equal to the F-Q center of mass (COM) distance, r_{COM}. The sum of the atomic charges on the quencher q_{quencher} is calculated based on Hirshfeld population analysis. Atomic charges from electrostatic potential (ESP) fits might be a better choice. [32] We compared Hirshfeld population analysis with other atomic charges including Mulliken and ESP fit charges and found that although these

different methods assign very different charges to each atom, only small differences in the molecular quantities $q_{quencher}$ and dipole moments are found among them.

LE states are usually identified by

$$q_{\mathrm{quencher}} < q_{\mathrm{quencher}}(0) + 0.2 \quad \text{and} \quad \Delta R < 0.2 r_{com} \ , \tag{2.19}$$

and CT states by:

$$q_{\mathrm{quencher}} > q_{\mathrm{quencher}}(0) + 0.8 \quad \text{and} \quad \Delta R > 0.8 r_{com} \ , \tag{2.20}$$

where $q_{\mathrm{quencher}}(0)$ is -1 for anionic quenchers and 0 for neutral quenchers. When the fluorophore is DCNA or CNA and the quencher is $N(CN)_2^-$, we use $\Delta R < 0.6 r_{com}$ for LE states because ΔR is not well defined in cases like this where the reaction free energy is small. The states below the lowest LE state are all CT states. The number of CT states between the LE state generally increases with reaction free energy, for CNA-$N(CN)_2^-$ or CNA-$C(CN)_3^-$ pairs, there is only one CT state below the LE state, but for TCNA-$SeCN^-$ pair, there are usually 4–7 CT states below the LE state. The oscillator strength connecting the ground state to the locally excited state is usually significantly larger than that to the CT states.

In most cases the CT and LE states are easily distinguished, but in some cases a CT state is nearly degenerate with the LE state. In such cases, these two states are of mixed character. Also, in some cases only partial electron transfer occurs, for example when the LE state shows some CT character, or when any state lower in energy than the LE state has some LE character. The electronic coupling between a mixed state with either the LE or CT states is usually extremely large. To avoid these complications, all pairs that have partially degenerate states are excluded from the HDA calculations. For each F-Q type, up to 20% the of the structures might have to be discarded based on this criterion.

2.3 Diffusion-Reaction Models

2.3.1 The Smoluchowski Model

We consider four reaction models of increasing complexity in order to investigate how much can be learned about the electron transfer process from the quenching data. First we attempt to fit the data to the seminal model of Smoluchowski [67, 68] and its extension by Collins and Kimball.[11, 12] Neither of these models, which assume reaction only at a single contact distance, are able to adequately fit the nonexponential fluorescence decays observed in the ionic liquids. Next we consider an *extended sink* (ES) model in which reaction occurs throughout a finite spatial region rather than at a single distance. This model provides good fits to the quenching data observed in all three solvents using only three adjustable parameters: the relative reactant diffusion coefficient, the width of the reaction zone, and the rate constant within the reaction zone. We finally consider reaction models based on electron transfer theories. In this classical Marcus (CM) model, we use the descriptions of non-adiabatic electron transfer provided by Marcus theory combined with Zusman's treatment of dynamical solvent effects [49, 50, 60, 83] to define the form of $\kappa(r)$, which again is separated into a first solvation shell region and regions of greater F-Q separation.

Smoluchowski solved the diffusion-reaction problem using an absorbing boundary condition and showed $k_q(t)$ can be written [67, 68]

$$k_q^{SM}(t) = k_d(1 + \frac{r_0}{\sqrt{\pi D t}}) \ . \tag{2.21}$$

where $k_d = 4\pi r_0 D$ is the steady-state solution to the diffusion equation discussed in the Introduction with $D = D_A + D_D$ and $r_0 = r_A + r_D$. The second term in Eq. 2.21 is the transient term describing approach to the steady-state condition. Integrating $k_q(t)$ provides $K_q(t)$ as:

$$-K_q^{SM}(t) = k_d t + 8r_0^2\sqrt{\pi D t} \ . \tag{2.22}$$

2.3.2 The Collins-Kimball Model

The Collins-Kimball theory assumes a non-zero reaction rate κ_0 at contact, and in this case $k_q(t)$ can be written: [11, 12, 28, 35, 51]

$$k_q^{CK}(t) = \frac{\kappa_0 k_d}{\kappa_0 + k_d}\left[1 + \frac{\kappa_0}{k_d}\exp(x)\,\mathrm{erfc}\,(\sqrt{x})\right] , \tag{2.23}$$

where $x = (1+\kappa_0/k_D)^2 Dt/r_0^2$. This $k_q(t)$ cannot be integrated analytically, but for the large values of x relevant here, $k_q^{CK}(t) \approx 4\pi D\, r_{eff}\left(1+\sqrt{r_{eff}^2/(\pi Dt)}\right)$ and

$$-K_q^{CK}(t) \approx 4\pi\, r_{eff} Dt + 8 r_{eff}^2\sqrt{\pi Dt} \quad \text{with} \quad r_{eff} = \kappa_0 r_0/(k_d+\kappa_0) . \tag{2.24}$$

2.3.3 The Dudko-Szabo Approximate Solution

The extended sink and classical Marcus models are treated using the approximate solution of diffusion-reaction equation by Dudko and Szabo. [18] In their solution, $k_q(t)$ is related to the $t \to \infty$ quenching rate k_∞ and a distance dependent electron transfer rate $\kappa(r)$ by the following equations: [18]

$$k_q(t) = k_\infty\left[1 + \alpha_1 e^{\gamma_1^2 t}\,\mathrm{erfc}\,(\sqrt{\gamma_1^2 t}) + \alpha_2 e^{\gamma_2^2 t}\,\mathrm{erfc}\,(\sqrt{\gamma_2^2 t})\right] , \tag{2.25}$$

$$\frac{1}{k_\infty} = \frac{1}{<\kappa>} + \frac{1}{k_d(\infty)} , \tag{2.26}$$

$k_d(\infty)$ is estimated using:

$$k_d(\infty) = \frac{D\,\langle\kappa\rangle^2}{4\pi\int_0^\infty(\int_0^r x^2\kappa(x)g(x)dx)^2/\left(r^2 g(r)\right)dr} , \tag{2.27}$$

$$\gamma_{1,2} = (\mu \mp \lambda)\frac{<\kappa^2>}{<\kappa>^2} \qquad \text{and} \qquad \alpha_{1,2} = \frac{<\kappa>}{2k_d(\infty)}(1 \pm \frac{\mu}{\lambda}) , \tag{2.28}$$

$$\mu = \frac{k_d^2(\infty)}{8\pi D^{3/2}} \qquad \text{and} \qquad \lambda^2 = \mu^2 - [<\kappa^2> + k_d(\infty)]\frac{<\kappa>^2}{<\kappa^2>} . \tag{2.29}$$

The r-weighted electron transfer rates, $< \kappa^n >$ are dependent on the equilibrium F-Q distribution $g(r)$ via:

$$< \kappa^n >= \int_0^\infty 4\pi r^2 g(r) \kappa^n(r) dr \ . \tag{2.30}$$

2.3.4 The Extended Sink Model

In the ES model, reaction is also allowed to occur beyond r_1, with a rate that decays exponentially with distance,

$$\kappa(r) = \begin{cases} 0 & r < r_0 \\ \kappa_0 & r_0 \leq r < r_1 \\ \kappa_0 \exp\left(-\beta(r - r_1)\right) & r \geq r_1 \end{cases} \tag{2.31}$$

2.3.5 The Classical Marcus Model

In the classical Marcus model, $\kappa(r)$ is calculated using: [60]

$$\kappa(r) = \frac{2\,\pi H_{DA}(r)^2}{\hbar} \left[\frac{1}{4\,\pi\,\lambda(r)\,k_B T}\right]^{1/2} \frac{1}{1 + g_{adiab.}(r)} \exp\left(\frac{-\Delta G^*(r)}{k_B T}\right) \ . \tag{2.32}$$

The electronic coupling $H_{DA}(r)$ is divided into two regions:

$$H_{DA}(r)^2 = \begin{cases} V_0^2 \exp\left[-\beta_1\,(r - r_0')\right] & r_0' < r < r_1 \\ V_0^2 \exp\left[-\beta_2\,(r - r_1) - \beta_1\,(r_1 - r_0')\right] & r \geq r_1 \end{cases} \tag{2.33}$$

with the region between $r_0' = 2.9$ Å and $r_1 = 8.2$ Å defining the first solvation shell. In that region, we use the values of V_0 and β_1 from Table 4.7. At larger separations, we use a value $\beta_2 = 1.5$ Å^{-1} to represent through-solvent coupling, [75, 76] as in the ES2 model. The adiabaticity parameter $g_{adiab.}$ is

$$g_{adiab.}(r) = \frac{4\pi H_{DA}^2(r)}{\hbar \lambda(r)} \tau_s \ . \tag{2.34}$$

This parameter interpolates between the nonadiabatic ($g_{adiab.} << 1$) and solvent-controlled adiabatic ($g_{adiab.} >> 1$) limits, depending on the effective time scale of solvent reorganization, τ_s. Finally, $\lambda(r) = \lambda_{in} + \lambda_{solv}(r)$ is the total nuclear reorganization energy, consisting of inner-sphere (λ_{in}) and solvation (λ_{solv}) components, and

ΔG^* is the activation free energy. For these latter quantities we use slightly modified versions of the continuum dielectric expressions for spherical reactants from Marcus theory, [50] as described in the method section.

The activation energy, $\Delta G^*(r)$, is calculated using the Marcus formula except that we subtract the electronic coupling from the activation energy:

$$\Delta G^*(r) = \max\left\{0, \frac{\left[\Delta G(r) + \lambda(r)\right]^2}{4\lambda(r)} - H_{DA}(r)\right\} \ . \tag{2.35}$$

$\Delta G(r)$ is calculated from:

$$\Delta G(r) = \begin{cases} \Delta G_0 & \text{anionic quenchers;} \\ \Delta G_0 - e^2/\left(4\pi\epsilon_0\epsilon_r r\right) & \text{neutral quenchers;} \end{cases} \tag{2.36}$$

ΔG_0 is determined from the oxidation potential of the quencher, $E_{ox}(Q)$, the reduction potential of fluorophore, $E_{red}(F)$, and the free energy of the S_1 (locally excited) state:[74]

$$\Delta G_0 = E_{ox}(Q) - E_{red}(F) - G_{S1}(F) \ . \tag{2.37}$$

G_{S1} is either obtained from the literature or estimated from the average of absorption and emission energies. The electrochemical data we use for calculating ΔG_0 were nearly all measured in CH_3CN. In order to estimate the corresponding values in the two ionic liquid solvents we assumed that the differences between the redox processes in different solvents could be expressed in terms of energy differences of the ionic species approximated using the Born equation. In the case of the neutral fluorophores and neutral or univalent quenchers studied here, ΔG_0 in a solvent with an electrical permittivity ϵ_1 is related to that in a reference solvent with permittivity ϵ_2 by

$$\Delta G_0(\epsilon_1) - \Delta G_0(\epsilon_2) = \frac{e^2}{8\pi\epsilon_0}\left(\frac{1}{\epsilon_1} - \frac{1}{\epsilon_2}\right)\left(\frac{(z_F - 1)^2 - z_F^2}{r_{solv}(F)} + \frac{(z_Q + 1)^2 - z_Q^2}{r_{solv}(Q)}\right) \tag{2.38}$$

where z_Q is the quencher charge (0 or -1) and $r_{solv}(Q)$ and $r_{solv}(F)$ are the effective radii of the quencher and fluorophore described below. For the ionic quenchers the

differences calculated in this manner are all <0.1 eV, however, for the neutral quenchers in $P^+_{14,6,6,6}$ / NTf_2^- the average correction is 0.26 eV.

The reorganization energy (λ) of an electron transfer reaction is the sum of inner-sphere (λ_{in}) and solvent or outer-sphere (λ_{solv}) components:

$$\lambda(r) = \lambda_{in} + \lambda_{solv}(r) \ . \tag{2.39}$$

Inner-sphere reorganization energies were calculated as the sum of isolated fluorophore and quencher energies at the B3LYP/6-311+G(d,p) level using Gaussian 09 software [24] and the relations:

$$\lambda_{in} = \lambda_{in}(F) + \lambda_{in}(Q) \ , \tag{2.40}$$

$$\lambda_{in}(F) = E(F^*)F^- - E(F^*)F^* \qquad \lambda_{in}(Q) = E(Q)Q^+ - E(Q)Q \ . \tag{2.41}$$

In these equations, $E(X)Y$ denotes the energy of X at the geometry optimized for Y, and F^* means a fluorophore molecule in its first excited state.

The solvent reorganization energy is calculated using the dielectric continuum expression:

$$\lambda_{solv}(r) = \begin{cases} \frac{e^2}{4\pi\epsilon_0}\left[\frac{1}{2r_{\mathrm{solv}(Q)}} + \frac{1}{2r_{\mathrm{solv}(F)}} - \frac{1}{r}\right]\left[\frac{1}{n^2} - \frac{1}{\epsilon_r}\right] & r > (r_{\mathrm{solv}}(Q) + r_{\mathrm{solv}}(F)) \\ \frac{e^2}{4\pi\epsilon_0}\left[\frac{1}{2r_{\mathrm{solv}(Q)}} + \frac{1}{2r_{\mathrm{solv}(F)}} - \frac{1}{r_{\mathrm{solv}(Q)}+r_{\mathrm{solv}(F)}}\right]\left[\frac{1}{n^2} - \frac{1}{\epsilon_r}\right] & r < (r_{\mathrm{solv}}(Q) + r_{\mathrm{solv}}(F)) \end{cases} \tag{2.42}$$

The effective solvent radii of the fluorophore and quencher, $r_{\mathrm{solv}}(F)$ and $r_{\mathrm{solv}}(Q)$, are estimated in the previous sections.

The refractive indices n_D used for these calculations were 1.341 for CH_3CN, 1.423 for $Im^+_{2,1}$ / NTf_2^-, and 1.449 for $P^+_{14,6,6,6}$ / NTf_2^-. [25, 64, 72] The relative permittivity of CH_3CN is 37.5. For the ionic liquids we do not use measured values of ϵ_r. Instead, we use effective ϵ_r that are calibrated against the solvatochromism of coumarin 153 in ionic liquids. [33, 81] On this basis ϵ_r is set to 10 for $P^+_{14,6,6,6}$ / NTf_2^- and infinity for $Im^+_{2,1}$ / NTf_2^-.

2.3.6 The Semi-Classical Marcus Model

The single-mode semi-classical calculations of electron transfer rates were analogous to those described for the CM model except that Eq. 29 is replaced by

$$\kappa(r) = \frac{2\,\pi H_{DA}(r)^2}{\hbar}\left[\frac{1}{4\,\pi\,\lambda_{solv}(r)\,k_B T}\right]^{1/2}\sum_{n=0}^{\infty}\frac{F_n}{1+g_n(r)}\exp\left(\frac{-(\Delta G_0(r)+\lambda_{solv}(r)+nh\nu)^2}{4\lambda_{solv}(r)k_B T}\right), \tag{2.43}$$

where

$$g_n(r) \equiv \frac{4\pi H_{DA}(r)^2\tau_s}{\hbar\lambda_{solv}(r)}F_n \quad \text{and} \quad F_n = \frac{S^n e^{-S}}{n!} \tag{2.44}$$

In these equations ν is the frequency of the single effective quantized vibration, 1500 cm^{-1} here, F_n the $0 \rightarrow n$ vibrational matrix element, and S the Huang-Rhys factor, $S = \lambda_{in}/h\nu$. Note that we do not reduce ΔG^* by HDA as done in Eq. 2.35.

Bibliography

[1] M. J. Abraham, T. Murtola, R. Schulz, S. Páll, J. C. Smith, B. Hess, and E. Lindahl. GROMACS: High performance molecular simulations through multi-level parallelism from laptops to supercomputers. *SoftwareX*, 1–2:19–25, 2015.

[2] B. Antalek. *Concepts Magn. Reson.*, 14:225–258, 2002.

[3] N. W. Ashcroft and D. C. Langreth. Structure of Binary Liquid Mixtures. I. *Phys. Rev.*, 156:685–692, Apr 1967.

[4] H. J. C. Berendsen, D. van der Spoel, and R. van Drunen. GROMACS: A message-passing parallel molecular dynamics implementation. *Comp. Phys. Comm.*, 91:43–56, 1995.

[5] C. M. Breneman and K. B. Wiberg. Determining atom-centered monopoles from molecular electrostatic potentials. The need for high sampling density in formamide conformational analysis. *J. Comput. Chem.*, 11:361–373, 1990.

[6] C. Carteret and A. Labrosse. Vibrational properties of polysiloxanes:from dimer to oligomers and polymers.1. Structural and vibrational properties of hexamethyldisiloxane (CH3)3SiOSi(CH3)3. *J. Raman Spectrosc.*, 41:996–1004, 2010.

[7] C. Carteret, A. Labrosse, and X. Assfeld. An ab initio and DFT study of structure and vibrational spectra of disiloxane H3SiOSiH3 conformers Comparison to experimental data. *Spectrochimica Acta Part A*, 67:1421–1229, 2007.

[8] E. W. Castner, Jr., C. J. Margulis, M. Maroncelli, and J. F. Wishart. Ionic Liquids: Structure and Photochemical Reactions. *Annu. Rev. Phys. Chem.*, 62:85–105, 2011.

[9] R. J. Cave and M. D. Newton. Generalization of the Mulliken-Hush treatment for the calculation of electron transfer matrix elements. *Chem. Phys. Lett.*, 249:15–19, 1996.

[10] J.-D. Chai and M. Head-Gordon. Long-range corrected hybrid density functionals with damped atom-atom dispersion corrections. *Phys. Chem. Chem. Phys.*, 10:6615–6620, 2008.

[11] F. C. Collins. Diffusion in chemical reaction processes and in the growth of colloid particles. *J. Colloid. Sci.*, 5:499–505, 1950.

[12] F. C. Collins and G. E. Kimball. Diffusion-controlled reaction rates. *J. Colloid Sci.*, 4:425–437, 1949.

[13] D. T. Cromer and J. B. Mann. X-ray scattering factors computed from numerical Hartree-Fock wave functions. *Acta Cryst.*, A24:321–324, 1968.

[14] T. Darden, D. York, and L. Pedersen. Particle mesh Ewald: An N*log(N) method for Ewald sums in large systems. *J. Chem. Phys.*, 98:10089–10092, 1993.

[15] K. B. Dhungana, L. F. O. Faria, B. Wu, M. Liang, M. C. C. Ribeiro, C. J. Margulis, and E. W. Castner, Jr. Structure of cyano-anion ionic liquids: X-ray scattering and simulations. *J. Chem. Phys.*, 145:024503, 2016.

[16] P. A. Doyle and P. S. Turner. Relativistic Hartree-Fock X-ray and Electron Scattering Factors. *Acta Cryst.*, A24:390–397, 1968.

[17] J. Du, C. J. Benmore, R. Corrales, R. T. Hart, and J. K. R. Weber. A molecular dynamics simulation interpretation of neutron and X-ray diffraction measurements on single phase Y_2O_3- Al_2O_3 glasses. *J. Phys.: Condens. Matter*, 21:205102, 2009.

[18] O. K. Dudko and A. Szabo. Time-Dependent Rate Coefficients for Diffusion-Influenced Reactions with Centrosymmetric Potentials. *J. Phys. Chem. B*, 109:5891–5894, 2005.

[19] J. T. Edward. Molecular Volumes and the Stokes-Einstein Equation. *J. Chem. Edu.*, 47:261, 1970.

[20] T. Endo, S. Nemugaki, Y. Matsushita, Y. Sakai, H. Ozaki, Y. Hiejima, Y. Kimura, and K. Takahashi. Fast solute diffusivity in ionic liquids with silyl or siloxane groups studied by the transient grating method. *Chem. Phys.*, 472(15):128–134, 2016.

[21] U. Essmann, L. Perera, M. L. Berkowitz, T. Darden, H. Lee, and L. G. Pedersen. A smooth particle mesh Ewald method. *J. Chem. Phys.*, 103:8577–8593, 1995.

[22] T. A. Fadeeva, P. Husson, J. A. DeVine, M. F. Costa Gomes, S. G. Greenbaum, and E. W. Castner, Jr. Interactions Between Water and 1-butyl-1-methylpyrrolidinium Ionic Liquids. *J. Chem. Phys.*, 143:064503, 2015.

[23] M. R. Frierson, M. R. Imam, V. B. Zalkow, and N. L. Allinger. The MM2 Force Field for Silanes and Polysilanes. *J. Org. Chem.*, 53:5248–5258, 1988.

[24] M. J. Frisch, G. W. Trucks, H. B. Schlegel, G. E. Scuseria, M. A. Robb, J. R. Cheeseman, G. Scalmani, V. Barone, B. Mennucci, G. A. Petersson, H. Nakatsuji, M. Caricato, X. Li, H. P. Hratchian, A. F. Izmaylov, J. Bloino, G. Zheng, J. L. Sonnenberg, M. Hada, M. Ehara, K. Toyota, R. Fukuda, J. Hasegawa, M. Ishida, T. Nakajima, Y. Honda, O. Kitao, H. Nakai, T. Vreven, J. A. Montgomery, Jr., J. E. Peralta, F. Ogliaro, M. Bearpark, J. J. Heyd, E. Brothers, K. N. Kudin,

V. N. Staroverov, R. Kobayashi, J. Normand, K. Raghavachari, A. Rendell, J. C. Burant, S. S. Iyengar, J. Tomasi, M. Cossi, N. Rega, J. M. Millam, M. Klene, J. E. Knox, J. B. Cross, V. Bakken, C. Adamo, J. Jaramillo, R. Gomperts, R. E. Stratmann, O. Yazyev, A. J. Austin, R. Cammi, C. Pomelli, J. W. Ochterski, R. L. Martin, K. Morokuma, V. G. Zakrzewski, G. A. Voth, P. Salvador, J. J. Dannenberg, S. Dapprich, A. D. Daniels, Ã. Farkas, J. B. Foresman, J. V. Ortiz, J. Cioslowski, and D. J. Fox. Gaussian 09 Revision D.01, 2009.

[25] A. P. Froba, H. Kremer, and A. Leipertz. Density, Refractive Index, Interfacial Tension, and Viscosity of Ionic Liquids [EMIM][EtSO4], [EMIM][NTf2], [EMIM][N(CN)2], and [OMA][NTf2] in Dependence on Temperature at Atmospheric Pressure. *J. Phys. Chem. B*, 112:12420–12430, 2008.

[26] M. Fujita, A. Ishida, T. Majima, and S. Takamuku. Lifetimes of radical anions of dicyanoanthracene, phenazine, and anthraquinone in the excited state from the selective electron-transfer quenching. *J. Phys. Chem.*, 100:5382–5387, 1996.

[27] A. M. Funston, T. A. Fadeeva, J. F. Wishart, and E. W. Castner, Jr. Fluorescence Probing of Temperature-Dependent Dynamics and Friction in Ionic Liquid Local Environments. *J. Phys. Chem. B*, 111:4963–4977, 2007.

[28] V. Gladkikh, A. I. Burshtein, G. Angulo, S. Pagès, B. Lang, and E. Vauthey. Kinetics and Yields of Electron Transfer in the Inverted Region. *J. Phys. Chem. A*, 108:6667–6678, 2004.

[29] C. R. Groom, I. J. Bruno, M. P. Lightfoot, and S. C. Ward. The Cambridge Structural Database. *Acta Cryst.*, B72:171–179, 2016.

[30] C. A. Guido, P. Cortona, B. Mennucci, and C. Adamo. On the Metric of Charge Transfer Molecular Excitations: A Simple Chemical Descriptor. *J. Chem. Theory Comput.*, 9:3118–3126, 2013.

[31] A. Hammersley, S. Svensson, M. Hanfland, A. Fitch, and D. Hausermann. Two-dimensional detector software: From real detector to idealised image or two-theta scan. *High Pressure Res.*, 14:235–248, 1996.

[32] D. Jacquemin, T. L. Bahers, C. Adamo, and I. Ciofini. What is the "best" atomic charge model to describe through-space charge-transfer excitations? *Phys. Chem. Chem. Phys.*, 14:5383–5388, 2012.

[33] H. Jin, G. A. Baker, S. Arzhantsev, J. Dong, and M. Maroncelli. Solvation and rotational dynamics of coumarin 153 in ionic liquids: comparisons to conventional solvents. *J Phys Chem B.*, 111:7291–7302, 2007.

[34] W. L. Jorgensen, D. S. Maxwell, and J. Tirado-Rives. Development and Testing of the OPLS All-Atom Force Field on Conformational Energetics and Properties of Organic Liquids. *J. Am. Chem. Soc.*, 118:11225–11236, 1996.

[35] N. Joshi, M. L. Johnson, I. Gryczynski, and J. R. Lakowicz. Radiation boundary conditions in collisional quenching of fluorescence; determination by frequency-domain fluorometry. *Chem. Phys. Lett.*, 135:200–207, 1987.

[36] H. K. Kashyap, C. S. Santos, H. V. R. Annapureddy, N. S. Murthy, C. J. Margulis, and E. W. Castner, Jr. Temperature-Dependent Structure of Ionic Liquids: X-ray Scattering and Simulations. *Faraday Discuss.*, 154:133–143, 2012.

[37] H. K. Kashyap, C. S. Santos, R. P. Daly, J. J. Hettige, N. S. Murthy, H. Shirota, E. W. Castner, Jr., and C. J. Margulis. How Does the Ionic Liquid Organizational Landscape Change when Nonpolar Cationic Alkyl Groups Are Replaced by Polar Isoelectronic Diethers? *J. Phys. Chem. B*, 117(4):1130–1135, 2013.

[38] H. K. Kashyap, C. S. Santos, N. S. Murthy, J. J. Hettige, K. Kerr, S. Ramati, J. Gwon, M. Gohdo, S. I. Lall-Ramnarine, J. F. Wishart, C. J. Margulis, and E. W. Castner, Jr. Structure of 1-Alkyl-1-methylpyrrolidinium Bis(trifluoromethylsulfonyl)amide Ionic Liquids with Linear, Branched, and Cyclic Alkyl Groups. *J. Phys. Chem. B*, 49:15328–15337, 2013.

[39] J. L. Lebowitz. Exact Solution of Generalized Percus-Yevick Equation for a Mixture of Hard Spheres. *Phys. Rev.*, 133:A895–A899, Feb 1964.

[40] H. Y. Lee, J. B. Issa, S. S. Isied, E. W. Castner, Jr., Y. Pan, C. L. Hussey, K. S. Lee, and J. F. Wishart. A Comparison of Electron-Transfer Dynamics in Ionic Liquids and Neutral Solvents. *J. Phys. Chem. C*, 116:5197–5208, 2012.

[41] M. Liang, A. Kaintz, G. A. Baker, and M. Maroncelli. Bimolecular Electron Transfer in Ionic Liquids: Are Reaction Rates Anomalously High? *J. Phys. Chem. B*, 116:1370–1384, 2012.

[42] M. Liang, S. Khatun, and E. W. Castner, Jr. Communication: Unusual structure and transport in ionic liquid-hexane mixtures. *J. Chem. Phys.*, 142:121101, 2015.

[43] J. N. C. Lopes, J. Deschamps, and A. A. H. Pádua. Modeling Ionic Liquids Using a Systematic All-Atom Force Field. *J. Phys. Chem. B*, 108:2038–2047, 2004.

[44] J. N. C. Lopes and A. A. H. Pádua. Molecular Force Field for Ionic Liquids Composed of Triflate or Bistriflylimide Anions. *J. Phys. Chem. B*, 108:16893–16898, 2004.

[45] J. N. C. Lopes and A. A. H. Pádua. Molecular Force Field for Ionic Liquids III: Imidazolium, Pyridinium, and Phosphonium Cations; Chloride, Bromide, and Dicyanamide Anions. *J. Phys. Chem. B*, 110:19586–19592, 2006.

[46] J. N. C. Lopes and A. A. H. Pádua. CL&P: A generic and systematic force field for ionic liquids modeling. *Theor Chem Acc*, 131:1129, 2012.

[47] E. Lorch. Neutron Diffraction by Germania, Silica and Radiation-damaged Silica Glasses. *J. Phys. C: Solid State Phys.*, 2:229–237, 1969.

[48] T. Lu and F. Chen. Multiwfn: A multifunctional wavefunction analyzer. *J. Comp. Chem.*, 33:580–592, 2012.

[49] R. A. Marcus. On The Theory of Oxidation-Reduction Reactions Involving Electron Transfer. I. *J. Chem. Phys.*, 24:966–978, 1956.

[50] R. A. Marcus and N. Sutin. Electron transfers in chemistry and biology. *Biochim. Biophys. Acta, Rev. Bioenerg.*, 811:265–322, 1985.

[51] T. L. Nemzek and W. R. Ware. Kinetics of diffusion-controlled reactions. Transient effects in fluorescence quenching. *J. Chem. Phys.*, 62:477–489, 1975.

[52] H. Niedermeyer, M. A. A. Rani, P. D. Lickiss, J. P. Hallett, T. Welton, A. J. P. White, and P. A. Hunt. Understanding siloxane functionalised ionic liquids. *Phys. Chem. Chem. Phys.*, 12:2018–2029, 2010.

[53] S. Nosé. A molecular dynamics method for simulations in the canonical ensemble. *Mol. Phys.*, 52:255–268, 1984.

[54] S. Nosé. A unified formulation of the constant temperature molecular dynamics methods. *J. Chem. Phys.*, 81:511–519, 1984.

[55] C. Oostenbrink, A. Villa, A. E. Mark, and W. F. V. Gunsteren. A Biomolecular Force Field Based on the Free Enthalpy of Hydration and Solvation: The GROMOS Force-Field Parameter Sets 53A5 and 53A6. *J Comput. Chem.*, 25:1656–1676, 2004.

[56] M. Parrinello and A. Rahman. Polymorphic transitions in single crystals: A new molecular dynamics method. *J. Appl. Phys.*, 52:7182–7190, 1981.

[57] E. Prince, editor. *International Tables for Crystallography : Volume C: Mathematical, Physical and Chemical Tables, Third Edition.* Kluwer Academic Publishers, 2004.

[58] S. Pronk, S. Pall, R. Schulz, P. Larsson, P. Bjelkmar, R. Apostolov, M. R. S. J. C. Shirts, P. M. Kasson, D. van der Spoel, B. Hess, and E. Lindahl. GROMACS 4.5: a high- throughput and highly parallel open source molecular simulation toolkit. *Bioinformatics*, 29:845–854, 2013.

[59] X. Qiu, J. W. Thompson, and S. J. L. Billinge. PDFgetX2: a GUI-driven program to obtain the pair distribution function from X-ray powder diffraction data. *J. Appl. Cryst.*, 37:678, 2004.

[60] I. Rips and J. Jortner. Dynamic solvent effects on outer-sphere electron transfer. *J. Chem. Phys.*, 87:2090–2104, 1987.

[61] R. C. Rizzo, , and W. L. Jorgensen. OPLS All-Atom Model for Amines: Resolution of the Amine Hydration Problem. *J. Am. Chem. Soc.*, 121:4827–4836, 1999.

[62] M. Rust, J. Lappe, and R. J. Cave. Multistate Effects in Calculations of the Electronic Coupling Element for Electron Transfer Using the Generalized Mulliken-Hush Method. *J. Phys. Chem. A*, 106:3930–3940, 2002.

[63] C. S. Santos, H. V. R. Annapureddy, N. S. Murthy, H. K. Kashyap, E. W. Castner, Jr., and C. J. Margulis. Temperature-dependent structure of methyltributylammonium bis(trifluoromethylsulfonyl)amide: X ray scattering and simulations. *J. Chem. Phys.*, 134:064501, 2011.

[64] K. Shimizu, M. Tariq, M. F. C. Gomes, L. P. N. Rebelo, and J. N. C. Lopes. Assessing the Dispersive and Electrostatic Components of the Cohesive Energy of Ionic Liquids Using Molecular Dynamics Simulations and Molar Refraction Data. *J. Phys. Chem. B*, 114:5831–5834, 2010.

[65] H. Shirota and E. W. Castner, Jr. Why Are Viscosities Lower for Ionic Liquids with -CH2Si(CH3)3 vs -CH2C(CH3)3 Substitutions on the Imidazolium Cations? *J. Phys. Chem. B*, 109:21576–21585, 2005.

[66] H. Shirota, J. F. Wishart, and E. W. Castner, Jr. Intermolecular Interactions and Dynamics of Room Temperature Ionic Liquids That Have Silyl- and Siloxy-Substituted Imidazolium Cations. *J. Phys. Chem. B*, 111:4819–4829, 2007.

[67] M. Smoluchowski. Three lectures on diffusion, Brownian movement and coagulation of colloidal particles. *Phys. Z.*, 17:585–599, 1916.

[68] M. Smoluchowski. Mathematical Theory of the Kinetics of the Coagulation of Colloidal Solutions. *Z. Phyik. Chem.*, 92:129–168, 1917.

[69] A. Solangi, A. M. Bond, I. Burgar, A. F. Hollenkamp, M. D. Horne, T. Rüther, and C. Zhao. Comparison of Diffusivity Data Derived from Electrochemical and NMR Investigations of the $SeCN^-/(SeCN)_2/(SeCN)_3^-$ System in Ionic Liquids. *J. Phys. Chem. B*, 115:6843–6852, 2011.

[70] H. Sun. Ab initio calculations and force field development for computer simulation of polysilanes. *Macromolecules*, 28:701–712, 1995.

[71] H. Sun and D. Rigby. Polysiloxanes: ab initio force field and structural, conformational and thermophysical properties. *Spectrochimica Acta Part A*, 53:1301–1323, 1997.

[72] M. Tariq, P. Forte, M. C. Gomes, J. C. Lopes, and L. Rebelo. Densities and Refractive Indices of Imidazolium- and Phosphonium-Based Ionic Liquids: Effect of Temperature, Alkyl Chain Length, and Anion. *J. Chem. Thermodyn.*, 41:790–798, 2009.

[73] E. K. Watkins and W. L. Jorgensen. Perfluoroalkanes: Conformational Analysis and Liquid-State Properties from ab Initio and Monte Carlo Calculations. *J. Phys. Chem. A*, 105:4118–4125, 2001.

[74] A. Weller. Photoinduced Electron Transfer in Solution: Exciplex and Radical Ion Pair Formation Free Enthalpies and their Solvent Dependence. *Z. Phys. Chem.*, 133:93–98, 1982.

[75] O. S. Wenger. How Donor–Bridge–Acceptor Energetics Influence Electron Tunneling Dynamics and Their Distance Dependences. *Acc. Chem. Res.*, 44:25–35, 2011.

[76] O. S. Wenger, B. S. Leigh, R. M. Villahermosa, H. B. Gray, and J. R. Winkler. Electron Tunneling Through Organic Molecules in Frozen Glasses. *Science*, 307:99–102, 2005.

[77] B. Wu, M. Liang, M. Maroncelli, and E. W. Castner, Jr. Photoinduced Bimolecular Electron Transfer from Cyano Anions in Ionic Liquids. *J. Phys. Chem. B*, 119:14790–14799, 2015.

[78] B. Wu, H. Shirota, and E. W. Castner, Jr. Structure of Ionic Liquids with Cationic Silicon-Substitutions. *J. Chem. Phys.*, 145:114501, 2016.

[79] B. Wu, Y. Yamashita, T. Endo, K. Takahashi, and E. W. Castner, Jr. Structure and Dynamics of Ionic Liquids: Trimethylsilylpropyl-Substituted Cations and Bis(sulfonyl)amide Anions. *J. Chem. Phys.*, 145:244506, 2016.

[80] D. Wu, A. Chen, and C. Johnson. An Improved Diffusion-Ordered Spectroscopy Experiment Incorporating Bipolar-Gradient Pulses. *J. Magn. Reson.*, A115:260–264, 1995.

[81] X.-X. Zhang, M. Liang, N. P. Ernsting, and M. Maroncelli. Complete Solvation Response of Coumarin 153 in Ionic Liquids. *J. Phys. Chem. B*, 117:4291–4304, 2013.

[82] Y. H. Zhao, M. H. Abraham, and A. M. Zissimos. Fast Calculation of van der Waals Volume as a Sum of Atomic and Bond Contributions and Its Application to Drug Compounds. *J. Org. Chem.*, 68:7368–7373, 2003.

[83] L. D. Zusman. Outer-Sphere Electron Transfer in Polar Solvents. *Chem. Phys.*, 49:295–304, 1980.

Chapter 3

Structure of Ionic Liquids

Ionic liquids are structured. Conventional liquids are also structured, almost all liquids have a strong X-ray scattering peak near 1.5 $Å^{-1}$, which indicates the interactions between adjacent particles. In ionic liquids, this adjacency peak also exists, which indicates the first solvation shell interactions, which are mostly interactions between differently charged ions, but there could be correlations between same charged ions as well, for example that occurring in nonpolar nano-domains.

Ionic liquids usually have a special peak centered near q=0.8 $Å^{-1}$, which reveals the interactions between ions and their second coordination shells. This peak is called the charge-charge correlation peak. It is unique for ionic liquids, compared to conventional liquids.

Intermediate range ordering also exists in ionic liquids. A pre-peak or first sharp diffraction peak (FSDP) appears at the lowest values of q, typically in the range from 0.2-0.6 $Å^{-1}$.[1, 24, 25] Most commonly, the FSDP results from intermediate range order arising from nano-domain segregation between non-polar alkyl tails on either the cations[19, 27, 31, 37, 42] or anions[35, 36]. Conventional liquids like water and alcohols may also have similar intermediate range ordering through hydrogen bonds.

3.1 Silicon-Substituted Ionic Liquids

The simulated and experimental densities of the studied ILs are shown in Table 3.1. The IL densities estimated using CL&P force field are usually larger than experiment for most imidazolium and pyrrolidinium ionic liquids. [28] According to our previous experience, a good match between experimental and simulated structure factors can still be achieved, although there are small discrepancies in some ionic liquids. [27, 30]

Table 3.1: Simulated and experimental densities (in g cm^{-3}), structure factors and experimental viscosities (in mPa-s) of the four Si-ILs at 298 K.

IL	ρ(sim)	ρ(exp) [a]	Viscosity [a]	Exp (sim) peak position in S(q) ($Å^{-1}$) adjacency	charge-charge correlation	FSDP
Si-mim$^+$ / NTf_2^-	1.49	1.46	98.3	1.31(1.31) 1.28	0.83	N/A
C-mim$^+$ / NTf_2^-	1.48	1.50	161	1.33(1.33)	0.84	N/A
SiOSi-mim$^+$ / NTf_2^-	1.42	1.32	77	1.01 1.28		0.41
Si-pyrr$^+$ / NTf_2^-	1.43		1.27	0.82	N/A	
Si-C_3-mim$^+$ / FSI^-	1.335	1.248	92.3	1.30 (1.34)	N/A	0.37
Si-C_3-mim$^+$ / NTf_2^-	1.420	1.317	127.5	1.30 (1.34)	0.88 (0.90)	0.39
Si-C_3-mim$^+$ / $BETI^-$	1.494	1.394	287.0	1.27 (1.31)	0.84 (0.86)	0.41
Si-C_3-Pyrr$^+$ / NTf_2^-	1.368	1.299	241.8	1.25 (1.27)	0.83 (0.83)	0.46

[a] From Refs. 12, 40, 41;

3.1.1 Total Structure Factors

The liquid structure factors $S(q)$ obtained from the high-energy X-ray scattering experiments and calculated from MD trajectory snapshots are compared in Fig. 3.1 and Fig. 3.2.

These MD trajectories were run using the new silicon atomic parameters that we added to the CL&P force field. Structure factors obtained from the high-energy X-ray scattering data are plotted in red, while the MD results are plotted in blue. Good agreement between simulations and X-ray experiments was achieved, with the deviation of simulated to experimental $S(q)$ values being less than 0.3 for all cases. Note that the scale of the $S(q)$ functions spans a range from 0 to 3. The q values for the adjacency peaks are shown in Table 3.1. One can see that the structure factors $S(q)$ for Si-mim$^+$ / NTf_2^-, C-mim$^+$ / NTf_2^- and Si-pyrr$^+$ / NTf_2^- are similar, displaying an adjacency peak from nearest neighbor interactions at q ~1.3 $Å^{-1}$ and a lower intensity charge-charge correlation peak at q ~0.8 $Å^{-1}$. For these three ILs, no FSDP (or pre-peak) is observed. The appearance of the structure factor $S(q)$ of SiOSi-mim$^+$ / NTf_2^- is rather different from for the other three NTf_2^--anion ionic liquids, showing a doublet with peaks at q = 1.01 $Å^{-1}$ and 1.28 $Å^{-1}$, respectively. A notable feature in the $S(q)$ for SiOSi-mim$^+$ / NTf_2^- is that it displays a prominent FSDP at q=0.41 $Å^{-1}$, indicating some intermediate range order for this liquid. The siloxy functional group on the SiOSi-mim$^+$ cation is very polar. This clearly shows that it is the size of the functional group and nature of the interactions with its neighbors, not whether it is nonpolar, that

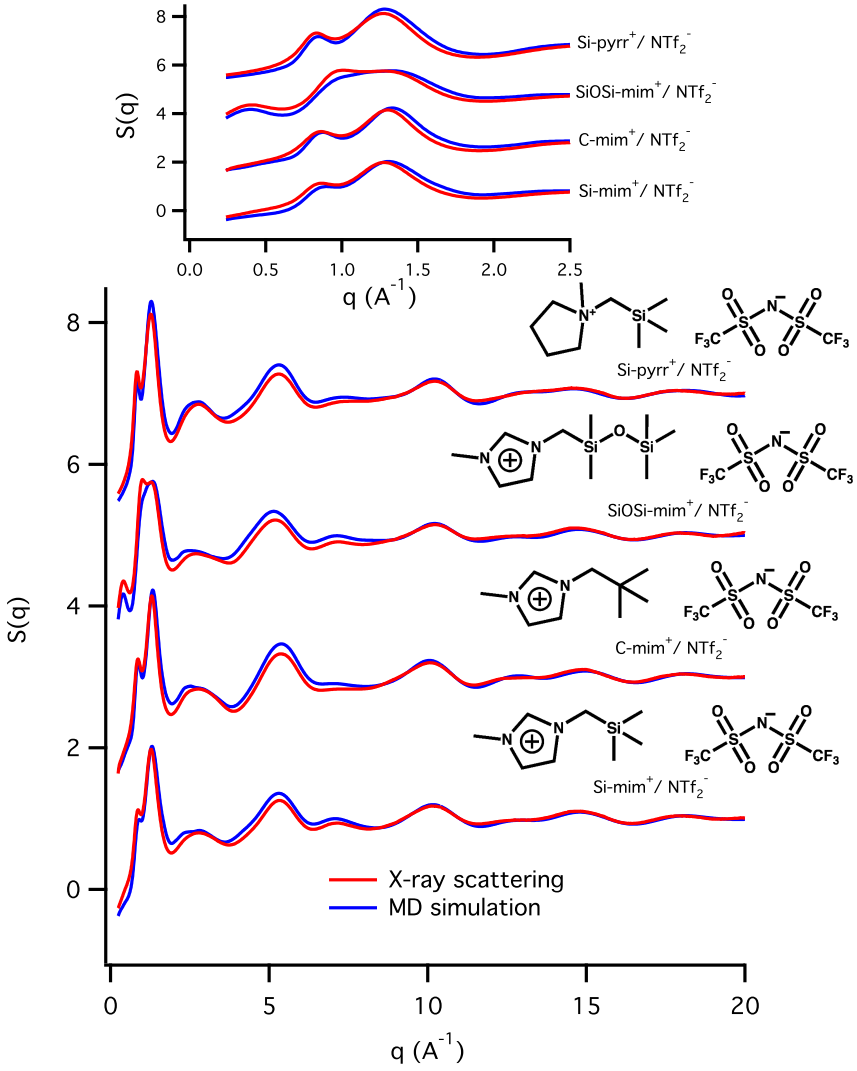

Figure 3.1: The experimental (red) and simulated (blue) structure factors $S(q)$ for the four ILs. The inset graph at top focuses on the region where inter-molecular interactions dominate the scattering. Arbitrary offsets of +2, +4 and +6 are applied to display the four $S(q)$ functions without overlap.

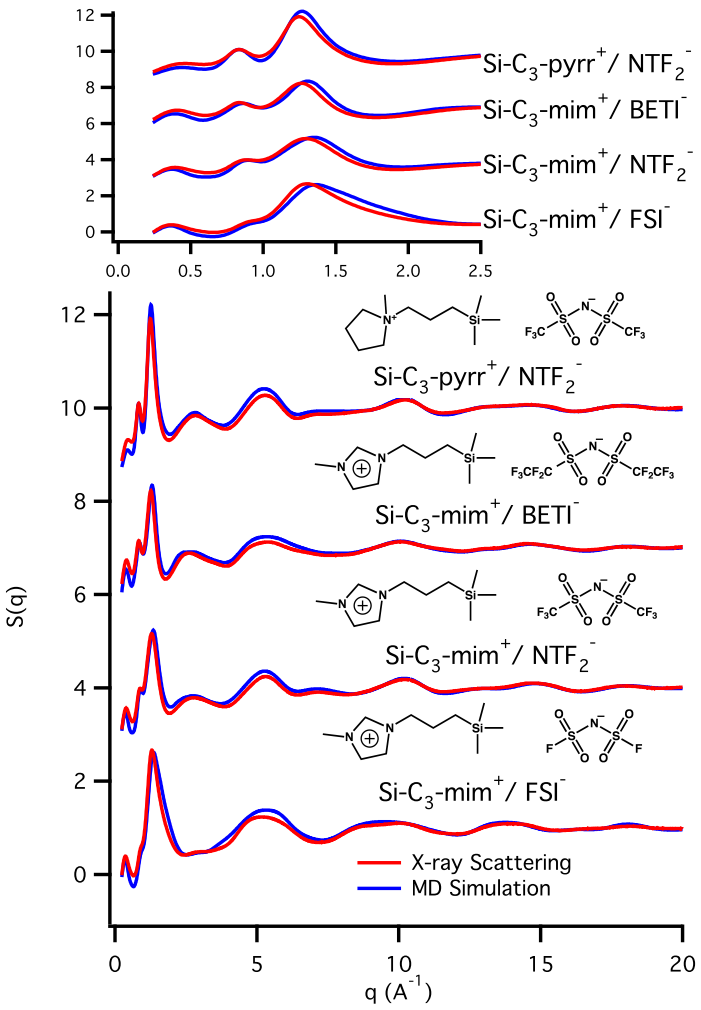

Figure 3.2: The experimental and simulated structure factors of four ionic liquids. The top graph shows the details for the intermolecular regime of $S(q)$ between 0 $<q<$2.5 Å^{-1}. Arbitrary offsets of +3, +6 and +9 are applied to display the four $S(q)$ functions without overlap.

determines the presence of the FSDP. It is well recognized that the sponge-like order observed for protic ionic liquids such as ethylammonium nitrate or propylammonium nitrate also leads to a FSDP, as a result of the mesoscopic order arising from the H-bond network.[6, 16, 18, 44] The structure factors calculated from the MD simulations match well with experimental results, so we will further analyze the ionic liquid structure using these simulation results by partitioning the structure factor $S(q)$ using Eqs. 2.7 and 2.11. The larger values of q for each of the simulated peak positions is a direct consequence of the over-estimation of the density. The incomplete agreement between calculated and measured peaks in the structure factors likely arises from imperfect function forms used for the new Si parameters in the force field, since quantitative agreement for calculated vs. measured X-ray structure factors has been obtained for the existing CL&P parameters for NTf_2^-.[30]

3.1.2 Ionic Partitioning of S(q)

The ionic partitioning of $S(q)$ is accomplished by writing $S(q)$ according to Eq. 2.7. The partial structure factor components of $S(q)$ are plotted in Figs. 3.3 and 3.4. Note that strong interference leads to partial $S(q)$ components that have significantly larger magnitudes than the total $S(q)$ function observed. Specifically, each of the four Si-ILs shows a magnitude of about 3 in the total $S(q)$, while the partial $S(q)$ magnitudes can be as large a 8 for the case of Si-C_3-$Pyrr^+/NTf_2^-$.

The adjacency peak (q$\sim$1.3Å^1) is seen to arise from constructive interference from the anion-cation and cation-cation interactions, with smaller contributions from the anion-anion interactions.

As is often observed for ILs having the NTf_2^- anion, the ionic partitioning of $S(q)$ leads to strong anti-correlations between anions and cations for the charge-alternation peak located at $q \sim 0.8$ Å^{-1}.[25–27, 38] It is common for the charge-alternation peak in the measured X-ray $S(q)$ to display positive and negative amplitude peaks in the ionic partitioning, and this is what is observed for the three NTf_2^- ILs having the smaller cations.

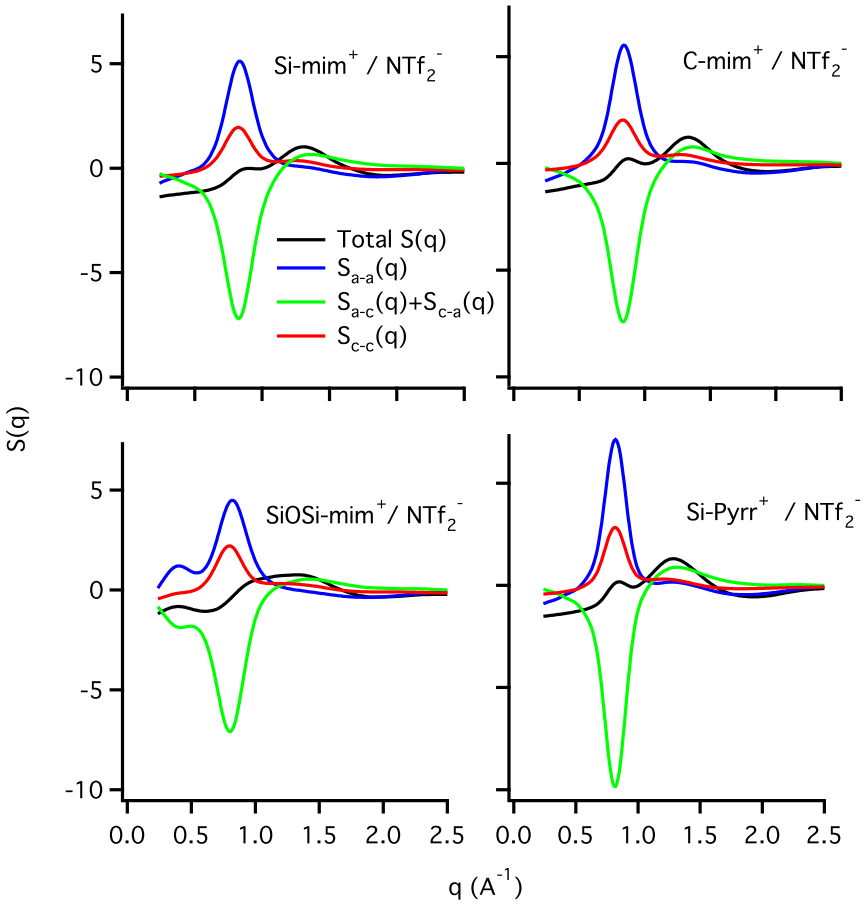

Figure 3.3: Ionic partitioning of the simulated structure factor $S(q)$ for ILs Si-mim$^+$ / NTf_2^-, C-mim$^+$ / NTf_2^-, Si-pyrr$^+$ / NTf_2^- and SiOSi-mim$^+$ / NTf_2^-.

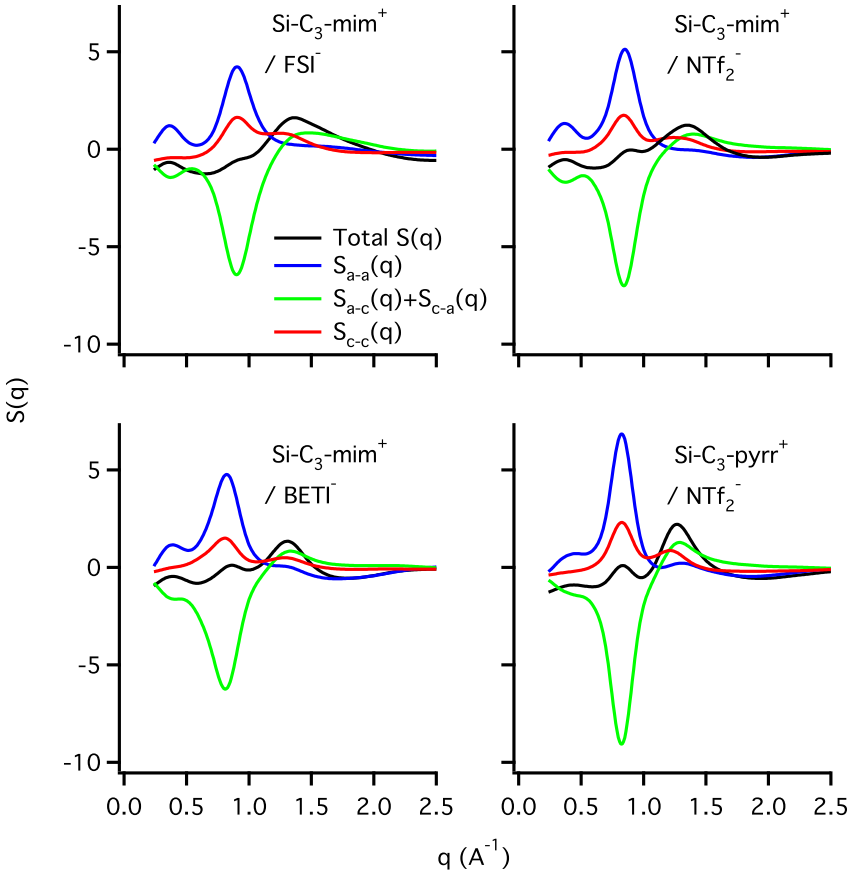

Figure 3.4: Ionic partitioning of the simulated structure factor $S(q)$ for ILs Si-C_3-mim$^+$ / FSI$^-$, Si-C_3-mim$^+$ / NTf_2^-, Si-C_3-mim$^+$ / BETI$^-$ and Si-C_3-Pyrr$^+$ / NTf_2^-.

The ionic partitioning for SiOSi-mim$^+$ / NTf$_2^-$ provides cautionary evidence against over-interpretation of the experimentally observed $S(q)$. While the double peaks in $S(q)$ for SiOSi-mim$^+$ / NTf$_2^-$ are observed at 1.01 and 1.28 Å^{-1}, the simulation results for the ionic partitioning reveal that the contributions to the charge-alternation peak lead to strong interference, since the charge-alternation peaks are found near q=0.81 Å^{-1}. While such interference between different terms contributing to the observable structure factor is no doubt a regular occurrence, unless the experimental X-ray (or neutron) data are compared with an ionic partitioning from a reasonable quality molecular simulation, such details would be overlooked. The observed peaks in the full $S(q)$ for SiOSi-mim$^+$ / NTf$_2^-$ do not directly reflect the charge-alternation and adjacency peaks, but rather are an interference from these and other interactions. The ionic partitioning also reveals that the dominant contribution to the FSDP for SiOSi-mim$^+$ / NTf$_2^-$ is caused by anion-anion interactions, as is often observed for NTf$_2^-$based ILs with hydrophobic substituents on the cations.[2, 9, 19, 27, 38] The distributions of anions surrounding a cation are shown below as spatial distribution functions, *vide infra.* A similar interference effect was also observed for cyano-anion ILs by Dhungana *et al.*[11]

Fig. 3.2 shows that the charge-charge correlation peak appears only as a shoulder at about 0.9 Å^{-1} for Si-C$_3$-mim$^+$ / FSI$^-$. The analogous charge-charge correlation peaks in the X-ray data for other ILs are listed in Table 3.1 Since the charge-charge correlation is due to the second coordination shell interactions, we can obtain more information about this peak from the ionic partitioning of $S(q)$ from Fig. 3.4. The ionic interaction extrema in Fig. 3.4 are observed at q-values of approximately 0.90 $\sim$ 0.91 Å^{-1} for Si-C$_3$-mim$^+$ / FSI$^-$, 0.84 $\sim$ 0.85 Å^{-1} for Si-C$_3$-mim$^+$ / NTf$_2^-$, 0.81 $\sim$ 0.82 Å^{-1} for Si-C$_3$-mim$^+$ / BETI$^-$ and 0.83 Å^{-1} for Si-C$_3$-Pyrr$^+$ / NTf$_2^-$. From the head-tail-anion partitioning in Fig. 3.6 we found that the charge-charge correlation peak is mainly contributed by the interactions between anions and cation heads, and all interactions involving cation tails have a very weak effect on this peak, which indicates that the charge ordering is mainly contributed by polar parts of the molecules. [27]

The cationic –(CH$_2$)$_3$Si(CH$_3$)$_3$ tail on both Si-C$_3$-mim$^+$ and Si-C$_3$-Pyrr$^+$ is sufficiently long to give rise to a clear FSDP, though the peak is broader and attenuated for

the case of Si-C_3-Pyrr$^+$ / NTf_2^-. From the ionic partitioning in Fig. 3.4 we observe that the FSDP is mainly arising from a positive-going anion-anion peak offset by a cation-anion anti-peak. These results are quite similar to the observations of the FSDP for ILs with cationic hydrocarbon tails reported previously. [1, 3, 7, 14, 15, 17, 27, 31, 37, 42, 45]

3.1.3 Subionic Partitioning of S(q)

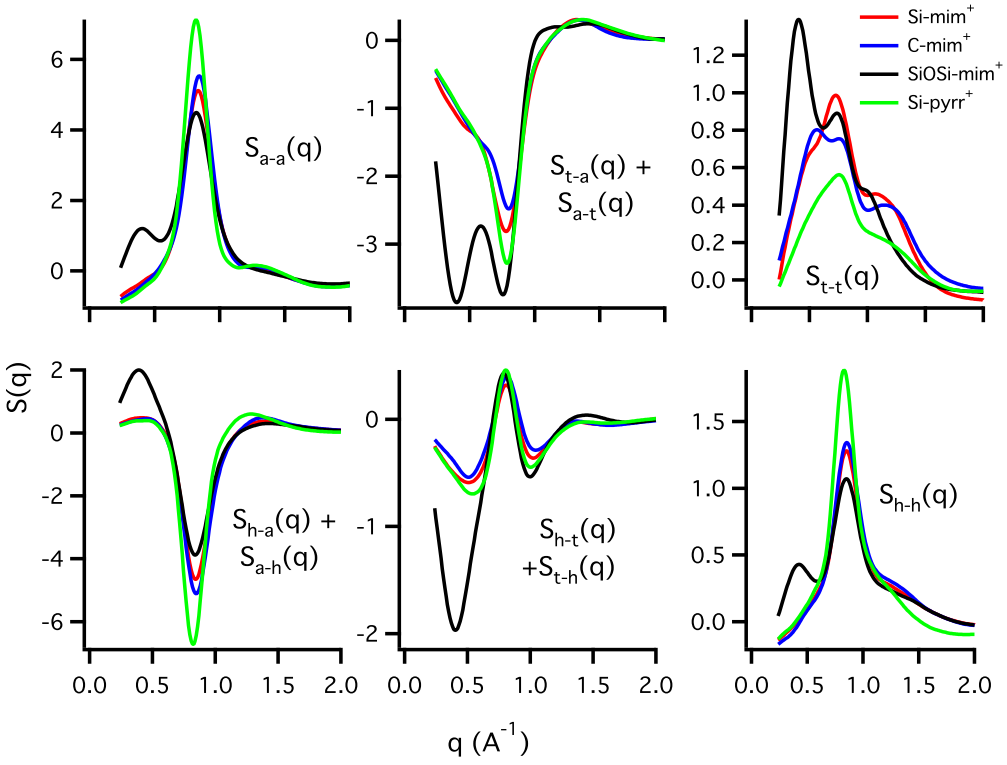

Figure 3.5: Sub-ionic partitioning of the simulated structure factor $S(q)$ for ILs Si-mim$^+$ / NTf_2^-, C-mim$^+$ / NTf_2^-, Si-pyrr$^+$ / NTf_2^- and SiOSi-mim$^+$ / NTf_2^-.

Further insight into the intermolecular interactions between the IL anions and cations can be gleaned by introducing a sub-ionic partitioning of the structure factor as given by Eq. 2.11. In the present case, the scheme is to consider the entire NTf_2^- anion and to partition the cation into two groups of atoms: those belonging to the imidazolium or pyrrolidinium ring and those comprising the functional group. The resulting sub-ionic structure factors are plotted in Fig. 3.5 and 3.6.

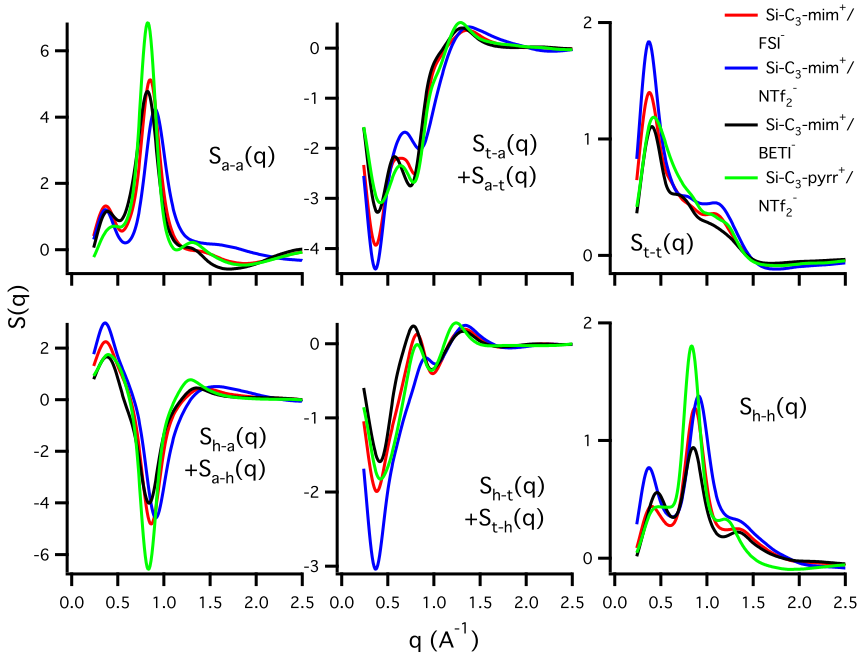

Figure 3.6: Sub-ionic partitioning of the simulated structure factor $S(q)$ for ILs Si-C_3-mim$^+$ / FSI^-, Si-C_3-mim$^+$ / NTf_2^-, Si-C_3-mim$^+$ / $BETI^-$ and Si-C_3-Pyrr$^+$ / NTf_2^-.

Strong positive constructive interferences in the anion-anion correlations contribute to the charge alternation peak in $S(q)$ (top left in Fig. 3.5), with a smaller contribution arising from the cationic head group self-interactions (bottom right in Fig. 3.5). The largest negative amplitude contributions to the charge alternation arise from interactions between the anions and the cationic ring. The FSDP at about 0.4 $Å^{-1}$, corresponding to a real space domain size of about 15 Å, is the major feature in the total $S(q)$ for SiOSi-mim$^+$ / NTf_2^-. Positive contributions to this intermediate range order arise from anion-anion interactions, interactions between the cationic rings and anions, and interactions between cationic functional groups on neighboring cations. These are offset by destructive interferences arising from interactions between neighboring cationic ring and cationic functional groups, as well as negative interferences between anions and cationic functional groups, in a manner similar to that previously reported by Kashyap *et al.*[27] C-mim$^+$ / NTf_2^- correlations show larger intensities than for Si-mim$^+$ / NTf_2^- in each these interactions, which provides another indication of stronger intermolecular

correlations in C-mim$^+$ / NTf$_2^-$. The two ionic liquids behave differently in $S(q)$ partitions that contain tail interactions, especially for $S_{t-t}(q)$, likely due to the different polarity and size of the two functional groups. Once again, the partitioned structure factors shown in Figs. 3.14 and 3.5 show that it is the anti-peaks in the partial structure factors that should be considered the true markers of structure, since these are insensitive to the interferences that determine the total structure factors.[11, 24, 26, 27]

A more pictorial means of understanding the sub-ionic partitioning is given in Fig. 3.7, which shows the snapshots of simulation boxes of Si-mim$^+$ / NTf$_2^-$, C-mim$^+$ / NTf$_2^-$, Si-pyrr$^+$ / NTf$_2^-$ and SiOSi-mim$^+$ / NTf$_2^-$. The cationic ring groups are shown in green, the cationic functional groups in red and the anions in blue. The Si-mim$^+$ / NTf$_2^-$ and C-mim$^+$ / NTf$_2^-$ boxes in Fig. 3.7 are qualitatively very similar. A key observation is that unlike other IL cations, the trimethylsilylmethyl and neopentyl groups do not show significant aggregation. There is a clear indication of the emergence of some functional group aggregation for the siloxy functional groups in SiOSi-mim$^+$ / NTf$_2^-$, demonstrating that aggregation of polar chains can lead to intermediate range order in the same way that hydrophobic interactions lead to intermediate range order in other ILs.[25–27, 31, 32, 37]

The significantly larger electron density for the anions than the cations is the reason that the scale for the sub-ionic components involving the anion are about a factor of three larger in magnitude than for purely cation-cation types of interactions. Specifically, the anion-anion (a-a), cationic head group-anion (h-a/a-h) and cationic tail group-anion (a-t/t-a) interactions are more intense that the cation-only interactions such as head-tail (h-t/t-h), tail-tail (t-t) and head-head (h-h). Note that the charge-alternation peak in $S(q)$ shows the strongest and sharpest contributions for the Si-C$_3$-Pyrr$^+$ / NTf$_2^-$ IL, while the contributions to the FSDP intensity are strongest for the Si-C$_3$-mim$^+$ / NTf$_2^-$ IL. In the ionic partitioning of $S(q)$ in Fig. 3.4 one sees that the FSDP consists primarily of anion-anion interactions, while the cation-cation interactions seem to have little effect on this peak. However, the sub-ionic partitioning of $S(q)$ shown in Fig. 3.6 shows that this is indeed a cancellation between positive head-head and tail-tail

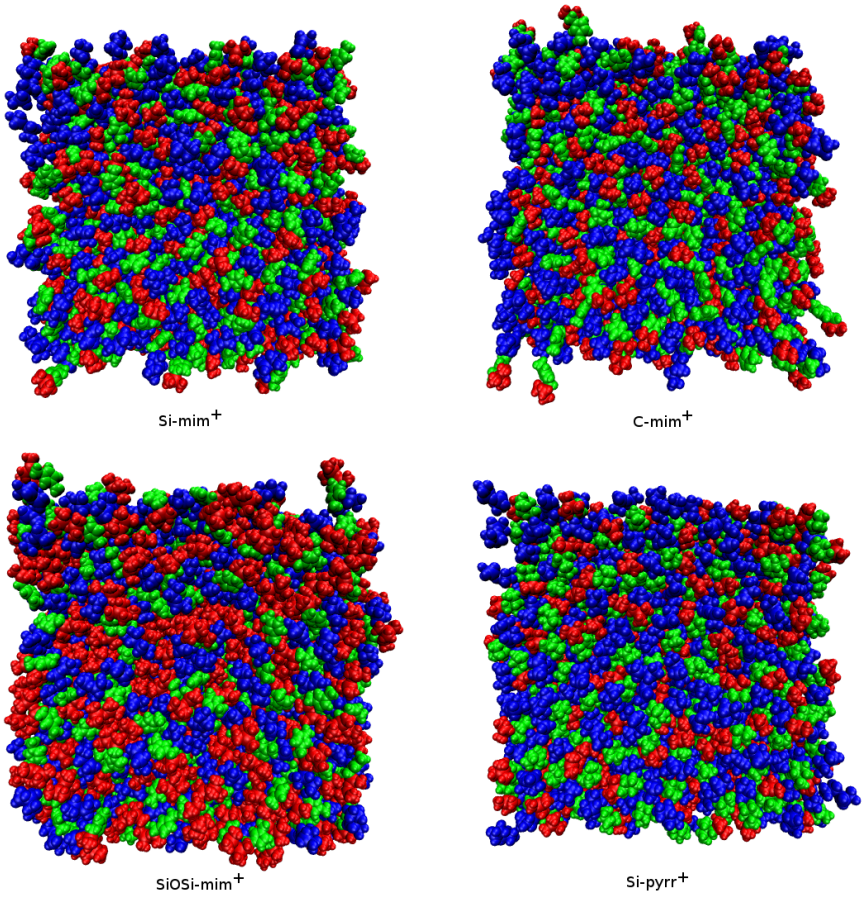

Figure 3.7: Sub-ionic partitioning of the equilibrated simulation boxes for Si-mim$^+$ / NTf_2^- (top left), C-mim$^+$ / NTf_2^- (top right), SiOSi-mim$^+$ / NTf_2^- (bottom left) and Si-pyrr$^+$ / NTf_2^- (bottom right). The cationic imidazolium or pyrrolidinium rings are green, the cationic functional groups are red, and anions are blue.

interactions with a negative contribution of head-tail interaction. This illustrates the complex nature of the interactions in the intermediate order in these ILs.

3.1.4 Spatial Distribution Functions

We also analyzed the spatial distributions among particles in simulated boxes using TRAVIS software[5] with visualization done using Visual Molecular Dynamics (VMD) program suite.[21] Figures 3.8, 3.10, and 3.12 show the spatial distribution functions in ILs Si-mim$^+$ / NTf_2^-, SiOSi-mim$^+$ / NTf_2^-, C-mim$^+$ / NTf_2^- and Si-pyrr$^+$ / NTf_2^-. In Fig. 3.8, the anionic probability density surrounding each of the four cations is shown in blue for a fixed position of the cationic functional group – trimethylsilylmethyl for Si-mim$^+$ and Si-pyrr$^+$, neopentyl for C-mim$^+$, and pentamethyldisiloxymethyl for SiOSi-mim$^+$. Because the functional group may adopt one of a number of possible orientations for each of the cations in the simulation, the red probability density shows the roughly three-fold symmetric probability density for the cationic head group (imidazolium or pyrrolidinium) for this fixed orientation of the functional group. Fig. 3.10 shows the blue anionic spatial density distribution of anions surrounding each of the four cations for a fixed orientation for the cationic ring. The orange colored isodensity shows the distribution of functional group orientations about this fixed cationic ring.

In Fig. 3.8 and Fig. 3.10, the isodensity values for Si-mim$^+$ / NTf_2^- and C-mim$^+$ / NTf_2^- are set to be equal to enable quantitative comparisons. When the cationic functional group is used as the reference point, local threefold symmetry results. Comparing the isodensity plots in Figs. 3.8 and 3.10, one can see that the anions have more intensity near the imidazolium ring for Si-mim$^+$ / NTf_2^-, while for C-mim$^+$ / NTf_2^-, the anion density is increased near the cationic functional group. This results directly from the more electropositive central Si atom in Si-mim$^+$ compared to the central neopentyl C atom in C-mim$^+$, as discussed previously based on electronic structure calculations of the bare cation.[40]

For each of the four ILs, Fig. 3.12 shows the red isodensity surfaces for the cationic centers-of-mass surrounding a NTf_2^- anion. Surrounding this first shell comprising predominantly cations is the second-shell anionic isodensity in blue. The shapes of

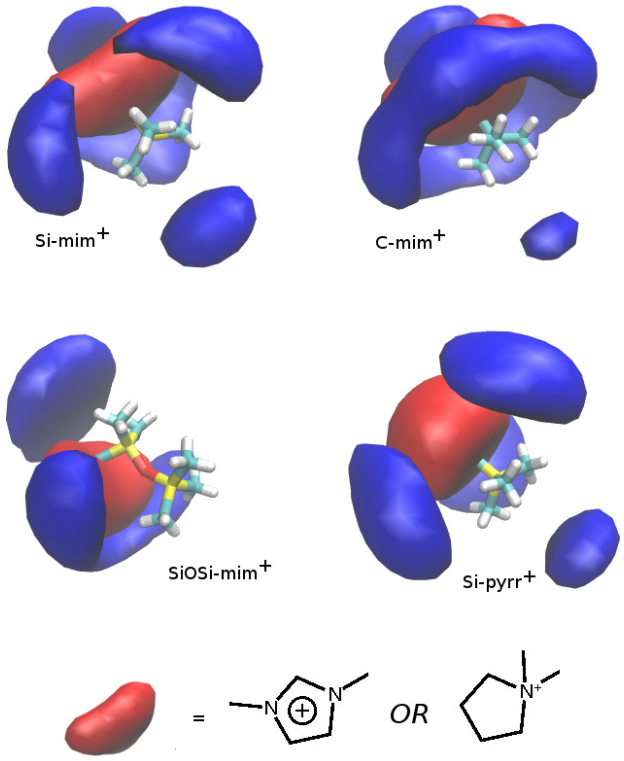

Figure 3.8: The spatial distribution of anions (blue) and the imidazolium or pyrrolidinium ring (red) are shown for fixed positions of the tail groups, when these –$Si(CH_3)_3$ or –$C(CH_3)_3$ groups are used as reference points. The value for the number density isosurface for the NTf_2^- anion is 2.60 nm^{-3} for Si-mim^+ / NTf_2^-, C-mim^+ / NTf_2^- and Si-$pyrr^+$ / NTf_2^-, and is 2.20 nm^{-3} for SiOSi-mim^+ / NTf_2^-.

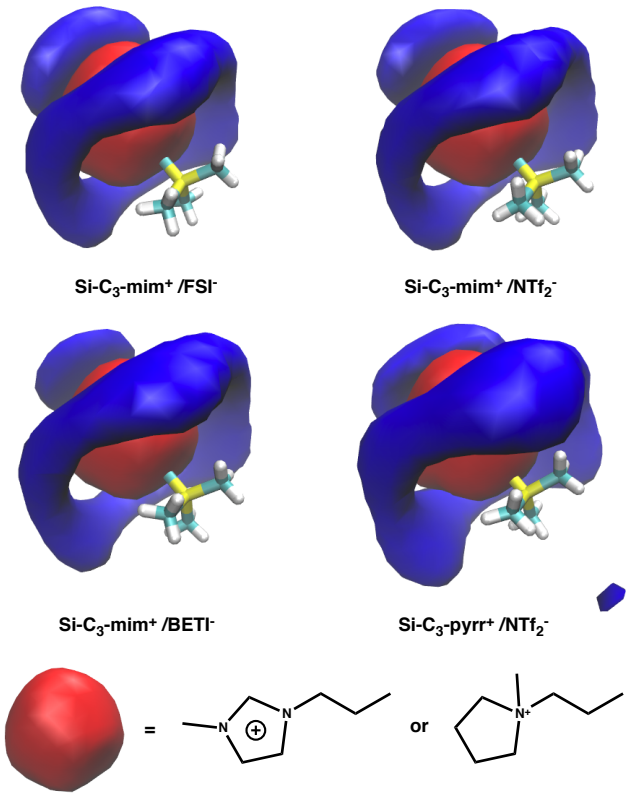

Figure 3.9: The intermolecular spatial distribution of anions (blue) and cationic head groups (red) around cation tails for fixed positions of the $Si(CH_3)_3$ groups; the average ring positions for all 1,000 ion pairs in the simulation box are shown. The isodensity values for the anions are 2.35 nm^{-3} for FSI^-, 2.8 nm^{-3} for Si-C_3-mim^+ / NTf_2^-, 2.0 nm^{-3} for $BETI^-$, and 2.1 nm^{-3} for Si-C_3-$Pyrr^+$ / NTf_2^-.

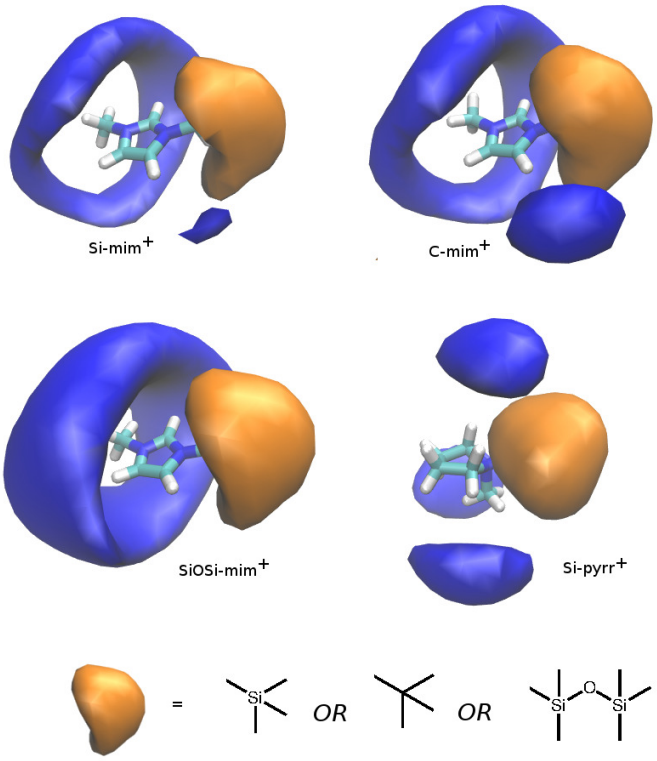

Figure 3.10: The spatial distribution of anions (blue) and the cationic tail groups (orange) for a fixed position of the imidazolium or pyrrolidinium ring. The value for the number density isosurface for the NTf_2^- anion is 3.00 nm^{-3} for Si-mim^+ / NTf_2^-, C-mim^+ / NTf_2^- and Si-$pyrr^+$ / NTf_2^-, and is 2.30 nm^{-3} for SiOSi-mim^+ / NTf_2^-.

the anionic isodensities are quite similar for all four ILs. Cations and anions are distributed ellipsoidally about the NTf_2^- anion. The spatial distribution of cations and anions around the anions in Si-mim$^+$ / NTf_2^- and C-mim$^+$ / NTf_2^- are similar in shape, though C-mim$^+$ / NTf_2^- has a larger spatial distribution than Si-mim$^+$ / NTf_2^- at same number density isovalue. This supports the previous conclusion that C-mim$^+$ / NTf_2^- has stronger intermolecular interactions than Si-mim$^+$ / NTf_2^-, as discussed by Shirota et al.[40, 41]

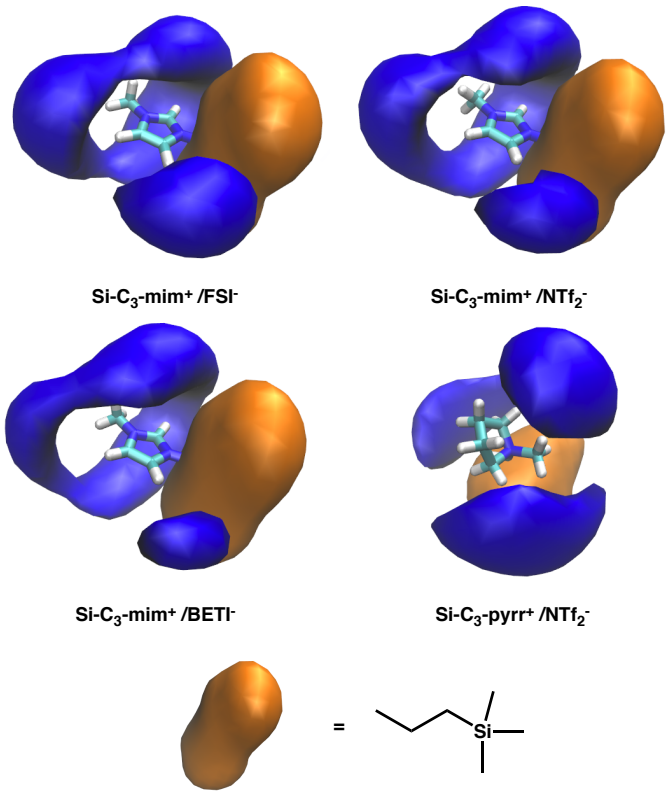

Figure 3.11: The spatial distribution of anions around cations, where the ring position is fixed and the cationic tail positions are averaged for the 1,000 ion pairs in the simulation box. The isovalues for the anion number densities are 2.6 nm^{-3} for Si-C_3-mim$^+$ / FSI^-, 3.2 nm^{-3} for Si-C_3-mim$^+$ / NTf_2^-, 2.2 nm^{-3} for Si-C_3-mim$^+$ / $BETI^-$, and 2.5 nm^{-3} for Si-C_3-Pyrr$^+$ / NTf_2^-.

The spatial distribution of anions around cations for ILs Si-C_3-mim$^+$ / FSI^-, Si-C_3-mim$^+$ / NTf_2^-, Si-C_3-mim$^+$ / $BETI^-$ and Si-C_3-Pyrr$^+$ / NTf_2^- are shown in Figs. 3.9 and 3.11. The spatial distributions are analyzed from simulation trajectory using

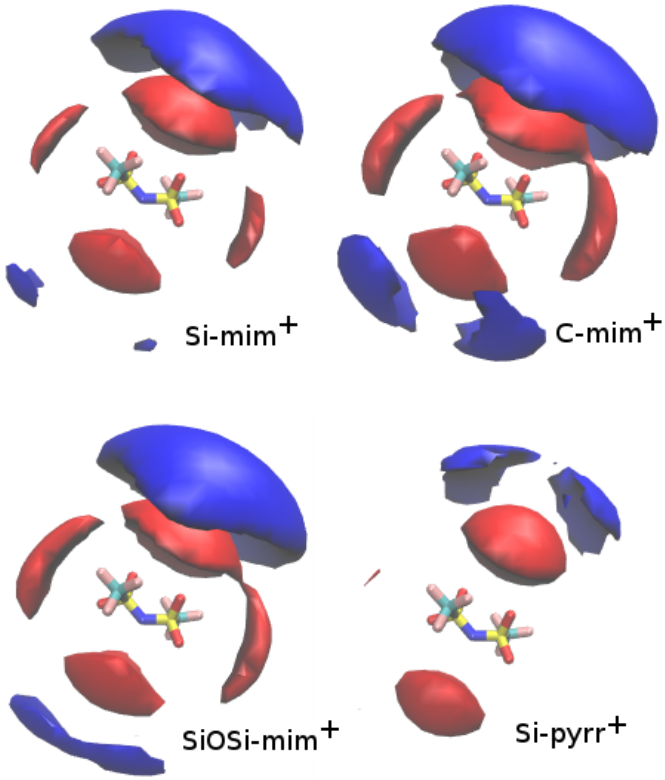

Figure 3.12: The spatial distribution of anions and cations surrounding a central NTf_2^- anion showing the first coordination shell of cations in red, the second shell of anions in blue for Si-mim$^+$ / NTf_2^- (top left) and C-mim$^+$ / NTf_2^- (top right) and SiOSi-mim$^+$ / NTf_2^- (lower left) and Si-pyrr$^+$ / NTf_2^- (lower right). The center N and two adjacent S atoms in NTf_2^- anion are set as references. The value for the number density isosurface is 2.50 nm^{-3} for the cations and 2.35 nm^{-3} for the NTf_2^- anion in Si-mim$^+$ / NTf_2^-, C-mim$^+$ / NTf_2^- and Si-pyrr$^+$ / NTf_2^-. The isovalue is set to 1.90 nm^{-3} for both cations and anions for SiOSi-mim$^+$ / NTf_2^-.

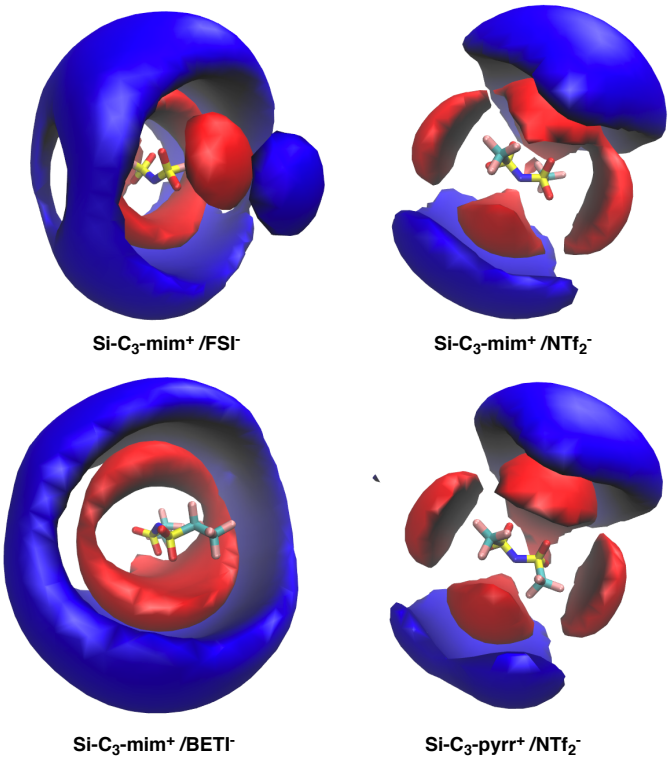

Figure 3.13: Spatial distributions around the Si-IL anions, for fixed angles of the anionic S–N–S bond angles. The cationic (anionic) isodensity values are 2.05 (2.00) nm^{-3} for Si-C_3-mim^+ / FSI^-; 2.50 (2.40) nm^{-3} for Si-C_3-mim^+ / NTf_2^-; 1.80 (1.65) nm^{-3} for Si-C_3-mim^+ / $BETI^-$; 2.00 (2.00) nm^{-3} for Si-C_3-$Pyrr^+$ / NTf_2^-.

TRAVIS software [5] and visualized using VMD. [21] In Fig. 3.9, the positions of cationic terminal $Si(CH_3)_3$ groups are fixed, with the anionic probability density shown in blue and the distribution of positions of the cationic ring shown in the red isodensity. The cationic ring probability density appears as it does as a result of the three-fold near symmetry around the Si-CH_2 bond.

In Fig. 3.11, spatial distribution is shown for a fixed position of the cationic head group, including the ring and polar atoms bonded to it. The anionic spatial isodensity is again shown in blue, with the orange indicating the averaged positions of the cationic tetramethylsilyl groups. These anionic distributions are similar to those we reported recently for Si-mim$^+$ / NTf_2^- and Si-pyrr$^+$ / NTf_2^-, respectively. This anion distribution from classical mechanics is remarkably similar to the results from quantum calculations. [22] For the four Si-ILs reported here, the anionic density is more centered around the cationic ring, because of the longer propylene linker. Despite the changes in anion size for the three ILs with Si-C_3-mim$^+$ the FSI^-, NTf_2^-, and $BETI^-$ anions, the shapes of these spatial distributions are nearly identical for these three Si-ILs. The distribution shape of anions in these ILs are similar to Si-mim$^+$ / NTf_2^- and Si-pyrr$^+$ / NTf_2^-, while the anion distribution is more favor the ring, due to the longer alkyl chain.

Fig. 3.13 is the spatial distribution function of cations (red) and anions (blue) around anions. The spatial distributions for both Si-C_3-mim$^+$ / NTf_2^- and Si-C_3-Pyrr$^+$ / NTf_2^- are similar. Rather different spatial distributions are obtained for the Si-ILs for Si-C_3-mim$^+$ paired with the FSI^- and $BETI^-$ anions. From the spatial distribution for Si-C_3-mim$^+$ / $BETI^-$ one observe that the coordination shell of cations will form a ring over the $BETI^-$ anion center, and they are repelled by the anionic fluorocarbon groups. This observation shows that the fluorocarbon chain will not favor cations, it's another evidence that they will not form a nonpolar domain together with cation tails.

3.1.5 The Effect of Silicon Substitution

It is well known that the change from a silicon atom in the Si-mim$^+$ cation to a carbon atom for C-mim$^+$ leads to a significant change of a factor of 1.6 in the ratio of observed

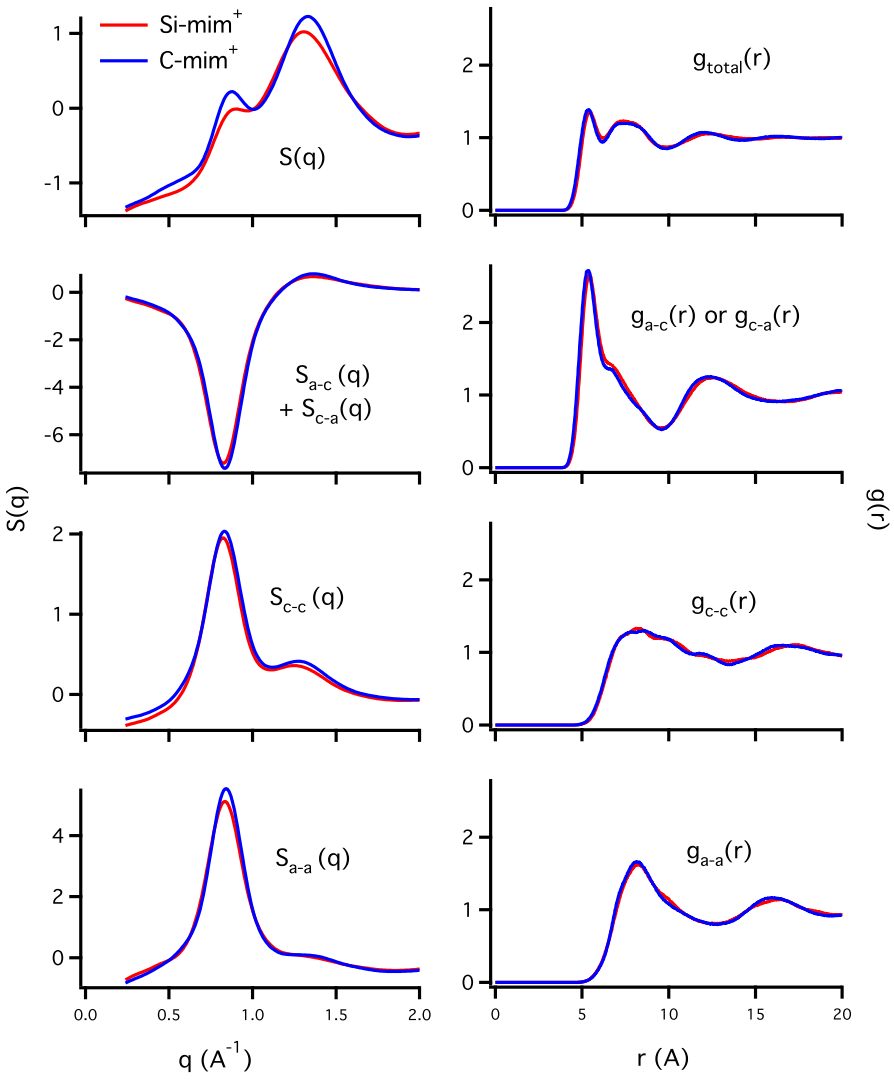

Figure 3.14: Comparison of the ionic partitioning of the structure factors $S(q)$ (left) and center-of-mass radial distributions $g(r)$ (right) for Si-mim$^+$ / NTf_2^- (red) and C-mim$^+$ / NTf_2^- (blue).

viscosities for these two NTf_2^--anion ILs.[40] At 298 K, the shear viscosities are 98.3 cP for Si-mim$^+$ / NTf_2^- and 161 cP for C-mim$^+$ / NTf_2^-.[40] To investigate connections between structure and viscosity, in Fig. 3.14 we consider the ionic partitioning of both the structure factor $S(q)$ and the radial pair distribution function $g(r)$ for both Si-mim$^+$ / NTf_2^- and C-mim$^+$ / NTf_2^-. The adjacency peak in the full $S(q)$ for C-mim$^+$ / NTf_2^- is found at 1.33 Å^{-1}, which is higher than that of Si-mim$^+$ / NTf_2^- at 1.31 Å^{-1}, indicating that the average Bragg domain spacing for adjacent species is 4.81 Å for Si-mim$^+$ / NTf_2^- and 4.71 Å for C-mim$^+$ / NTf_2^-. The larger size of the Si-mim$^+$ cation leads to this increase in adjacency spacing between nearest neighbors of about 1.75%, which correlates with our initial assignment of the lower viscosity for Si-mim$^+$ / NTf_2^- as arising from the increased intermolecular spacing in the liquid compared to the case for C-mim$^+$ / NTf_2^-. Using the experimental densities of Si-mim$^+$ / NTf_2^- and C-mim$^+$ / NTf_2^-, the estimated ion pair volume is 511 Å^3 for Si-mim$^+$ / NTf_2^- and 480 Å^3 for C-mim$^+$ / NTf_2^-. Assuming that these two ILs have similar arrangements of anions and cations, the cation-anion distance ratio between these two ionic liquid would be 1.022 based on densities, compared to the ratio of 1.018 calculated from positions of the adjacency peaks for Si-mim$^+$ / NTf_2^- and C-mim$^+$ / NTf_2^-.

The two ionic liquids show very similar positions for the maxima of the charge-charge correlation peak but this peak in C-mim$^+$ / NTf_2^- is sharper and more intense than for Si-mim$^+$ / NTf_2^-. From the $S(q)$ partitioning we can see that difference in the anion-anion correlations ($S_{a-a}(q)$) makes the biggest contribution to this difference, meaning that the larger charge-charge correlation peak in C-mim$^+$ / NTf_2^- is due to the stronger second coordination shell interactions. This result is consistent with the conclusion of Shirota et al. that weaker intermolecular interactions in silicon substituted ionic liquids are correlated with lower viscosity and faster diffusion coefficients.[10, 40] Considering the full pair distribution functions $g_{total}(r)$ on the right side of Fig. 3.14, we find that the nearest neighbor distances are virtually indistinguishable between Si-mim$^+$ / NTf_2^- and C-mim$^+$ / NTf_2^-, while the difference in the second peak of the $g_{a-c}(r)$ is slightly reduced for C-mim$^+$ / NTf_2^- relative to Si-mim$^+$ / NTf_2^-.

The new parameters for silicon reported here augment the existing CL&P force field.[7, 29–32] There are a number of significant differences between the parameters for the Si-mim$^+$ and C-mim$^+$ cations. Since silicon is about 20% more electropositive than carbon, the surrounding methyl groups are slightly more electronegative for Si-mim$^+$ than for C-mim$^+$. Silicon has a larger van der Waals radius than carbon. The $Si(CH_3)_3$ group has a larger volume than $C(CH_3)_3$ group, because the Si-C bond length is typically 0.187 nm, which is more than 20% longer than 0.153 nm C-C bond length. Lastly, the N-C-Si-C dihedral potential energy barrier in Si-mim$^+$ is much smaller than for the N-C-C-C dihedral potential energy barrier in C-mim$^+$, making Si-mim$^+$ significantly more flexible than C-mim$^+$, and likely also reducing the viscosity.

To investigate how the small differences in charge between the parameter set for Si-mim$^+$ and C-mim$^+$ affect the total potential energy, we carried out a numerical experiments in which 11 snapshots of the C-mim$^+$ / NTf_2^- geometries were used to calculate the potential energy when the C-mim$^+$ charges were replaced by the Si-mim$^+$ charges. These 11 snapshots were taken from the simulation production run between 1.9 and 2.0 ns. The effect of replacing the C-mim$^+$ charges for the equilibrated box of C-mim$^+$ / NTf_2^- with the Si-mim$^+$ charges lead to a -129.1 kJ/mol change in the intramolecular potential energy (1,4 part of the Coulomb term) and a +20.8 kJ/mol change in the short-range (remaining terms of the intra- and inter-molecular) Coulomb potential. The change in the long-range part of the PME energy was +42.0 kJ/mol. Thus, while use of the Si-mim$^+$ charges leads to a more favorable intramolecular energy, the net effect on the intermolecular interactions on replacing the C-mim$^+$ charges with Si-mim$^+$ parameters is to make the intermolecular interactions less favorable.

3.1.6 The Effect of Anion Size

We found that the adjacency peak shapes and positions in $S(q)$ do not show a consistent trend as the anion size in increased on going from FSI^- to NTf_2^- to $BETI^-$. Despite the larger volume of the NTf_2^- relative to the FSI^- anion, the adjacency peak position for Si-C_3-mim$^+$ / NTf_2^- is at the same position as for Si-C_3-mim$^+$ / FSI^-, while Si-C_3-mim$^+$ / $BETI^-$ only shifts to a slightly lower value of q. Si-C_3-mim$^+$ / NTf_2^- and

Si-C_3-mim^+ / $BETI^-$ have approximately same adjacency peak amplitude, while Si-C_3-mim^+ / FSI^- adjacency peak is significantly larger. If we consider the effective ion pair volumes calculated from the experimental density, the ion pair volumes with Si-C_3-mim^+ are 470 Å^3 for FSI^-, 559 Å^3 for NTf_2^-, and 642 Å^3 for $BETI^-$. This difference in ion pair volumes should lead to concomitant shifts in the adjacency peak, which are not observed. This is probably due to the change of packing style of ions in IL structure. The adjacency peak is not only contributed by the coordination of different charged ions, but also arises from the contract of tail groups in the nano-segregation. [26, 27] From the position of FSDP we know that there is a bigger nano-domain in Si-C_3-mim^+ / FSI^- than Si-C_3-mim^+ / NTf_2^-, so in Si-C_3-mim^+ / FSI^- the contact of cation tails may be playing a more important role in Si-C_3-mim^+ / NTf_2^-, which may lead to an adjacency peak shift. From Fig. 5 and Fig. 6 we also find the evidence that the anion is more favoring cation tail than cation ring in Si-C_3-mim^+ / FSI^-.

The intensity of the charge-charge correlation peak in Si-C_3-mim^+ / NTf_2^- is smaller than for Si-C_3-mim^+ / $BETI^-$, while Si-C_3-mim^+ / FSI^- only shows a shoulder in this q regime. A larger charge-charge correlation peak intensity here does not necessarily indicate a stronger anion-anion interaction, because the X-ray scattering cross section increases for the anions with more heavy atoms. The position of the charge-charge correlation peak as well as the position of charge correlation from ionic partitioning of $S(q)$ shows a shift to lower q values for the large anions, as expected. However, the ionic partitioning of the structure factors shows that for all cation-cation, anion-anion, cation-anion interactions, the trend of peak amplitude in $S(q)$ scales as Si-C_3-mim^+ / NTf_2^- <Si-C_3-mim^+ / FSI^- <Si-C_3-mim^+ / $BETI^-$.

When the size of the anion increases from FSI^- to NTf_2^- to $BETI^-$, the intensity of the FSDP in $S(q)$ increases while the peak shifts to larger q. Instead of taking part in forming a non-polar domain in IL structure, the fluorous- or perfluorocarbon ends of the anion prevent the non-polar domains in the ILs from growing. The FSDP intensity follows the trend FSI^- <NTf_2^- <$BETI^-$ because of the larger X-ray scattering cross section for the anion.

How the polarity and chain length will affect the silicon-substituted ILs can be studied by comparing the structures of Si-C_3-mim$^+$ / NTf_2^- and Si-C_3-Pyrr$^+$ / NTf_2^- with those of Si-mim$^+$ / NTf_2^-, SiOSi-mim$^+$ / NTf_2^- and Si-pyrr$^+$ / NTf_2^- in Ref. 49. Changing the cationic functionality from the trimethylsilylmethyl group to the trimethylsilylpropyl group leads to the introduction of a FSDP in $S(q)$ because the latter –$(CH_2)_3Si(CH_3)_3$ tail is long enough. The FSDP in Si-C_3-mim$^+$ / NTf_2^- is more intense and occurs at lower q value of 0.39 Å^{-1}, compared to q = 0.41 Å^{-1}for SiOSi-mim$^+$ / NTf_2^-, which has the same chain length. This indicates a larger and stronger nano-aggregation of side chains than in Si-C_3-mim$^+$ / NTf_2^-.

The adjacency peak in $S(q)$ is found at q = 1.28 Å^{-1} for Si-mim$^+$ / NTf_2^- and 1.27 Å^{-1} for Si-pyrr$^+$ / NTf_2^-. We found that increasing cation chain length will lead the adjacency peak moving to higher q value, which indicates a smaller Bragg domain for an ion pair. This is in contrast to the larger molecular volume of the longer chain cation. This may be explained by the differences in the packing in the ionic liquids. As we have discussed for the spatial distribution in Figs. 3.9 and 3.11, one clearly sees that anions show increased correlation with the cationic rings, which may lead to decreased distances between anions and cationic head groups.

The charge-charge correlation peak is 0.87 Å^{-1} for Si-mim$^+$ / NTf_2^- and 0.83 Å^{-1} for Si-pyrr$^+$ / NTf_2^- while the second coordination interactions analyzed from partitioned S(q) are at 0.83 for Si-mim$^+$ / NTf_2^- and 0.82 for Si-pyrr$^+$ / NTf_2^-. Though the position of charge-charge correlation peak changes noticeably on changing from the trimethylsilylmethyl group to the trimethylsilylpropyl group, the average distance charge-charge interactions from $S(q)$ partitioning do not have a significant change. Since charge-charge correlation peak largely build on the adjacency peak, this peak shift may mainly be related to different adjacency peak broadening.

3.1.7 Structural Differences of Imidazolium vs. Pyrrolidinium Cations

The FSDP in $S(q)$ for the Si-C_3-mim$^+$ / NTf_2^- Si-IL is much more intense than for Si-C_3-Pyrr$^+$ / NTf_2^- and is observed at a lower q value. This is consistent with the behavior

manifested by ILs having hydrocarbon side chains, because C[n]-imidazolium cations have a longer effective length than the homologous C[n]-pyrrolidiniums.[27, 39, 42]

For the Si-ILs having –$CH_2Si(CH_3)_3$ groups, the position of the adjacency peak in $S(q)$ is the same for both Si-mim$^+$ / NTf_2^- and Si-pyrr$^+$ / NTf_2^-.[49] However, for the –$(CH_2)_3Si(CH_3)_3$ cationic group, the imidazolium-cation Si-C_3-mim$^+$ / NTf_2^- adjacency peak is observed at a lower value of q relative to the pyrrolidinium-cation Si-C_3-Pyrr$^+$ / NTf_2^-. The peak positions for each of these interactions for Si-C_3-Pyrr$^+$/NTf_2^- IL are shifted to lower values of q relative to the three ILs with the Si-C_3-mim$^+$-cation ILs, indicating that the former pyrrolidinium-cation IL has larger spatial dimensions for each of the three inter-molecular domains.

From the ionic partitioning of $S(q)$ presented in Fig. 3.4 we found that the pyrrolidinium Si-ILs have much sharper ionic partial structure factors do the imidazolium ILs. One sees in Fig. 3.6 that the same holds true for the sub-ionic partitioning of $S(q)$.

3.2 Comparison of Zwitterionic Liquids vs. Homologous Ionic Liquids

Molecular simulations have been widely used to explore the charge-ordering and formation of nanoscale polar and apolar domains in ionic liquids.[8, 23, 46, 47] In the first studies, much attention was given to the anisotropic arrangements of the packing of anions and cations in the periodic boxes for the molecular simulations. Introduction of strongly amphiphilic ions with cationic or anionic alkyl tails led to the appearance of significant intermediate range order[8] that was soon verified by X-ray scattering experiments.[37, 42]

To obtain a qualitative comparison between the liquid structures of Zw-ILs and ILs, it is useful to first consider the overall arrangements of ions that are revealed in snapshots of the MD simulation boxes, reminiscent of the pioneering work of Canongia Lopes and Pádua.[8] The equilibrated simulation boxes were found to have a density for $Im_{2,1}^+/OAc^-$ of 1.117 g cm^{-3} at 298 K, close to the experimental value of 1.102 g cm^{-3} at this temperature.[13, 51] Limited quantities of OE_2imC_3C and OE_2imC_5C samples precluded accurate density measurements for the Zw-IL samples.

In Fig. 3.15, we show snapshots of the periodic boxes from the equilibrated molecular simulation trajectories for our Zw-IL and homologous IL systems. Red coloring indicates the more polar cationic moiety, comprising the imidazolium ring and nearby atoms, while blue denotes the anionic moieties. Green colors indicate the 2-(2-methoxyethoxy)ethyl tails bonded to one of the imidazolium ring nitrogens. The spatial distributions for the OE_2imC_3C Zw-IL (top left) and its homologous IL OE_2eim^+/OAc^-(top right) appear to be almost identical. The $Im^+_{2,1}/OAc^-$ box at lower right shows the salt-like charge ordering for an IL that does not display any significant intermediate range order, while the more complex pattern observed at lower left for OE_2imC_5C illustrates that this Zw-IL can display significant intermediate range order. Compared to the other systems, the simulation box for $Im^+_{2,1}/OAc^-$ is necessarily smaller because of the significantly smaller number of total atoms for the same number of ion pairs.

3.2.1 Comparing Charge Densities for Zw-ILs and ILs

Electronic structure calculations on a simple model allow us to conclude that while the *anionic* and *cationic* charge distributions could be different between the Zw-IL and homologous IL, they in fact are quite similar. The simple model we used was to randomly select one of the anions from the MD simulation box, together with the 8 nearest-neighbor cations and 7 nearest anions. For the Zw-ILs, a cluster including a central molecule together with the 7 nearest neighbors is selected. This cluster of 8 ion pairs (or molecules) is an arbitrary snapshot of the model liquid, equilibrated in GROMACS using the CL&P potentials, as described above. This cluster is optimized using dispersion-corrected PM6-D3 semi-empirical Hamiltonian, and atomic dipole moment corrected Hirshfeld (ADCH) charges on the central anion are then calculated at B3LYP-D3/6-31G(d,p) level.[33, 34] Using 7 input configurations for each Zw-IL or IL, the averaged partial charges on anionic carboxylate group were -0.52 ± 0.07 for OE_2imC_3C and -0.45 ± 0.04 for OE_2eim^+/OAc^-, indicating a 15% excess charge density for the Zw-IL relative to the IL.

Population analysis for a single OE_2imC_3C molecule using the B3LYP-D3/6-31G(d,p) method described above with charges obtained from the ADCH model showed that the

partial charges on the three atoms of the carboxylate group sum to $-1.00 \pm 0.03e$ for all the stable conformations observed. This indicates that there is almost no intramolecular charge transfer occurs between the cationic part and the anionic parts of the OE_2imC_3C molecule.

3.2.2 Liquid Structure Factors $S(q)$

When the structure factors $S(q)$ are factored appropriately, interference between strong positive and negative correlations provides an unambiguous marker for underlying structure. We have taken to calling these positive and negative correlation in $S(q)$ *peaks* and *anti-peaks*, respectively.[11, 24, 26, 27, 38, 49, 50] Standard X-ray experiments observe total scattered X-ray intensities and are thus homodyne experiments for which the minimum observable signal is zero. The negative correlations, or *anti-peaks*[24, 26, 27] are not directly observable, but because the observable is a total intensity that is a positive definite quantity, and anti-peak must be offset by an equal or larger positive-going peak, both of which arise because of positive and negative structural correlations. We have shown recently that the interferences between peaks and anti-peaks can lead to observed peaks in the total $S(q)$ that are shifted relative to the true underlying structural features.[49] For this reason, we feel it is important to model structural data for the presence of anti-peaks in $S(q)$ to avoid mis-interpreting the experimental structure factors obtained from X-ray scattering data.

The experimental and simulated structure factors $S(q)$ of the four ionic liquids are shown in Fig. 3.16, where one sees that good agreement is obtained. The ionic partitioning described by Eq. 2.7 and sub-ionic partitioning defined by Eq. 2.11 are shown in Figs. 3.17 and 3.18, respectively. The experimental (simulated) peak positions are summarized in Table 3.2.

The adjacency peak in the intermolecular part of $S(q)$ arises from nearest-neighbor interactions and for these liquids appears near 1.5 $Å^{-1}$. From the top three graphs in Fig. 3.16, one observes a slight shift in the adjacency peak from 1.53 $Å^{-1}$ for the OE_2imC_3C Zw-IL to 1.58 $Å^{-1}$ for the OE_2eim^+/OAc^- IL, indicating that the average distances between nearest neighbors increases slightly for the Zw-IL relative to the IL.

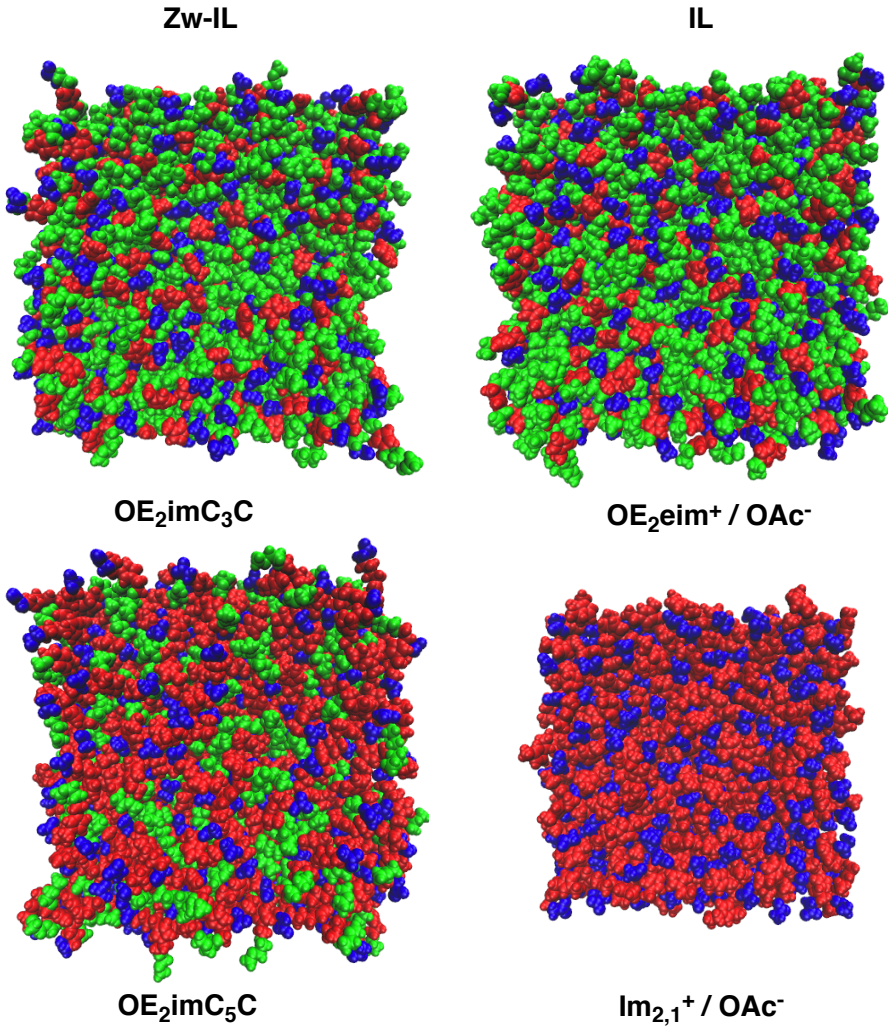

Figure 3.15: Snapshots from the MD simulation periodic boxes for (left) 1,000 Zw-IL molecules (right) 1,000 IL ion pairs. Red: cationic moieties; blue: anionic moieties; green: diether cation tails.

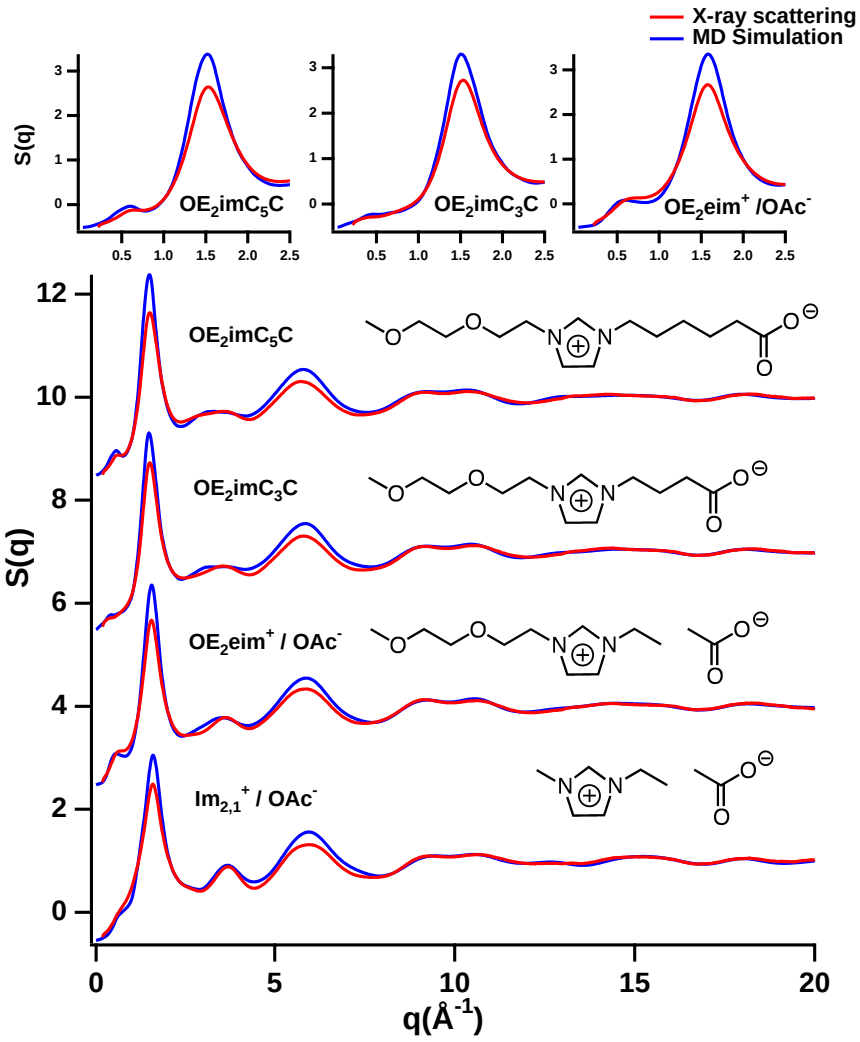

Figure 3.16: The total structure factor $S(q)$ for the four ionic liquids. X-ray experimental results are shown in red and results calculated from MD simulations in blue.

This is as expected, since the difference of the single carbon-carbon bond between the OE_2eim^+/OAc^- IL relative to the OE_2imC_3C Zw-IL can result in a slight increase in the average distance between imidazolium ring and the carboxylate tails.

The charge-charge correlation peak is typically observed at about 0.8–0.9 $Å^{-1}$ and appears to be suppressed in the total liquid structure factor $S(q)$ shown in Fig. 3.17. However, the ionic partitioning of $S(q)$ given by Eq. 2.7 reveals that while the X-ray scattering shows only a small amplitude in the charge-charge correlation peak region, this is because the strongly interfering peaks and anti-peaks near q=1.0 $Å^{-1}$ reveal the true location of the charge-charge correlation structure, while the total intensity in $S(q)$ at this position is negligible. The IL with the smallest anion and cation, $Im^+_{2,1}/OAc^-$, shows the sharpest structural features of the set of four liquids. The charge-charge correlation peak for the two Zw-ILs is qualitatively quite similar, though the peaks are broader for OE_2imC_3C than for OE_2imC_5C, indicating a more diffuse local structure. Comparing the $S(q)$ for the OE_2imC_3C Zw-IL with the IL homolog OE_2eim^+/OAc^-, we can see that the charge-charge correlations are quite similar between the two species, but stronger for the IL than the Zw-IL. Thus, ionic partitioning of $S(q)$ shows that the second-shell charge-charge correlation peak is just as important a structural feature for Zw-ILs as it is for standard ILs.

Three ionic liquids, OE_2imC_3C, OE_2imC_5C and OE_2eim^+/OAc^-, show a small FSDP between the range of $0.4 \sim 0.7$ $Å^{-1}$. $Im^+_{2,1}/OAc^-$ does not display a FSDP because the ethyl tail is neither long enough nor nonpolar enough to lead to nanophase segregation of the alkyl alkyl chains that can lead to observation of FSDPs.[8, 25, 27, 37, 39, 42] All of these FSDPs are quite small amplitude relative to the sharper, more intense peaks observed for ILs with significant alkyl chains.[25, 27, 37, 39] This small amplitude of the FSDPs for these liquids is not unexpected, because the 2-(methoxy-ethoxy)ethyl diether tail is expected to suppress the FSDP, as has been reported for similar systems by Triolo, *et al.*[43] Kashyap, *et al.*[26] and Hettige, *et al.*[20] Fig. 3.17 shows that only for the anion-anion component of $S(q)$ is there even a clearly discernible contribution to the FSDP for OE_2imC_3C and OE_2imC_5C.

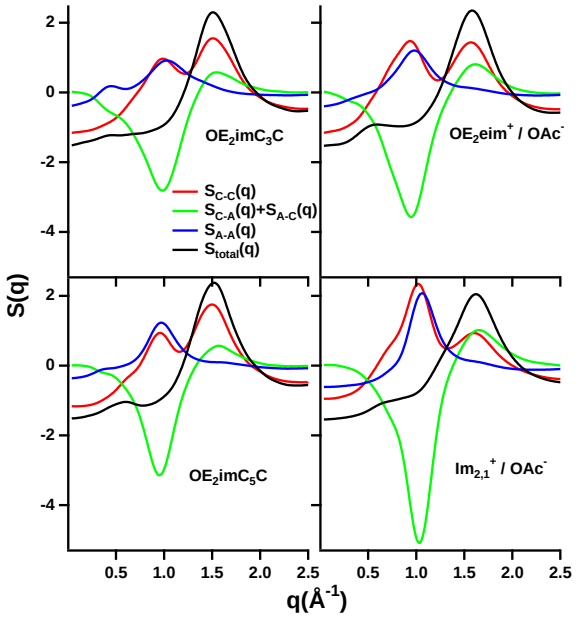

Figure 3.17: Ionic partitioning of the MD-simulated structure factors $S(q)$ following Eq. 2.7. The total $S(q)$ is shown in black; the cation-cation component in red, anion-anion in blue, and anion-cation cross-terms in green. The Zw-ILs are shown in the left and the monovalent ILs on the right side.

Table 3.2: The positions of peaks in the experimental(simulated) structure factors for the four liquids.

IL	Peak positions	
	Adjacency	FSDP
OE_2imC_3C	1.53 (1.53)	0.42 (0.45)
OE_2eim^+/OAc^-	1.58 (1.58)	0.67 (0.59)
OE_2imC_5C	1.53 (1.52)	0.62 (0.61)
$Im^+_{2,1}/OAc^-$	1.62 (1.62)	– (–)

Analysis of the MD simulations enables us to obtain an improved interpretation of the intermediate range order for these liquids. Specifically, a sub-ionic partitioning of the structure factor $S(q)$ is required to more fully reveal the underlying structure and this analysis is shown in Fig. 3.18. Structural features for the two Zw-ILs and the homologous IL are very similar for four of the six groups of structural correlations: the ring-ring, ring-tail, ring-anion, and tail-tail sub-components of $S(q)$. Strong positive contributions to the FSDP arise from ring-ring, anion-ring, and tail-tail interactions, which are offset by anti-peaks in the ring-tail correlations. Simply put, the diether tails do not coil to localize near the imidazolium rings, in contrast to other ether-substituted imidazolium systems reported by Triolo, *et al.*[43] For these three liquids, subtle differences in the anion-anion and anion-tail correlations in $S(q)$ are noted. Anion-tail interactions give rise to a moderate intensity anti-peak for the OE_2eim^+/OAc^- and OE_2imC_5C Zw-IL and a larger amplitude anti-peak for OE_2imC_3C; positive contributions to the FSDP occur for the anion-anion interactions, with the OE_2imC_3C amplitude being larger than for the other two liquids. Thus, the positive contributions to a FSDP from tail-tail interactions of the diether groups provide another contrast to what has been observed for ILs with 1-(alkoxy)-3-methylimidazolium or 1-alkoxy-1-methylpyrrolidinium cations.[26, 43] The key difference for the set of liquids reported here is that the the cationic ring is more centrally located in the charge distribution of the liquid, such as for OE_2imC_5C. The deconstruction of the total structure factor $S(q)$ reveals that the overall liquid properties of the two Zw-ILs studied here are qualitatively very similar to the features of the homologous IL.

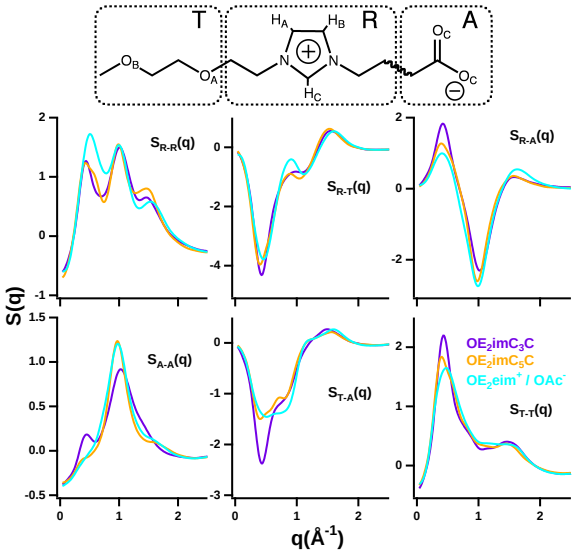

Figure 3.18: Sub-ionic partitioning of the MD-simulated structure factors $S(q)$ following Eq. 2.11. Data for OE_2imC_3C are in red, for OE_2imC_5C in blue, and for OE_2eim^+/OAc^- in green. Partitioning of the Zw-IL into ether tail, cationic ring and anionic components is illustrated at the top. Specific structural correlations are shown for ring-ring interactions (upper left), ring-tail (upper center), ring-anion (upper left), anion-anion (lower left), tail-anion (lower center), and tail-tail (lower right).

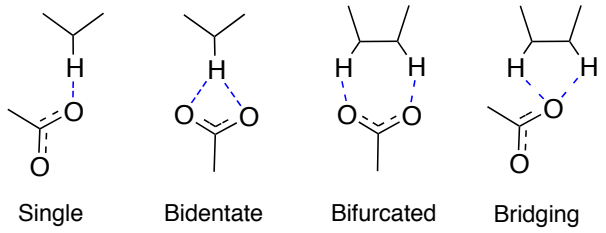

Figure 3.19: The type of interactions between carboxylate group and imidazolium ring summarized by Bowron in Ref. 4.

3.2.3 Analysis of Hydrogen Bonding in the Zw-ILs and ILs

The previous discussions conclude that the FSDP in OE_2imC_3C is from nano-domain aggregation, and excludes the possibility that the FSDP in OE_2eim^+/OAc^- arises from the same interaction. The intermediate range order in the OE_2eim^+/OAc^- IL likely results from the hydrogen bonding network, which is known to be the source of the FSDP in protic ILs such as the alkylammonium nitrate.[4, 16, 18, 44, 48] To explore the influence of hydrogen bonding networks in this set of Zw-ILs and ILs, we analyzed the hydrogen bonds present in the MD trajectories. Networks of H-bonds were found to occur between the hydrogens on the imidazolium rings and the carboxylate groups.

The types of H-bond interactions between carboxylate oxygen atoms in acetate and imidazolium ring protons are described by Bowron, *et al.* as single , bidentate , bifurcated or bridging interactions.[4] Illustrations of these H-bond types are shown in Fig. 3.19. To further understand the hydrogen bond types, electronic structure calculations on gas-phase $Im^+_{2,1}/OAc^-$ ion pairs were performed at the M06-2X/6-311+G(d,p) level. The results are shown in Fig. 3.20. We found that single H-bond interactions between a carboxylate oxygen and an imidazolium hydrogen are the most stable structures. This structure is further stabilized by weak interaction between another carboxylate oxygen atom and the α-hydrogen. Bidentate, bifurcated, bridging interactions are all not as stable as single interactions.

The molecular conformations and intramolecular hydrogen bonds for an isolated OE_2imC_3C Zw-ILmolecule were also studied at the same level of electronic structure

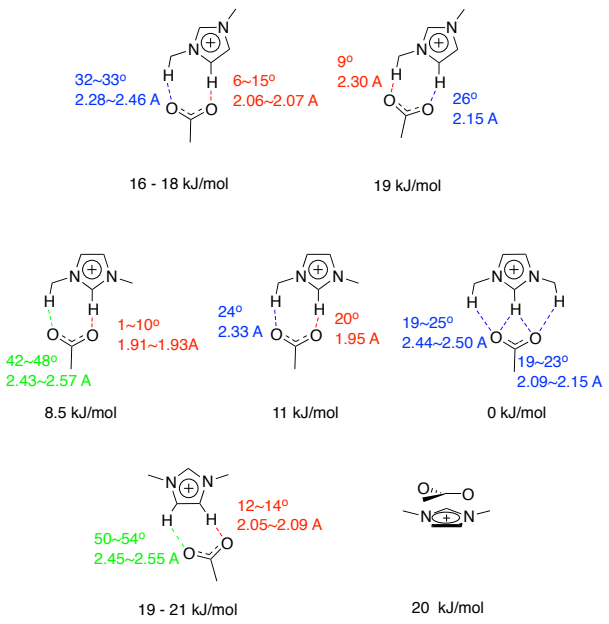

Figure 3.20: The major conformations between $Im^{+}_{2,1}$ and OAc^{-}.

theory. We observed that an intramolecular hydrogen bond can be formed, but the conformations with intramolecular hydrogen bonds do not have a significantly lower free energy than those with no hydrogen bonds. That indicates that intramolecular hydrogen bonds are unlikely to be a determining factor in liquid structure, which is consistent with what is shown in the spatial distribution functions from the MD simulations.

In order to locate the oxygen and hydrogen atoms with strong interactions between them, we studied the partial radial distribution functions $g_{ij}(r)$ between all hydrogen and oxygen types in these ionic liquids. The graphs are shown in Fig. 3.22. We find strong interactions between the carboxylate O atoms and the hydrogens on imidazolium rings, and some weaker interactions between carboxylate O atoms and hydrogens on alkyl carbons directly bonded to nitrogen atoms (specifically, the α-carbon hydrogen atoms). These five types of hydrogen atoms are labeled as H_A to H_E, as shown in Table 3.3. The probability for H-bond formation is ranked $H_C > H_A \approx H_B > H_D > H_E$. Only very weak hydrogen bonding interactions were observed between ether oxygens for any of the fives types of H-bond donors. The H-bonds between hydrogen atoms and carboxylate oxygens can also been shown by the intermolecular and intramolecular spatial distribution of carboxylate oxygens against imidazolium rings, as shown in Fig.

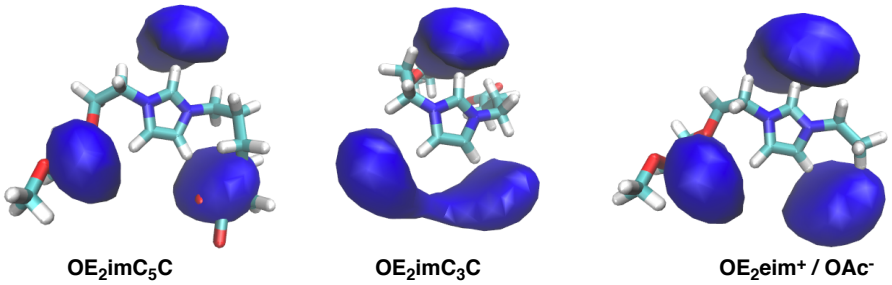

Figure 3.21: The intermolecular distribution of carboxylate oxygen atoms around imidazolium ring on three ionic liquids.

3.21. These spatial distribution functions indicate that hydrogen bonds are formed between the three imidazolium ring protons and that most of them intermolecular.

In the MD trajectories, we defined the distance and angle parameters for a hydrogen bond to be $r_{O-H} < 2.65$ Å and for C-H-O angles $> 120°$. Electronic structure calculations show that hydrogen bond lengths in these systems are about 1.9 Å, but the 2.68 Å definition in the OPLS-AA force field requires us to use a larger value to parametrize H-bonds in the classical MD system. The numbers of H-bonds in the simulation box were calculated for each of the five potential H-bond donor atoms. These results are summarized in Table 3.3. A similar analysis is also performed to determine the number of H-bonds observed for each of the carboxylate oxygens and the results are listed in Table 3.4. From Table 3.3 we find that most hydrogen atoms favor single interactions with only rare bidentate interactions observed. Intermolecular hydrogen bonds dominate in zwitterionic liquids, with only 5% $\sim$ 10% of the hydrogen bonds being intramolecular, in agreement with the electronic structure calculations.

Both tables 3.3 and 3.4 show that the numbers of hydrogen bonds for the OE_2eim^+/OAc^- IL is greater than for the OE_2imC_3C Zw-IL. This is evidence that the H-bonding network in OE_2eim^+/OAc^- is likely to be stronger than for the Zw-IL, indicating that the larger amplitude FSDP in OE_2eim^+/OAc^- may correlate with the degree of H-bonding. We also find that the hydrogen bond numbers for OE_2imC_5C lie between those for OE_2imC_3C and OE_2eim^+/OAc^-, indicating that the degree of H-bonding for OE_2imC_5C is between OE_2imC_3C and OE_2eim^+/OAc^-. That is consistent with the

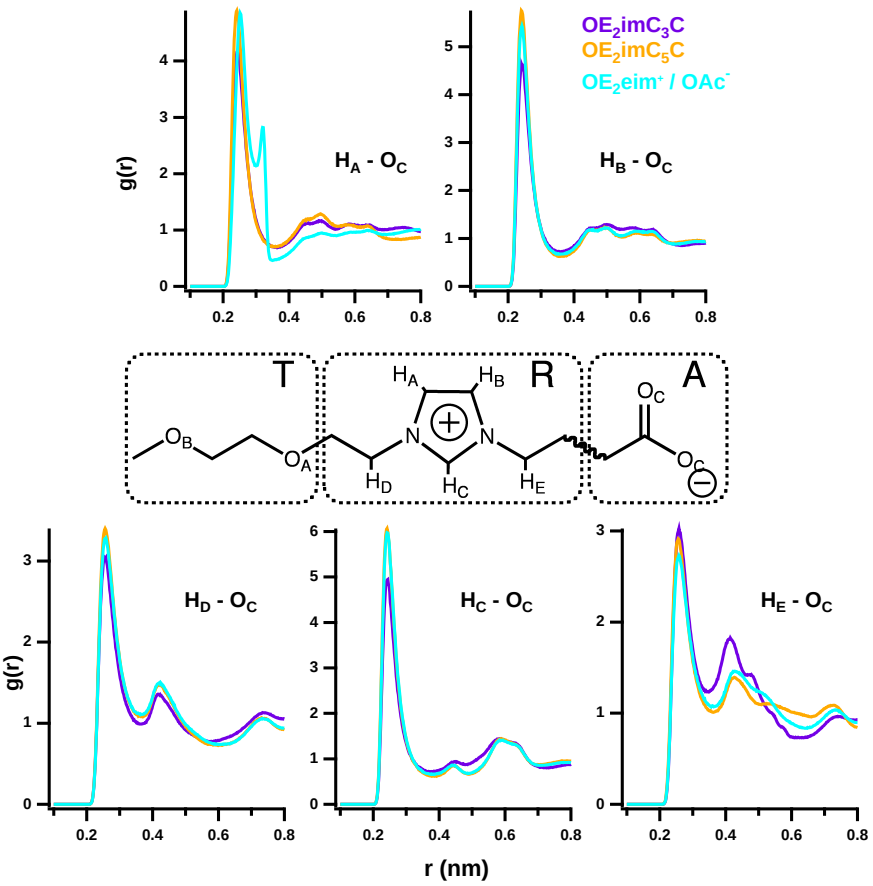

Figure 3.22: The radial distribution functions $g(r)$ between imidazolium hydrogens and carboxylate oxygens.

Table 3.3: The percentage distribution of different H-bond types between the hydrogen atoms H_A–H_E (defined below) and both the ether (O_A and O_B) and carboxylate (O_C) oxygens for both the Zw-IL and monovalent OE_2eim^+/OAc^-IL systems calculated from the MD simulation trajectories. The percentages in a given row sum to the total percentage of H-bonds, while the remainder are assigned to have no H-bonding.

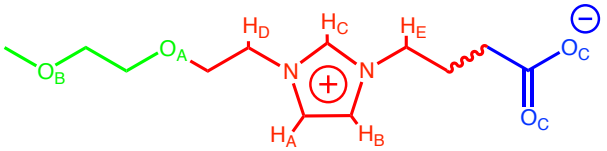

$$p(H_i - O_j) = \frac{\text{time average of total number of hydrogen bonds between } H_i \text{and } O_j \text{types}}{\text{total number of hydogen type } H_i} \times 100\%$$

$$p(H_i, \text{total}) = \sum_{j=A,B,C}^{\text{single}} p(H_i - O_j) + \sum_{j=O_C+O_C, O_A+O_B}^{\text{bidentate}} p(H_i - O_j) + \sum_{j}^{\text{all other H-bond types}} p(H_i - O_j)$$

H	Single O_C		Single O_A		Single O_B		Bidentate O_C+O_C^b	Bidentate O_A+O_B^c		Other[a]	Total	
type	intra	inter	intra	inter	intra	inter	inter	intra	inter		H-bond[d]	no H-bond[e]
OE_2imC_3C												
H_A	0.0	43.5	0.7	0.9	2.1	1.8	3.7	0.1	0.2	0.3	53.2	46.8
H_B	4.9	44.4	0.0	1.3	0.0	2.4	4.2	0.0	0.3	0.2	57.8	42.2
H_C	2.9	42.6	0.2	0.7	2.1	1.8	5.6	0.1	0.2	0.3	56.5	43.5
H_D	0.0	26.7	0.0	1.9	0.1	2.7	0.7	0.0	0.3	0.1	32.4	67.6
H_E	2.5	17.7	0.0	1.4	0.0	2.4	0.4	0.0	0.1	0.1	24.5	75.5
OE_2eim^+/OAc^-												
H_A	0.0	47.0	0.6	1.1	2.2	1.6	3.8	0.1	0.1	0.2	56.7	43.3
H_B	0.0	56.6	0.0	0.8	0.0	1.6	4.4	0.0	0.2	0.1	63.8	36.2
H_C	0.0	49.9	0.1	0.6	1.9	0.7	6.8	0.0	0.1	0.3	60.5	39.5
H_D	0.0	26.8	0.0	1.1	0.0	1.7	0.6	0.0	0.1	0	30.4	69.6
H_E	0.0	23.9	0.0	1.8	0.0	2.3	0.5	0.0	0.2	0	28.6	71.4
OE_2imC_5C												
H_A	0.0	45.6	0.6	1.3	2.5	1.8	4.1	0.1	0.3	0.3	56.6	43.4
H_B	2.6	52.1	0.0	1.2	0.0	1.8	4.7	0.0	0.3	0.2	62.9	37.1
H_C	2.9	44.1	0.2	0.6	2.4	1.0	5.9	0.1	0.1	0.3	57.5	42.5
H_D	0.4	25.3	0.0	1.5	0.1	2.2	0.8	0.0	0.1	0.1	30.6	69.4
H_E	0.4	24.1	0.0	1.5	0.0	2.0	0.6	0.0	0.2	0.1	28.8	71.2

[a] Other hydrogen bonding types, including H forming two H-bonds with two oxygen from different molecule, or $O_{A/B}$ and O_C from same molecule; [b] H forming H-bonds with 2 oxygens in one carboxylate group, these are all intermolecular interactions; [c] H forming H-bonds with 2 ether oxygens on one chain. [d] The total percentage of this kind of hydrogen that has any type of H-bonds on it; [e] The total percentage of this kind of hydrogen that doesn't have any H-bonds on it;

Table 3.4: The number of observed hydrogen bonds per carboxylate oxygen atom from the MD simulations.

Average numbers of	OE_2imC_3C	OE_2eim^+/OAc^-	OE_2imC_5C
Hydrogen bonds on each O atom	1.32	1.45	1.42
Molecules that have H-bond with each O atom	1.20	1.31	1.26
Molecules that have H-bond with each carboxylate group	2.12	2.29	2.19

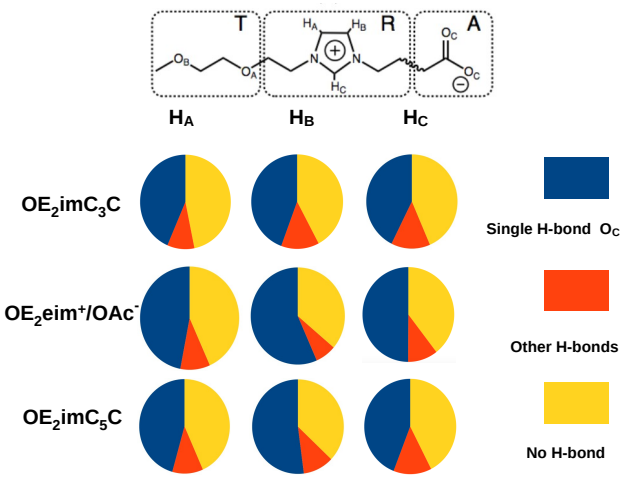

Figure 3.23: Graphical representations of the H-bond probability distributions for the imidazolium rings hydrogens H_A, H_B and H_C. Blue indicates the fraction of hydrogen atoms forming single H-bonds to the carboxylate oxygen atoms O_C, yellow indicates the fraction of hydrogens that do not form H-bonds, and red indicates the set of all other types of H-bonds observed. Hydrogens located on the C_α positions, H_D and H_E, were found to have negligible H-bonding, so these data are not included in the charts.

preceding analysis of the liquid structure factor $S(q)$, which indicates that increasing the distance between positively charged parts and negatively charged parts has a similar effect to eliminating the carbon-carbon bond in OE_2imC_3C to make OE_2eim^+/OAc^-. Graphs of the data given in Table 3.3 are provided in Fig. 3.23.

Bibliography

[1] H. V. R. Annapureddy, H. K. Kashyap, P. M. De Biase, and C. J. Margulis. What is the Origin of the Prepeak in the X-ray Scattering of Imidazolium-Based Room-Temperature Ionic Liquids? *J. Phys. Chem. B*, 114:16838–16846, 2010.

[2] J. C. Araque, J. J. Hettige, and C. J. Margulis. Modern Room Temperature Ionic Liquids, a Simple Guide to Understanding Their Structure and How It May Relate to Dynamics. *J. Phys. Chem. B*, 119:12727–12740, 2015.

[3] C. E. S. Bernardes, K. Shimizu, A. I. M. C. L. Ferreira, L. M. N. B. F. Santos, and J. N. C. Lopes. Structure and Aggregation in the 1,3-Dialkyl-imidazolium Bis(trifluoromethylsulfonyl)imide Ionic Liquid Family: 2. From Single to Double Long Alkyl Side Chains. *J. Phys. Chem. B*, 118:6885–6895, 2014.

[4] D. T. Bowron, C. D'Agostino, L. F. Gladden, C. Hardacre, J. D. Holbrey, M. C. Lagunas, J. McGregor, M. D. Mantle, C. L. Mullan, and T. G. A. Youngs. Structure and Dynamics of 1-Ethyl-3-methylimidazolium Acetate via Molecular Dynamics and Neutron Diffraction. *J. Phys. Chem. B*, 114:7760–7768, 2010.

[5] M. Brehm and B. Kirchner. TRAVIS - A Free Analyzer and Visualizer for Monte Carlo and Molecular Dynamics Trajectories. *J. Chem. Inf. Model.*, 51:2007–2023, 2011. TRAVIS Version 20160101.

[6] M. Campetella, S. De Santis, R. Caminiti, P. Ballirano, C. Sadun, L. Tanzi, and L. Gontrani. Is a medium-range order pre-peak possible for ionic liquids without an aliphatic chain? *RSC Adv.*, 5:50938–50941, 2015.

[7] J. N. Canongia Lopes, K. Shimizu, A. A. H. Pádua, Y. Umebayashi, S. Fukuda, K. Fujii, and S.-i. Ishiguro. A Tale of Two Ions: The Conformational Landscapes of Bis(trifluoromethanesulfonyl)amide and N,N-Dialkylpyrrolidinium. *J. Phys. Chem. B*, 112(5):1465–1472, 2008.

[8] J. N. A. Canongia Lopes and A. A. H. Pádua. Nanostructural Organization in Ionic Liquids. *J. Phys. Chem. B*, 110:3330–3335, 2006.

[9] E. W. Castner, Jr., C. J. Margulis, M. Maroncelli, and J. F. Wishart. Ionic Liquids: Structure and Photochemical Reactions. *Annu. Rev. Phys. Chem.*, 62:85–105, 2011.

[10] S. H. Chung, R. Lopato, S. G. Greenbaum, H. Shirota, E. W. Castner, Jr., and J. F. Wishart. A nuclear magnetic resonance study of room temperature ionic liquids with $CH_2Si(CH_3)_3$ vs. $CH_2C(CH_3)_3$ substitutions on the imidazolium cations. *J. Phys. Chem. B*, 111:4885–4893, 2007.

[11] K. B. Dhungana, L. F. O. Faria, B. Wu, M. Liang, M. C. C. Ribeiro, C. J. Margulis, and E. W. Castner, Jr. Structure of cyano-anion ionic liquids: X-ray scattering and simulations. *J. Chem. Phys.*, 145:024503, 2016.

[12] T. Endo, S. Nemugaki, Y. Matsushita, Y. Sakai, H. Ozaki, Y. Hiejima, Y. Kimura, and K. Takahashi. Fast solute diffusivity in ionic liquids with silyl or siloxane groups studied by the transient grating method. *Chem. Phys.*, 472(15):128–134, 2016.

[13] A. P. Fröba, M. H. Rausch, K. Krzeminski, D. Assenbaum, P. Wasserscheid, and A. Leipertz. Thermal Conductivity of Ionic Liquids: Measurement and Prediction. *Int. J. Thermophys.*, 31:2059–2077, 2010.

[14] K. Fujii, R. Kanzaki, T. Takamuku, Y. Kameda, S. Kohara, M. Kanakubo, M. Shibayama, S. ichi Ishiguro, and Y. Umebayashi. Experimental evidences for molecular origin of low-Q peak in neutron/x-ray scattering of 1-alkyl-3-methylimidazolium bis(trifluoromethanesulfonyl)amide ionic liquids. *J. Chem. Phys.*, 135(24):244502, 2011.

[15] K. Fujii, Y. Soejima, Y. Kyoshoin, S. Fukuda, R. Kanzaki, Y. Umebayashi, T. Yamaguchi, S.-i. Ishiguro, and T. Takamuku. Liquid Structure of Room-Temperature Ionic Liquid, 1-Ethyl-3-methylimidazolium Bis-(trifluoromethanesulfonyl) Imide. *J. Phys. Chem. B*, 112(14):4329–4336, 2008.

[16] T. L. Greaves, D. F. Kennedy, S. T. Mudie, and C. J. Drummond. Diversity Observed in the Nanostructure of Protic Ionic Liquids. *J. Phys. Chem. B*, 114:10022–10031, 2010.

[17] C. Hardacre, J. D. Holbrey, C. L. Mullan, T. G. A. Youngs, and D. T. Bowron. Small angle neutron scattering from 1-alkyl-3-methylimidazolium hexafluorophosphate ionic liquids (C(n)mim PF6 , n=4, 6, and 8). *J. Chem. Phys.*, 133(7):074510, 2010.

[18] R. Hayes, S. Imberti, G. G. Warr, and R. Atkin. Pronounced sponge-like nanostructure in propylammonium nitrate. *Phys. Chem. Chem. Phys.*, 13:13544–13551, 2011.

[19] R. Hayes, G. G. Warr, and R. Atkin. Structure and Nanostructure in Ionic Liquids. *Chem. Rev.*, 115:6357–6426, 2015.

[20] J. J. Hettige, W. D. Amith, E. W. Castner, Jr., and C. J. Margulis. Ionic Liquids with Symmetric Diether Tails: Bulk and Vacuum-Liquid Interfacial Structures. *J. Phys. Chem. B*, 121:174–179, 2017. PMID: 28005353.

[21] W. Humphrey, A. Dalke, and K. Schulten. VMD – Visual Molecular Dynamics. *J. Mol. Graph. Model.*, 14:33–38, 1996.

[22] P. A. Hunt, C. R. Ashworth, and R. P. Matthews. Hydrogen bonding in ionic liquids. *Chemical Society Reviews*, 44(5):1257–1288, 2015.

[23] W. Jiang, Y. Wang, and G. A. Voth. Molecular Dynamics Simulation of Nanostructural Organization in Ionic Liquid/Water Mixtures. *J. Phys. Chem. B*, 111(18):4812–4818, 2007.

[24] H. K. Kashyap, J. J. Hettige, H. V. R. Annapureddy, and C. J. Margulis. SAXS anti-peaks reveal the length-scales of dual positive-negative and polar-apolar ordering in room-temperature ionic liquids. *Chem. Commun.*, 48:5103–5105, 2012.

[25] H. K. Kashyap, C. S. Santos, H. V. R. Annapureddy, N. S. Murthy, C. J. Margulis, and E. W. Castner, Jr. Temperature-Dependent Structure of Ionic Liquids: X-ray Scattering and Simulations. *Faraday Discuss.*, 154:133–143, 2012.

[26] H. K. Kashyap, C. S. Santos, R. P. Daly, J. J. Hettige, N. S. Murthy, H. Shirota, E. W. Castner, Jr., and C. J. Margulis. How Does the Ionic Liquid Organizational Landscape Change when Nonpolar Cationic Alkyl Groups Are Replaced by Polar Isoelectronic Diethers? *J. Phys. Chem. B*, 117(4):1130–1135, 2013.

[27] H. K. Kashyap, C. S. Santos, N. S. Murthy, J. J. Hettige, K. Kerr, S. Ramati, J. Gwon, M. Gohdo, S. I. Lall-Ramnarine, J. F. Wishart, C. J. Margulis, and E. W. Castner, Jr. Structure of 1-Alkyl-1-methylpyrrolidinium Bis(trifluoromethylsulfonyl)amide Ionic Liquids with Linear, Branched, and Cyclic Alkyl Groups. *J. Phys. Chem. B*, 49:15328–15337, 2013.

[28] T. Köddermann, D. Paschek, and R. Ludwig. Molecular Dynamic Simulations of Ionic Liquids: A Reliable Description of Structure, Thermodynamics and Dynamics. *ChemPhysChem*, 8:2464–2470, 2007.

[29] J. N. C. Lopes, J. Deschamps, and A. A. H. Pádua. Modeling Ionic Liquids Using a Systematic All-Atom Force Field. *J. Phys. Chem. B*, 108:2038–2047, 2004.

[30] J. N. C. Lopes and A. A. H. Pádua. Molecular Force Field for Ionic Liquids Composed of Triflate or Bistriflylimide Anions. *J. Phys. Chem. B*, 108:16893–16898, 2004.

[31] J. N. C. Lopes and A. A. H. Pádua. Molecular Force Field for Ionic Liquids III: Imidazolium, Pyridinium, and Phosphonium Cations; Chloride, Bromide, and Dicyanamide Anions. *J. Phys. Chem. B*, 110:19586–19592, 2006.

[32] J. N. C. Lopes and A. A. H. Pádua. CL&P: A generic and systematic force field for ionic liquids modeling. *Theor Chem Acc*, 131:1129, 2012.

[33] T. Lu and F. Chen. Atomic dipole moment corrected hirshfeld population method. *J. Theor. Comput. Chem.*, 11:163–183, 2012.

[34] T. Lu and F. Chen. Multiwfn: A multifunctional wavefunction analyzer. *J. Comp. Chem.*, 33:580–592, 2012.

[35] M. Macchiagodena, F. Ramondo, A. Triolo, L. Gontrani, and R. Caminiti. Liquid Structure of 1-Ethyl-3-methylimidazolium Alkyl Sulfates by X-ray Scattering and Molecular Dynamics. *J. Phys. Chem. B*, 116:13448–13458, 2012.

[36] O. Russina, L. Gontrani, B. Fazio, D. Lombardo, A. Triolo, and R. Caminiti. Selected chemical-physical properties and structural heterogeneities in 1-ethyl-3-methylimidazolium alkyl-sulfate room temperature ionic liquids. *Chem. Phys. Lett.*, 493:259–262, 2010.

[37] O. Russina, A. Triolo, L. Gontrani, R. Caminiti, D. Xiao, J. Hines, Larry G., R. A. Bartsch, E. L. Quitevis, N. Pleckhova, and K. R. Seddon. Morphology and intermolecular dynamics of 1-alkyl-3-methylimidazolium bis(trifluoromethane)sulfonylamide ionic liquids: structural and dynamic evidence of nanoscale segregation. *J. Phys.: Condens. Matter*, 21(42):424121, 2009.

[38] C. S. Santos, H. V. R. Annapureddy, N. S. Murthy, H. K. Kashyap, E. W. Castner, Jr., and C. J. Margulis. Temperature-dependent structure of methyltributylammonium bis(trifluoromethylsulfonyl)amide: X ray scattering and simulations. *J. Chem. Phys.*, 134:064501, 2011.

[39] C. S. Santos, N. S. Murthy, G. A. Baker, and E. W. Castner, Jr. Communication: X-ray scattering from ionic liquids with pyrrolidinium cations. *J. Chem. Phys.*, 134(12):121101, 2011.

[40] H. Shirota and E. W. Castner, Jr. Why Are Viscosities Lower for Ionic Liquids with -CH2Si(CH3)3 vs -CH2C(CH3)3 Substitutions on the Imidazolium Cations? *J. Phys. Chem. B*, 109:21576–21585, 2005.

[41] H. Shirota, J. F. Wishart, and E. W. Castner, Jr. Intermolecular Interactions and Dynamics of Room Temperature Ionic Liquids That Have Silyl- and Siloxy-Substituted Imidazolium Cations. *J. Phys. Chem. B*, 111:4819–4829, 2007.

[42] A. Triolo, O. Russina, H.-J. Bleif, and E. Di Cola. Nanoscale segregation in room temperature ionic liquids. *J. Phys. Chem. B*, 111(18):4641–4644, 2007.

[43] A. Triolo, O. Russina, R. Caminiti, H. Shirota, H. Y. Lee, C. S. Santos, N. S. Murthy, and E. W. Castner, Jr. Comparing intermediate range order for alkyl- vs. ether-substituted cations in ionic liquids. *Chem. Commun.*, 48:4959–4961, 2012.

[44] Y. Umebayashi, W.-L. Chung, T. Mitsugi, S. Fukuda, M. Takeuchi, K. Fujii, T. Takamuku, R. Kanzaki, and S.-i. Ishiguro. Liquid Structure and the Ion-Ion Interactions of Ethylammonium Nitrate Ionic Liquid Studied by Large Angle X-Ray Scattering and Molecular Dynamics Simulations. *J. Comput. Chem. Jpn*, 7(4):125–134, 2008.

[45] S. M. Urahata and M. C. C. Ribeiro. Structure of ionic liquids of 1-alkyl-3-methylimidazolium cations: A systematic computer simulation study. *J. Chem. Phys.*, 120(4):1855–1863, 2004.

[46] Y. Wang and G. A. Voth. Unique Spatial Heterogeneity in Ionic Liquids. *J. Am. Chem. Soc.*, 127(35):12192–12193, 2005.

[47] Y. Wang and G. A. Voth. Tail Aggregation and Domain Diffusion in Ionic Liquids. *J. Phys. Chem. B*, 110(37):18601–18608, 2006.

[48] Y.-L. Wang, A. Laaksonen, and M. D. Fayer. Hydrogen bonding versus $\pi - \pi$ stacking interactions in imidazoliumâĂŞoxalatoborate ionic liquid. *J. Phys. Chem. B*, 121:7173–7179, 2017.

[49] B. Wu, H. Shirota, and E. W. Castner, Jr. Structure of Ionic Liquids with Cationic Silicon-Substitutions. *J. Chem. Phys.*, 145:114501, 2016.

[50] B. Wu, Y. Yamashita, T. Endo, K. Takahashi, and E. W. Castner, Jr. Structure and Dynamics of Ionic Liquids: Trimethylsilylpropyl-Substituted Cations and Bis(sulfonyl)amide Anions. *J. Chem. Phys.*, 145:244506, 2016.

[51] A. Yokozeki, M. B. Shiflett, C. P. Junk, L. M. Grieco, and T. Foo. Physical and Chemical Absorptions of Carbon Dioxide in Room-Temperature Ionic Liquids. *J. Phys. Chem. B*, 112(51):16654–16663, 2008.

Chapter 4

Photo-Induced Electron Transfer in Ionic Liquids

4.1 Fluorophore and Quencher Properties (Choice of Excitation and Emission Wavelengths)

The absorption and emission spectra of the five fluorophores in the three solvents are shown in Fig. 4.1. The spectral maxima of the various fluorophores vary by less than 3 nm in this set of solvents. The energies of their first excited states are provided as ΔG_{S1} in Table 4.1. No indication of the formation of ground or excited state complexes with quenchers was found any of the spectra. However, at higher concentrations, Rosspeintner et al. did observe a change from the absorption band of TCNA, TrCNA and DCNA in CH_3CN solutions with DMA. [44] These ground-state complexes are not emissive and, based on the equilibrium constants determined in Ref. 44, such complexes are expected to have a negligible effect on the results described here.

The ground state reduction potentials of all fluorophores are taken from the literature, they are ordered CNMeA $\approx$ CNA <DCNA <TrCNA <TCNA (see Table 4.1). The oxidation potentials of the neat quencher ionic liquids $Im^+_{2,1}/Q^-$ are 0.5 V (vs SCE) for $SeCN^-$, 1.1 V for SCN^-, 1.2 V for $C(CN)_3^-$ and 1.7 V for $N(CN)_2^-$. [61] The oxidation potentials of DMA and DMPT in acetonitrile are 0.74 V [33] and 0.69 V, [26, 59] respectively.

The excited-state lifetimes of all fluorophores are also shown in Table 4.1. They vary over a modest range ($\pm$11%). These fluorophores are susceptible to quenching by molecular oxygen, which manifests as a reduction in the unquenched emission lifetime τ_0 by 10%$\sim$35% in CH_3CN. Thus, all solutions were prepared under an argon atmosphere in a glovebox.

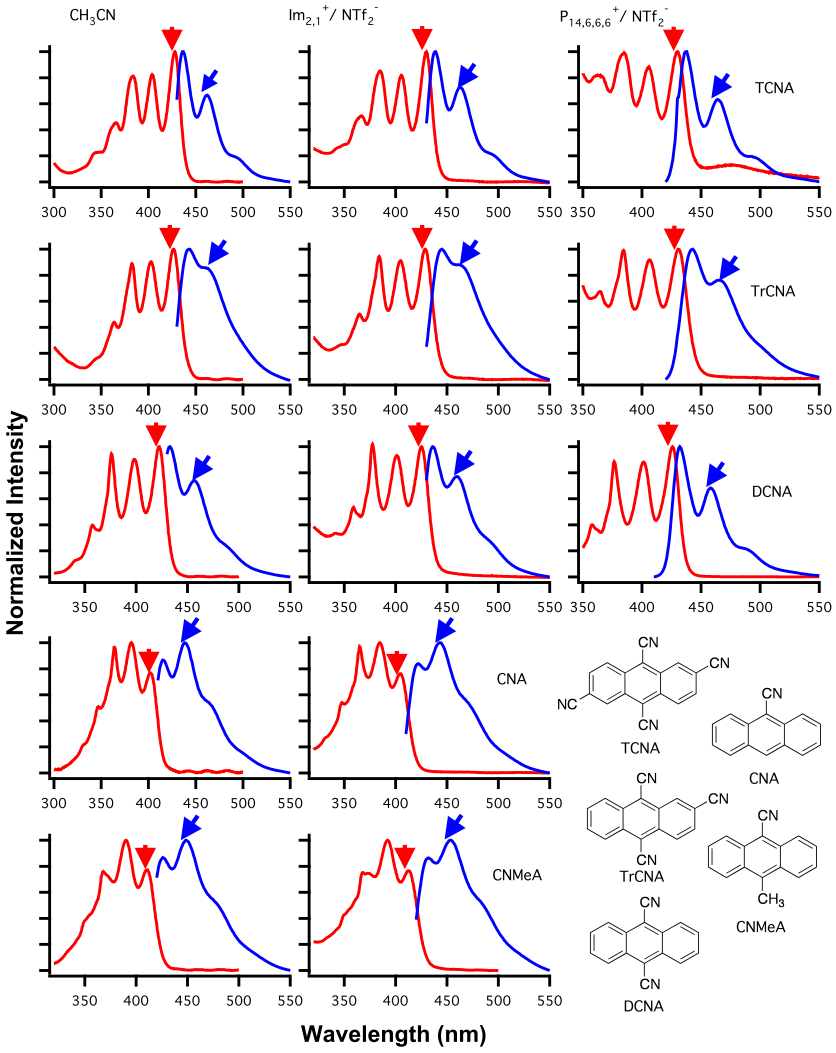

Figure 4.1: The absorption (red curves) and emission (blue curves) spectra of the five cyano-anthracene fluorophores. From left to right are spectra for solutions in CH_3CN, $Im^+_{2,1}$ / NTf^-_2 and $P^+_{14,6,6,6}$ / NTf^-_2, respectively. From top to bottom the spectra are shown for the five fluorophores, TCNA, TrCNA, DCNA, CNA and CNMeA. Red and blue arrows point to excitation and emission wavelengths.

Table 4.1: Properties of the fluorophores.

Fluorophore	G_{S1} (eV)	E_{red} (V)	λ_{ex} (nm)	τ_0 (ns)		
				CH_3CN	$Im^+_{2,1}$/ NTf_2^-	$P^+_{14,6,6,6}$/ NTf_2^-
CNMeA	2.92[a]	-1.41[b]	410	15.8	14.8	
CNA	2.96[c]	-1.39[c]	403	16.9	15.8	
DCNA	2.88[c]	-0.98[c]	422	14.9	13.8	12.1
TrCNA	2.89[d]	-0.70[d]	426	18.6	16.1	15.5
TCNA	2.82[e]	-0.45[e]	428	16.6	14.5	14.3

ΔG_{S1} is the excited state free energy, E_{red} the reduction potential (vs. SCE) and λ_{ex} the excitation wavelength in CH_3CN, and τ_0 the unquenched fluorescence lifetime in the three solvents. [a]Estimated based on absorption and emission spectra ; [b]in DMSO solution, Ref. 3 ; [c]Ref. 37 ; [d]Ref. 28 ; [e]Ref. 18 .

4.2 Stern-Volmer Analysis of Fluorescence Quenching

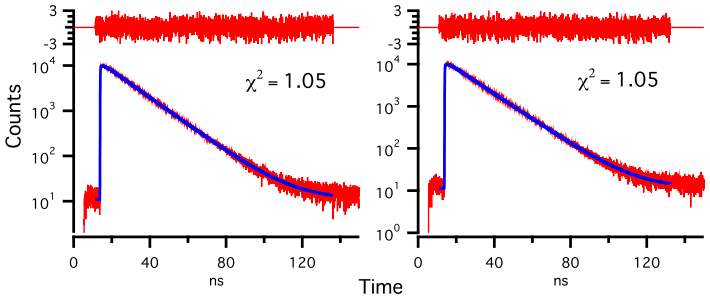

Figure 4.2: TCSPC fits of TCNA in $Im^+_{2,1}$ / NTf_2^-. Left panel is 462 nm and right panel is 464 nm.

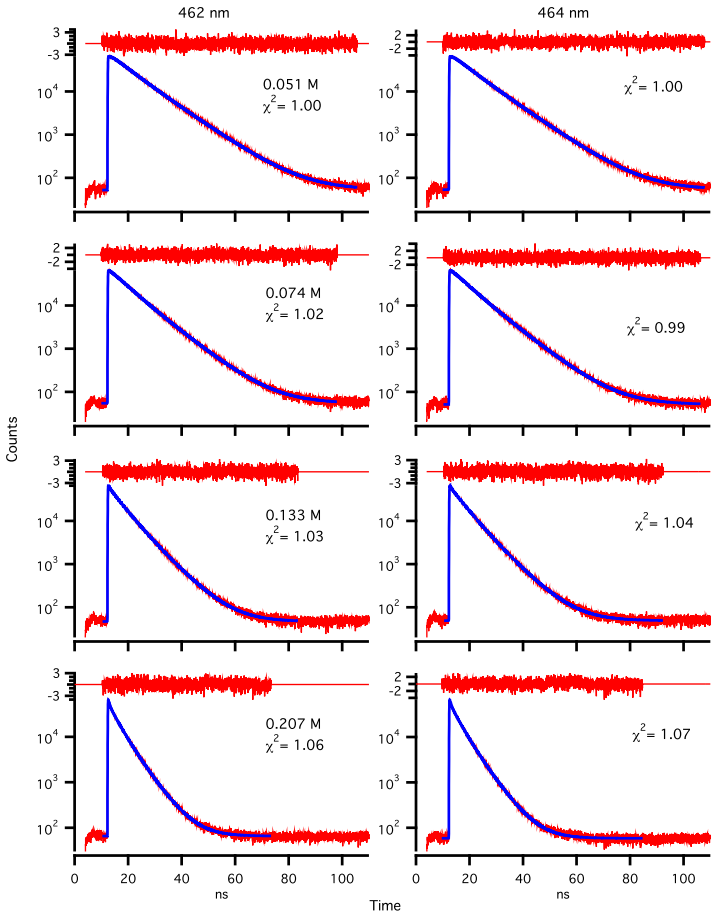

Figure 4.3: TCSPC fits of TCNA quenched by $SeCN^-$ in $Im^+_{2,1}$ / NTf^-_2. Left panel is 462 nm and right panel 464 nm emission.

All time resolved quenching data from the TCSPC experiments were fit to multi-exponential decays. Typical fits are shown in Figs. 4.2 and 4.3. Usually 1 or 2 components were required to fit the fluorescence transients in acetonitrile solutions but 2–5 decay terms were needed to fit data in ionic liquids, due to their more complicated dynamics. [42, 48, 63] The steady-state and time resolved quenching data were first analyzed using a standard Stern-Volmer (S-V) analysis. Representative S-V plots of the TCNA-$C(CN)^-_3$ and TCNA-DMA pairs in all three solvents are shown in Fig. 4.4. As typified by Fig. 4.4, nonlinear S-V plots are observed for most fluorophore-quencher-solvent systems. This nonlinearity, as well as the non-exponentiality of the decays observed here, indicate the need for the more detailed analysis provided by

diffusion-reaction modeling in the following sections. Nevertheless, useful information can still be obtained from analysis of such S-V plots. We note that the S-V plots from steady-state data are more non-linear than the corresponding time-resolved plots. In ionic liquids, the S-V plots observed using neutral quenchers are more non-linear than those with the anion quenchers. In all cases the concentration dependence can be accurately characterized using quadratic equations:

$$\mathrm{I}_0/\mathrm{I} \quad \text{and} \quad \tau_0/ < \tau >= 1 + a\,[Q] + b\,[Q]^2 \tag{4.1}$$

Effective quenching rate constants k_q(TR) and k_q(SS) can be determined from such fits to the time resolved fluorescence and time integrated fluorescence data, respectively. We define these k_q to be the instantaneous slope of the S-V plots at [Q]=0.05 M using $k_q = (a + 0.05b)/\tau_0$. The value 0.05 M is chosen rather than the value of 0.1 M used previously [33, 61] because in this work the largest quencher concentrations used in some acetonitrile solutions was 0.05 – 0.06 M.

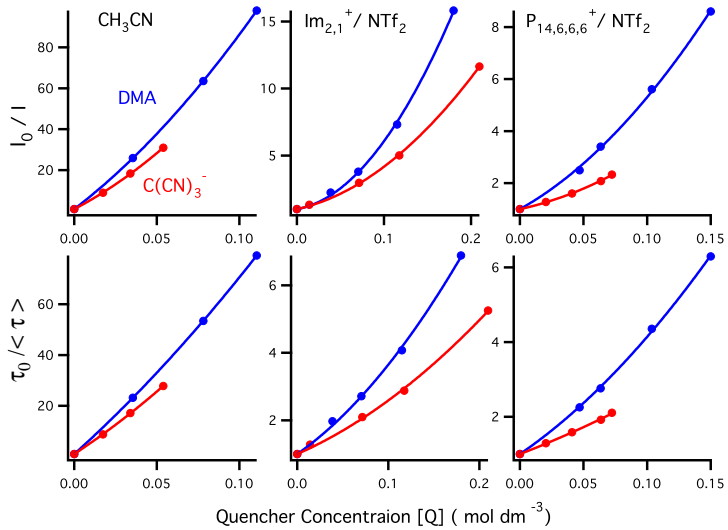

Figure 4.4: Steady-state (top) and time-resolved (bottom) Stern-Volmer plots showing the quenching of TCNA by DMA (blue) and $C(CN)_3^-$ (red) in the three solvents.

The quenching rate constants from S-V analysis are summarized in Table 4.2 and plotted *vs.* reaction free energy ΔG_0 in the top panel of Fig. 4.5. Details of the

Table 4.2: The reaction free energies and quenching rate constants obtained from steady-state (SS) and time resolved (TR) Stern-Volmer analysis. All rate constants are in units of $M^{-1}ns^{-1}$ and taken from the slopes of S-V plots at $[Q] = 0.05$ M.

			CH_3CN		$Im^+_{2,1}$ / NTf^-_2		$P^+_{14,6,6,6}$ / NTf^-_2	
Fluorophore	Quencher	ΔG_0 (eV)	k_q(SS)	k_q(TR)	k_q(SS)	k_q(TR)	k_q(SS)	k_q(TR)
CNMEA	$C(CN)_3^-$	−0.31	8.8	9.1	0.60	0.40		
	$N(CN)_2^-$	0.19	0.027	0.006	< 0.01	< 0.01		
CNA	$SeCN^-$	−1.07	26.0	30.3	0.77	0.50		
	SCN^-	−0.47	18.4	20.5	0.55	0.52		
	$C(CN)_3^-$	−0.37	12.7	14.3	0.62	0.45		
	$N(CN)_2^-$	0.13	0.031	0.010	< 0.01	< 0.01		
DCNA	$SeCN^-$	−1.4	34.3	29.8	1.04	1.04	1.01	0.46
	SCN^-	−0.8	26.6	25.5	0.66	0.64	0.64	0.17
	$C(CN)_3^-$	−0.7	25.1	25.1	1.00	0.92	0.70	0.28
	$N(CN)_2^-$	−0.2	15.0	15.4	0.45	0.48	0.20	0.09
	DMA	−1.16	38.3	36.2	1.74	1.51	1.84	1.08
	DMPT	−1.21	41.7	37.3	2.41	1.42	1.82	1.05
TrCNA	$SeCN^-$	−1.69	38.8	35.0	1.27	1.05	1.02	0.73
	SCN^-	−1.09	24.9	24.3	0.83	0.71	0.77	0.58
	$C(CN)_3^-$	−0.99	29.1	27.3	1.12	0.92	0.89	0.56
	$N(CN)_2^-$	−0.49	17.0	16.7	0.54	0.52	0.36	0.59
	DMA	−1.45	42.6	36.2	1.99	1.63	2.15	1.37
	DMPT	−1.50	46.1	40.0	2.21	1.75	1.68	1.23
TCNA	$SeCN^-$	−1.87	49.1	42.3	1.49	1.05	1.24	1.00
	SCN^-	−1.27	32.7	30.7	1.14	0.76	1.13	0.99
	$C(CN)_3^-$	−1.17	32.9	29.7	1.59	0.96	1.11	0.97
	$N(CN)_2^-$	−0.67	20.7	18.9	0.71	0.58	0.53	
	DMA	−1.63	44.3	38.6	2.15	1.57	2.47	1.92
	DMPT	−1.68	47.5	38.5	2.24	1.54	2.46	1.93

calculation of ΔG_0 are provided in the method chapter. In each solvent, the quenching rate increases as the driving force increases. The only exception is that the ordering of k_q for SCN^- and $C(CN)_3^-$ is reversed. For each of the five fluorophores, the quenching rate constants are $SeCN^- > C(CN)_3^- > SCN^- > N(CN)_2^-$, and DMPT > DMA. For each quencher, the trend in observed rate constants is TCNA > TRCNA > DCNA > CNA > CNMEA.

Fig. 4.5 shows that the quenching rate constants of the neutral quenchers are almost the same as those of the strongest anionic quenchers in acetonitrile, but they are significantly greater in both ionic liquids. One reason lies in the different diffusion rates of anionic and neutral solutes in ILs. In the top panel of Fig. 4.5, we show the diffusion-limited rate constants calculated using Eq. 1.1 as dashed lines. We find that k_d predicted by Eq. 1.1 underestimates the largest values of k_q by a factor of ~ 2.5 in CH_3CN solutions. In the ionic liquid solvents the error is much greater. Here Eq. 1.1

Table 4.3: Measured or estimated diffusion coefficients of each solute in each solvent at 298.15 K (cm^2/s)

Solute	Diffusivity in solvent		
	$Im^+_{2,1}$ / NTf^-_2	$P^+_{14,6,6,6}$ / NTf^-_2	CH_3CN
DCNA	2.48×10^{-7}	6.07×10^{-8}	1.66×10^{-5}
TCNA	1.36×10^{-7}	3.33×10^{-8}	1.57×10^{-5}
TrCNA	1.82×10^{-7}	4.44×10^{-8}	1.61×10^{-5}
CNA	3.50×10^{-7}	8.56×10^{-8}	1.71×10^{-5}
CNMeA	2.56×10^{-7}	6.25×10^{-8}	1.65×10^{-5}
$SeCN^-$	4.23×10^{-7}	4.67×10^{-8}	2.52×10^{-5}
SCN^-	4.36×10^{-7}	4.80×10^{-8}	2.59×10^{-5}
$C(CN)^-_3$	3.73×10^{-7}	4.11×10^{-8}	2.22×10^{-5}
$N(CN)^-_2$	4.17×10^{-7}	4.59×10^{-8}	2.48×10^{-5}
DMA	5.87×10^{-7}	3.35×10^{-7}	3.23×10^{-5}
DMPT	5.55×10^{-7}	3.19×10^{-7}	3.04×10^{-5}
C_4DMAP^+	3.79×10^{-7}		1.99×10^{-5}
C_8DMAP^+	2.89×10^{-7}		1.59×10^{-5}
$C_{10}DMAP^+$	2.32×10^{-7}		1.47×10^{-5}

underestimates the maximum k_q values by 1 – 2 orders of magnitude. This observation is consistent with previous studies. [30, 33]

In order to calculate k_d more accurately than possible with Eq. 1.1, we measured or estimated the reactant sizes and diffusion coefficients using various approaches detailed in the method chapter. Ideally one would measure all diffusion coefficients experimentally. However, this ideal was achieved only for the neutral quenchers DMA and DMPT using pulsed field gradient NMR measurements. For the fluorophores and anionic quenchers, we relied on empirical estimates calibrated on the charge and size scaling found in previous studies of similar solutes. [25, 61] As shown in Table 4.3, the measured diffusivities of neutral quenchers are close to those estimated for the charged quenchers in CH_3CN, almost 2-fold larger in $Im^+_{2,1}$ / NTf^-_2, and an order of magnitude larger in $P^+_{14,6,6,6}$ / NTf^-_2. It should be noted that we do not attempt to correct for possible quencher concentration affecting the solution viscosity and thus the diffusion coefficients. It should be noted that we do not attempt to correct for changes to the solution viscosity and thus the diffusion coefficients with added quencher as such effects are expected to be small.[33].

In the bottom panel of Fig. 4.5 these improved estimates of diffusion coefficients are used to plot the ratios k_q/k_d *vs.* ΔG_0. For the reactions with the greatest driving force, where the diffusion limit is expected, k_q/k_d is still > 1 in all solvents. In CH_3CN, k_q/k_d

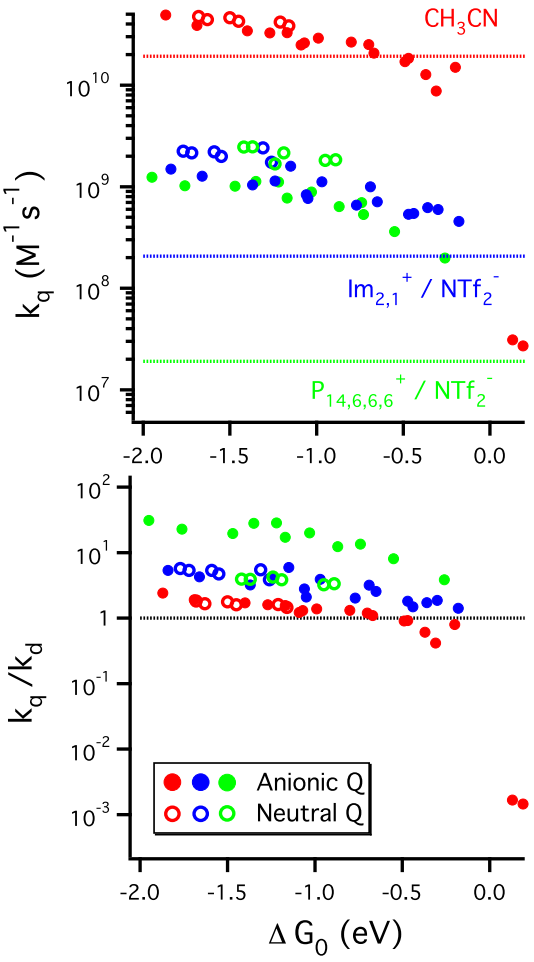

Figure 4.5: Top panel: Rehm-Weller plots of the quenching rate constants k_q obtained from Stern-Volmer analysis of the steady-state data ([Q]=0.05 M). The dashed lines are diffusion-limited rate constants calculated using Eq. 1.1. The bottom panel shows k_q/k_d, where k_d values are calculated using diffusivities from PG-SE NMR measurements or empirical estimations. Solvents are colored as red=CH_3CN, blue=$Im^+_{2,1}$ / NTf_2^- and green=$P^+_{14,6,6,6}$ / NTf_2^-.

~ 2 for both neutral and ionic quenchers, indicating steady-state Smoluchowski predictions are reasonably accurate. However, while use of best estimations of D decreases the extend to which the observed k_q are under-predicted, k_q is still much greater than k_d. Thus, although more accurate estimates of diffusion rates reduce the discrepancies compared to use of Eq. 1.1, factors other than inaccurate diffusion estimates must be responsible for a large portion of the deviations observed in the ionic liquid solvents. As has been discussed previously, [30, 33] both the fact that much of the quenching occurs prior to achieving steady-state conditions as well as the possibility of long-distance reaction are important in ionic liquids (and other high-viscosity solvents).

Before leaving Fig. 4.5, it should be noted that we do not observe evidence for a turnover in k_q at larger driving forces. Contrary to what has been found in many studies in conventional low-viscosity solvents, [10, 41, 44] an apparent turnover was reported in several studies of coumarin fluorescence quenching in ionic liquid solvents. [9, 50, 51] Proper interpretation of these experiments is still under debate in the literature. [2, 31, 46] Here we only note that no turnover is evident in the present data, despite the fact that we examine a wider range of ΔG_0. In this regard the k_q data ionic liquid solvents do not differ from those in CH_3CN.

4.3 Using Simple Diffusion-Reaction Models to Fit the Quenching Data

We now attempt to interpret the complete time-resolved quenching data using the spherical diffusion-reaction approach. Diffusion-reaction models provide a more sophisticated description than S-V analysis by considering the time evolution of the F-Q pair distribution $p(r,t)$ based on a spherically symmetric diffusion-reaction equation: [5, 32, 45, 57]

$$\frac{\partial p(r,t)}{\partial t} = (\hat{L}(r) - \kappa(r))p(r,t) \ , \tag{4.2}$$

where the diffusion operator $\hat{L}(r)$ is given by:

$$\hat{L}(r) = D\frac{1}{r^2}\frac{\partial}{\partial r}r^2 g(r)\frac{\partial}{\partial r}(\frac{1}{g(r)}) \ . \tag{4.3}$$

In these expressions $\kappa(r)$ is the distance-dependent reaction rate, and $g(r)$ is the equilibrium F-Q radial distribution function ($p(r,t)$ at $t = 0$). The time-dependent quenching rate coefficient, $k_q(t)$, is related to $p(r,t)$ and $\kappa(r)$ by:

$$k_q(t) = 4\pi \int_0^\infty r^2 p(r,t)\kappa(r)dr \tag{4.4}$$

It is only when $p(r,t)$ approaches its stationary limit before most quenching occurs that one can assume k_q to be time-independent and where simple approximations such as Eq. 1.1 are expected to be accurate.

We consider the four reaction models $\kappa(r)$ illustrated in Figure 4.6. These models correspond to increasingly complex descriptions of the distance dependence of reaction. The first three are phenomenological models, whereas the fourth is based on a Marcus-type description of electron transfer. The motivation for examining this series of models is to better appreciate how much it is possible to determine $\kappa(r)$ based on quenching data of the sort collected here.

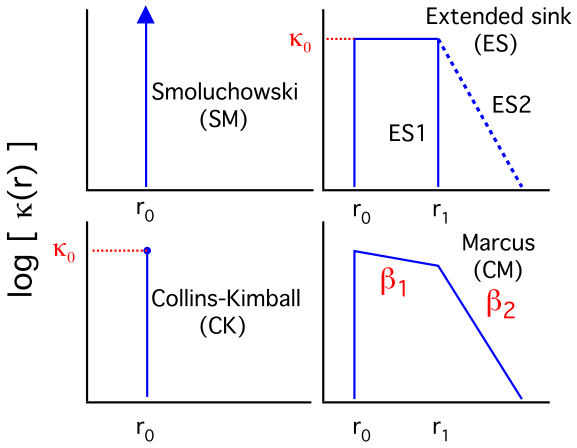

Figure 4.6: Schematic plots of the distance dependent reaction rates, $\kappa(r)$, of the four models examined here.

The first diffusion-reaction model (SM) is the one first used by Smoluchowski in deriving Eq. 1.1. Smoluchowski solved the spherically symmetric diffusion equation assuming a uniform reactant distribution and an absorbing boundary condition at a reaction distance r_0, which is equivalent to assuming $\kappa(r) = \delta(r - r_0)$. [54, 55] The second model, by Collins and Kimball (CK model), assumes a non-zero reaction rate κ_0, again occurring only at a single distance r_0. [7, 8, 15, 24, 39]. These first two reaction models permit analytic solutions for $k_q(t)$ and at least approximate equations describing the time-dependent fluorescence. The last two models do not admit simple analytic solutions. For these models we use the approximate solution of Eq. 4.2 given by Dudko and Szabo. [11] In the extended sink model, $\kappa(r)$ is non-zero over a finite thickness first solvation shell, $r_0 \leq r \leq r_1$. We either assume there is no reaction outside of the first solvation shell (ES1) or allow for an exponentially decreasing rate beyond the first shell (ES2). In the classical Marcus (CM) model, we use the descriptions of non-adiabatic electron transfer provided by Marcus theory combined with Zusman's treatment of dynamical solvent effects [34, 35, 43, 66] to define the form of $\kappa(r)$, which again is separated into a first solvation shell region and regions of greater F-Q separation.

As discussed in detail in the method section, we fit multi-exponential parameterizations of TCSPC and steady-state data to these various quenching models. Such fits essentially correspond to fitting what we will call the *quenching kernel*, $K_q(t)$. This function is defined for a given model by

$$K_q^{model}(t) \equiv \int_0^t k_q(\tau) d\tau \tag{4.5}$$

The experimental equivalent for comparison is obtained from steady-state and time-resolved fluorescence data by

$$K_q^{obs}(t;[Q]) \propto -\frac{1}{[Q]} \ln\left(I_{[Q]}(t)/I_{[Q]=0}(t)\right), \tag{4.6}$$

where $[Q]$ denotes the quencher concentration. The proportionality constant for any $[Q]$ is related to the difference in the net amount of quenching reported by steady-state and time-resolved data. If quenchers act independently, as assumed by each of our

models, for a given fluorophore-quencher-solvent system $K_q^{obs}(t;[Q])$ should be the same for all $[Q] > 0$. Concentration-averaged $K_q^{obs}(t)$ functions are therefore a convenient means of representing the experimental quench data and making comparisons to models. Moreover, the variations in $K_q^{obs}(t;[Q])$ with $[Q]$ in a given system can be used to assess the quality of a given data set. Figure 4.7 shows sampled values of $-K_Q^{obs}(t;[Q])$ for six representative systems in order to illustrate the variety of time dependence and data quality in the present study.

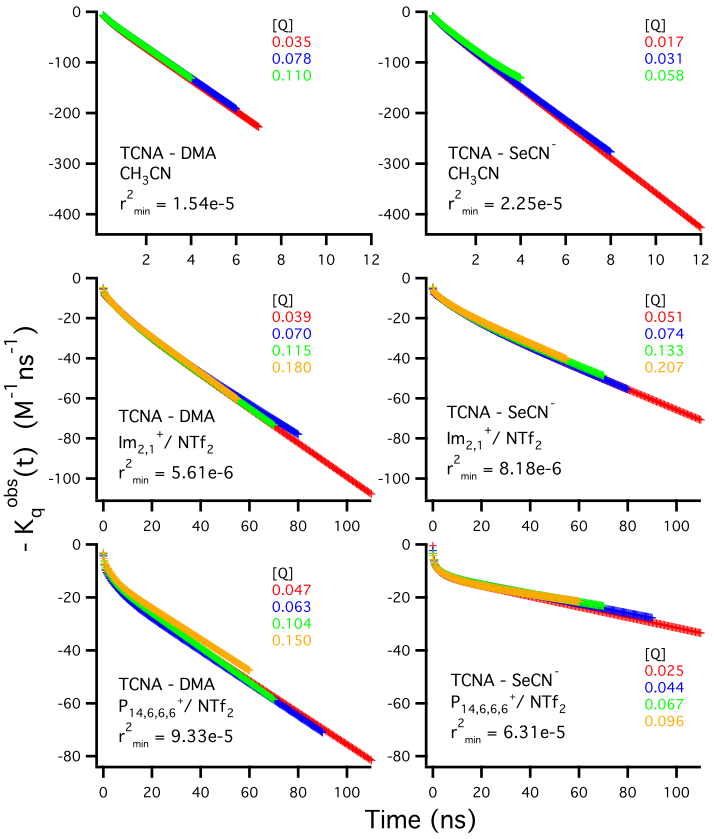

Figure 4.7: Representative $K_q^{obs}(t;[Q])$ data sets for TCNA quenched by DMA and $SeCN^-$.

As a quantitative measure of the fidelity with which a given model reproduces the observed fluorescence decays, we use a quantity ρ, the ratio of the sum of squared residuals of the fit to a data set using a model $K_q(t)$ to the same quantity obtained

with $K_q(t)$ optimized to provide the best possible fit of the experimental data. The latter $K_q(t)$ is a weighted averaged of the $K_q^{obs}(t;[Q])$ in a data set.

4.3.1 A. The Smoluchowski and Collins-Kimball Models

We first attempted to fit quenching data to the Smoluchowski and Collins-Kimball models. The equations describing $k_q(t)$ and $K_q(t)$ for these models are provided in the method section. In the Smoluchowski model, two parameters, r_0 and D, were optimized. In the case of the Collins-Kimball model, κ_0 was also varied.

Experimental data and fits to these data in several systems are represented by their quenching kernels (K_q, Eqs. 4.5 and 4.6) in Fig. 4.8. The negative of $K_q(t)$ is plotted here in order to emphasize its relationship to fluorescence decays, *i. e.*, $-K_q(t)$ is the natural logarithm of a hypothetical fluorescence decay when [Q]=1 M for a fluorophore having an infinite unquenched lifetime. Before considering the model functions, it is useful to note the varied character of the experimental quenching kernels (bold dashed curves) in the different solvents studied. In CH_3CN, all $K_q^{obs}(t)$ are close to linear functions of time, i.e. the fluorescence decays are nearly exponential. In contrast, in the IL solvents, for most F-Q pairs the $K_q^{obs}(t)$ are highly nonlinear functions of time (fluorescence decays nonexponential). Characterizing these functions using $K_q^{obs}(t) \approx a + bt^{\beta}$ one finds average values of the stretching exponents $\beta = 0.94$, 0.88, and 0.84 in CH_3CN, $Im_{2,1}^{+}$ / NTf_2^{-}, and $P_{14,6,6,6}^{+}$ / NTf_2^{-}, respectively.

Returning to the Smoluchowski and Collins-Kimball models, the best fit $K_q^{model}(t)$ functions are shown as the blue curves in Fig. 4.8. Table 4.5 summarizes some indicators of the quality of these fits in the three solvent systems. Despite the extra parameter of the Collins-Kimball model, we found little difference between the Smoluchowski and Collins-Kimball models for analyzing the present data. For example, in all four systems in Fig. 4.8, the two models give virtually identical fits, so that only the Collins-Kimball results are shown. In CH_3CN, where $K_q^{obs}(t)$ is nearly linear in time, both models provide accurate fits, with the Collins-Kimball model being slightly better in a few cases. The parameters r_0 and D obtained by fitting the CH_3CN data are also physically reasonable. Table 4.5 lists averages of the ratios of these quantities to independent

Table 4.4: The inner-sphere and solvent reorganization energies (λ_{in} and λ_{solv} in eV), effective solvation radii ($r_{\rm solv}$ in Å) and van der Waals volumes (in Å^3) and radii (in Å) calculated by two methods

	λ_{in}	$\lambda_{sol,\rm CH_3CN}$	$r_{\rm solv}$	$V^a_{\rm vdw}$	$r^a_{\rm vdw}$	$V^b_{\rm vdw}$	$r^b_{\rm vdw}$
$SeCN^-$	0.0754	1.38	2.76	67.4	2.52	53.1	2.33
SCN^-	0.0894	1.39	2.73	61.8	2.45	42.3	2.16
$C(CN)_3^-$	0.0038	1.16	3.29	98.4	2.86	78.8	2.66
$N(CN)_2^-$	0.0060	1.26	3.01	70.7	2.57	56	2.37
DMA	0.1226	1.05	3.61	148.8	3.29	127.7	3.12
DMPT	0.1476	1.02	3.72	167.0	3.42	145.1	3.26
TCNA	0.0328	0.82	4.64	279.1	4.05	242.8	3.87
TrCNA	0.0347	0.84	4.52	260.6	3.96	223.7	3.77
DCNA	0.0334	0.86	4.41	236.7	3.84	204.6	3.66
CNA	0.0343	0.89	4.28	215.5	3.72	185.5	3.54
CNMeA	0.0351	0.88	4.34	238.8	3.85	202.9	3.65
C_4DMAP^+	0.0917	1.00	3.81	213.4	3.71		
C_8DMAP^+	-	0.99	3.84	299.4	4.15		
$C_{10}DMAP^+$	-	0.99	3.84	331.3	4.29		
$Im^+_{2,1}$				128.0	3.13	116.5	3.03
NTf_2^-				175.2	3.47	158.7	3.36
$P^+_{14,6,6,6}$				653.6	5.38	575.9	5.16

[a] van der Waals volumes and radii from electron densities; [b] van der Waals volumes and radii calculated using the volume increment method. [12]

estimates, D_{fit}/D_{est} and r_0/r_{vdw}, where D_{est} is the best estimate of D (as in Table 4.3) and r_{vdw} is the contact F-Q distance assuming spherical reactants having radii determined by their van der Waals volumes (Table 4.4). For reaction in CH_3CN these ratios are $D_{fit}/D_{est} = 1.2 \pm 0.4$ (1.3 ± 0.4) and $r_0/r_{vdw} = 1.1 \pm 0.4$ (1.5 ± 0.3) using the Smoluchowski (or Collins-Kimball) models. For the Smoluchowski model there is also a reasonable correlation between r_0 and the estimated driving force for reaction, $-\Delta G_0$. In the Collins-Kimball model no such correlation exists between these two parameters; instead there is a good correlation between $\ln(\kappa_0)$ and $-\Delta G_0$ ($R^2 = 0.72$).

In the ionic liquid solvents, where diffusion is much slower, the situation is quite different. As shown in Fig. 4.8 , cases in which $K_q^{obs}(t)$ is significantly nonlinear are poorly reproduced by the Smoluchowski/Collins-Kimball models (average values of $\rho >$ 40). In all cases, in order to achieve the substantial nonlinearities in $K_q(t)$ demanded by the data, the Smoluchowski and Collins-Kimball models require unphysical values of the diffusion coefficient and reaction radius: average values of $D_{fit}/D_{est} < 0.02$ and $r_0/r_{vdw} > 3$ (Table 4.5). As illustrated with the TCNA/$SeCN^-$ case in Fig. 4.8, when either D or r_0 are constrained to more reasonable values, the Smoluchowski and Collins-Kimball models do not resemble the experimental data. At least in the ionic

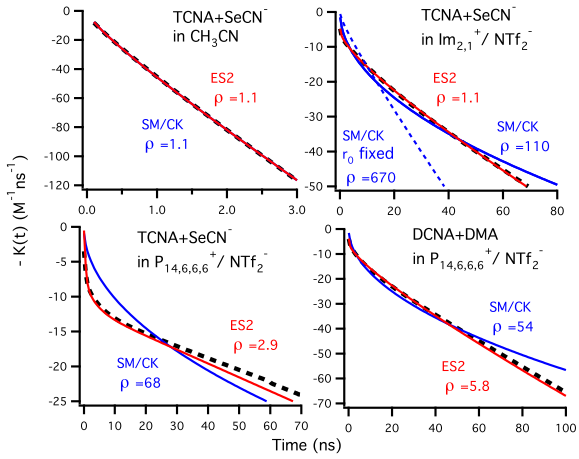

Figure 4.8: Representative quenching kernels $K_q(t)$ from experiments (black dashed lines) as well as from fits to the SM/CK (blue) and ES2 (red) models. ρ is a measure of fit quality defined in the method section. A value $\rho = 1$ indicates the best possible fit of a given data set.

liquid solvents, these results suggest that reaction at more than a single contact distance is required to properly interpret the quenching data.

4.3.2 B. The Extended Sink Models:

To explore whether allowing a constant reaction rate over some finite distance would provide better fits to the ionic liquid data, we developed the *extended sink* models shown in Scheme 4.6. Part of the motivation for these models is the fact that contact between the non-spherical F-Q pairs studied here occurs over a range of center-of-mass (COM) distances, as will be seen in the following section. In this sense, the rate constant κ_0 in the extended reaction zone can be interpreted as the reaction rate averaged over the different directions of approach and angles of the F-Q pair within the first solvation shell. In the ES1 model, $\kappa(r)$ is only nonzero within the region $[r_0, r_1]$. The value of r_0 is fixed at 3.0 Å to represent the closest center-of-mass separations found in simulation and r_1 is used as a fitting parameter, which is expected to approximate the largest COM separation still within the first solvation shell (8–9 Å). In the ES2 model, reaction is also allowed to occur beyond r_1, with a rate that decays exponentially with distance,

$$\kappa(r) = \begin{cases} 0 & r < r_0 \\ \kappa_0 & r_0 \leq r < r_1 \\ \kappa_0 \exp\left(-\beta(r - r_1)\right) & r \geq r_1 \end{cases} \tag{4.7}$$

The decaying tail of $\kappa(r)$ in the ES2 model can be viewed as representing reaction outside of the first solvation shell, which might be expected to be of importance for the electron transfer reactions studied here.

The extended sink models are solved using the approximation of Dudko and Szabo, [11] which allows for inclusion of solvation structure via $g(r)$ in Eq. 4.3. For the fits described below we assumed no solvation structure beyond volume exclusion at $r < r_0$, which was achieved using an approximate step function, $g(r) = 1/2[1+\tanh\{\alpha(r-r_0)\}]$, with $\alpha = 30$ Å^{-1}. We also examined models in which the value of $g(r)$ in the first solvation shell was allowed to differ from unity, but this additional flexibility did not improve the fits obtained.

Three to four parameters are adjustable in the extended sink models, the diffusion coefficient D, the rate constant within the first solvation shell κ_0, the extent of the first solvation shell r_1, and in the ES2 model the decay constant beyond first solvation shell, β. However, the latter value was fixed at 1.5 Å^{-1} to represent a typical value of the decay constant for electronic coupling in solvents. [60]

Table 4.5: Summary of the performance of all diffusion-reaction models.

Model	Optimized Params		CH_3CN	$Im^+_{2,1}$ / NTf^-_2	$P^+_{14,6,6,6}$ / NTf^-_2
Smoluchowski(SM)	D, r_0	$\langle\rho\rangle(\rho_{max})$	1.6(3.4)	48	71
		$< D_{\rm fit}/D_{\rm est} >$	0.9±0.3	0.015	0.0010
		$< r_0/r_{\rm vdw} >$	1.1±0.3	4	14
Collins-Kimball(CK)	D, r_0, κ_0	$\langle\rho\rangle(\rho_{max})$	1.4(2.3)	49	71
		$< D_{\rm fit}/D_{\rm est} >$	0.8±0.3	0.2	0.0014
		$< r_0/r_{\rm vdw} >$	1.5±0.3	4	17
Extended sink(ES1)	D, r_1, κ_0	$\langle\rho\rangle(\rho_{max})$	1.8(5.2)	2.1(6.0)	7.9(49)
		$< D_{\rm fit}/D_{\rm est} >$	1.1±0.4	0.9±0.2	1.2±0.4
		$< r_1/r_{\rm vdw} >$	1.7±0.3	1.6±0.2	1.9±0.2
Extended sink(ES2) ($\beta = 1.5$)	D, r_1, κ_0	$\langle\rho\rangle(\rho_{max})$	1.3(3.7)	1.3(2.0)	3.0(5.8)
		$< D_{\rm fit}/D_{\rm est} >$	1.0±0.2	1.0±0.2	1.1±0.3
		$< r_1/r_{\rm vdw} >$	1.5±0.5	1.4±0.3	1.8±0.2
Classical Marcus(CM)	$D, \Delta G_0$	$\langle\rho\rangle(\rho_{max})$	3.1(20)	2.1(12)	9.1(62)
		$< D_{\rm fit}/D_{\rm est} >$	1.1±0.2	1.0±0.2	1.2±0.3

ρ is a measure of fit quality defined in the method section. A value $\rho = 1$ indicates the best possible fit of a given data set. $\langle X\rangle \pm y$ indicates the average of X over all F-Q pairs in a particular solvent and its standard deviation y. Values of ρ in parentheses indicate the maximum value of ρ (ρ_{max}).

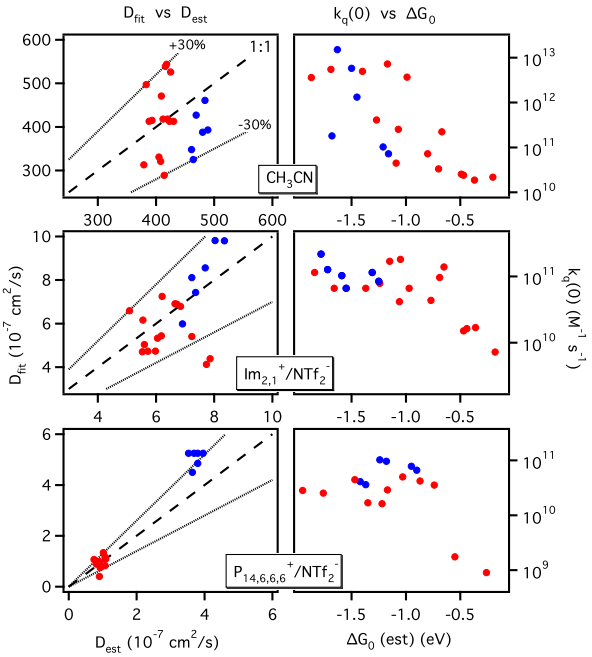

Figure 4.9: Parameters obtained from ES2 model fits. Left: Diffusivities from fits (D_{fit}) *vs.* D_{est} from measurements or estimates, Right: Initial rate constants $k_q(0)$ *vs.* reaction free energy ΔG_0. Red points are anionic and blue points neutral quenchers.

Average results obtained with these two models are summarized in Table 4.5 and representative fits are shown in Fig. 4.8. As illustrated in Fig. 4.8, the ES2 model, as

well as ES1 (not shown) are both able to reproduce the type of nonlinear $K_q(t)$ functions observed in the ionic liquid solvents. The substantial improvement over the SM and CK models suggests that it is critical to include reaction over an extended region rather than only within a thin shell around the solute. As can be seen by the differences in $\langle\rho\rangle$ values of the ES1 and ES2 fits, allowing this region to extend beyond the first solvation shell improves the agreement with experiment significantly; however, also allowing β to vary does not afford further improvement. Even the ES1 model is a vast improvement over the SM and CK models. Both models are markedly better at reproducing the quenching data, and in the case of the CH_3CN and $Im^+_{2,1}$ / NTf_2^- solvents, they do so to nearly within the accuracy expected of these experiments. The fits are not quite as accurate for reaction in $P^+_{14,6,6,6}$ / NTf_2^-, as indicated by the value $\langle\rho\rangle$=3, but, as illustrated in Fig. 4.8, even the poorest ES2 fit (DCNA + DMA) captures the essential features of $K_q(t)$. What is not well represented is the behavior at earliest times (t<300 ps, see Fig. 4.12).

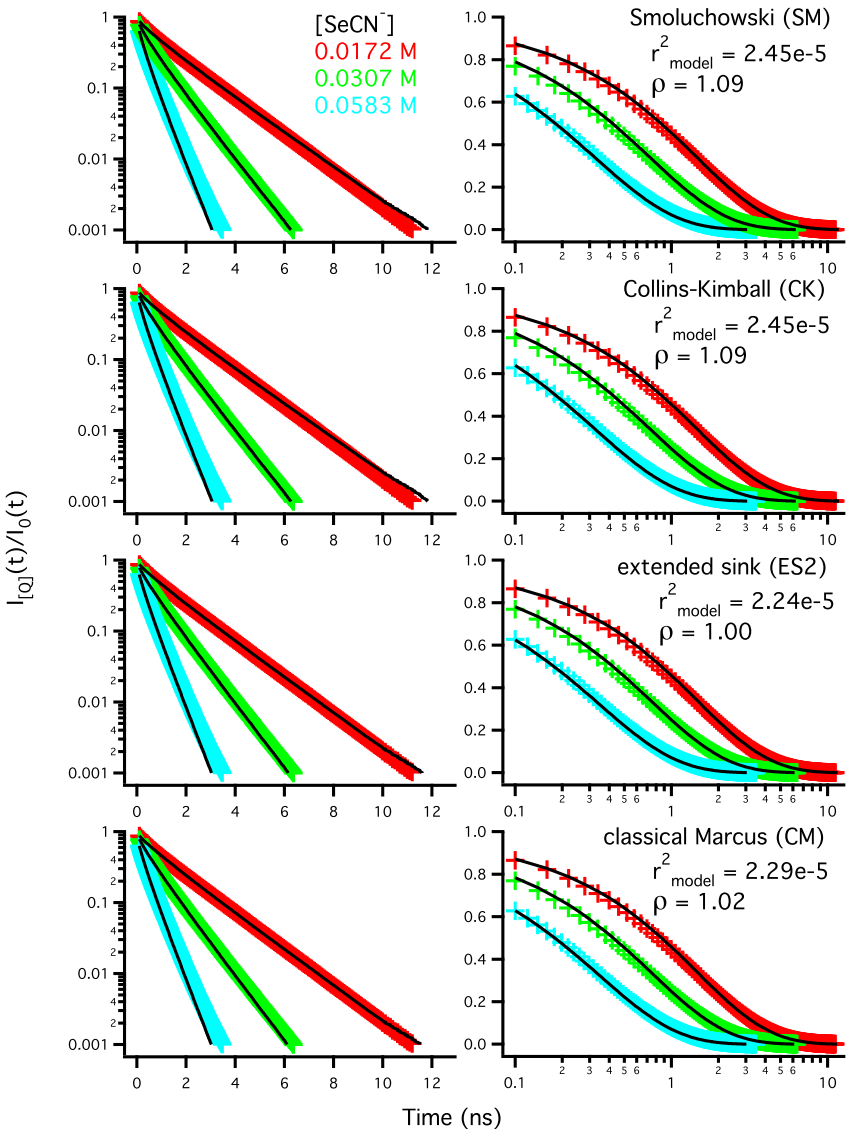

Figure 4.10: The diffusion-reaction fits for the system TCNA+$SeCN^-$ in CH_3CN.

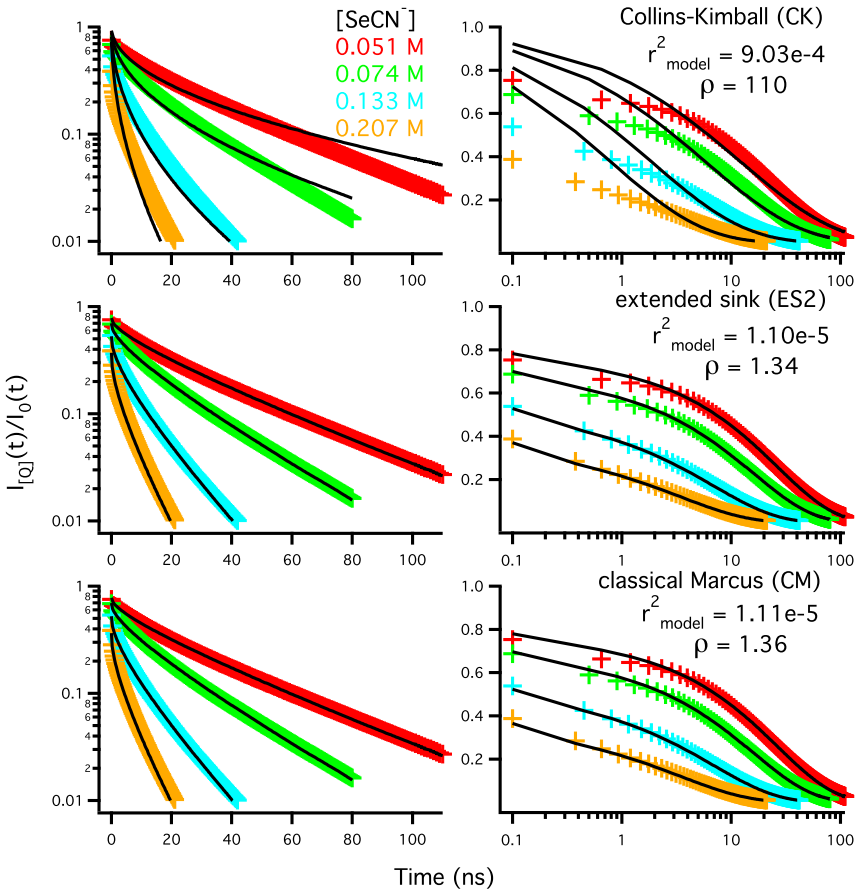

Figure 4.11: The diffusion-reaction fits for the system TCNA+$SeCN^-$ in $Im^+_{2,1}$ / NTf^-_2.

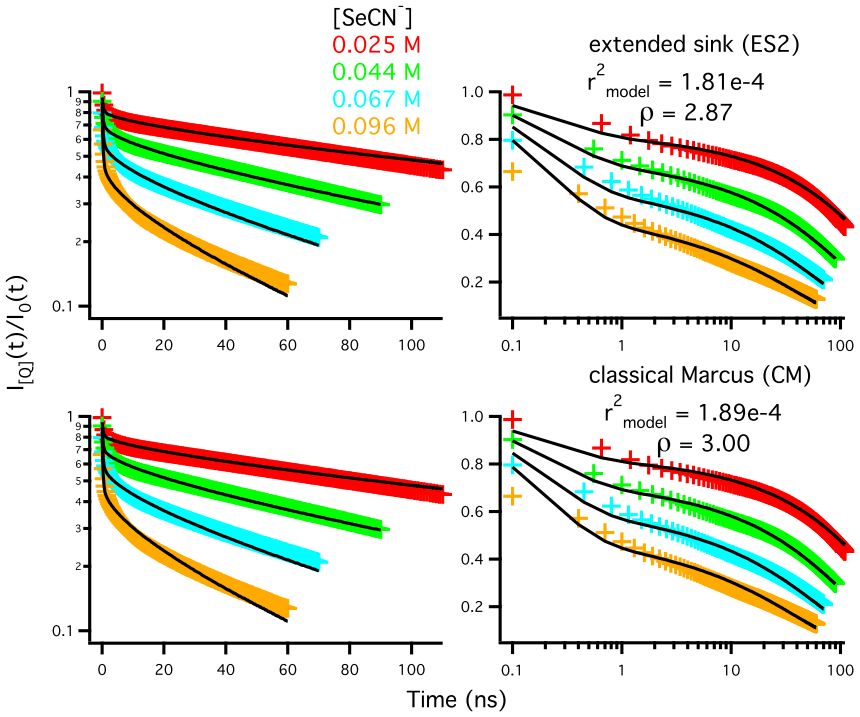

Figure 4.12: The diffusion-reaction fits for the system TCNA+$SeCN^-$ in $P^+_{14,6,6,6}$ / NTf_2^-.

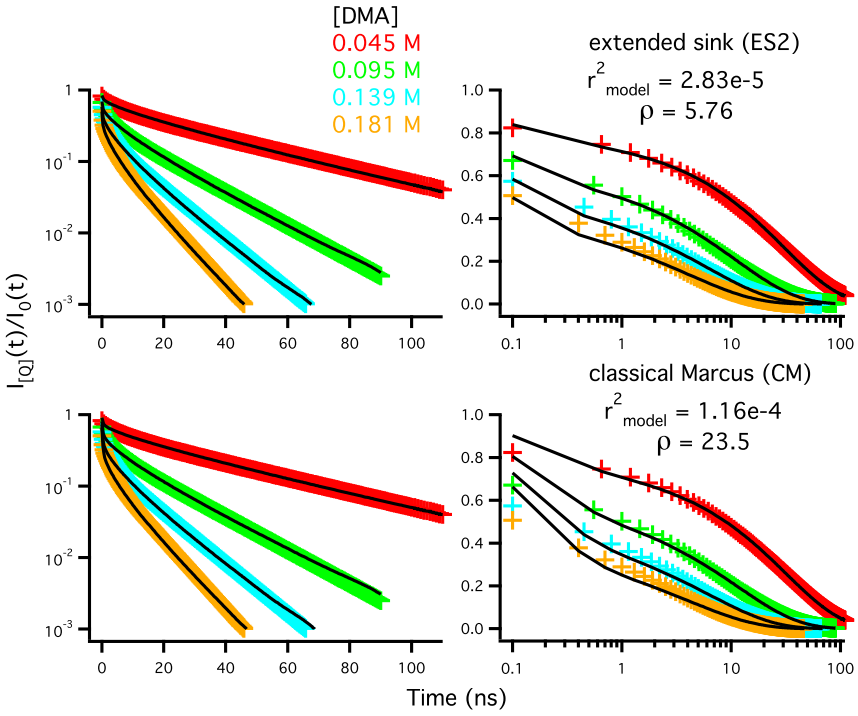

Figure 4.13: The diffusion-reaction fits for the system TCNA+DMA in $P^+_{14,6,6,6}$ / NTf_2^-.

In contrast to the fits obtained with the SM and CK models, the model parameters extracted from the extended sink models are all physically reasonable. As shown in Table 4.5, the optimized values of D and r_1 are on average close to expected values. The average value of $r_1/r_{\rm vdw}$ is ∼1.6 rather than 1.0; however, the MD simulations in the following section indicate the extent of the first solvation shell of these fluorophores is ∼9 Å, which is close to $1.6\,r_{\rm vdw}$. Table 4.5 also shows that although the ES2 fits are superior, the ES1 fits provide very similar values for these parameters, and for κ_0.

Fig. 4.9 shows two characteristics of the ES2 fits for all systems studied. In the left panels, the net diffusion coefficients obtained from fits to the quenching data are plotted *vs.* estimated values. With few exceptions, the values of $D_{\rm fit}$ are within ±30% of $D_{\rm est}$. Given the uncertainties associated with most of the estimated values, this level of agreement is acceptable. The marked difference in diffusion rates expected for charged (red) *vs.* neutral (blue) quenchers in the $P^+_{14,6,6,6}$ / NTf_2^- ionic liquid (Table 4.3) is reasonably captured by the fits to the quenching data. However, in three of

the fluorophore + neutral quencher pairs in the $P^+_{14,6,6,6}$ / NTf_2^- solvent $D_{\rm fit} > 1.4 D_{\rm est}$. Given that the $D_{\rm est}$ are based on measured values of the diffusion coefficients in the case of the neutral quenchers, this deviation is probably due to more than inaccuracies in $D_{\rm est}$. Nevertheless, the overall quality of the fits obtained with the ES2 model (and even the ES1 model), as well as the reasonableness of the parameters derived from them, indicate that these simple extensions of the SM and CK models are valid descriptions of the quenching process in these systems.

The right-hand panels of Fig. 4.9 show the initial rate constants,

$$k_q(0) = 4\pi \int_0^\infty \kappa(r) g(r) r^2 dr \tag{4.8}$$

plotted *vs.* the reaction free energies, ΔG_0. The correlations between $k_q(0)$ and ΔG_0 are much stronger than between κ_0 and ΔG_0, because the contribution from the first shell $k_{q1}(0) = \frac{4}{3}\pi\kappa_0(r_1^3 - r_0^3)$, dominates $k_q(0)$, and the product $\kappa_0 r_1^3$ largely eliminates the effect anti-correlation with r_1 has on κ_0, at least in the ionic liquid solvents. (In CH_3CN κ_0 and $k_q(0)$ behave similarly.) Like κ_0, these initial rate constants should reflect the intrinsic rate of electron transfer between proximate F-Q pairs, i.e. after the limitations of diffusion are removed. Nevertheless, like the earlier Rehm-Weller plots of k_q, there is no indication of a turnover with increasing driving force in these systems.

4.4 Simulations of Fluorophore-Quencher Radial Distributions and Electronic Coupling

Although the extended sink model provides a good representation of the quenching data with only 3 adjustable parameters, a more physical interpretation requires a more explicit treatment of the reaction. For this purpose we will use a description based on the Marcus electron transfer theory [35, 66] in the following section. However, such a description requires many more parameters than can be determined from the experimental data alone. In this section, we use a combination of classical MD simulations and electronic structure calculations in order to estimate some of these parameters and thereby constrain our fitting to optimizing only a small number of parameters.

4.4.1 Solvation Structure and Preferential Solvation

We first consider the solvation structure and possible models for the equilibrium F-Q distribution, $g(r)$. Different groups have previously employed various approximations for this structure when analyzing quenching data, for example using hard-sphere estimates for the neat solvent [56, 58] or for the solute-solvent distribution functions [1, 30, 44–46], or functions based on Lennard-Jones potentials of mean force.[33, 61] Here we use MD simulations to explore the distributions likely to exist in the experimental systems. Although the experiments consist of dilute (< 0.3 M) solutions of quenchers in nonreactive ionic liquids and in CH_3CN, at such dilutions, sampling F-Q distributions in unbiased simulations is highly inefficient, especially in the ionic liquid solvents. To gain at least some appreciation for the solvation structure likely to be present, we approximated the experimental situation using simulations of fluorophores in neat quencher solvents DMA, DMPT, and in $Im^+_{2,1}/Q^-$ in the case of the anion quenchers Q^-. We also simulated all quenchers in CH_3CN solutions but at quencher concentrations $\sim$10-fold higher than experiment.

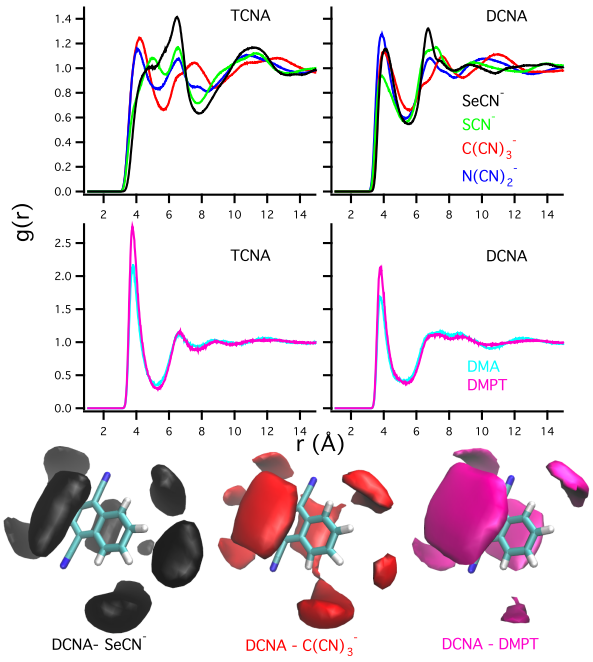

Figure 4.14: The center of mass radial distribution functions between TCNA and DCNA and the six quenchers, and the spatial distribution of $SeCN^-$, $C(CN)_3^-$ and DMPT around DCNA, from simulations in solutions of pure quencher, e.g., $Im_{2,1}^+$ / $SeCN^-$ or DMPT.

The simulations in the neat quencher solvents consisted of a single fluorophore, either TCNA or DCNA, in several hundred neutral solvent molecules or ion pairs. Fig. 4.14 shows all of the center-of-mass (COM) radial distribution functions (RDFs) of these two fluorophores in the six quencher solvents, together with 3d spatial distribution functions in select systems.

In the case of the anionic quenchers, all RDFs show two comparable maxima near 4 Å and 7 Å, corresponding to facial and peripheral approaches, respectively. $C(CN)_3^-$ and $N(CN)_2^-$ favor facial approach more than do $SeCN^-$ or SCN^-. In contrast, for the neutral aromatic quenchers, cofacial approach is preferred. Table 4.6 shows coordination numbers (C. N.) obtained by integrating the RDFs between 0 and two COM distances, $r_f \sim 5.5$ Å, to approximate the number of quencher molecules above and below the fluorophore plane (N_f), and $r_1 \sim 8$ Å, for the total number of first solvation shell

quenchers (N_1). As shown in Table 4.6, these calculations indicate 1.5–2 quencher molecules reside on the planar surfaces of the fluorophore and 7–9 quencher molecules occupy the first solvation shell.

We also attempted to estimate the preferential solvation of fluorophores by dilute quenchers in inert solvents, but adequate sampling required much higher quencher concentrations (∼1.7 M) than actually used in experiments. In CH_3CN, reasonable convergence was achieved in 200 ns simulations. From these RDFs, enhancement factors, f_f and f_1, defined as the relative regional/bulk concentrations of quenchers within distances r_f and r_1, were calculated. These values are also listed in Table 4.6. In CH_3CN both TCNA and DCNA show an enhanced presence of the neutral quenchers within the first solvation shell ($< f_1 > \approx 1.5$), whereas anionic quenchers are slightly underrepresented ($< f_1 > \approx 0.9$). This difference between neutral and anionic quenchers is amplified at the shorter distances representative of residence at facial locations.

4.4.2 Electronic Coupling

We estimated the electronic coupling elements between the excited fluorophores and quenchers, H_{DA}, using the effective 2-state Generalized Mulliken-Hush model. [6, 49] We first studied how the F-Q distance and orientation affect electronic coupling using the TCNA/$C(CN)_3^-$ pair (Fig. 4.15). After optimizing the geometries of the isolated molecules at the CAM-B3LYP/6-311+G(d,p) level, they were placed in a cofacial arrangement and H_{DA} calculated as the $C(CN)_3^-$ quencher was translated and rotated relative to the TCNA fluorophore. We started from the two geometries (A) and (B) shown in Fig. 4.15, and varied the separation between the molecular planes, while maintaining coplanarity. The results are shown in the top panels of Fig. 4.15. The electronic coupling decreases approximately exponentially with distance, with a decay constant $\beta \approx 3.5$ Å^{-1}. This value is close to those previously reported for other F-Q pairs in vacuum. [60] Note the >20-fold difference in the magnitude of H_{DA} between these two $C(CN)_3^-$ orientations. This angular dependence is further examined in Fig. 4.15(C), where the interplanar distance is fixed while the quencher is rotated.

The electronic coupling is also significantly dependent upon the particular location on the fluorophore the quencher approaches. This is shown in Fig. 4.16, where we plot H_{DA} between coplanar molecules as the center of $C(CN)_3^-$ in the (A) orientation is translated in the xy plane. (Note that the difference in rotational symmetries of these two molecules renders the H_{DA} surface less symmetrical than might initially be expected.) These representative calculations demonstrate that reaction models based only on COM separation oversimplify the actual electron transfer process in these systems.

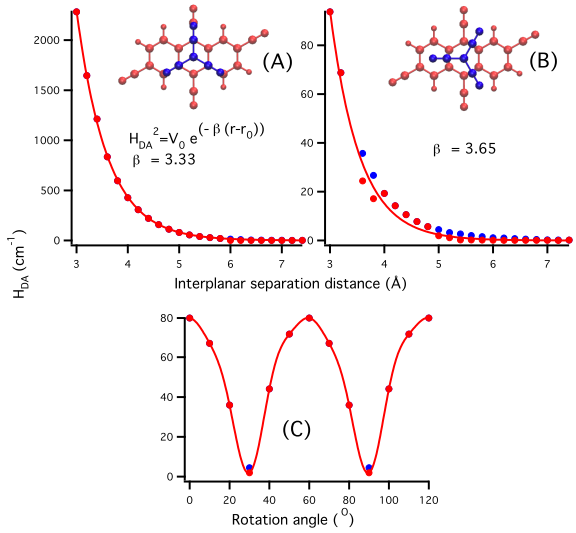

Figure 4.15: Variations of electronic coupling between TCNA and $C(CN)_3^-$. (A) and (B) illustrate the effect of separation in coplanar geometries and (C) the effect of in-plane rotation of $C(CN)_3^-$ with the distance between the TCNA ring plane and the plane of $C(CN)_3^-$ fixed at 5 Å. Red dots are values for electron transfer between the LE state and the CT state having the largest oscillator strength with the LE state. Blue dots indicate the electron transfer between the LE and the lowest CT states.

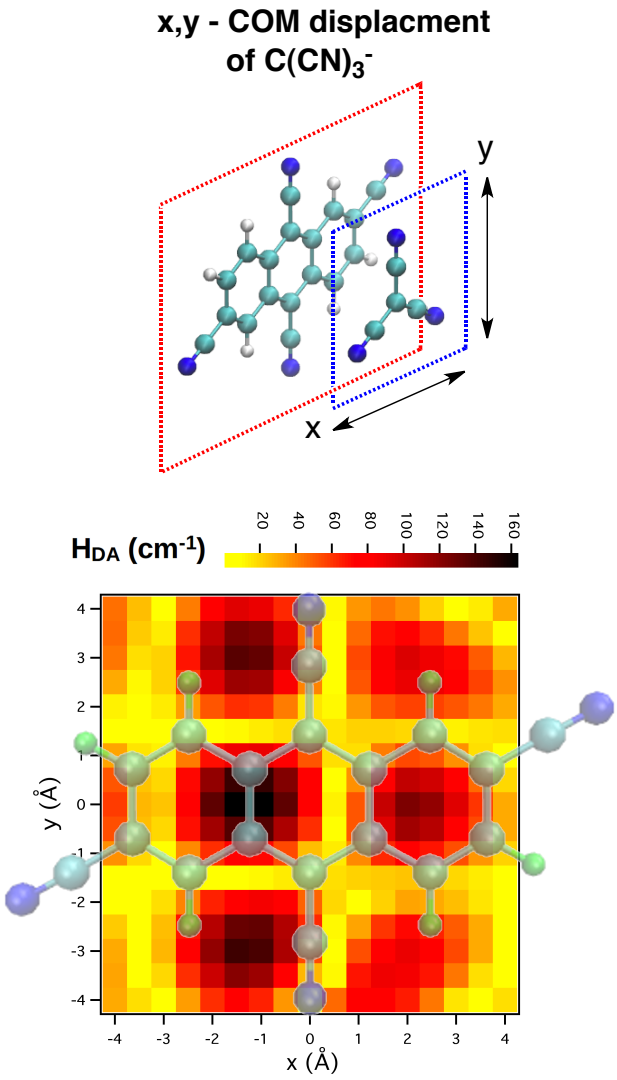

Figure 4.16: The effect of relative in-plane translations on the electronic coupling between TCNA and $C(CN)_3^-$. $C(CN)_3^-$ is translated relative to TCNA (in COM coordinates) while the interplanar separation remains fixed at 5 Å. The $C(CN)_3^-$ orientation and coordinate origin are those of (A) in Fig. 4.15.

We then studied the range of electronic couplings present in the neat quencher liquids by performing electronic coupling calculations between nearest-neighbor F-Q pairs sampled from MD trajectories. The F-Q pairs were selected when any atom in the quencher was within 3.3 Å of any fluorophore atom, excluding hydrogens. A total of 200–400 F-Q pairs were selected for these calculations in each system. Since we only

Table 4.6: Fluorophore coordination numbers in neat quencher liquids and quencher concentration enhancements in CH_3CN solutions.

fluorophore	quencher	Cutoff/ Å r_f	r_1	Quencher C.N. N_f	N_1	$Im^+_{2,1}$ C.N. N_f	N_1	Quencher Enhancement (in CH_3CN solution) f_f	f_1
TCNA	$SeCN^-$	5.6	7.9	2.0	7.2	1.0	6.7	0.87	0.94
TCNA	SCN^-	5.7	7.7	2.3	6.7	1.4	6.2	0.59	0.76
TCNA	$C(CN)_3^-$	5.6	8.8	1.7	8.1	0.6	8.6	1.34	1.07
TCNA	$N(CN)_2^-$	5.2	8.4	1.5	7.9	0.6	8.3	1.05	1.00
TCNA	DMA	5.2	7.7	1.8	7.2			2.23	1.54
TCNA	DMPT	5.3	7.8	1.9	6.8			2.60	1.66
DCNA	$SeCN^-$	5.5	8.3	1.6	8.3	1.0	8.6	0.33	0.76
DCNA	SCN^-	5.3	8.4	1.4	9.0	1.0	9.2	0.24	0.71
DCNA	$C(CN)_3^-$	5.5	8.8	1.5	8.2	0.9	8.9	0.75	1.01
DCNA	$N(CN)_2^-$	5.3	8.3	1.5	7.7	0.8	8.3	0.43	0.75
DCNA	DMA	5.2	8.0	1.5	8.5			1.59	1.42
DCNA	DMPT	5.4	8.0	1.7	7.4			1.78	1.45

r_f and r_1 define the regions approximating COM distances of facial and 1^{st} solvation shell contact about a given fluorophore. N_f and N_1 are the fluorophore-quencher (or counter ion) numbers in these regions from simulations of neat quencher liquids. f_f and f_1 are the enhancements, ratios of the concentrations of Q in these regions to the bulk [Q], measured in simulations of quenchers (Q^0 or $Im^+_{2,1}/Q^-$) in CH_3CN.

performed MD simulations of the TCNA and DCNA fluorophores, CNA and TRCNA couplings were calculated by replacing one CN group by an H atom from F-Q pairs extracted from the DCNA and TCNA trajectories, respectively.

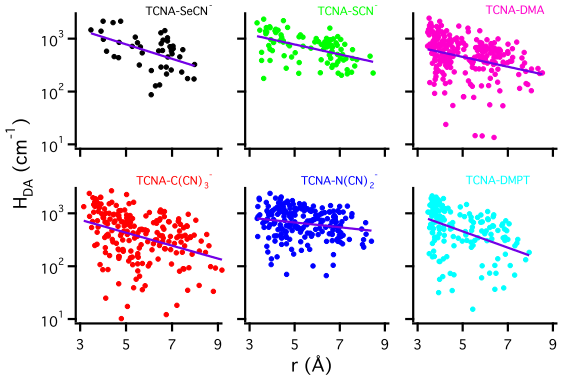

Figure 4.17: The electronic coupling between TCNA and the six quenchers as functions of center-of-mass separation within the first solvation shell sampled from simulations in neat quencher liquids.

The electronic couplings observed for all six quenchers within the first solvation shell of TCNA are plotted in Fig. 4.17. Although there is a great deal of scatter in these data, some correlation between H_{DA} and COM separation exists, which can be

Table 4.7: Summary of H_{DA} dependence on COM separation.

	$\ln H_{DA}(r) = \ln V_0 - \beta_1(r - r'_0)/2$							
	TCNA		TrCNA		DCNA		CNA	
	β_1	V_0	β_1	V_0	β_1	V_0	β_1	V_0
$SeCN^-$	0.63	1514	0.30	889	0.64	1237	0.71	1385
SCN^-	0.43	1225	0.34	951	0.44	938	0.64	1271
$C(CN)_3^-$	0.56	777	0.54	656	0.70	784	0.68	769
$N(CN)_2^-$	0.21	838	0.32	826	0.45	621	0.55	590
DMA	0.43	707	0.30	582	0.51	568		
DMPT	0.71	958	0.65	878	0.43	538		

V_0 in cm^{-1} and β_1 in $Å^{-1}$, $r'_0 = 2.9Å$.

represented by $\ln[H_{DA}(r)] = \ln(V_0) - \beta_1(r - r'_0)/2$ with $r'_0 = 2.9$ Å. Values of V_0 and β_1 for all F-Q pairs are summarized in Table 4.7. Such functions average over the dependencies on relative location and orientation illustrated in Figs. 4.15 and 4.16 to provide crude characterizations of $H_{DA}(r)$ suitable for use in the spherically symmetric reaction analysis discussed next. In most cases the distance dependence for randomly oriented first solvation shell pairs is much weaker, $\beta \sim 0.5$ $Å^{-1}$, compared to the values of $\sim$3.5 $Å^{-1}$ shown in Fig. 4.15 for fixed relative orientations. The values of H_{DA} displayed in Fig. 4.17 do not vary greatly among the different F/Q combinations and there is no obvious correlation between the values of H_{DA} and properties of the F-Q pairs. The root-mean-square values of H_{DA} in the first solvation shells of all of these pairs average 800 $\pm$ 100 cm^{-1}.

4.5 Diffusion-Reaction Analysis using Electron Transfer Models

Having obtained an appreciation for the solvation structure and electronic coupling in these systems, we now fit the quenching data using the spherical diffusion-reaction formalism coupled to a reaction model based on the classical Marcus electron transfer theory. The results in the previous section make it clear that any such modeling, which subsumes the strong angular dependence of the coupling into an average $\kappa(r)$ function, cannot be considered a complete description. As in prior work,[1, 16, 32, 33, 38, 61] we use this approach as the only tractable method for learning more about the electron transfer reactions in these systems, keeping in mind that the results obtained may be subject to multiple interpretations.

As in Ref. 61, we assume $\kappa(r)$ to be described using Equation 2.32. [43]

For modeling the effect of solvation structure, we initially tried the radial distribution functions from the simulations. However, because fits to the quenching data depended very little on the details of these functions, we adopted a simpler step-function representation of $g(r)$. In this approximation the population of the first solvation shell (as defined above) is allowed to differ from the bulk by an enhancement factor f_1:

$$g(r) = \frac{1}{2}\left[\,1 + f_1 \tanh\left(\alpha(r - r_0)\right) + (1 - f_1)\tanh\left(\alpha(r - r_1)\right)\right] \ . \tag{4.9}$$

where r_0 is the contact distance, which is set to 3.0 Å, and r_1 is the outer limit of the first solvation shell, ~8.2 Å. α is fixed to 30 Å^{-1}. For fitting CH_3CN data, we used the values of f_1 listed in Table 4.6, whereas for the ionic liquid data, we approximated these values using $f_1 = 1$ for the anionic and $f_1 = 1.5$ for neutral quenchers. There is little difference using $g(r)$ defined in Equation 4.9 and using $g(r)$ from MD simulations plotted in Fig. 4.14.

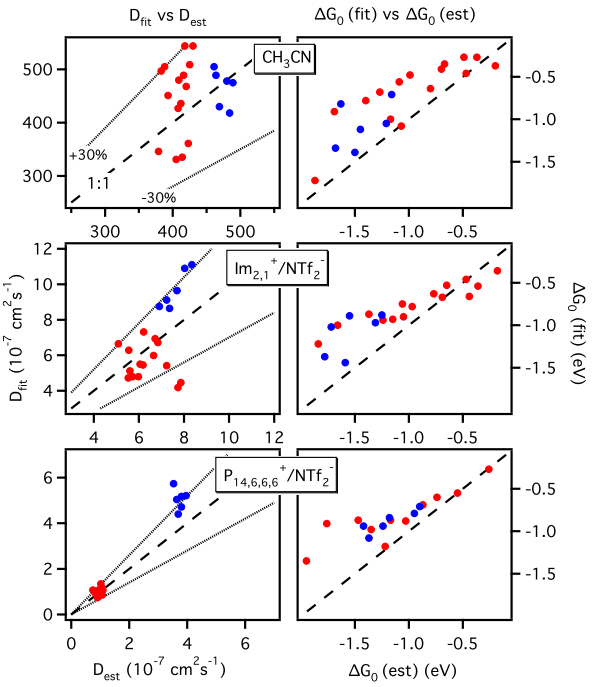

Figure 4.18: Comparison of D and ΔG_0 from fits and from measurements or estimates. Red points are anionic and blue points neutral quenchers.

With these choices, three parameters remain to be determined: the net diffusion coefficient D, the reaction free energy ΔG_0 (required for $\Delta G^*(r)$), and the effective solvation time τ_s. The solvation time was assumed to depend only on the solvent and was chosen by coarse manual optimization to be 0.5, 35, and 150 ps in CH_3CN, $Im^+_{2,1}$ / NTf_2^- and $P^+_{14,6,6,6}$ / NTf_2^-, respectively. These values may be compared to the (integral) solvation times $\langle\tau_s\rangle$ measured in these solvents using coumarin 153: 0.26 ps, 150 ps and 11 ns. [20, 22, 64] D and ΔG_0 were freely varied for each fluorophore/quencher/solvent data set using an automated least-squares minimization procedure.

The overall quality of the fits ($\langle\rho\rangle$) achieved using this classical Marcus model are summarized in Table 4.5. Not surprisingly, with one fewer fully adjustable parameter, the fits are not as good as with the ES2 model, although they are comparable to the ES1 fit results. (If one optimizes τ_s for each F-Q pair, the fit quality approaches that of ES2.) Fig. 4.18 compares the optimized values of the diffusion coefficients and reaction free energies with best estimates of these quantities. Comparison of Figs. 4.9 and 4.18 shows that the values D_{fit} obtained from the extended sink and classical Marcus models are quite similar. In CH_3CN, the average absolute difference is ∼12%, and in the ionic liquids, only a few values differ by more than 10%. Given that most of the systems studied are nearly diffusion-limited and thus closely constrained by the data, it is not surprising that different reaction models should agree in this fashion. As with the ES2 fits, with few exceptions (most notably the neutral quenchers in $P^+_{14,6,6,6}$ / NTf_2^-), the values of D_{fit} are within ±30% of best estimates.

The right-hand plots in Fig. 4.18 compare optimized versus estimated values of the free energy of reaction, ΔG_0. Before interpreting these comparisons, we digress to comment on the anticipated accuracy of the experimental estimates of ΔG_0. The ΔG_0(est) are based on electrochemical measurements of redox properties in multiple solvents rather than being measured for each fluorophore/quencher/solvent system. They are corrected for the different solvents using the dielectric continuum model described in the method section. We anticipate the ion and dipole solvating properties of CH_3CN, $Im^+_{2,1}/Q^-$, and $Im^+_{2,1}$ / NTf_2^- are all reasonably similar and estimates based on redox properties in mixed media to provide ΔG_0 values accurate to roughly 0.2 eV. $P^+_{14,6,6,6}$ /

NTf_2^- is less polar than these other solvents and here the estimates are likely to be less accurate. But errors are still expected to be less than ±0.3 eV.

Returning to Fig. 4.18, we observe that although the ΔG_0(fit) agree reasonably with ΔG_0(est) at larger values of ΔG_0 (smaller driving force), the optimized values are systematically higher for the smallest ΔG_0 (the largest driving forces). The deviation is most obvious in the ionic liquid solvents, because these fits are more narrowly constrained by the quenching data than are the CH_3CN fits. For ΔG_0(est) < -1 eV the deviation in the IL solvents is > 0.5 eV, well beyond the expected uncertainties in the estimates. These deviations represent failure of the classical Marcus model to adequately represent the quenching observed here. What is causing ΔG_0(fit) to be much larger than ΔG_0(est) can be understood based on the quantities characterizing electron transfer in these systems and their dependence on F-Q separation. Some of these quantities are summarized for all F-Q pairs in $Im_{2,1}^+$ / NTf_2^- in Table 4.8. Adequate fits to the quenching data require rapid reaction of F-Q pairs in contact ($r \leq r_1$), and this speed cannot be achieved with significant barriers (ΔG^*) to electron transfer. In the case of the more exergonic reactions (ΔG_0 (est) < -0.8 eV) when estimated values are used directly, it places reaction in the Marcus inverted regime at contact, which implies increasing barrier heights and slower reaction with increasing exergonicity, contrary to observation. When ΔG_0 is instead used as a fitting parameter, it takes on values such that throughout the first solvation shell nearly all F-Q pairs have barriers $\Delta G^* < 2k_BT$, as required to ensure fast reaction. Similar observations hold true in all three solvents. Thus, the systematic deviation in ΔG_0 is another manifestation of the lack of turnover already noted from the values of k_q themselves (Fig. 4.5) and from the $k_q(0)$ of the ES2 fits (Fig. 4.9).

The need to adjust barrier heights could simply be due to use of the classical Marcus model being inappropriate because most of the reactions at contact are estimated to fall within the inverted regime. Inclusion of quantized vibrational modes in this regime opens channels with lower activation energies and would have a similar effect to artificially increasing ΔG_0 as required to fit the data with the classical model. But the inner-sphere reorganization energies calculated here (Table 4.4) are all small, λ_{in} =

Table 4.8: Key electron transfer properties from CM model fits in $Im^{+}_{2,1}$ / NTf^{-}_{2} solution at selected distances. All energies are in units of RT at 298 K.

Fluorophore	Quencher	Distance	ΔG	λ	ΔG^{*}	H_{DA}	$g_{adiab.}$
TCNA	$SeCN^{-}$	r_0	47.32	44.1	0.06	7.03	1.92×10^{4}
		r_1	47.32	47.74	0	1.37	670
		r_∞	47.32	81.15	3.53	0	0
	SCN^{-}	r_0	36.57	44.9	0.39	5.75	1.26×10^{4}
		r_1	36.57	48.69	0.75	1.86	1.22×10^{3}
		r_∞	36.57	82.1	6.31	0	0
	$C(CN)^{-}_{3}$	r_0	36.19	38.34	0.03	3.62	5.88×10^{3}
		r_1	36.19	39.48	0.07	0.84	304
		r_∞	36.19	72.89	4.62	0	0
	$N(CN)^{-}_{2}$	r_0	20.77	41.05	2.51	3.97	6.60×10^{3}
		r_1	20.77	43.47	2.96	2.3	2.09×10^{3}
		r_∞	20.77	76.88	10.24	0	0
TrCNA	$SeCN^{-}$	r_0	39.07	44.35	0.16	4.19	6.81×10^{3}
		r_1	39.07	48.61	0.47	1.9	1.28×10^{3}
		r_∞	39.07	82.02	5.62	0	0
	SCN^{-}	r_0	29.24	45.14	1.4	4.48	7.64×10^{3}
		r_1	29.24	49.56	2.08	1.86	1.20×10^{3}
		r_∞	29.24	82.97	8.7	0	0
	$C(CN)^{-}_{3}$	r_0	30.39	38.67	0.44	3.06	4.16×10^{3}
		r_1	30.39	40.35	0.61	0.74	235
		r_∞	30.39	73.76	6.37	0	0
	$N(CN)^{-}_{2}$	r_0	18.02	41.34	3.29	3.9	6.31×10^{3}
		r_1	18.02	44.34	3.9	1.72	1.14×10^{3}
		r_∞	18.02	77.75	11.47	0	0
DCNA	$SeCN^{-}$	r_0	33.8	44.48	0.64	5.74	1.27×10^{4}
		r_1	33.8	49.32	1.22	1.1	421
		r_∞	33.8	82.73	7.23	0	0
	SCN^{-}	r_0	24.63	45.27	2.35	4.4	7.33×10^{3}
		r_1	24.63	50.27	3.27	1.4	665
		r_∞	24.63	83.68	10.42	0	0
	$C(CN)^{-}_{3}$	r_0	26.21	38.87	1.03	3.63	5.81×10^{3}
		r_1	26.21	41.06	1.34	0.59	147
		r_∞	26.21	74.47	7.82	0	0
	$N(CN)^{-}_{2}$	r_0	13.94	41.51	4.58	2.91	3.50×10^{3}
		r_1	13.94	45.05	5.37	0.91	316
		r_∞	13.94	78.46	13.26	0	0
CNA	$SeCN^{-}$	r_0	35.11	44.75	0.52	6.4	1.57×10^{4}
		r_1	35.11	50.31	1.15	1	340
		r_∞	35.11	83.72	7.06	0	0
	SCN^{-}	r_0	25.65	45.54	2.17	5.9	1.31×10^{4}
		r_1	25.65	51.26	3.2	1.11	415
		r_∞	25.65	84.67	10.29	0	0
	$C(CN)^{-}_{3}$	r_0	20.96	39.24	2.13	3.56	5.56×10^{3}
		r_1	20.96	42.05	2.64	0.61	151
		r_∞	20.96	75.46	9.84	0	0
TCNA	DMA	r_0	39.78	40.59	0	3.32	4.66×10^{3}
		r_1	39.66	40.59	0.01	1.09	503
		r_∞	39.6	73.8	3.96	0	0
	DMPT	r_0	53.61	40.87	0.99	4.43	8.25×10^{3}
		r_1	53.49	40.87	0.97	0.7	207
		r_∞	53.43	73.64	1.39	0	0
TrCNA	DMA	r_0	34.8	40.96	0.23	2.75	3.17×10^{3}
		r_1	34.68	41.25	0.26	1.24	644
		r_∞	34.61	74.66	5.37	0	0
	DMPT	r_0	56.16	41.26	1.35	4.07	6.91×10^{3}
		r_1	56.04	41.26	1.32	0.76	241
		r_∞	55.97	74.5	1.15	0	0
DCNA	DMA	r_0	34.37	41.21	0.28	2.65	2.93×10^{3}
		r_1	34.25	41.96	0.35	0.71	205
		r_∞	34.19	75.37	5.63	0	0
	DMPT	r_0	38.13	41.51	0.07	2.52	2.63×10^{3}
		r_1	38.01	41.8	0.09	0.83	284
		r_∞	37.94	75.21	4.62	0	0

0.04–0.18 eV, and not expected to cause a substantial change from the classical Marcus model. Nevertheless, we attempted to fit the quenching data with a single-mode semiclassical model, [17, 23] close to that used in a recent study of related fluorescence quenching by Rosspeintner et al.[44] Fits with this model also failed to provide better agreement with the experimental data unless values of ΔG_0 were again allowed to differ considerably from estimated values. Rather than discuss these fits, it is more instructive to consider how the semiclassical predictions for the dependence of quenching rate on driving force compare to the dependence observed. Following Rosspeintner et al., we use the initial quenching rates $k_q(0)$, defined by Eq. 4.8, in order to remove the effects of the diffusive approach of reactants from the overall rates. In what follows we use the $k_q(0)$ values extracted from the classical Marcus fits; however, similar $k_q(0)$ are obtained using the ES2 model fits, indicating that these quantities are not strongly model dependent.

In Fig. 4.19(a) we compare the dependence of $k_q(0)$ on ΔG_0 observed here in CH_3-CN to that reported by Rosspeintner et al.[44] These authors collected steady-state and both femtosecond and picosecond quenching data on 14 neutral F-Q pairs in CH_3-CN in a re-examination of the Rehm-Weller experiment.[41] Their data set included pairs for which ΔG_0 approached -2.5 eV, as well as three of the F-Q pairs examined here (TNCA, TrCNA, and DCNA + DMA). By fitting steady-state and 100 fs - 50 ns fluorescence decays (up to [Q] = 1 M) and solving the spherical reaction-diffusion equation numerically, they obtained initial quenching rates $k_q(0)$ quite similar to those determined with the classical Marcus fits here. Despite the substantial differences in quencher concentration, time-resolution, and analysis approach, for the three systems in common, the values of $k_q(0)$ agree to within an average of 14%. Moreover, as shown in Fig. 4.19(a), the general trends of $k_q(0)$ with driving force are also comparable.

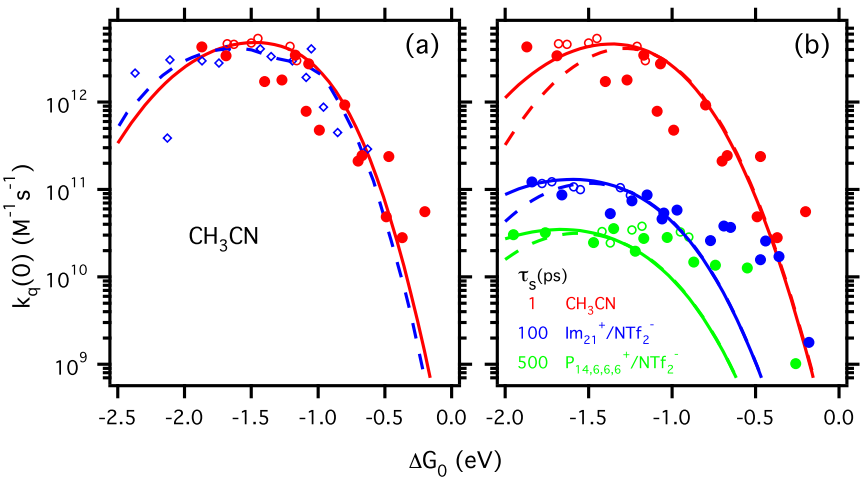

Figure 4.19: Initial quenching rate constants $k_q(0)$ versus (estimated) reaction free energies ΔG_0. (a) Comparison of $k_q(0)$ obtained from fits to the classical Marcus model here (red points and dashed curve) and from Rosspeintner et al.[44] (blue points and curve) (b) $k_q(0)$ determined from the classical Marcus fits in all three solvents (dots) and predictions of the semi-classical ET model (curves). In both panels open/filled symbols denote neutral/anionic quenchers.

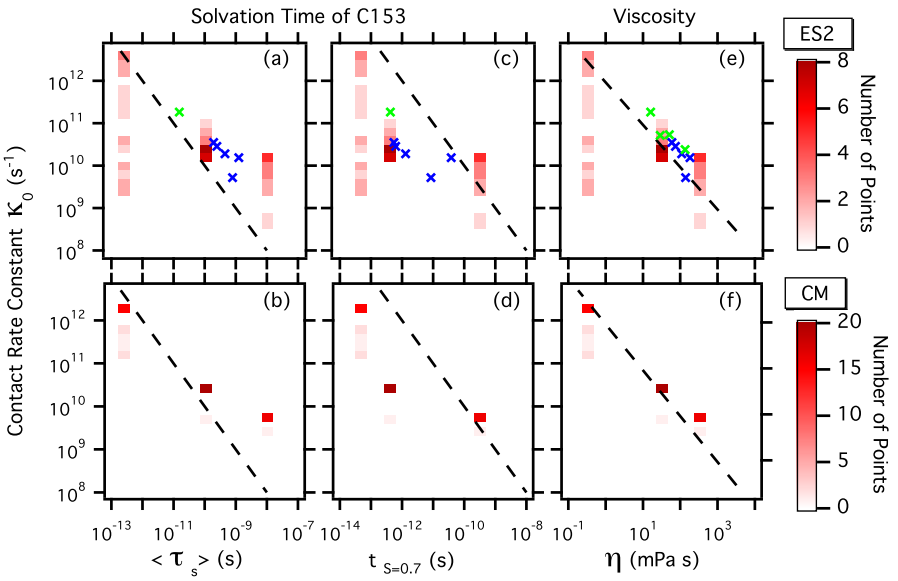

Figure 4.20: First solvation shell rate constants κ_0 (red squares) from the ES2 and CM models *vs.* solvation times [20, 22, 64] ($\langle\tau_s\rangle$ and $t_{S=0.7}$, see text) and solvent viscosity (η) [14, 33]. Additional data from Ref. 33 (DCNA+DMA in pyrrolidinium ILs (blue) and ethylene glycol + glycerol mixtures (green)) fit to the ES2 model are shown as crosses. The lines depict equality or proportionality to inverse solvation times and viscosities, as indicated.

The curves in Fig. 4.19(a) are predictions of the semiclassical equivalents of Eq. 2.32 using average electron transfer parameters. (See Section 2.3.6 in the Supporting Information for details.) Both curves do a reasonable job explaining the dependence of $k_q(0)$ on ΔG_0 in CH_3CN. However, this same approach fails in the ionic liquid solvents, as shown in Fig. 4.19(b). The pairs of curves in Fig. 4.19(b) are calculations using values of λ_{in} = 0.18 eV (solid), a value estimated for DMA and DMPT donors, and 0.08 eV (dashed), the average value from DFT calculations of all systems (Table 4.4). Both curves in (a) assume λ_{in} = 0.32 eV and solvent reorganization energies, $\lambda_{solv}(r)$, between 1 eV (r = r_0) -2 eV (r = ∞). In the Ref. 44 calculations assumed r_0 = 7 Å, V_0 = 720 cm^{-1}, β = 1.55 $Å^{-1}$, and τ_s = 0.26 ps, whereas the calculations here assume the 2-region description of $H_{DA}(r)$ used for the classical Marcus model with average values V_0 = 886 cm^{-1}, β_1 = 0.51 $Å^{-1}$, and τ_s = 1 ps. Curves in panel (b) are

calculated with the same parameters used in (a) except λ_{in} = 0.18 eV (solid curves) and 0.08 eV (dashed curves) and the values of τ_s indicated. The three values of τ_s indicated are chosen to provide agreement with the maximum values of $k_q(0)$ observed in each solvent. As illustrated by Fig. 4.19(b), the larger value of λ_{in} softens the rate decrease in the inverted regime. However, neither value (nor even an implausibly large value) provides a rate dependence that deviates substantially from the parabolic shape of classical Marcus theory over ΔG_0 range of most of the experimental data, justifying our use of the classical Marcus model. More importantly, no value of λ_{in} is able to reproduce the very weak dependence of $k_q(0)$ on ΔG_0 in the normal regime ($\Delta G_0 >$ -1 eV). In fact, our explorations of parameter space suggest it is impossible to account for the nearly constant values of $k_q(0)$ observed over such a large ΔG_0 range in the ionic liquids using the semiclassical theory with physically reasonable parameter values. Thus, the primary reason for being unable to fit these quenching data using estimated values of ΔG_0 is not the neglect of quantized vibrations in the classical Marcus model.

Several other causes of this lack of agreement seem plausible. First, at higher driving forces it is possible that reaction proceeds to products in excited electronic states, which would decrease ΔG^* relative to that calculated from ΔG_0(est). This explanation has been suggested in multiple studies previously, [27, 36, 40, 47, 53] and excited radical products have been observed recently in F-Q systems. [29]

Another possibility is that the effect of solvation dynamics on electron transfer cannot be properly described by the simplified treatment employed here. Solvation in ionic liquids is a broadly distributed process often having important contributions spanning the range 100 fs to >10 ns.[22, 64] This reality stands in stark contrast to the simple exponential relaxation assumed in deriving Eq. 2.32. It could be that a more sophisticated treatment, one able to account for such a distributed response, would be better able to capture the observed dependence of $k_q(0)$ on ΔG_0. Although several treatments of electron transfer accommodating more complex solvation dynamics exist, [4, 19, 21, 65] it is not clear how one would apply them over the range of conditions encountered in the bimolecular quenching problem, and we do not attempt to do so here.

A final possibility we consider is that the leveling of $k_q(0)$ exhibited in Fig. 4.19 is due to some limiting nuclear dynamics not directly tied to polar solvation. Given the marked sensitivity of H_{DA} to small changes in relative position and orientation of the fluorophore and quencher, small angular and/or translational motions of contact pairs ("in-cage" motions) might be rate limiting, rather than solvation dynamics as assumed in the theory. To examine this possibility further, we compare the values of the contact rate constants κ_0 extracted using the ES2 and classical Marcus models to solvation times and solvent viscosities in Fig. 4.20. These κ_0 values show similar, albeit more scattered, dependence on ΔG_0 compared to the bimolecular rate constants $k_q(0)$ in Fig. 4.19; they are preferred here because, being unimolecular, they may be directly compared to solvation times.

As illustrated in Fig. 4.20, the values of κ_0 are much more tightly constrained by the classical Marcus fits than by the ES2 fits. In both cases, the values in CH_3CN are much more varied than in the ionic liquid solvents. Nevertheless, the two fits show the same behavior, and the mean values of κ_0 found in the two models are nearly identical. Most importantly, both models clearly show that the 1st shell rates in CH_3CN are substantially larger than in $Im^+_{2,1}$ / NTf_2^-, which are in turn much larger than the rates in $P^+_{14,6,6,6}$ / NTf_2^-. The maximum rates in these three solvents exhibit approximately the same ratios as do the $k_q(0)$ in Fig. 4.19, and they reflect the same leveling effect observed there. The new point to be made from Fig. 4.20 is that these κ_0 values are better correlated to solvent viscosity than to solvation time.

In order to reflect the distributed character of solvation, we display two solvation times in Fig. 4.20, both obtained from measurements of coumarin 153.[20, 22, 64] Panels (a) and (b) show what is usually meant by solvation time, the integral of the normalized solvation response function $S(t)$, $\langle\tau_s\rangle$. This time emphasizes the longest portions of the solvent response. A number of treatments of dynamical effects on electron transfer point to the fastest portion of the response being most relevant, at least when significant barriers to reaction are present.[4, 13, 21, 52, 65] To represent the faster components of solvation, panels (c) and (d) show the times at which $S(t)$ has decreased to 0.7, i.e. the time for relaxation of the first 30% of the solvation energy. (Given the nature of

experimental $S(t)$ data, these $t_{S=0.7}$ are the most accurate experimental measures of the faster times of solvation.[64]).

The dashed lines in panels (a)-(d) indicate equality between κ_0 and inverse solvation time. Fig. 4.20 shows that the limiting rates at contact are nearly equal to $\langle \tau_s \rangle$ in CH_3-CN and $Im^+_{2,1}$ / NTf^-_2 but are roughly 100-fold larger in $P^+_{14,6,6,6}$ / NTf^-_2. Use of $t_{S=0.7}$ as a solvation measure shifts all data to shorter times and provides close agreement in $P^+_{14,6,6,6}$ / NTf^-_2 but also produces inverse solvation times much greater than κ_0 in the other two solvents. Neither measure of solvation time seems to scale in a manner inverse to the limiting rate constants in these three solvents. In contrast, the values of κ_0 correlate much better with inverse viscosity. To amplify this observation, we have reanalyzed data from our earlier study of DCNA quenching by DMA in multiple solvents [33] using the ES2 model, and these data are shown as the smaller symbols in the top panels of Fig. 4.20. (Only those data sets from Ref. 33 of sufficient quality to produce good fits to the ES2 model are included here.) Estimates of κ_0 both in a series of ionic liquids (blue) and in mixtures of ethylene glycol + glycerol (green) are also better correlated to viscosity than solvation times. Consistent with previous studies, [30, 33] the results do not reveal any distinction between the reaction kinetics in ionic liquids and highly viscous conventional solvents.

To consider the meaning of the viscosity correlation further, one can estimate the extent of the motions possible using simple hydrodynamic calculations.(These estimations assume a spherical solute of radius ∼2.9 Å, stick boundary conditions, and the relations $D_{rot} = k_B T/(6V\eta), D_{trans} = k_B T/6\pi R\eta, \Delta\theta(t) = \sqrt{4D_{rot}t}$, and $\Delta R(t) = \sqrt{6D_{trans}t}$.) Such calculations indicate a typical quencher undergoes angular displacements of ∼20° and translational displacements of ∼1 Å during a time κ_0^{-1}. While crude, these estimates, along with the data in Figs. 4.15 and 4.16, imply substantial modulation of H_{DA} occurs during these reaction times, making such motions a plausible limiting factor in the contact electron transfer rates. Thus, rather than the usual picture of solvent control due to solvent polarization (dielectric) dynamics, we propose instead that local reactant motions, controlled by mechanical (viscous) friction, may serve to limit electron transfer in high-viscosity environments such as ionic liquids.

4.6 Ionic Liquids with Electron Donating Cations as Quenchers

We also report parallel results for a new class of 1-alkyl-4-dimethylaminopyridinium (1-alkyl DMAP) electron-donating cations. The reductive quenching of cyano-substituted anthracene fluorophores by these cationic quenchers is studied in solutions of acetonitrile and the ionic liquid 1-ethyl-3-methylimidazolium bis(trifluoromethylsulfonyl)-imide. Varying the length of alkyl chain permits tuning of the quencher diffusivities in solution. The NTf_2^- anion was also used as the DMAP counterion. The molecular structures of fluorophores, quenchers and solvents are shown in Figure 4.21.

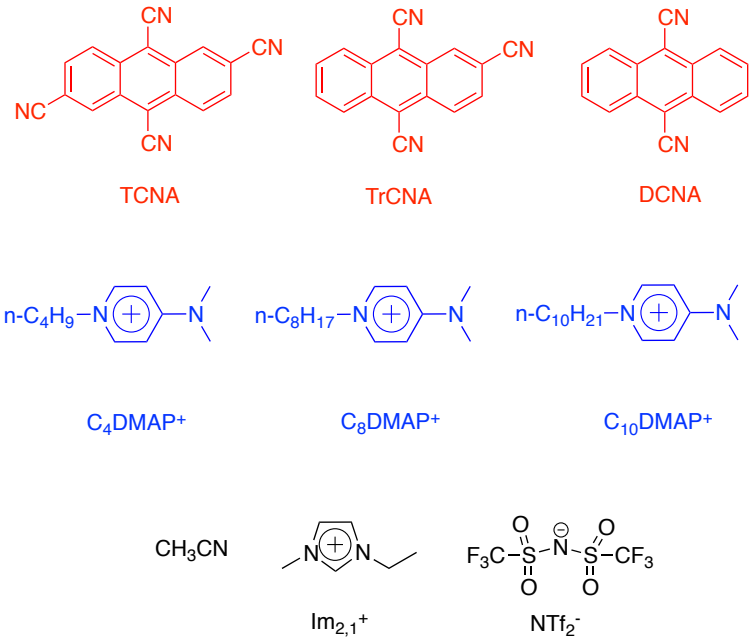

Figure 4.21: The fluorophores (electron acceptors), quenchers (electron donors) and solvents used in this work.

The steady-state quenching rates k_q are plotted in Figure 4.22. The quenching of same series of fluorophores by neutral and anion quenchers is plotted in the same graph. We find that the points by cation quenchers falls well on the scatter curves for anionic and neutral quenchers. Fig. 4.22 suggests that the same electron transfer mechanism underlies all of these quenching reactions.

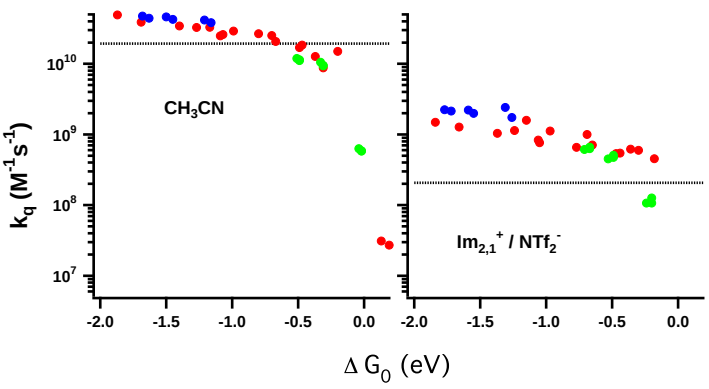

Figure 4.22: Plots of steady-state k_q versus ΔG_0 in CH_3CN (left) and ionic liquid $Im^+_{2,1}$ / NTf^-_2 (right). The neutral, anionic and cationic donors are represented using blue, red and green colors, respectively.

We applied our data sets to the extended sink model and the classical Marcus model. Good fits and physically reasonable output parameters are obtained. Both models fits all data well with a ρ value below 2.5.

The output parameters from fits to the extended sink model are shown in Figure 4.23 In the left panels, the net diffusion coefficients calculated from the model are compared to those from the measured DMAP cations and estimated fluorophores diffusivities, also described in the Supporting Information. We again plot the present data (green points) to gather with data on neutral (blue) and anionic (red) quenchers. The DMAP data shows a strong correlation between D_{fit} and D_{est} in the ionic liquid solvent (R^2=0.94). In CH_3CN, where the fits are not as well constrained by the data, the correlation is weaker, (R^2=0.73), Nevertheless, D_{fit} is within $\pm$30% of D_{est} in nearly all cases.

In the right panel of Fig. 4.23, we plot the initial reaction rate $k_q(0)$ versus the reaction free energy ΔG_0. The new data for the cationic DMAP quenchers exhibit the same overall trend of $k_q(0)$ with ΔG_0 previously established by the anionc and neutral quenching data. (The broad scatter of the CH_3CN data previously reflect the fact that κ_0 is poorly constrained by the data.) Similar to the Stern-Volmer analysis, the more detailed analysis using the extended sink model suggests a common quenching mechanism largely unaffected by quencher charge.

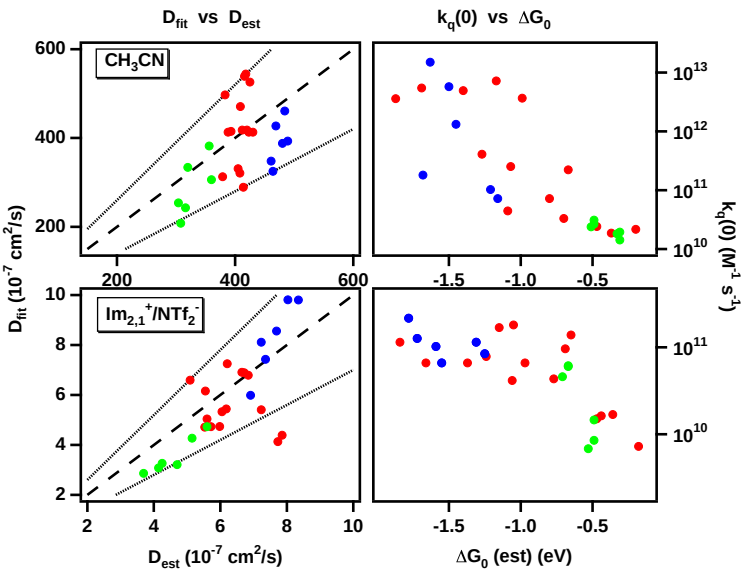

Figure 4.23: Results from the extended sink model. Left: D_{fit}, diffusion coefficients from fits *vs.* D_{est}, diffusivities from measurements or best estimates. The dashed lines indicate and 1:1 and ±30% ; Right: $k(0)$ *vs.* ΔG_0(est) for cationic (green), anionic (red) and neutral (blue) quenchers. The data points for neutral and anionic quenchers are from Ref. 62.

This model also afforded good quality fits to the DMAP fluorescence quenching data. The two parameters fit to classical Marcus model are shown in Fig. 4.24. The left panels compares D_{fit} to D_{est}, as done in Fig. 4.23 for the ES model. In all the cases, the values of D_{fit} obtained from fits to the ES and CM models are nearly the same and need no further comment. In the right panels, the fitted reaction free energy ΔG_0(fit) is plotted versus the estimated free energy ΔG_0(est). For these cationic donors, ΔG_0(fit) values are very close to ΔG_0(est) values. Since the reaction free energies are only weakly negative, the DMAP quenching reactions all fall in the normal Marcus region.

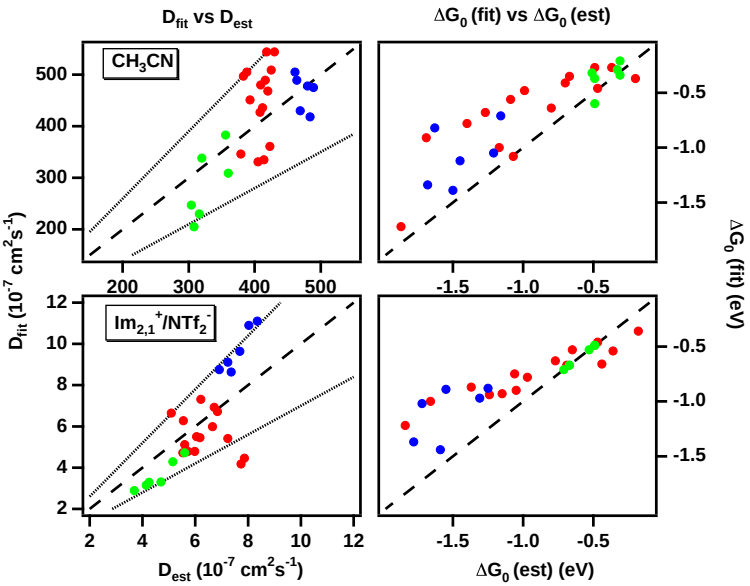

Figure 4.24: Results from analysis using the classical Marcus model. Left: D_{fit}, diffusion coefficients from fits *vs.* D_{est}, diffusivities from measurements or best estimates; right: $\Delta G_0(\text{fit})$ *vs.* $\Delta G_0(\text{est})$ for cationic (green), anionic (red) and neutral (blue) quenchers.

Bibliography

[1] G. Angulo, D. R. Kattnig, A. Rosspeintner, G. Grampp, and E. Vauthey. On the Coherent Description of Diffusion-Influenced Fluorescence Quenching Experiments II: Early Events. *Chem.–Eur. J.*, 16:2291–2299, 2010.

[2] G. Angulo, A. Rosspeintner, M. Koch, and E. Vauthey. Comment on "observation of the marcus inverted region for bimolecular photoinduced electron-transfer reactions in viscous media". *J. Phys. Chem. B*, 120, 2016.

[3] M. J. Bausch, C. Cuadalupe-Fasano, and A. Koohang. Observation of a Linear Correlatlon between Dimethyl Sulfoxide Solution Reduction Potentlala and Equilibrium Acklties for Substituted Methylanthracenes. *J. Phys. Chem.*, 95:3420–3422, 1991.

[4] D. J. Bicout and A. Szabo. Electron transfer reaction dynamics in non-Debye solvents. *J. Chem. Phys.*, 109:2325–2338, 1998.

[5] A. I. Burshtein. Non-Markovian Theories of Transfer Reactions in Luminescence and Chemiluminescence and Photo- and Electrochemistry. *Adv. Chem. Phys*, 129:105–418, 2004.

[6] R. J. Cave and M. D. Newton. Generalization of the Mulliken-Hush treatment for the calculation of electron transfer matrix elements. *Chem. Phys. Lett.*, 249:15–19, 1996.

[7] F. C. Collins. Diffusion in chemical reaction processes and in the growth of colloid particles. *J. Colloid. Sci.*, 5:499–505, 1950.

[8] F. C. Collins and G. E. Kimball. Diffusion-controlled reaction rates. *J. Colloid Sci.*, 4:425–437, 1949.

[9] A. K. Das, T. Mondal, S. Sen Mojumdar, and K. Bhattacharyya. Marcus-like Inversion in Electron Transfer in Neat Ionic Liquid and Ionic Liquid-Mixed Micelles. *J. Phys. Chem. B*, 115(16):4680–4688, 2011.

[10] B. Dereka, M. Koch, and E. Vauthey. Looking at photoinduced charge transfer processes in the ir: Answers to several long-standing questions. *Acc. Chem. Res.*, 50:426–434, 2017.

[11] O. K. Dudko and A. Szabo. Time-Dependent Rate Coefficients for Diffusion-Influenced Reactions with Centrosymmetric Potentials. *J. Phys. Chem. B*, 109:5891–5894, 2005.

[12] J. T. Edward. Molecular Volumes and the Stokes-Einstein Equation. *J. Chem. Edu.*, 47:261, 1970.

[13] T. Fonseca. Outer-sphere electron transfer reactions in non-debye solvents. theory and numerical results. *J. Chem. Phys.*, 91:2869–2880, 1989.

[14] A. P. Froba, H. Kremer, and A. Leipertz. Density, Refractive Index, Interfacial Tension, and Viscosity of Ionic Liquids [EMIM][EtSO4], [EMIM][NTf2], [EMIM][N(CN)2], and [OMA][NTf2] in Dependence on Temperature at Atmospheric Pressure. *J. Phys. Chem. B*, 112:12420–12430, 2008.

[15] V. Gladkikh, A. I. Burshtein, G. Angulo, S. Pagès, B. Lang, and E. Vauthey. Kinetics and Yields of Electron Transfer in the Inverted Region. *J. Phys. Chem. A*, 108:6667–6678, 2004.

[16] V. S. Gladkikh, A. I. Burshtein, H. L. Tavernier, and M. D. Fayer. Influence of Diffusion on the Kinetics of DonorâĹŠAcceptor Electron Transfer Monitored by the Quenching of Donor Fluorescence. *J. Phys. Chem. A*, 106:6982–6990, 2002.

[17] I. R. Gould, D. Ege, J. E. Moser, and S. Farid. Efficiencies of photoinduced electron-transfer reactions: role of the Marcus inverted region in return electron transfer within geminate radical-ion pairs. *J. Am. Chem. Soc.*, 112:4290–4301, 1990.

[18] I. R. Gould, J. E. Moser, B. Armitage, S. Farid, J. L. Goodman, and M. S. Herman. Electron-transfer reactions in the Marcus inverted region. Charge recombination versus charge shift reactions. *J. Am. Chem. Soc.*, 111:1917–1919, 1989.

[19] H. Heitele. Dynamic Solvent Effects on Electron-Transfer Reactions. *Angew. Chem. Int. Ed.*, 32:359–377, 1993.

[20] M. L. Horng, J. A. Gardecki, A. Papazyan, and M. Maroncelli. Subpicosecond Measurements of Polar Solvation Dynamics: Coumarin 153 Revisited. *J. Phys. Chem.*, 99:17311–17337, 1995.

[21] J. T. Hynes. Outer-sphere electron-transfer reactions and frequency-dependent friction. *J. Phys. Chem.*, 90(16):3701–3706, 1986.

[22] H. Jin, G. A. Baker, S. Arzhantsev, J. Dong, and M. Maroncelli. Solvation and rotational dynamics of coumarin 153 in ionic liquids: comparisons to conventional solvents. *J Phys Chem B.*, 111:7291–7302, 2007.

[23] J. Jortner and M. Bixon. Intramolecular vibrational excitations accompanying solvent-controlled electron transfer reactionsn. *J. Chem. Phys.*, 88:167–170, 1988.

[24] N. Joshi, M. L. Johnson, I. Gryczynski, and J. R. Lakowicz. Radiation boundary conditions in collisional quenching of fluorescence; determination by frequency-domain fluorometry. *Chem. Phys. Lett.*, 135:200–207, 1987.

[25] A. Kaintz, G. Baker, A. Benesi, and M. Maroncelli. Solute Diffusion in Ionic Liquids, NMR Measurements and Comparisons to Conventional Solvents. *J. Phys. Chem. B*, 117:11697–11708, 2013.

[26] R. S. Khnayzer, C. E. McCusker, B. S. Olaiya, and F. N. Castellano. Robust Cuprous Phenanthroline Sensitizer for Solar Hydrogen Photocatalysis. *J. Am. Chem. Soc.*, 135:14068–14070, 2013.

[27] K. Kikuchi, T. Katagiri, T. Niwa, Y. Takahashi, T. Suzuki, H. Ikeda, and T. Miyashi. Evidence for generation of electronically excited radical ion in very exothermic electron-transfer fluorescence quenching. *Chem. Phys. Lett.*, 193:155 – 160, 1992.

[28] K. Kikuchi, Y. Takahashi, M. Hoshi, T. Niwa, T. Katagiri, and T. Miyashi. Free enthalpy dependence of free-radical yield of photoinduced electron transfer in acetonitrile. *J. Phys. Chem.*, 95:2378–2381, 1991.

[29] M. Koch, A. Rosspeintner, K. Adamczyk, B. Lang, J. Dreyer, E. T. J. Nibbering, and E. Vauthey. Real-Time Observation of the Formation of Excited Radical Ions in Bimolecular Photoinduced Charge Separation: Absence of the Marcus Inverted Region Explained. *J. Am. Chem. Soc.*, 134:9843–9848, 2013.

[30] M. Koch, A. Rosspeintner, G. Angulo, and E. Vauthey. Bimolecular Photoinduced Electron Transfer in Imidazolium-Based Room-Temperature Ionic Liquids Is Not Faster than in Conventional Solvents. *J. Am. Chem. Soc.*, 134:3729–3736, 2012.

[31] M. Kumbhakar, A. Manna, M. Sayed, A. Kumar, and H. Pal. Observation of the Marcus Inverted Region for Bimolecular Photoinduced Electron-Transfer Reactions in Viscous Media. *J. Phys. Chem. B*, 118:10704–10715, 2014.

[32] T. Kumpulainen, B. Lang, A. Rosspeintner, and E. Vauthey. Ultrafast Elementary Photochemical Processes of Organic Molecules in Liquid Solution. *Chem. Rev.*, 117:10826–10939, 2017.

[33] M. Liang, A. Kaintz, G. A. Baker, and M. Maroncelli. Bimolecular Electron Transfer in Ionic Liquids: Are Reaction Rates Anomalously High? *J. Phys. Chem. B*, 116:1370–1384, 2012.

[34] R. A. Marcus. On The Theory of Oxidation-Reduction Reactions Involving Electron Transfer. I. *J. Chem. Phys.*, 24:966–978, 1956.

[35] R. A. Marcus and N. Sutin. Electron transfers in chemistry and biology. *Biochim. Biophys. Acta, Rev. Bioenerg.*, 811:265–322, 1985.

[36] N. Mataga. Multi-channel Possibility of Electron Transfer Reaction in the Excited State. *Bulletin of the Chemical Society of Japan*, 43:3623–3624, 1970.

[37] S. L. Mattes and S. Farid. *Organic Photochemistry; Vol. 6.* Dekker, New York, 1983.

[38] S. Murata, S. Y. Matsuzaki, and M. Tachiya. Transient Effect in Fluorescence Quenching by Electron Transfer. 2. Determination of the Rate Parameters Involved in the Marcus Equation. *J. Phys. Chem.*, 99:5354–5358, 1995.

[39] T. L. Nemzek and W. R. Ware. Kinetics of diffusion-controlled reactions. Transient effects in fluorescence quenching. *J. Chem. Phys.*, 62:477–489, 1975.

[40] S. Pagès, B. Lang, and E. Vauthey. Ultrafast Spectroscopic Investigation of the Charge Recombination Dynamics of Ion Pairs Formed upon Highly Exergonic Bimolecular Electron-Transfer Quenching:âĂĽ Looking for the Normal Region. *J. Phys. Chem. A*, 108:549–555, 2004.

[41] D. Rehm and A. Weller. Kinetics of Fluorescence Quenching by Electron and H-atom Transfer. *Isr. J. Chem.*, 8:259–271, 1970.

[42] Z. Ren, A. S. Ivanova, D. Couchot-Vore, and S. Garrett-Roe. Ultrafast Structure and Dynamics in Ionic Liquids: 2D-IR Spectroscopy Probes the Molecular Origin of Viscosity. *J. Phys. Chem. Lett.*, 5:1541–1546, 2014.

[43] I. Rips and J. Jortner. Dynamic solvent effects on outer-sphere electron transfer. *J. Chem. Phys.*, 87:2090–2104, 1987.

[44] A. Rosspeintner, G. Angulo, and E. Vauthey. Bimolecular Photoinduced Electron Transfer Beyond the Diffusion Limit: The Rehm-Weller Experiment Revisited with Femtosecond Time Resolution. *J. Am. Chem. Soc.*, 136:2026–2032, 2014.

[45] A. Rosspeintner, D. Kattnig, G. Angulo, S. Landgraf, G. Grampp, and A. Cuetos. On the Coherent Description of Diffusion-Influenced Fluorescence Quenching Experiments. *Chem.–Eur. J.*, 13:6474–6483, 2007.

[46] A. Rosspeintner, M. Koch, G. Angulo, and E. Vauthey. Spurious Observation of the Marcus Inverted Region in Bimolecular Photoinduced Electron Transfer. *J. Am. Chem. Soc.*, 134:11396–11399, 2012.

[47] A. Rosspeintner and E. Vauthey. Bimolecular photoinduced electron transfer reactions in liquids under the gaze of ultrafast spectroscopy. *Phys. Chem. Chem. Phys.*, 16:25741–25754, 2014.

[48] C. A. Rumble, A. Kaintz, S. K. Yadav, B. Conway, J. C. Araque, G. A. Baker, C. Margulis, and M. Maroncelli. Rotational Dynamics in Ionic Liquids from NMR Relaxation Experiments and Simulations: Benzene and 1-Ethyl-3-Methylimidazolium. *J. Phys. Chem. B*, 120:9450–9467, 2016.

[49] M. Rust, J. Lappe, and R. J. Cave. Multistate Effects in Calculations of the Electronic Coupling Element for Electron Transfer Using the Generalized Mulliken-Hush Method. *J. Phys. Chem. A*, 106:3930–3940, 2002.

[50] S. Sarkar, S. Mandal, C. Ghatak, V. G. Rao, S. Ghosh, and N. Sarkar. Photoinduced electron transfer in an imidazolium ionic liquid and in its binary mixtures

with water, methanol, and 2-propanol: Appearance of marcus-type of inversion. *J. Phys. Chem. B*, 116:1335–1344, 2012.

[51] S. Sarkar, R. Pramanik, C. Ghatak, V. G. Rao, and N. Sarkar. Photoinduced intermolecular electron transfer in a room temperature imidazolium ionic liquid: An excitation wavelength dependence study. *Chem. Phys. Lett.*, pages 211–216, 2011.

[52] Y. Shim and H. J. Kim. Adiabatic electron transfer in a room-temperature ionic liquid: Reaction dynamics and kinetics. *J. Phys. Chem. B*, 113:12964–12972, 2009.

[53] P. Siders and R. A. Marcus. Quantum effects for electron-transfer reactions in the "inverted region". *J. Am. Chem. Soc.*, 103:748–752, 1981.

[54] M. Smoluchowski. Three lectures on diffusion, Brownian movement and coagulation of colloidal particles. *Phys. Z.*, 17:585–599, 1916.

[55] M. Smoluchowski. Mathematical Theory of the Kinetics of the Coagulation of Colloidal Solutions. *Z. Phyik. Chem.*, 92:129–168, 1917.

[56] S. F. Swallen, K. Weidemaier, H. L. Tavernier, and M. D. Fayer. Experimental and Theoretical Analysis of Photoinduced Electron Transfer– Including the Role of Liquid Structure. *J. Phys. Chem.*, 100:8106–8117, 1996.

[57] A. Szabo. Theory of diffusion-influenced fluorescence quenching. *J. Phys. Chem.*, 93:6929–6939, 1989.

[58] H. L. Tavernier and M. D. Fayer. Solute–solute spatial distribution in hydrogen bonding liquids probed with time-dependent intermolecular electron transfer. *J. Chem. Phys.*, 114:4552, 2001.

[59] Y. Tsujii, A. Tsuchida, Y. Onogi, and M. Yamamoto. Stabilization of carbazole radical cation formed in poly(N-vinylcarbazole) by charge delocalization. *Macromolecules*, 23:4019–4023, 1990.

[60] O. S. Wenger. How Donor–Bridge–Acceptor Energetics Influence Electron Tunneling Dynamics and Their Distance Dependences. *Acc. Chem. Res.*, 44:25–35, 2011.

[61] B. Wu, M. Liang, M. Maroncelli, and E. W. Castner, Jr. Photoinduced Bimolecular Electron Transfer from Cyano Anions in Ionic Liquids. *J. Phys. Chem. B*, 119:14790–14799, 2015.

[62] B. Wu, M. Maroncelli, and J. Edward W. Castner. Photoinduced bimolecular electron transfer in ionic liquids. *J. Am. Chem. Soc.*, page ASAP, 2017.

[63] S. A. Yamada, H. E. Bailey, A. Tamimi, C. Li, and M. D. Fayer. Dynamics in a Room-Temperature Ionic Liquid from the Cation Perspective: 2D IR Vibrational Echo Spectroscopy. *J. Am. Chem. Soc.*, 139:2408–2420, 2017.

[64] X.-X. Zhang, M. Liang, N. P. Ernsting, and M. Maroncelli. Complete Solvation Response of Coumarin 153 in Ionic Liquids. *J. Phys. Chem. B*, 117:4291–4304, 2013.

[65] L. Zusman. Dynamical solvent effect in electron transfer reactions occurring in a mixture of two polar solvents. *J. Chem. Phys.*, 102:2580–2584, 1995.

[66] L. D. Zusman. Outer-Sphere Electron Transfer in Polar Solvents. *Chem. Phys.*, 49:295–304, 1980.

Chapter 5

Conclusions

Ionic liquids have great potential for energy applications. [4, 8, 15, 17] In this work, we studied the structures of some special ionic liquids, including silicon substituted ILs and zwitterionic liquids. We also systematically studied the photo-induced bimolecular electron transfer properties in ionic liquids. The key conclusions of these studies are described below

5.1 The Structure of Silicon Substituted ILs

Using high-energy X-ray diffraction and molecular dynamics simulations, we measured and calculated the bulk liquid structures for four silicon containing ionic liquids, Si-C_3-mim$^+$ / FSI$^-$, Si-C_3-mim$^+$ / NTf_2^-, Si-C_3-mim$^+$ / BETI$^-$ and Si-C_3-Pyrr$^+$ / NTf_2^- and compared them with other silicon or hydrocarbon side chain ILs including Si-mim$^+$ / NTf_2^-, C-mim$^+$ / NTf_2^-, SiOSi-mim$^+$ / NTf_2^- and Si-pyrr$^+$ / NTf_2^-. We achieved good agreement between the structure factors $S(q)$ obtained from experiments and simulations.

Comparing the structure factors and spatial distributions in Si-mim$^+$ / NTf_2^- and C-mim$^+$ / NTf_2^- (Figure 5.1), we found that the intermolecular correlation is stronger in C-mim$^+$ / NTf_2^- than in Si-mim$^+$ / NTf_2^-. This result supports the conclusion by Shirota et al.[14] that the low viscosity of Si-mim$^+$ / NTf_2^- is related to the weaker interactions between ions.

Despite its polar nature, the pentamethyldisiloxymethyl side chain in SiOSi-mim$^+$ / NTf_2^- is still long enough to display a FSDP in the liquid structure factor $S(q)$. Other ILs with mildly polar functional groups, such as diethers, do not display a FSDP because of the predominant coiled conformations of the ether substituents.[5, 16] To our

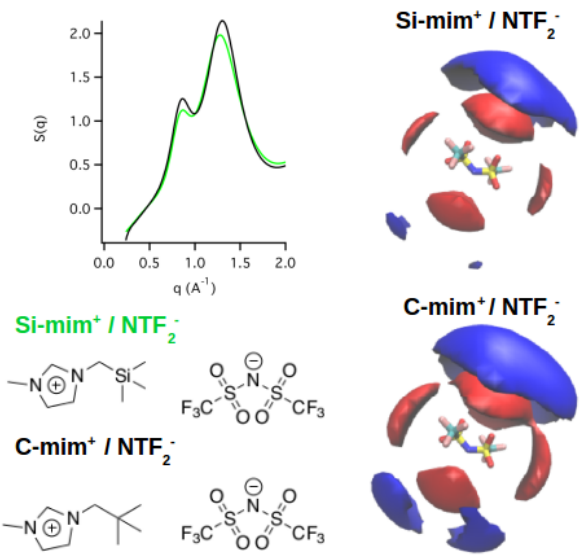

Figure 5.1: Effect of Silicon substitution. Top left shows the comparison of experimental structure factors, and right panels shows the spatial distributions of cations (red) and anions (blue) around anions.

knowledge, this report of the FSDP in the $S(q)$ for SiOSi-mim$^+$ / NTf$_2^-$ is the first time that one has been observed for an IL having a polar group instead of a hydrophobic functional group. This result indicates that if the side chain is long enough and has sufficiently different interactions between the cationic head group and the functional group tail, polar chains can also segregate and form FSDP in ionic liquids.

An anion with a larger fluorinated group changes the relative fraction of contributions to $S(q)$ from polar head groups vs. hydrophobic perfluorocarbon groups, which will in turn cause a shift of the adjacency peak to lower q values. The longer fluorinated segment in the anion will lead to a smaller intermediate-range-domain in the IL structure, as indicated by the FSDP shifting to higher q range.

5.2 Structure of Zwitterionic Liquids

The results obtained by comparing the structural properties of the Zw-ILs and corresponding ILs are summarized graphically in Fig. 5.2. While our electronic structure calculations reveal that the charge densities of the anionic and cationic moieties are quite

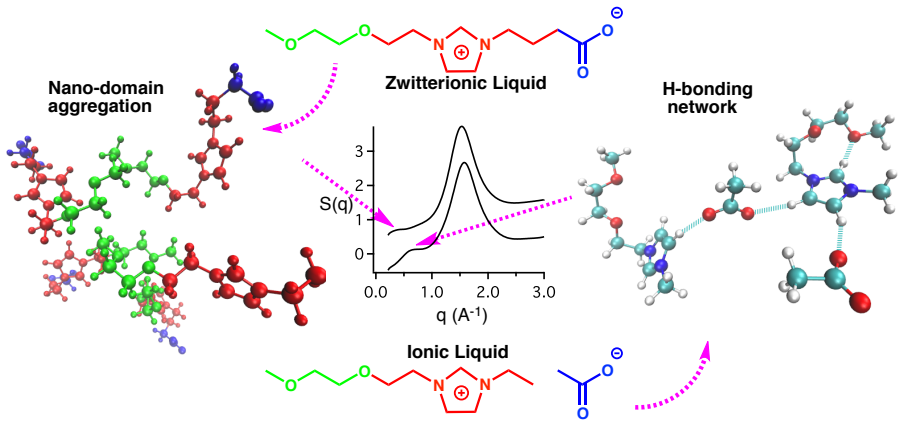

Figure 5.2: Detailed analyses of $S(q)$ show that the intermediate range ordering in Zw-IL vs. the IL arise from subtly different interactions.

similar between the Zw-ILs and the ILs, the possibilities for developing H-bonding networks are more extensive for the acetate-anion ILs. In contrast, the Zw-ILs are shown to display nano-domain aggregation, as revealed by the ionic partitioning of the liquid structure factor $S(q)$. Fig. 5.2 illustrates these two points on the right and left sides of the image, respectively.

We have measured and compared the structure factors $S(q)$ of the zwitterionic liquids OE_2imC_3C, OE_2imC_5C and compared these with the conventional ionic liquids OE_2eim^+/OAc^- and $Im^+_{2,1}/OAc^-$. The ionic partitioning of the structure factors shows that charge ordering is still a significant feature for zwitterionic liquids, but is weaker than in conventional ionic liquids. A first sharp diffraction peak is observed for each of the liquids except the smallest, $Im^+_{2,1}/OAc^-$, but the FSDP has subtly different origins between Zw-ILs and ILs. In OE_2imC_3C, the FSDP is mostly due to nano-domain aggregation, but in OE_2eim^+/OAc^-, it is most likely due to the hydrogen bonding network. The structure of OE_2imC_5C is between those of OE_2imC_3C and OE_2eim^+/OAc^-, which shows that increasing positive and negative charge separation has a similar effect to eliminating the carbon-carbon bond in OE_2imC_3C to make the zwitterionic OE_2eim^+/OAc^-.

The interactions between these structural features observed in the total and deconstructed $S(q)$ data indicate that H-bonding is an important structural motif for these

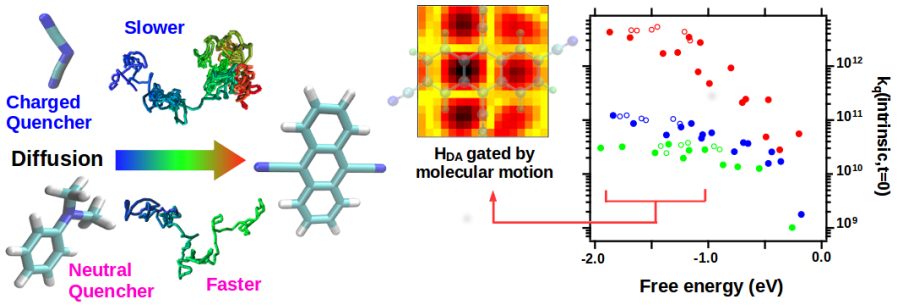

Figure 5.3: Neutral and anionic donors have very different diffusion coefficients in ionic liquids, which leads to different observed steady-state quenching rate. But they have no difference in intrinsic electron transfer rate.

liquids, which may be the reason that the only ambient temperature liquid zwitterions have an imidazolium core, as opposed to the common tetraalkyl ammonium or phosphonium cations.

5.3 Photo-Induced Bimolecular Electron Transfer

The primary experimental results discussed in Chapter 4 include both time-resolved and steady-state fluorescence quenching of a series of five photo-excited fluorophores in solutions of two ionic liquids and acetonitrile. The two ionic liquids share the same bistrifylamide (NTf_2^-) anion, while the cations ($Im_{2,1}^+$ and $P_{14,6,6,6}^+$) are chosen to present the two extremes of amphiphilicity. Two neutral aromatic quenchers, and four cyano-functionalized anionic quenchers were used. The resulting F-Q sets provide us with a range of reaction free energies in excess of 2.0 eV, permitting a systematic Rehm-Weller type analysis and a check for Marcus inverted rate regime behavior, which was not observed. The 1000-fold variation of the solvent viscosities permits detailed and quantitative testing of reaction diffusion models.

Rate constants obtained at low quencher concentrations (0.05 M) from Stern-Volmer analysis showed neutral and anionic quenchers to have similar diffusion-limited rates in acetonitrile, while in both ionic liquids, neutral quenchers are much faster. Relative to predictions of simple diffusion-limited reaction models, the effective quenching rate

constants observed are all greater, by a factor of 2 in CH_3CN and factors of 10 in $Im^+_{2,1}$ / NTf_2^- and 30 in $P^+_{14,6,6,6}$ / NTf_2^-, even when the best measured or estimated values for quencher and fluorophore diffusivities are used. As previously discussed, [6, 7] such simplified kinetic treatments are generally not applicable for analyzing quenching data in ionic liquid solutions. Nonlinear Stern-Volmer plots and nonexponential fluorescence transients in the ionic liquid solvents indicate that these reactions occur well outside of the stationary reaction limit.

We therefore used an approximate solution of the spherically symmetric diffusion-reaction problem [3] to test models having different distance dependence reaction rates, $\kappa(r)$, against the experimental data. The simplest of these, the Smoluchowski and Collins Kimball models, which assume reaction occurs only at a single F-Q distance, were found to be inadequate to model the nonexponential character of the fluorescence transients observed in the ionic liquids. An extended-sink model, which allows for reaction over a range of F-Q distances was then tested. This model has only three adjustable parameters: D, the relative diffusion coefficient between quencher and fluorophore, r_1, the extent of the first solvation shell, and κ_0, the rate constant for contact F-Q pairs. It fit nearly all of the data to within the expected uncertainties, with most values of D falling within $\pm 30\%$ of the measured or best estimated values. Values of r_1 were found to be close to the simulated first solvation shell radii, and the initial quenching rates, $k_q(0)$, to correlate reasonably with the reaction free energies ΔG_0.

The most intricate diffusion-reaction model we considered includes a full treatment of the electron transfer process covering both the nonadiabatic and solvent-controlled adiabatic regimes. [11] Classical all-atom molecular dynamics simulations were used to constrain some of the key parameters required in this model and to provide insight into the simplifications it entails. The simulated solvation structures in CH_3CN solutions showed that neutral quenchers are slightly enhanced within the first solvation shell of fluorophore, while anionic quenchers are under represented. DFT calculations on F-Q pairs extracted from simulations in neat quenching solvents were used to estimate the electronic coupling values, H_{DA}, via the Generalized Mulliken-Hush method. [12] As with previous studies, [2, 13] values of H_{DA} were found to be very sensitive to

both the relative orientations and separations between the quencher and fluorophore. This sensitivity highlights the severe approximation made by spherically-symmetric diffusion-reaction models, which consider only on the center-of-mass separations between quencher and fluorophore (r).

Information from these simulations was nevertheless used to create simplified radial distribution functions $g(r)$ and orientationally averaged coupling functions $H_{DA}(r)$ needed for electron transfer modeling of the quenching data. The treatment included a distinct radial dependence beyond the first solvation shell, and only two parameters optimized for each F/Q/solvent system: the net diffusivity D and the reaction free energy ΔG_0. The diffusion coefficients obtained from this model were found to be very close to those from the extended sink model and to estimated values. Apart from the faster diffusion of neutral *vs.* anionic quenchers, no evidence was found for a significant effect of quencher charge in these reactions.

Values of the reaction free energies required to fit the quenching data to this electron transfer model deviated from estimated values by much more than expected uncertainties, especially in the case of ionic liquid solvents. In order to fit the quenching data, optimized values of ΔG_0 had to be artificially reduced in systems with large driving force (ΔG_0 <-0.8 eV) in order to reproduce the relatively weak dependence of the observed rates of contact reaction, $k_q(0)$, on driving force. The relatively flat Marcus plots ($k_q(0)$ vs. ΔG_0(est)) in the ionic liquids suggest that some factor not accounted for in the standard model is limiting reaction rates in these solvents. Several possible sources of this shortcoming were considered. The one we believe most likely is the neglect of the strong orientation dependence of H_{DA} (and other quantities) when using a spherically symmetric diffusion equation. This proposal is similar to that proposed to account for the fluorophore dependence of quenching in neat DMA.[1, 9, 10] We hypothesize that reaction rates in ionic liquids may be limited by small relative adjustments within contact pairs, which serve to gate the electron transfer in a manner not accounted for by spherical diffusion-reaction models.

We also measure the photo-induced electron-transfer reaction rates between a series of cationic DMAP donors and three cyano-substituted anthracene acceptors. The

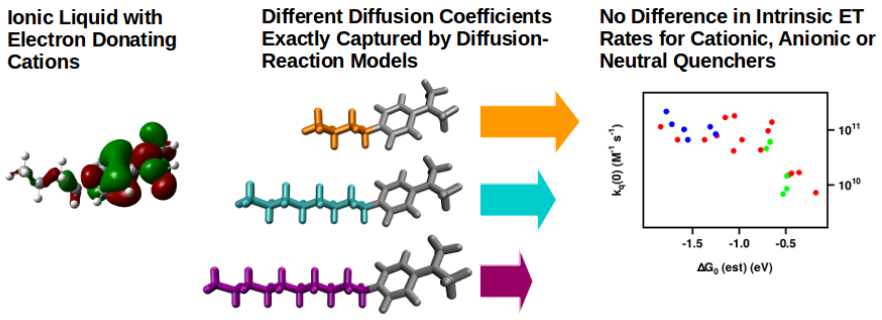

Figure 5.4: Cations could also be electron donors. Despite diffusion, there no apparent distinction exists as a function of quencher charge.

three DMAP quenchers have very similar oxidation potentials of 1.88 V, making them about 1.2 V less favorable as reductants than the neutral analogous 1-alkyl-N,N'-dimethylanilines. Analysis of the data collected here using either simple Stern-Volmer treatments or more appropriate reaction-diffusion modeling show that these cationic quenchers follow the same general trends established by the neutral and anionic quenchers studied previously. Thus, we conclude that these weakly exergonic reactions occur via the same electron transfer mechanism operative in the other quenchers and that there no apparent distinction exists as a function of quencher charge.

Bibliography

[1] G. Angulo, A. Cuetos, A. Rosspeintner, and E. Vauthey. Experimental evidence of the relevance of orientational correlations in photoinduced bimolecular reactions in solution. *J. Phys. Chem. A*, 117:8814–8825, 2013.

[2] E. W. Castner, Jr., D. Kennedy, and R. J. Cave. Solvent as Electron Donor: Donor/Acceptor Electronic Coupling Is a Dynamical Variable. *J. Phys. Chem. A*, 104:2869–2885, 2000.

[3] O. K. Dudko and A. Szabo. Time-Dependent Rate Coefficients for Diffusion-Influenced Reactions with Centrosymmetric Potentials. *J. Phys. Chem. B*, 109:5891–5894, 2005.

[4] G. G. Eshetu, M. Armand, H. Ohno, B. Scrosati, and S. Passerini. Ionic liquids as tailored media for the synthesis and processing of energy conversion materials. *Energy Environ. Sci.*, 9:49–61, 2016.

[5] H. K. Kashyap, C. S. Santos, N. S. Murthy, J. J. Hettige, K. Kerr, S. Ramati, J. Gwon, M. Gohdo, S. I. Lall-Ramnarine, J. F. Wishart, C. J. Margulis, and E. W. Castner, Jr. Structure of 1-Alkyl-1-methylpyrrolidinium Bis(trifluoromethylsulfonyl)amide Ionic Liquids with Linear, Branched, and Cyclic Alkyl Groups. *J. Phys. Chem. B*, 49:15328–15337, 2013.

[6] M. Koch, A. Rosspeintner, G. Angulo, and E. Vauthey. Bimolecular Photoinduced Electron Transfer in Imidazolium-Based Room-Temperature Ionic Liquids Is Not Faster than in Conventional Solvents. *J. Am. Chem. Soc.*, 134:3729–3736, 2012.

[7] M. Liang, A. Kaintz, G. A. Baker, and M. Maroncelli. Bimolecular Electron Transfer in Ionic Liquids: Are Reaction Rates Anomalously High? *J. Phys. Chem. B*, 116:1370–1384, 2012.

[8] D. R. MacFarlane, N. Tachikawa, M. Forsyth, J. M. Pringle, P. C. Howlett, G. D. Elliott, J. James H. Davis, M. Watanabe, P. Simon, and C. A. Angell. Energy applications of ionic liquids. *Energy Environ. Sci.*, 7:232–250, 2014.

[9] A. Morandeira, A. Fürstenberg, J.-C. Gumy, and E. Vauthey. Fluorescence quenching in electron-donating solvents. 1. influence of the soluteâĹŠsolvent interactions on the dynamics. *J. Phys. Chem. A*, 107:5375–5383, 2003.

[10] A. Morandeira, A. Fürstenberg, and E. Vauthey. Fluorescence quenching in electron-donating solvents. 2. solvent dependence and product dynamics. *J. Phys. Chem. A*, 108:8190–8200, 2004.

[11] I. Rips and J. Jortner. Dynamic solvent effects on outer-sphere electron transfer. *J. Chem. Phys.*, 87:2090–2104, 1987.

[12] M. Rust, J. Lappe, and R. J. Cave. Multistate Effects in Calculations of the Electronic Coupling Element for Electron Transfer Using the Generalized Mulliken-Hush Method. *J. Phys. Chem. A*, 106:3930–3940, 2002.

[13] P. O. J. Scherer and M. Tachiya. Computer simulation studies of electron transfer parameters for cyanoanthracene/n,n-dimethylaniline solutions. *J. Chem. Phys.*, 118:4149–4156, 2003.

[14] H. Shirota and E. W. Castner, Jr. Why Are Viscosities Lower for Ionic Liquids with -CH2Si(CH3)3 vs -CH2C(CH3)3 Substitutions on the Imidazolium Cations? *J. Phys. Chem. B*, 109:21576–21585, 2005.

[15] R. P. Swatloski, S. K. Spear, J. D. Holbrey, and R. D. Rogers. Dissolution of cellose with ionic liquids. *J. Am. Chem. Soc.*, 124(18):4974–4975, 2002. PMID: 11982358.

[16] A. Triolo, O. Russina, R. Caminiti, H. Shirota, H. Y. Lee, C. S. Santos, N. S. Murthy, and E. W. Castner, Jr. Comparing intermediate range order for alkyl- vs. ether-substituted cations in ionic liquids. *Chem. Commun.*, 48:4959–4961, 2012.

[17] J. F. Wishart. Energy applications of ionic liquids. *Energy Environ. Sci.*, 2:956–961, 2009.

List of Publications

(10) B. Wu, M. Liang, S. Lall-Ramnarine, J. F. Wishart, M. Maroncelli and E. W. Castner Jr., "Photo-induced Bimolecular Electron Transfer in Ionic Liquids: Cationic Electron Donors", manuscript in preparation.

(9) J. Fetherolf, B. Wu, S. Ramati, S. Lall-Ramnarine, J. Mukhlall, M. Gohdo, J. F. Wishart, C. J. Margulis and Edward W. Castner, Jr. "Structural Diferences between Bistriflimide-Anion Ionic Liquids: Imidazolium vs. Pyrrolidinium Cations with Straight or Branched Alkyl Tails", *J. Chem. Phys.*, submitted.

(8) A. B. Biedron, B. Wu, T. Endo, K. Takahashi, R. A. Bartynski, E. L. Garfunkel, E. W. Castner, Jr., and S. Rangan, "The Vacuum-Liquid Interface of Silicon Functionalized Ionic Liquids.", *J. Chem. Phys.*, submitted.

(7) B. Wu, K. Kuroda, K. Takahashi, and E. W. Castner, Jr., "Structural Analysis of Zwitterionic Liquids vs. Homologous Ionic Liquids.", *J. Chem. Phys.*, submitted.

(6) B. Wu, M. Maroncelli, and E. W. Castner, Jr., "Photoinduced Bimolecular Electron Transfer in Ionic Liquids.", *J. Am. Chem. Soc.*, **2017**, *139*, 14568–14585, doi: 10.1021/jacs.7b07611.

(5) A. Mariani, M. Bonomo, B. Wu, B. Centrella, D. Dini, E. W. Castner, Jr. and L. Gontrani "Intriguing transport dynamics of ethylammonium nitrate–acetonitrile binary mixtures arising from nano-inhomogeneity.", *Phys. Chem. Chem. Phys.*, **2017**, *19*, 27212–27220, doi:10.1039/C7CP04592A.

(4) B. Wu, Y. Yamashita, T. Endo, K. Takahashi, and E. W. Castner, Jr., "Structure and Dynamics of Ionic Liquids: Trimethylsilylpropyl-Substituted Cations and Bis(sulfonyl)amide Anions.", J. Chem. Phys., **2016**, *145*, 244506, doi: 10.1063/1.4972410.

(3) B. Wu, H. Shirota, S. I. Lall-Ramnarine, E. W. Castner, Jr., "Structure of ionic liquids with cationic silicon-substitutions.", J. Chem. Phys., **2016**, *145*, 114501, doi: 10.1063/1.4962257.

(2) K. B. Dhungana, L. F. O'Faria, B. Wu, M. Liang, M. C. C. Ribeiro, C. J. Margulis, E. W. Castner, Jr., "Structure of cyano-anion ionic liquids: X-ray scattering and simulations.", J. Chem. Phys., **2016**, *145*, 024503, doi: 10.1063/1.4955186.

(1) B. Wu, M. Liang, M. Maroncelli, and E. W. Castner, Jr., "Photo-Induced Bimolecular Electron Transfer from Cyano-Anions in Ionic Liquids.", J. Phys. Chem. B, **2015**, *119*, 14790–14799, doi: 10.1021/acs.jpcb.5b09216.